Freshwater Variability in the Arctic Eurasian Shelf Seas: Satellite Sea Surface Salinity and Inter-Annual Variability to Predict Arctic System Change

Phoebe Hudson

Thesis submitted in fulfilment of the requirements for the degree of Doctor of Philosophy to the University of Edinburgh

2024

I. Declaration

I declare that this thesis has been composed solely by myself, and that it contains only my work except where otherwise specified, or where the work is explicitly indicated below to have formed part of a jointly-authored publication. This work has not been submitted for any other degree or professional qualification. The candidate confirms that appropriate credit has been given within the thesis where reference has been made to the work of others.

Chapter 3 Laptev Sea

Citation: Hudson, P.A., Martin, A.C.H., Josey, S.A., Marzocchi, A., Angeloudis, A., 2024. Drivers of Laptev Sea interannual variability in salinity and temperature. Ocean Sci. 20, 341–367. https://doi.org/10.5194/os-20-341-2024

Author contributions: PH: conceptualization, methodology, validation, formal analysis, visualization, writing (original draft and review and editing). AM: supervision, funding acquisition, conceptualization, analysis, writing (review and editing). SJ: supervision, analysis, writing (review and editing). AM: supervision, analysis, writing (review and editing). AA: supervision, analysis, writing (review and editing).

II. Acknowledgements

It is only fitting that I submit around Thanksgiving as this thesis wouldn't have been possible without everyone who has supported me along the way.

First off, a big thank you to NOC for hosting me and to all my supervisors - I couldn't have hoped for a better team to go through this with. Especially to Adrien - you've taught me so much and injected so much humour into our meetings - our discussions were sometimes the highlight of my week and I almost always left with a smile on my face.

I also want to thank everyone at SPIRE but especially Phil, Matt and Jess for a fantastic industry placement and for immediately making me feel like part of the team.

This thesis also wouldn't have been possible without all the friends who have supported me along the way including:

- All my INSPIREing friends especially Clara, Izzy, Mark and Shaun - rain or shine, up or down, soup or biscuit, our ridiculous conversations brightened Southampton even on the grimmest of days.
- SENSE and especially the SENSE COVID cohort for keeping me going, especially through the challenging first year of lockdowns and remote working.
- My other "Southampton" friends - Alex, Tim for the many weekend(+) trips (Sanne that also includes you - thank you for letting me escape the COVID-ridden world to come live with you for a few months!)
- All my remote friends around the world especially Bea for always being there.
- Everyone that I met on JC238, and at the various other conferences, hackathons and bootcamps that I have attended over the course of my PhD.
- Coaches and team mates at Eastleigh / Bursledon / Sholing and everyone at Totton Octopush Club - for being a much-needed outlet for my body and my fried brain.

A special thanks to Ghost Fishing UK- for giving me a purpose in life outside my PhD. The days I have spent recovering ghost gear have been the most rewarding and enjoyable of the last 4 years and to have been able to do them with some of the most wonderful, caring and fun people is just incredible.

Lastly, this wouldn't have been possible without James and my family - for the many read throughs and discussions, for everything you've taught me and for the never-ending love and support.

Thank you.

III. Abstract

Eurasian Rivers provide a quarter of total fresh water to the Arctic, maintaining a persistent fresh layer that covers the surface Arctic Ocean. This freshwater export controls Arctic Ocean stratification, circulation, and basin-wide sea ice concentration. The Russian Arctic receives around 2/3 of the river runoff to the Arctic, primarily from the Ob, Yenisei and Lena Rivers which outflow into the Kara and Laptev Sea as a particularly shallow plume. Previous in-situ and modelling studies suggest that local wind forcing is a driver of variability in Eurasian Arctic sea surface salinity (SSS) but there is no consensus on the roles river runoff and sea ice cover have in contributing to this variability or on the dominant driver of variability. The dominant controls on SSS variability have also been suggested to vary regionally, with suggested differences in the Kara and Laptev Sea.

Until recently, satellite SSS retrievals were insufficiently accurate for use in the Arctic. However, retreating sea ice cover and continuous progress in satellite product development have significantly improved SSS retrievals. This thesis first shows the value and potential of satellite SSS as a useful tool to strengthen our understanding of Arctic SSS dynamics. Satellite SSS is found to agree well with in situ data ($r \geq 0.81$) with notably better agreement than reanalysis products and in situ data ($r \leq 0.76$).

Satellite SSS is then used in combination with reanalysis and in-situ products to first compare and contrast the processes controlling the interannual variability of summer SSS, sea surface temperature (SST) and sea ice concentration (SIC) variability and their interactions in the Laptev and Kara Sea and in the Vilkitsky Strait.

In the Laptev Sea, zonal wind is the dominant driver of offshore/alongshore Lena River plume transport, with eastward wind driving alongshore transport (and westward wind driving offshore transport). This drives differences in both SSS and SST and spatial variability in SIC across the Laptev and East Siberian Sea. Conversely, Lena runoff does not appear to play a role in controlling interannual variability in SSS, SST, or SIC in the Laptev and East Siberian Sea.

In the Kara Sea, zonal (and meridional) wind and Ob and Yenisei runoff all appear to be key drivers of whether the fresh plume is transported offshore or alongshore. Whilst eastward wind forcing is the dominant driver of alongshore transport, as is true in the Laptev Sea, a high ratio of summer Yenisei runoff/ spring Ob runoff can accentuate the low SSS anomalies offshore driven by westward wind forcing. Zonal wind forcing also has an influence on SST but is not the dominant driver of variability in SST, as it is in the Laptev Sea. Therefore, SSS and SST are notably less closely coupled in the Kara Sea and the zonal wind does not drive differences in Kara SIC.

In the Vilkitsky Strait, strong eastward wind drives buoyancy driven transport of the Ob-Yenisei plume through Vilkitsky Strait and into the western Laptev Sea and can occur over one summer season. Plume transport has a consistent SST signature, suggesting co-variability between SSS and SST but is not drive a notable difference in SIC. After a summer of westward wind forcing, plume transport through the strait appears to occur over winter. However, differences in timing drive very different SSS/SST patterns and in turn stratification dynamics.

The dominant controls on Eurasian-wide interannual variability are then identified and the implications of these on sea ice persistence and Arctic-wide freshwater storage are assessed. The Arctic Oscillation Index (AOI) is found to be a dominant control on local wind forcing in all three regions, and drives a consistent pattern of freshwater transport across all Eurasian shelf seas, which appears to be accelerating in recent decades. This pattern of freshwater transport

persists until at least the following year and appears to have implications on autumn and spring sea ice persistence.

Finally, the implications of these findings are inferred in the context of climate change. The dominance of zonal wind and the AOI as a key driver of SSS (and SST) interannual variability suggests that understanding variability in wind stress and its changes is key to predicting future freshwater transport from the Eurasian shelf seas and its impacts on Arctic circulation.

IV. Lay summary:

Eurasian rivers, particularly Russia's Ob, Yenisei, and Lena Rivers, supply a quarter of the total amount of freshwater to the Arctic Ocean. This freshwater predominantly sits in a layer on top of other Arctic Ocean water and plays a crucial role in shaping ocean transport around the Arctic and in controlling how much sea ice there is. Previous studies suggest that local wind forcing is one of the main controls of variability in Eurasian Arctic sea surface salinity (SSS) but there is no consensus on the roles river runoff and sea ice cover in contributing to this variability.

Sea surface salinity provides a way to map this freshwater and how it moves around the Arctic. However, historically, data from satellites wasn't accurate enough for studying Arctic SSS, but recent improvements in satellite technology, combined with the decrease in sea ice with climate change, now allow for more accurate measurements over more of the ocean.

This thesis examines how these satellite SSS measurements can enhance our understanding of Arctic Ocean processes. By combining satellite data with other observation methods, this study explores how different factors, such as wind and river runoff, affect salinity, temperature, and sea ice in different parts of the Eurasian Arctic, specifically the Kara and Laptev Sea and the Vilkitsky Strait.

Key findings reveal that eastward/westward wind greatly influences SSS in all these areas, with eastward winds pushing fresh river plumes along the coast and westward winds pushing them offshore. Conversely, river runoff impacts SSS differently in different regions: the magnitude of Lena River runoff has no effect on the Laptev Sea's salinity, whereas Ob and Yenisei River runoff significantly influence the Kara Sea.

Large-scale atmospheric circulation is the main control on local wind patterns and drives a consistent pattern of freshwater transport across the Eurasian coastal areas. This pattern of freshwater transport remains present until at least the following year and seems to affect how long sea ice persists into the autumn and following spring. The strong role of local, and large-scale wind patterns on freshwater transport suggests that understanding wind variability and how it changes over time is crucial for predicting future Arctic circulation and sea ice cover.

Table of Contents

V. List of Acronyms

AOI:	Arctic Oscillation Index
AVHRR:	Advanced Very High Resolution Radiometer
AW:	Atlantic Water
CCI:	Climate Change Initiative
CERSAT:	Centre ERS d'Archivage et de Traitement
CMEMS:	Copernicus Marine Environment Monitoring Service
CORA:	Coriolis Ocean database for ReAnalysis
CTD:	conductivity temperature, depth
ECMWF:	European Centre for Medium-Range Weather Forecasts
ERA5:	ECMWF Reanalysis v5
HadISST:	Hadley Centre Sea Ice and Sea Surface Temperature data set
JPL:	Jet Propulsion Laboratory
MDT:	mean dynamic topography
METSS:	mean eastward turbulent surface stress
MNTSS:	mean northward turbulent surface stress
NABOS:	Nansen and Amundsen Basins Observational System
NCEI:	National Centers for Environmental Information
Pi-MEP:	Pilot-Mission Exploitation Platform
PW:	Pacific Water
RMSD:	root mean square difference
RSS:	Remote Sensing Systems
SASSIE:	Salinity and Stratification at the Sea Ice Edge
SIC:	sea ice concentration
SLA:	sea level anomaly
SMAP:	Soil Moisture Active Passive
SMOS:	Soil Moisture and Ocean Salinity
SSS:	sea surface salinity
SST:	sea surface temperature
UDASH:	Unified Database for Arctic and Subarctic Hydrography

List of Tables

List of Figures

Chapter 1 Introduction

The Arctic Ocean is a very fresh basin, which contains only 1% of global ocean volume. This includes the confluence from the North Atlantic and Pacific oceans as well as the widespread northern hemisphere rivers, which amount to 10% of global river runoff (Aagaard and Carmack, 1989; McClelland et al., 2012). The ocean is topped by a seasonally varying sea ice layer, which acts as a strong control on circulation dynamics and distinguishes the Arctic from other regions. The sea ice cover is also a dominant control on nutrient cycling and primary productivity, which in turn supports the fisheries and ecosystems that are vital to local communities. However, this sea ice cover also restricts maritime accessibility. As more summer sea ice melts due to climate change, this remote and seasonally-isolated region may soon experience drastic change, impacting local ecosystems and downstream freshwater transport but also presenting new viable shipping routes. Such impacts place increased interest in how the Arctic Ocean is changing.

1.1 Overview of current Arctic Ocean circulation and freshwater transport

Ocean circulation in the Arctic (Figure 1.1) is dominated by relatively warm and salty Atlantic Water (AW) that enters the Arctic basin via the Barents Sea and Fram Strait and the warm and relatively fresh Pacific waters (PW) that enter the Arctic through the Bering Strait (Rudels et al., 2013; Timmermans and Marshall, 2020). These waters are cooled and freshened as they are circled around the Arctic Ocean, typically clockwise in the Beaufort Gyre in the Canadian Arctic and anticlockwise in the Eurasian Arctic (Armitage et al., 2018). They are eventually then exported across the Central Arctic to the Nares and Fram straits, and eventually to the deep North Atlantic, via the Transpolar Drift (LeBlond, 1980; Münchow et al., 2006; Woodgate et al., 1999). The transformation and cooling of this Atlantic Water drives densification and sinking, which drives the Atlantic Meridional Overturning Circulation and helps regulate global climate.

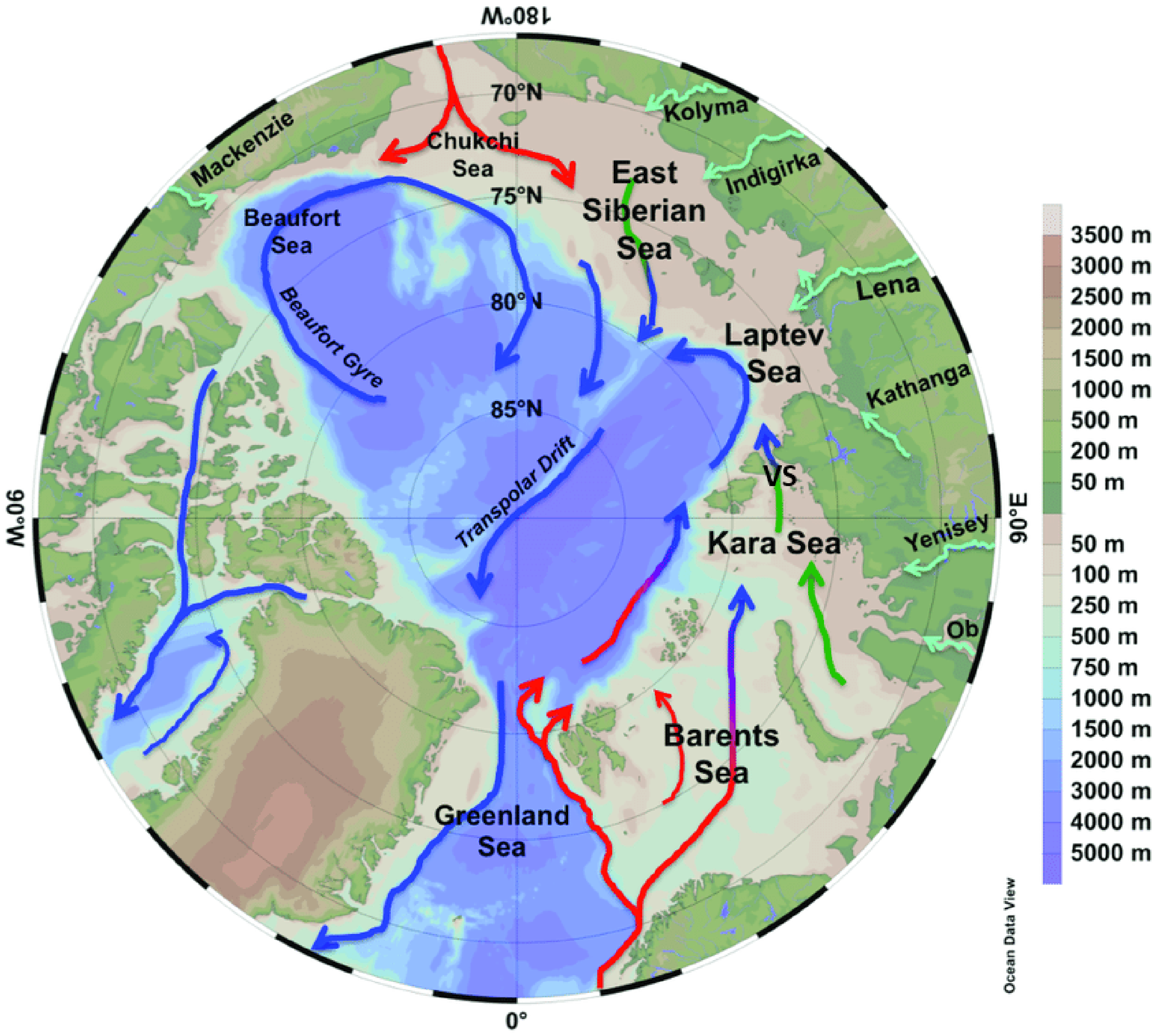

Figure 1.1: Overview diagram of Arctic Ocean circulation modified from (Gonçalves-Araujo, 2016). Inflowing relative warms surface currents are shown in red with colder surface currents in blue and with intermediate and rivers and riverine input in green. Key features of the Arctic Ocean include: Beaufort Gyre, Transpolar Drift, Vilkitsky Strait (VS). The main study regions of this thesis are the Kara, Laptev and East Siberian Sea and the Vilkitsky Strait.

The extensive shallow shelves of the Arctic Ocean, and its many freshwater sources, means it is strongly influenced by surface freshwater processes which makes it a region with dramatic salinity variability (Tarasenko et al., 2021). Freshwater from precipitation, river runoff and land and sea ice melt together generate a cold, fresh, buoyant surface layer, which sits above the inflowing Atlantic / Pacific Water, creating the halocline that governs Arctic Ocean stratification (Timmermans and Marshall, 2020). This fresh surface layer minimizes heat exchange between Atlantic / Pacific Water and the overlying sea ice, in turn maintaining the sea ice barrier that partially covers the Arctic Ocean year-round, and regulating the seasonal cycle of stratification and sea ice (Polyakov et al., 2017a). The presence of both sea ice and this fresh surface layer limit the exchange of heat, freshwater and momentum between the atmosphere and deeper ocean, and are a key control on Arctic Ocean circulation (Ricker et al., 2017). However, untangling the respective role of each of the above freshwater processes in controlling this state and how they interact proves complicated due to their intensely coupled nature and their strong inter-annual, seasonal and regional variations (Brown et al., 2020).

1.2 Individual observations and predictions of Arctic system change in the context of our changing climate

Understanding Arctic Ocean freshwater processes is becoming increasingly important to predict how climate change will impact the Arctic system. The Arctic atmosphere has been warming at two to four times the global average rate over the last half century (Rantanen et al., 2022; Walsh, 2014). Dramatically warming Arctic surface air temperatures have altered Arctic atmospheric circulation and caused ocean warming, an intensification of the hydrological cycle, snow and ice melt, and increases in river runoff (Overland and Wang, 2010; Prowse et al., 2015). Arctic surface air temperatures are projected to warm at least a further 4 °C regardless of emissions scenario but up to 10 °C by 2100, which will only accelerate these changes (Masson-Delmotte et al., 2021; Ono et al., 2022).

Arctic atmospheric warming has caused increases in the temperature and ocean heat transport of waters entering the Arctic from the Atlantic and Pacific, which are contributing to the warming Arctic ocean (Masson-Delmotte et al., 2021; Woodgate et al., 2012). This warming has caused a thinning and decrease in sea ice extent and led to a more mobile sea ice cover (Stroeve and Notz, 2018a). This will likely result in at least one sea ice free summer before 2050 and may occur as early as 2030 (Heuzé and Jahn, 2024; Masson-Delmotte et al., 2021). The diminishing seasonal sea ice cover and rapid warming is driving Atlantic Water to higher latitudes (Arctic Borealisation) (Polyakov et al., 2020a). The loss of sea ice cover also exposes the Arctic Ocean, decreasing the albedo, or reflectivity, over the Arctic, and enhancing atmosphere/ocean heat and momentum exchange. This decrease in albedo causes the ocean to absorb more heat, increasing sea surface temperatures, limiting further sea ice growth and further amplifying Arctic atmospheric warming (Praetorius et al., 2018). The thinner and more mobile sea ice cover also has the potential to increase momentum transfer to the ocean, in turn accelerating Arctic surface currents, but the manifestation of this change is currently poorly understood (Giles et al., 2012; Nummelin et al., 2015). Both Arctic Borealisation and the loss of sea ice, and resulting increasing atmosphere-ocean heat and momentum transfer, have the potential to drive a very different, increasingly well-mixed Arctic Ocean state (Intergovernmental Panel on Climate Change (IPCC), 2019). This increasingly well-mixed state could further accelerate additional sea-ice loss by allowing more heat to reach the surface. This potential future would represent a complete change to current Arctic circulation, which has not been seen since the Last Interglacial Period (Sime et al., 2022, 2023). However, the warming Arctic and loss of sea ice have already been linked to changes in atmospheric circulation, and in turn to increased extreme weather over the mid-latitudes (Cohen et al., 2014; Screen, 2017; Ye et al., 2024).

The rapid rate of atmospheric warming over the Arctic, compared to that at lower latitudes, has also decreased the temperature gradient between low and high latitudes and caused increased moisture and heat transport to high latitudes (Zhang, 2008). In turn, this has also led to a general increase in precipitation over the Arctic and has altered the mean state of Arctic atmospheric circulation (Vihma et al., 2016; Cohen et al., 2013). In addition, atmospheric and oceanic warming has led to a general freshening of the surface Arctic Ocean (Carmack et al., 2016), with increasing contribution from sea and land ice melt and river runoff (Alkire et al., 2017; Haine et al., 2015). The freshwater contribution from net P-E (precipitation minus evaporation) is predicted to increase 30% by 2100, and runoff is predicted to increase by 14% (Haine et al., 2015). This excess freshwater has the potential to further freshen the surface Arctic Ocean, and in turn drive a strengthening of the Arctic Ocean surface halocline. However, the impacts of this freshening appear to have been compensated so far by a strengthening of surface geostrophic currents, with sea ice loss and the resulting increase in atmosphere-ocean momentum transfer (Armitage et al., 2018). Understanding the interplay between these changes, particularly the potential for increased stratification or mixing, is crucial for predicting the future state of the Arctic system. In turn, this will impact the storage / export of water from the Arctic, which will likely have implications on the Atlantic Meridional Overturning Circulation (AMOC) and on mid-latitude weather (Haine et al., 2023; Oltmanns et al., 2024). Untangling the causes and impacts of these various changes requires an integrated understanding of Arctic dynamics and how components of the Arctic system interact.

1.3 Eurasian Arctic – key role and place in wider context

The Arctic is separated in two sections by the ~1500m deep Lomonosov Ridge, the Eurasian and Amerasian/Canadian basins (Figure 1.1). These two basins have multiple distinct differences, particularly in their circulation regimes. The Amerasian Arctic has persistent anticyclonic (clockwise) circulation, more commonly known as the Beaufort Gyre, whereas the Eurasian Arctic has cyclonic (anticlockwise) circulation which connects the Russian shelf seas to the central Arctic. The Eurasian Arctic receives a larger volume of riverine freshwater input, due to the many rivers in the Russian Arctic, most notably from the Ob, Yenisei and Lena. Conversely, the Amerasian Basin has much higher freshwater storage (accumulated freshwater anomaly of ~20 m thickness in Amerasian compared to 5-10 m thick in Eurasian) and stronger stratification. This increased stratification is primarily due to the larger volume of fresh Pacific Water which enters the Amerasian and forms a subsurface warm, fresh layer, and due to the flow convergence present in the anticyclonic Beaufort Gyre (Aagaard et al., 2006; Bluhm et al., 2015; Haine et al., 2015). There are also notable differences in sea ice dynamics between the two regions. The Eurasian has a strong seasonal ice cover and is a key region of sea ice formation so primarily exports young, thin ice to the Amerasian and Transpolar Drift. The Amerasian basin contains and stores older multi-year ice as the thicker halocline isolates sea ice from upward heat transfer.

The anticyclonic circulation in the Eurasian Arctic consists of Atlantic Water inflowing through the Barents Sea and Fram Strait before encountering Arctic surface waters and subducting (Timmermans and Marshall, 2020). These surface waters then travel through the Kara Sea, where they are freshened by the Ob and Yenisei rivers and then transported via the Vilkitsky Strait to the Laptev Sea, where they are further freshened by the Lena River, evolving into low salinity shelf waters (Rudels et al., 2004). This low salinity shelf waters can then be transported eastward to East Siberian Sea or northward to central Arctic. Over winter, this mixes with deeper AW forming halocline waters. It then gets transported to the Amerasian Arctic and incorporated into the Beaufort Gyre, or incorporated into Transpolar Drift and transported to the Fram Strait and out of Arctic. In turn, the freshwater content of the Amerasian Basin is anticorrelated with freshwater content of the Eurasian Basin (McPhee et al., 2009; Proshutinsky et al., 2009). Hence, processes controlling freshwater transport around the Eurasian Arctic are a key influence on whether freshwater is stored in or exported from the Arctic.

Neglecting the Russian Shelf results in a 25% error in assessing Arctic Ocean freshwater circulation (Hall et al., 2023). Hence, the Eurasian Arctic seas are key to understanding the future Arctic system as they receive over half of the total Arctic riverine discharge, or a quarter of the total surface freshwater flux to the Arctic (Janout et al., 2015; Osadchiev et al., 2020). This river runoff is mostly from the Ob (407 km^3/yr), Yenisei (591 km^3/yr) and Lena (543 km^3/yr) rivers (Osadchiev et al., 2020; Wang et al., 2021). Due to the Arctic's remote and challenging nature and the associated lack of data coverage, the processes that govern riverine freshwater exchange, and their interactions with sea ice and precipitation, are relatively poorly understood. Over the shallow Russian shelf seas, river runoff contributes around half of the total freshwater, precipitation around a fifth and sea ice around a third. However, this contribution has been decreasing significantly in recent decades (this is further discussed in section 6.2 (p104)). In addition, the strong seasonal cycles of both Arctic river runoff and sea ice make differentiating their influence particularly difficult in coastal regions. Freshwater from the Russian Arctic is a key contribution to the Arctic halocline, the fresh layer that sits above inflowing warm AW and PW and protects the surface sea ice (Rudels et al., 2004, 1996). As sea ice cover contracts and river runoff increases with climate change, understanding their present contributions and interactions in coastal regions will become increasingly important to predict and prepare for the impact these changes will have.

1.4 Motivation: Gaps in current Eurasian Arctic system understanding

The weaker stratification, larger seasonal sea ice cycle and observed Atlantification in the Eurasian Arctic mean it is a less stable system, at risk of more rapid influences of climate change. Therefore, understanding it is more urgent given its higher potential for rapid change and as it may be a case study of future changes in the Amerasian. To understand large-scale, long-term controls on freshwater transport, this thesis aims to improve our understanding of drivers of interannual variability, focusing on the common and isolated drivers of salinity, temperature and sea ice variability and the interactions between them. The Russian shelf seas have previously been suggested to behave independently and considerably differently from one another (Osadchiev et al., 2024), primarily due to differing bathymetry, freshwater sources, sea ice seasonal cycles and dominant atmospheric circulation. Therefore, the interannual variability of freshwater transport, and the processes controlling it, are suggested to be considerably different in the Laptev and Kara Sea and need to be studied independently. This thesis seeks to understand the differences in dynamics of these regions and their causes, and explore how these findings suggest climate change will impact the Eurasian Arctic.

1.5 Satellite sea surface salinity (SSS) as a tool to address these barriers

Understanding Eurasian Arctic processes is all the more challenging due to the sparsity of open-access in-situ measurements over this region, particularly over the shallow shelf seas. Whilst in situ measurements of salinity have long been sparse and infrequent throughout the Arctic, due to the persistent sea ice cover that restricts access throughout most of the year, these issues are only exaggerated in the Eurasian Arctic, where geopolitical conflicts have also restricted data transparency.

Therefore, satellite SSS has the potential to be an invaluable tool as salinity is the dominant driver of density at high latitudes and plays a key role in controlling transport around the Arctic. Satellite acquisitions of SSS, such as from the Aquarius (2011–2015, (Lagerloef et al., 2008)), SMOS (Soil Moisture and Ocean Salinity) ((2010- present), (Font et al., 2010; Kerr et al., 2010)) and SMAP (Soil Moisture Active Passive) (2015-present, (Piepmeier et al., 2017)) missions, have helped lessen this issue by providing high spatial and temporal resolution data over most of the globe. Whilst satellites have allowed observations of open water regions within the Arctic, they remain unable to observe the ocean through sea ice and even the presence of partial sea ice cover increases the number of contaminated retrievals. In addition, the L-band signal used to measure SSS in regions of open water is less sensitive in colder waters, making retrievals at high latitudes more challenging and less accurate (Meissner et al., 2016). Until now, these inaccuracies have presented a barrier to understanding Arctic Ocean dynamics.

However, recent advances to SMOS and SMAP SSS data processing, using prior information from sea ice concentration (SIC) and sea surface temperature (SST) data, have enabled greater confidence in acquisitions. These developments have considerably increased the number of viable observations and lowered bias compared to in-situ data in the Arctic, making satellite SSS data a valuable resource for Arctic studies (Fournier et al., 2019; Supply et al., 2020a). Even just over the timeline of this thesis, one SSS product (ESA CCI SSS) has gone from having almost no viable observations in the Eurasian Arctic to a useful product capable of capturing observed variability. In addition, retreating Arctic sea ice cover and rapid atmospheric warming is increasing the spatial cover of satellite based SSS measurements. Whilst SSS retrievals at high latitudes still have larger uncertainties relative to the rest of the globe, previous studies have shown that accuracy is sufficient to capture regions with large and sharp SSS gradients such as Eurasian river plumes (Kubryakov et al., 2016; Olmedo et al., 2018; Supply et al., 2020a; Tang et al., 2018; Zhuk and Kubryakov, 2021). The novelty of these advances means there is a relatively long time-series of reprocessed data that has been validated in this region but that few studies have made full use of yet (Tarasenko et al., 2021).

1.6 Research aim and research questions

This thesis aims to improve our understanding of the common and isolated drivers of interannual variability in sea surface salinity, temperature and sea ice in the Laptev and Kara seas and through the Vilkitsky Strait. The differences in dynamics between these regions will be explored as well as what they imply for how climate change will impact the Eurasian Arctic.

To address this aim, I will integrate satellite SSS data with in-situ and reanalysis SSS and measurements of other freshwater processes (precipitation, sea ice freshwater flux and river run-off) to answer the following research questions:

1. How does satellite SSS data add value to Arctic based process studies when used in combination with in-situ and reanalysis data?
2. What are the processes that control the interannual variability of summer salinity, temperature and sea ice variability and how do they interact in the Laptev and Kara Sea and through the Vilkitsky Strait?

3. What are the dominant controls on Eurasian-wide interannual variability and what implications do these have on sea ice persistence and Arctic-wide freshwater storage?
4. What implications do these findings have for freshwater transport in the context of climate change?

1.7 Thesis structure

Following this introduction, Chapter 2 (p9) reviews the overall data and general methodology used in this thesis, including validation of the satellite and reanalysis products used against in-situ data.

Chapter 3 (p23) focuses on the Laptev Sea and has already been published in the journal Ocean Science (Hudson et al., 2024). The Laptev Sea receives inflow from the Lena River as a relatively wide, shallow plume, which is one of the most pronounced SSS signals in the Arctic, providing a particularly strong signal clearly identifiable from satellite SSS data. The drivers of interannual variability in summer SSS, SST and SIC, including roles of wind stress and Lena runoff, are assessed using a combination of reanalyses, satellite and in-situ data. The chapter demonstrates that satellite SSS is definitely a useful tool to study Arctic processes and confirms that the zonal wind is the dominant driver of interannual variability in SSS and SST and drives spatial differences in SIC.

A similar analysis is then conducted in the Kara Sea, considering the roles of wind stress and Ob and Yenisei runoff, in Chapter 4 (p47). This chapter shows that, as was true in the Laptev Sea, the zonal wind appears to be the main driver of interannual variability in SSS but that unlike in the Laptev, variability in (Ob and Yenisei) river runoff also plays a role. Whilst zonal wind also plays a role in controlling SST, these changes are less related to differences in plume transport, and less coupled to changes in SSS. In addition, unlike in the Laptev Sea, differences in SST do not drive differences in early autumn SIC.

The controls of freshwater transport through the Vilkitsky Strait, the main pathway between the Kara and Laptev Sea, are then considered in Chapter 5 (p79). The analysis in this chapter shows that zonal wind plays a dominant role in controlling transport through the Vilkitsky Strait, and drives consistent differences in SSS and SST. However, as in the Kara Sea, these differences do not appear to have a notable impact on September SIC.

The combined implications of this interannual variability in freshwater transport on sea ice persistence and longer-term freshwater storage/transport are then assessed in Chapter 6 (p103), as well as the implications of these findings in the broader context of climate change.

Chapter 7 presents the key findings related to each of the thesis objectives, their implications and suggested future work related to these findings.

Chapter 2 Data and Methods Overview

This chapter describes the data used throughout the rest of this thesis and then validates satellite and reanalysis products against available in-situ data. First, the in-situ data used for validation is described in section 2.1. The reanalysis and satellite products used throughout this thesis are then described in section 2.2 and 2.3. The results from validation against in-situ data are then described in section 2.4.

2.1 In-situ data description

Table 2.1: Cruises, vessels and time-periods of salinity and temperature in-situ data used for analysis of vertical profiles and comparison with satellite data

Cruise Name / Vessel	**Time Period**	**Reference**
UDASH dataset (incl NABOS cruises 2013, 2015) – numerous data sources	2010-2015	(Behrendt et al., 2017)
NABOS cruise 2018 UCTD (Akademik Tryoshnikov)	3rd -17th October 2018	(Janout et al., 2019)
Akademik Mstislav Keldysh Professor Shtokman Akademik Mstislav Keldysh	Sept 2011 Aug 2014 July 2016	Supplementary materials (Osadchiev et al., 2021)
Akademik Mstislav Keldysh	24 - 26th July 2016 17 - 18th Sept 2017	Supplementary materials (Osadchiev et al., 2020)
Akademik Lavrentyev Victor Buynitskiy Akademik Mstislav Keldysh Akademik Lavrentyev Akademik Mstislav Keldysh	18 – 30th Sept 2011 8 – 25th Sept 2012 5th Sept 2015 8th Oct 2016 4 – 21st Sept 2017 23rd Aug – 19th Oct 2018 24th Sept – 14th Oct 2019	Supplementary materials (Osadchiev et al., 2020)
Akademik Lavrentyev Akademik Mstislav Keldysh	20th Sept– 20th Oct 2016 23rd Sept – 13th Oct 2019	Supplementary materials (Osadchiev et al., 2021)
Akademik Mstislav Keldysh Professor Logachev Aleksey Maryshev	25 - 26th Oct 2020 13 - 28th Oct 2021 19 - 20th Oct 2022	Supplementary materials (Osadchiev et al., 2023b)

In-situ data from conductivity temperature depth (CTD) probes, floats, ice-tethered profilers, oceanographic cruises and other platforms in the Eurasian shelf seas are used for validation of satellite and reanalysis products from a number of sources (UDASH (Unified Database for Arctic and Subarctic Hydrography) dataset, NABOS (Nansen and Amundsen Basins Observational System) and other cruises). All the cruises, vessels, time periods and sources of in-situ data used are detailed in Table 2.1 and their spatial cover over the SMOS and SMAP time periods is visible in Figure 2.1 and Figure 2.2.

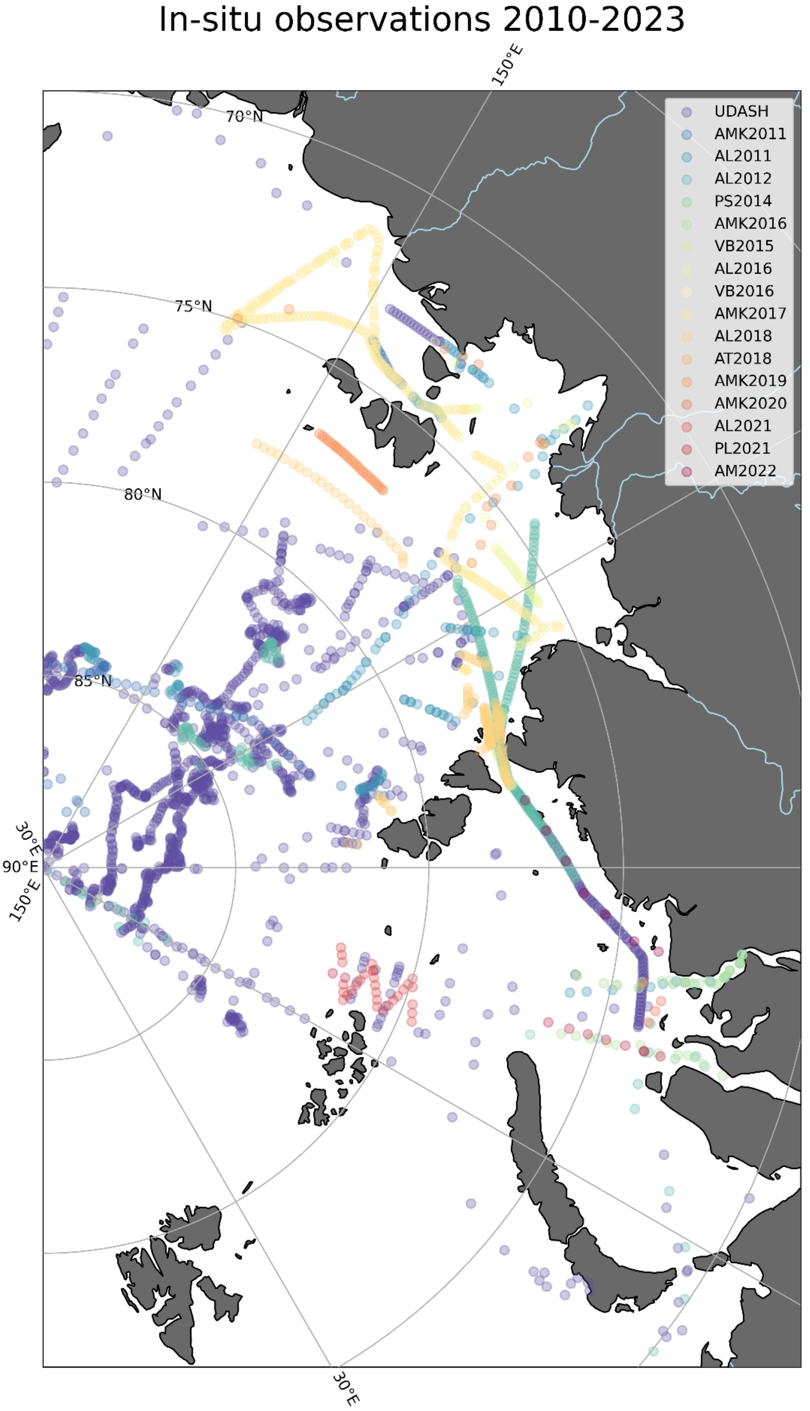

Figure 2.1: In-situ data (shallower than10 m) used for validation of satellite and reanalysis products, coloured by the cruise/dataset they were collected from including UDASH (Unified Database for Arctic and Subarctic Hydrography), AMK (Akademik Mstislav Keldysh), AL (Akademik Lavrentyev), PS (Professor Shtokman), VB (Victor Buynitskiy). AT (Akademik Tryoshnikov) and PL (Professor Logachev).

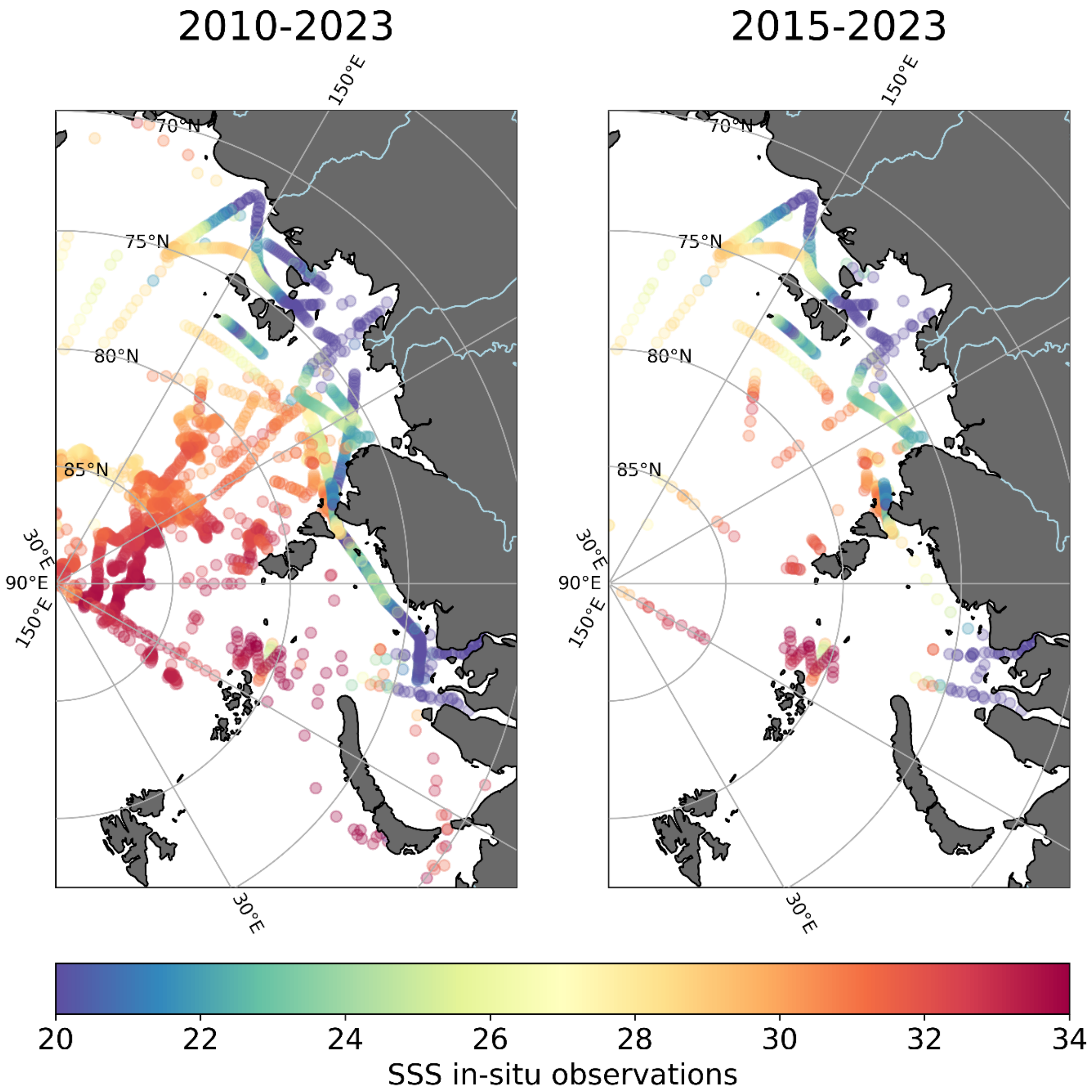

2010-2023

2015-2023

Figure 2.2: In-situ data (shallower than10 m) used for validation of satellite and reanalysis products, coloured by their salinity value, collected over the SMOS period (2010-2023) (left) and the SMAP period (2015-2023) (right).

River runoff data from the Arctic Great Rivers Observatory (GRO) dataset is used to identify the main drivers of interannual variability in the Kara and Laptev Sea (Shiklomanov et al., 2021).

2.2 Reanalysis description

The 1/12 degree CMEMS (Copernicus Marine Environment Monitoring Service) GLORYS12V1 reanalysis (hereafter referred to as GLORYS12V1) (Lellouche et al., 2021) is used as a comparison dataset alongside the satellite products over the common observational periods (since 2011/2015) in the Eurasian shelf seas (Table 2.2). This reanalysis is chosen for its high spatial resolution, its good representation of Arctic SIC and its previous application to salinity variability in the Subpolar North Atlantic and Arctic (Biló et al., 2022; Hall et al., 2021; Lellouche et al., 2021; Liu et al., 2022). For consistency with the satellite SSS products, the GLORYS12V1 reanalysis is re-gridded (coarsened and interpolated by nearest-neighbour interpolation) onto a 0.25° grid for comparison with in-situ data.

Three 1/4 degree reanalysis products (Table 2.2) are also validated against in-situ data (Table 2.4, Table 2.5) and used throughout the thesis for comparison with GLORYS12V1. These include: GLORYS2V4 from Mercator Ocean (GLOR), ORAS5 from ECMWF (ORAS), and C-GLORS05 from CMCC (CGLO) (Masina et al., 2017). Whilst the results/figures from these reanalyses are not included in text in all chapters, they typically support the findings observed in GLORYS12V1.

All four of these reanalyses are built to be as close to observations as possible but with model physics. They all use the NEMO ocean model and LIM2 sea ice model and are forced with ECMWF ERA-Interim (and ERA5 from 2019 to present for GLORYS12V1). All reanalyses are forced with climatological river runoff (Dai et al., 2009; Dai and Trenberth, 2002; Winkelbauer et al., 2022). All four reanalyses assimilate both in-situ and satellite observations including along track altimeter data (sea level anomaly), satellite SST and SIC data and in-situ salinity and temperature profiles. However, the exact observations assimilated differ by product (see Table 2.2). Regardless, all of these products assimilate some data in the Arctic, including the NABOS cruise data, but not the shallow shelf data obtained in supplementary materials.

Table 2.2: Reanalysis products used in this study and their start and end dates, their native and used temporal and spatial grid resolutions, the number of vertical levels they have in total and in the top 10m, their ocean models and the observations they assimilate

Reanalyses	GLORYS12V1	GLORYS2V4	ORAS5	C-GLORS05
Start date used	1993-01	1993-01	1993-01	1993-01
End date used	2024-01	2022-12	2022-12	2022-12
Native / used temporal resolution	Monthly	Monthly	Monthly	Monthly
Vertical levels	50	75	75	75
Vertical levels less than 10m	8	8	8	8
Native / used grid spatial resolution	0.083° 0.25° used only for validation	0.25°	0.25°	0.25°
Ocean Model	NEMO 3.1	NEMO 3.1	NEMO 3.4	NEMO 3.4
Tidal mixing	Parameterized according to (Koch-Larrouy et al., 2008)	Parameterized according to (Koch-Larrouy et al., 2008)	Parameterized according to (Koch-Larrouy et al., 2008)	Parameterized according to (Koch-Larrouy et al., 2008)
Runoff implementation	Climatological Runoff (Dai et al., 2009) into surface layer	Climatological runoff (Dai et al., 2009) into surface layer	Climatological runoff BT06 (Bourdalle-Badie and Treguier, 2006)	Climatological runoff BT06 (Bourdalle-Badie and Treguier, 2006)
Assimilated Observations	Reynolds 0.25° AVHRR-only SST, Delayed Time SLA from all altimetric satellites, in situ T/S profiles from Copernicus Marine CORAv4.1 database, CERSAT SIC	SAM2 (SEEK) Large scale bias correction 7-day assimilation window Merge MDT (obsv+model) Reynolds SST, CORA	OceanVar (3Dvar) Large scale bias correction 7-day assimilation window Model MDT Reynolds SST, EN4	NEMOVAR (3Dvar) 5-day assimilation window HadlSSTv2 SST, EN4

ECMWF's (European Centre for Medium-Range Weather Forecasts) 5th generation reanalysis of global weather and climate (ERA5) monthly eastward and northward turbulent surface stress is used in assessing the main drivers of interannual variability over the Eurasian shelf seas (Hersbach et al., 2020). The monthly mean NCEI (National Centers for Environmental Information) Climate Prediction Center (CPC) Arctic Oscillation Index (AOI) (NOAA National Centers for Environmental Information, 2024) is also used to relate local wind stress patterns to larger scale atmospheric circulation.

2.3 Satellite data description

To validate and identify strengths and weaknesses of satellite-based SSS measurements over the Eurasian Arctic, this study uses various level-3 SMOS, level-3 SMAP and level-4 merged monthly products which are described below (Table 2.4). These have a spatial resolution of around 25km over the Arctic and a bi-weekly revisit time. Monthly data is chosen due to the interannual nature of the analysis performed. Higher temporal resolution satellite products were considered for analysis but comparison with in-situ data in the Laptev Sea (Chapter 3) suggested they do not notably improve correlations with in-situ data. Therefore, these results do not justify their use over monthly products.

The two SMAP products are global products and are not specific for the Arctic: JPL (Jet Propulsion Laboratory) v5 and RSS v4 (Remote Sensing Systems). Given the SMAP satellite's later launch, the SMAP products are compared over 2015-04 to 2024-01. The SMAP JPL product provides a large coverage including close to the sea ice edge, so was chosen for use throughout this thesis. To investigate the impact of this more extensive data coverage on similarity with in situ data, JPL data are masked to only include SSS where the SSS uncertainty provided in the product is lower than 1 pss. No masking is used for the SMOS products.

The SMOS products are Arctic Ocean focused products: the L3 BEC (Barcelona Expert Centre) Arctic+ v3.1 and L3 LOCEAN (Laboratory of Ocean and Climatology) Arctic v1.1 and v2 products (Martínez et al., 2022; Supply et al., 2020a). Monthly means are calculated from the 3-day BEC product to enable comparison with the other monthly satellite products. The SMOS products are regridded onto a regular 0.25° grid (consistent with the SMAP grid) for easier comparison with reanalysis and in-situ data.

A number of products were only released after completion of the Laptev Sea (Chapter 3), including the LOCEAN Arctic v2 product (L3 LOCEAN SMOS Artic v2). Hence, the LOCEAN v2 product is validated here and used throughout the rest of the thesis. Conversely, the shorter LOCEAN v1.1 product (2011-01 to 2019-12) is only used and validated in the Laptev Sea (Chapter 3) and not more extensively throughout the thesis. Similarly, the BEC product only has a short timeseries (2011-01 to 2019-12) so is used solely in the Laptev Sea (Chapter 3) and not used more extensively throughout the thesis. As BEC and LOCEAN v1.1 have very short timeseries, and are validated in the Laptev Sea chapter, they are not included in the Eurasian-wide validation here.

A level-4 SMOS/SMAP combined product, L4 CCI V4.4, is also used. This product was only released after completion of the Laptev Sea (Chapter 3), so is validated here and used throughout the rest of this thesis.

Whilst the level-3 JPL SMAP v5 product is used throughout this thesis, the masked product is only used in the Laptev Sea chapter (Chapter 3) to be consistent with the published paper (Hudson et al., 2024) and the unmasked product is used throughout the rest of this thesis for maximum data availability.

Table 2.3: Satellite sea surface salinity products used in this study and their start and end dates, and native and used temporal and grid resolutions

SSS Products	Start date used	End date used	Native temporal resolution	Temporal resolution used	Native grid resolution	Grid resolution used	Chapters Used In
L3 LOCEAN SMOS Artic v1.1	2010-06	2019-12	Monthly	Monthly	25km EASE	0.25°	Laptev (Chapter 3)
L3 LOCEAN SMOS Arctic V2	2010-06	2023-08	Monthly	Monthly	25km EASE	0.25°	All except Laptev (Chapters 4-6)
L3 BEC SMOS ARCTIC+ v3.1	2011-01	2019-12	3day	Monthly	25km EASE	0.25°	Laptev (Chapter 3)
L3 JPL SMAP v5*	2015-04	2022-01	Monthly	Monthly	0.25°	0.25°	All (Chapter 3-6) (masked product used for Chapter 3, unmasked used elsewhere)
L3 RSS SMAP v4	2015-04	2022-01	Monthly	Monthly	0.25°	0.25°	Laptev (Chapter 3)
L4 CCI V4.4	2010-06	2022-10	Monthly	Monthly	0.25°	0.25°	All except Laptev (Chapter 4-6)

* JPL SMAP v5 has no data for September 2022 so this year was excluded from analysis in relevant chapters. However, this year was never identified to be one of the most extreme years in the timeseries considered for the composite analysis conducted in this thesis so excluding this year did not impact results.

SST measurements are taken from the gap-filled L4 CCI (Climate Change Initiative) SST CDR (Climate Data Record) v2.1 (Merchant et al., 2019). A monthly product of this data regridded at 0.1 ° resolution is used over the SSS satellite period. This product only extends until the end of 2021.

2.4 SSS product validation (vs in-situ data) over the Eurasian shelf seas

Only in-situ observations in the upper 10 m are used for comparison with satellite data (Figure 2.2). Most of these observations are also within the top 5 m but the exact depth is not known of all observations. The same analysis was conducted using only data in the upper 5 m with no significant improvement in correlation coefficients or RMSD values. The analysis shown here is for the upper 10 m to retain as much data as possible.

All satellite and reanalysis products described above (other than those used exclusively in the Laptev Sea (Chapter 3)) are compared with in-situ data over 2015-2023. The regridded LOCEAN SMOS v2 data and GLORYS12V1 reanalysis (on a 0.25 ° grid) are used for comparison with in-situ data. Both Pearson correlation coefficients and root-mean square difference (RMSD) values are calculated for each individual product at all collocations (across the entire area and time period) between in-situ data and that product (all observations < 10 m). Correlation coefficients and RMSD values are also calculated only where all satellite and reanalysis products have a common collocation with in-situ data (common observations < 10 m. In both cases, collocations are identified by nearest neighbour interpolation. However, over 2015-2023, few in-situ observations are collected sufficiently near the surface (< 10 m) over regions where all satellite products obtain an SSS measurement (only 268 collocations). Therefore, RMSDs and correlation coefficients are also calculated for SMOS products and reanalyses over the longer SMOS time period (2011-2023) to obtain more collocations (532).

Table 2.4: Correlation coefficients from in-situ SSS data < 10 m over 2015-2023 (left) and 2010-2023 (right) with GLORYS12V1, LOCEAN SMOS products regridded at a 0.25 degree spatial resolution, JPL SMAP in regions where the provided SSS uncertainty is less than 1, RSS SMAP and the three CMEMS global ensemble reanalysis products: GLORYS2V4, ORAS5, and C-GLORS05. Correlation coefficients are calculated both at all points where an individual product is collocated with in-situ data (All obsv <10 m) and for only where all products had a collocation point near in-situ data (Common obsv <10 m). There are 268 collocations between all products over 2015-2023 and 532 collocations over 2010-2023. The p values associated with correlation coefficients are not included but are all << 0.01.

	2015-2023				**2010-2023**			
	All observations < 10 m		**Common observations < 10 m**		**All observations < 10 m**		**Common observations < 10 m**	
	Num obsv	**Corr coeff**	**Num obsv**	**Corr coeff**	**Num obsv**	**Corr coeff**	**Num obsv**	**Corr coeff**
JPL SMAP	504	**0.86**	268	**0.86**				
JPL SMAP (where uncertainty < 1)	441	**0.86**						
RSS SMAP	516	**0.78**		**0.88**				
LOCEAN SMOS regridded onto 0.25° grid	378	**0.83**		**0.75**	658	**0.79**	532	**0.81**
CCI	445	**0.88**		**0.88**	853	**0.82**		**0.88**
CCI (all flagged data removed)	357	**0.89**			583	**0.88**		
CCI (all land flags removed)	382	**0.90**			656	**0.88**		
GLORYS12V1 regridded onto 0.25° grid	693	**0.76**		**0.68**	2177	**0.74**		**0.76**
C-GLORS05	695	**0.80**		**0.46**	2459	**0.80**		**0.67**
GLORYS2V4	695	**0.68**		**0.60**	2459	**0.72**		**0.69**
ORAS5	695	**0.85**		**0.57**	2459	**0.87**		**0.73**

Table 2.5: Root mean square differences (RMSD) from in-situ SSS data < 10 m over 2015-2023 (left) and 2010-2023 (right) with GLORYS12V1 and LOCEAN SMOS products regridded at a 0.25 degree spatial resolution, JPL SMAP in regions where the provided SSS uncertainty is less than 1, RSS SMAP and the three CMEMS global ensemble reanalysis products: GLORYS2V4, ORAS5, and C-GLORS05. RMSDs are calculated both at all points where an individual product is collocated with in-situ data (All obsv <10 m) and for only where all products had a collocation point near in-situ data (Common obsv <10 m). There are 268 collocations between all products over 2015-2023 and 532 collocations over 2010-2023.

	2015-2023				**2010-2023**			
	All observations < 10 m		**Common observations < 10 m**		**All observations < 10 m**		**Common observations < 10 m**	
	Num obsv	**RMSD**	**Num obsv**	**RMSD**	**Num obsv**	**RMSD**	**Num obsv**	**RMSD**
JPL SMAP	504	**3.40**	268	**2.71**				
JPL SMAP (where uncertainty < 1)	441	**3.37**						
RSS SMAP	516	**4.37**		**2.25**				
LOCEAN SMOS regridded onto 0.25° grid	378	**3.10**		**3.11**	658	**3.56**	532	**3.19**
CCI	445	**3.28**		**3.29**	853	**3.52**		**2.93**
CCI (all flagged data removed)	357	**3.10**			583	**2.92**		
CCI (all land flags removed)	382	**3.12**			656	**2.96**		
GLORYS12V1 regridded onto 0.25° grid	693	**6.22**		**4.65**	2177	**4.99**		**4.25**
C-GLORS05	695	**4.97**		**4.59**	2459	**4.11**		**4.29**
GLORYS2V4	695	**6.64**		**4.49**	2459	**5.03**		**4.14**
ORAS5	695	**4.45**		**4.37**	2459	**3.56**		**4.17**

Over the full time period (2010-2023), satellite products agree well with in-situ data (r > 0.79 and RMSD < 3.56 for all individual products and r > 0.81 and RMSD < 3.19 with all common observations) (Table 2.4 and Table 2.5). The CCI product with land flagged data removed (r = 0.88, RMSD = 2.96) and the product with all flagged data removed (r = 0.88, RMSD = 2.92) agree better with in-situ data than the non-masked product (r = 0.82, RMSD = 3.52). The masked and unmasked CCI products agree better with in-situ data than LOCEAN v2, both when you consider all observations (r = 0.79, RMSD = 3.56 for LOCEAN) and considering only common observations (r = 0.81 and RMSD = 3.19).

When comparing only the region of common observations over the full time period, satellite data also agrees better with in-situ data (r > 0.81, RMSD < 3.19) than all reanalyses considered (r < 0.76 and RMSD > 4.13). Of the reanalyses considered, over the region of common observations, GLORYS12V1 is most strongly correlated to in-situ data (r = 0.76) compared to CGLO (r = 0.67), GLOR (r = 0.69) and ORAS (r = 0.73). Conversely, GLOR has the lowest RMSD value (RMSD =4.14) compared to GLORYS12V1 (RMSD = 4.25), CGLO (4.29) and ORAS (4.17). However, when comparing the reanalyses over all collocations with in-situ data, ORAS (r = 0.87, RMSD = 3.56) agrees best with in-situ data, then CGLO (r = 0.80, RMSD = 4.11) then the two GLORYS products (r = 0.74 and RMSD = 4.99 for GLORYS12V1 and r = 0.72 and RMSD = 5.03 for GLOR).

Over the shorter SMAP timeseries, satellite products agree well with in-situ data (r > 0.78 and RMSD < 4.37 for all individual products and r > 0.75 and RMSD < 3.29 with all common observations). The CCI product with land flagged data removed (r = 0.90, RMSD = 3.12) and with all flagged data removed (r = 0.89, RMSD = 3.10) agrees slightly better with in-situ data than the non-masked product (r = 0.88, RMSD = 3.28).

Whilst there is little difference in correlation coefficient between the JPL masked (r = 0.86, RMSD = 3.37) and unmasked products (r = 0.86, RMSD = 3.40), there is a small decrease in RMSD with the masked product. When considering all observations, RSS agrees least well with in-situ data and has the lowest r value and highest RMSD (r = 0.78, RMSD = 4.37). When considering only the region of common observations, LOCEAN v2 has the weakest correlation coefficient (r = 0.75) but CCI has the largest RMSD (RMSD = 3.29).

The unmasked CCI, JPL SMAP and LOCEAN SMOS products are chosen for use throughout this thesis (in all except Chapter 3) (Table 2.3). These three products are chosen to have a SMOS-only, a SMAP-only and a merged product, which are all subject to independent processing. Whilst the masked CCI products (and JPL product) agree slightly better with in-situ data, the unmasked products are chosen for use throughout this thesis to have the maximum data available, and as these differences in agreement are negligible. All four reanalysis products are used throughout this thesis, but GLORYS12V1 is used (and shown) most extensively, due to its higher spatial resolution and good correlation with in-situ data over the common observation region.

2.5 Methods overview

A relatively consistent methodology is applied in the Laptev Sea, Kara Sea and Vilkitsky Strait Chapters so a generic overview is detailed here below. The month of September is chosen for study throughout this thesis as the month of minimum sea ice coverage / maximum open water area and hence the largest area of satellite and in-situ data for comparison with reanalysis products. In addition, the ocean is warmest during this period, and there is the least sea ice and hence sea ice contamination, yielding the highest quality SSS data. Globally, in the CCI version used throughout this thesis, the correlations with Pi-MEP (Pilot-Mission Exploitation Platform) data in water temperatures < 5 °C was 0.75, compared to that in water between 5 – 15 °C ($r = 0.965$) (Martin et al., 2024). Whilst this is not representative of the seasonal difference in agreement, it gives an idea of the scale of difference in agreement that a change in temperature can drive.

GRO river runoff is calculated for different integration times (i.e. cumulative runoff until a certain Julian day of each year). Cumulative runoff is calculated for spring (Julian day 150), summer (Julian day 200), autumn (Julian day 250) and for the full-year (Julian day 365) for all rivers considered. Cumulative runoff is calculated over these four integration times to take into account differences in runoff timing as well as the total magnitude of runoff. For each river and time period, the trends in runoff timeseries are assessed over the GLORYS12V1 (1993-2023) and SMOS satellite (2010-2023) time periods to determine if significant trends exist. Where a significant trend is present, this trend is removed from the runoff timeseries prior to analysis. The same analysis is conducted with the original and detrended timeseries and any notable differences are discussed in text. When a de-trended timeseries is used in the place of the original, this is discussed in the relevant chapter.

To investigate the contribution of key drivers to interannual variability, a lagged correlation analysis is conducted between GRO runoff, ERA5 eastward turbulent surface stress and GLORYS12V1 SSS, SST and SIC over the full GLORYS12V1 timeseries (1993-2022 for Chapter 3 and 1993-2023 for Chapters 4-5). Pearson correlation coefficients are calculated between cumulative GRO runoff until spring (Julian day 150), autumn (Julian day 250) and over the full year (Julian day 365) and GLORYS12V1 September SSS for each grid cell. The same correlations are calculated with GLORYS12V1 September SST and SIC at each grid cell.

Pearson correlation coefficients were also calculated between ERA5 eastward turbulent surface stress in April, May, June, July, August and September and GLORYS12V1 September SSS (over 1993-2022 for Chapter 3 and over 1993-2023 for Chapters 4-5) in each grid cell to identify the months that appear to most strongly drive variability in September SSS. The same correlations are calculated over the same time period with GLORYS12V1 September SST and SIC at each grid cell.

To identify years of anomalous eastward/westward wind over the shorter satellite timeseries, the mean ERA5 eastward and northward turbulent surface stress are calculated for June to August over the relevant region i.e. the Laptev Sea shelf (120-160 °E, 70-80 °N) for Chapter 3, the Kara Sea shelf (60-80 °E, 70-80 °N) for Chapter 4 and the Vilkitsky Strait (80-110 °E, 72-80 °N) for Chapter 5. The period of June to August is chosen because of the particularly strong correlations found in the lagged correlation analysis between eastward turbulent surface stress in June, July and August and GLORYS12V1 September SSS (in all three regions). A three-month mean is chosen to reduce the high temporal variability in wind stress (± 0.05 N m^{-2}) and only keep the lower frequency signal the ocean reacts to.

Correlations are calculated between runoff and eastward turbulent surface stress over the satellite timeseries (2010-2022 for Chapter 3 and 2010-2023 for Chapters 4-5) and over a longer timeseries (1993-2022 for Chapter 3 and 1993-2023 for Chapters 4-5). Whilst this thesis focuses on the satellite timeseries (and hence this is the period shown in timeseries figures), correlations are also calculated over the longer timescale to ensure robustness and consistency of correlations found.

To be able to calculate "eastward" and "westward" SSS and SST composites, the 3 years of maximum and minimum eastward turbulent surface stress are identified for each of the two satellite periods (SMOS: 2010-2020 and SMAP: 2015-2022 for Chapter 3 and SMOS: 2010-2023 and SMAP: 2015-2023 for Chapters 4-5). The chosen years differ by Chapter so are detailed in the relevant chapter.

This composite approach was chosen as a simple method to clearly visualize the differences in SSS under different wind forcing. More statistically based methods were considered (see section 2.5.1 for further discussion) but the relatively short SSS timeseries (especially for SMAP) complicates interpretation. Hence, the correlation approach is used on GLORYS12V1 to clearly establish the relationship between wind/runoff and SSS, and the composite approach is used to then test this in satellite products.

The "eastward" and "westward" SSS composite is then calculated as the September mean of the three most eastward / westward years for GLORYS12V1 SSS, LOCEAN SMOS and JPL SMAP. The same years are used to calculate "eastward" and "westward" September SST composites using GLORYS12V1 SST and L4 v2.1 CCI SST as well as for GLORYS12V1 September SIC.

"Eastward" and "westward" current velocity composites (for both eastward and northward velocity components) are also calculated from GLORYS12V1 mean June-August eastward and northward current velocity components. These current velocity composites are calculated to show the difference in current velocity observed eastward and westward wind forcing.

The surface Ekman current expected from the wind stress is computed for each region according to Equations (1) and (2) (Price et al., 1987). The surface Ekman current in the u and v directions (u' and v') are calculated from Ekman depth (d), the Coriolis parameter (f), surface density (ρ_0), depth of flow (z) and wind stress in the x and y direction (τ^x and τ^y).

$$u' = \frac{\sqrt{2}}{\rho_0 f d} e^{z/\mathrm{d}} \left(\tau^x \cos\left(\frac{z}{d} - \frac{\pi}{4}\right) - \tau^y \sin\left(\frac{z}{d} - \frac{\pi}{4}\right)\right) \quad (1)$$

$$v' = \frac{\sqrt{2}}{\rho_0 f d} e^{z/\mathrm{d}} \left(\tau^x \sin\left(\frac{z}{d} - \frac{\pi}{4}\right) - \tau^y \cos\left(\frac{z}{d} - \frac{\pi}{4}\right)\right) \quad (2)$$

Surface Ekman currents (for z=0 m) are calculated using an Ekman depth (d) of 10 m (roughly equivalent to the average plume depth found from in-situ data) and a surface density (ρ_0) of 1020 kg m^{-3} (roughly equivalent to an SSS of 25 pss and SST of 5 °C). Whilst previous studies have suggested an Ekman depth of 37 m in this region (Baumann et al., 2018; Tarasenko et al., 2021), a notably shallower 10 m is used here to be consistent with the plume depth found in in-situ data and to obtain surface current velocities roughly similar in magnitude to those in GLORYS12V1.

The expected surface Ekman current under average eastward and westward wind forcing is then calculated from the mean June-August eastward and northward wind stress for identified most eastward and westward years. This surface current is calculated for each pixel within the relevant region for each Chapter. These expected Ekman surface currents under eastward and westward wind forcing are then compared with those observed in GLORYS12V1 to visualise the contribution of the Ekman component to the overall surface current. The surface Ekman currents are calculated, rather than the overall Ekman transport, as they appear to align better with the difference in SSS pattern observed (north/south rather than east/west).

An PCA (principal component analysis) was also conducted using GLORYS12V1 SSS over 1993-2023 to identify the dominant modes of variability in SSS over the Eurasian Shelf Seas. This analysis was conducted both using the full GLORYS12V1 timeseries, and removing the average seasonal cycle (to try and isolate only interannual and decadal variability in SSS). However, due to the nature of the amplifying Arctic seasonal cycle with climate change, seasonal components remained regardless meaning it was a challenge to isolate the seasonal and interannual components of variability. Hence, this analysis was also conducted used only GLORYS12V1 September SSS (Figure 6.8, Figure 6.9). This analysis is discussed further in Chapter 6.

2.5.1 Alternative methods considered

The interannual variability in freshwater content was also calculated from both GLORYS12V1 and satellite products. However, comparisons between vertical profiles in GLORYS12V1 and in in situ data in the Laptev Sea suggested considerable interannual variability in plume stratification and mixed layer depth (see section 3.3.1). This variability suggested that it would not be appropriate to use a constant mixed layer depth to estimate freshwater content. In addition, GLORYS12V1 seemed unable to accurately represent this variability, suggesting that it would also not be accurate to use GLORYS12V1 mixed layer depths to calculate plume freshwater content.

Chapter 3 Laptev Sea

The majority of this chapter have been published in the Journal Ocean Science (Hudson et al., 2024). However, some alterations have been made from its published format. These changes include: removing the abstract and key points, moving some of the introduction and methods from the paper into the thesis introduction and methods and moving some of the discussion relating to local and large-scale atmospheric dynamics to the Eurasian Shelf Seas chapter (Chapter 6). Given the differing products and time-period used in this chapter, specific validation of these products is conducted for this region. In addition, composites are now also calculated from GLORYS12V1 current velocities and the expected surface Ekman transport is calculated from ERA5 wind stress for eastward and westward wind forcing for consistency with other thesis chapters. In the paper, summer runoff is described as being for Julian day 250 but this is described as autumn runoff in this thesis (as cumulative runoff is also calculated to Julian day 200, which is described throughout this thesis as cumulative summer runoff). Hence, this has also been changed here for consistency with the rest of the thesis.

3.1 Introduction:

The Laptev Sea, within the Eurasian Arctic (Figure 3.1), provides an ideal region to study the interactions between the changes the Arctic is experiencing, as it is a hotspot of Arctic warming, sea ice loss, and increases in river runoff (Kraineva and Golubeva, 2022; Stadnyk et al., 2021). Changes in this region will likely have considerable influence on the wider Arctic as the Laptev Sea is a key region of Arctic sea ice production and dominant contributor to Arctic-wide thermohaline structure, including to the surface Transpolar Drift and to the Beaufort Gyre (Johnson and Polyakov, 2001; Morison et al., 2012; Reimnitz et al., 1994; Thibodeau et al., 2014). The combination of these changes will also have considerable local impacts, including by increasing coastal erosion, altering nutrient availability and primary productivity (Juhls et al., 2020; Nielsen et al., 2020; Paffrath et al., 2021; Polyakova et al., 2021).

The Laptev Sea primarily receives runoff from the Lena River, the largest river in the Arctic, which outflows as a particularly shallow plume due to the confined depth (~2-3m) of the Lena Delta (Are and Reimnitz, 2000). Lena River fresh water dominates the spatial pattern of Laptev SSS and is the main control on stratification in this region (Janout et al., 2020). Lena runoff is very seasonal with very low flow throughout the winter, when the Lena River is partially frozen, and a strong peak between May and June following the melt of snow and land ice (Shiklomanov et al., 2021; Wang et al., 2021). Other rivers in this region, including the Khatanga, Olenyok and Indigirka, also contribute fresh water to the Laptev but all combined provide a five times smaller contribution than the Lena (Pasternak et al., 2022). Kara Sea fresh water can also contribute riverine fresh water to some of the western and northern Laptev shelf via the Vilkitsky Straight but contributions vary considerably interannually (Janout et al., 2020, 2015; Osadchiev et al., 2023a). Sea ice melt also provides fresh water to the Laptev Sea but has a negligible impact in summer/autumn as the freshwater contribution from sea ice melt is several orders of magnitudes smaller than the contribution from the Lena River (Dubinina et al., 2017), see section 6.2 (p104) for more information on the magnitudes of freshwater contributions from different sources.

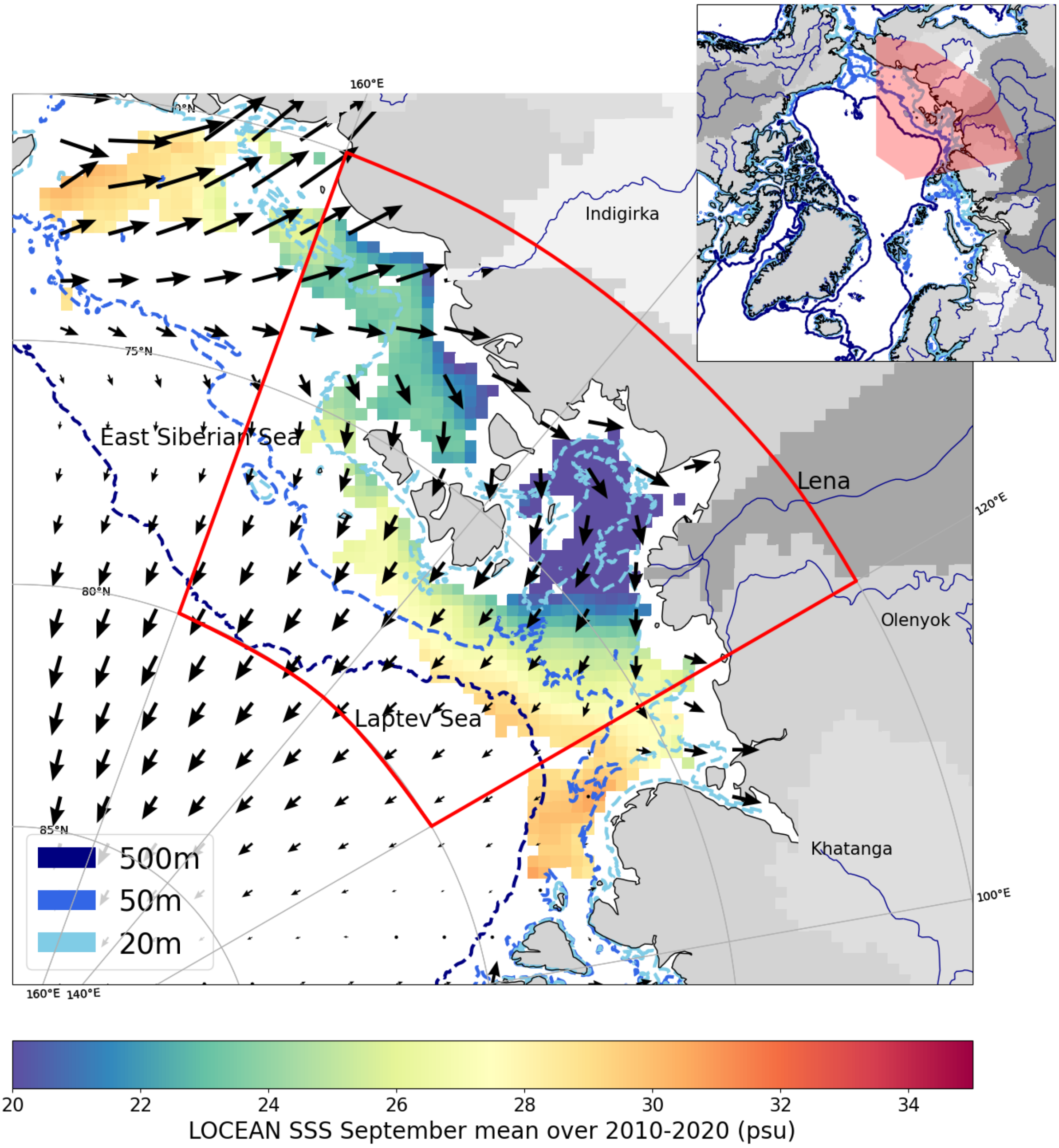

Figure 3.1: 2010-2020 LOCEAN SMOS satellite mean September SSS with GEBCO bathymetry contours for 20m, 50m and 500m overlaid in blue with mean 2010-2020 ERA5 June-August wind vectors overlaid over the ocean. The inset in the top right corner depicts Arctic wide GEBCO bathymetry and the location of this region within the wider Arctic in red. The box used to calculate mean eastward/northward turbulent surface stress is overlaid in red.

Laptev Sea surface fresh water is typically characterized by eastward (cyclonic) circulation and weak tidal influence (Fofonova et al., 2014; Timokhov, 1994). This fresh surface layer exhibits considerable interannual variability, varying in meridional extent by over 500km, and has been widely studied using in-situ data and model output (Anderson et al., 2004; Dmitrenko et al., 2005, 2008; Fofonova et al., 2014; Janout et al., 2020; Osadchiev et al., 2021a). The shallow Laptev shelf (depth ~20-25 m) is mostly controlled by wind forcing and bottom friction, and the strong stratification on this shallow shelf prevents a full Ekman spiral from developing and aligns the surface current ~45 degrees to the right of the wind (Dmitrenko et al., 2005; Kubryakov et al., 2016; Osadchiev et al., 2021a; Zhuk and Kubryakov, 2021). Summer precipitation and sea ice melt contribute significantly less freshwater than rivers and are only suggested to provide a minimal direct contribution to altering summer SSS (Dubinina et al., 2017). River discharge variability has also been suggested as a driver of fluctuations in freshwater content and plume structure (Horner-Devine et al., 2015; Umbert et al., 2021). However, whilst there is general agreement that wind forcing is a driver of variability on the shelf, there is some debate as to the role of river discharge in controlling plume variability (Dmitrenko et al., 2005; Osadchiev et al., 2021a).

Whilst Lena River water typically remains in the Laptev Sea for 2-3 years, its longer-term fate exhibits considerable variability as it can be transported out of the Laptev Sea either northward into the Transpolar Drift or eastward towards the Beaufort Gyre (Bauch et al., 2013; Johnson and Polyakov, 2001; Paffrath et al., 2021). The initial transport of the fresh layer have been suggested as the main control on its eventual transit (Johnson and Polyakov, 2001; Morison et al., 2012).

In this chapter, I first establish that the reanalysis and satellite products used in this study capture the interannual variability in Laptev SSS observed in in-situ data (section 3.3.1). The dominant drivers of this variability are then investigated using GLORYS12V1: including the contribution of Lena River runoff and of local atmospheric forcing in driving these patterns of variability (section 3.3.2). The findings of this analysis are then tested using satellite SSS data (section 3.3.3). A similar analysis is also conducted with sea surface temperature (SST) and sea ice concentration (SIC) data to understand common and differing drivers of variability and how the components of this system interact (sections 3.3.2 and 3.3.4).

3.2 Methods

3.2.1 Data products

3.2.1.1 In-situ data

A subset of the data described and used for Eurasian wide validation is used for validation here, described below.

CTD profiles from cruises in 2016 and 2019 are used for comparison with reanalysis data to study vertical salinity stratification in this region and to complement surface salinity data (supplementary materials (Osadchiev et al., 2021a). Additional in-situ data from CTD probes, floats, ice-tethered profilers, oceanographic cruises and other platforms in the Laptev Sea are used for validation of satellite and reanalysis products from a number of sources (UDASH, NABOS cruises, and cruises on Akademik Mstislav Keldysh). See Appendices for details on in-situ data used to validate satellite SSS products used in this chapter (Appendix Figure A.1, Appendix Table A.1).

Lena River runoff data from the Arctic Great Rivers Observatory (GRO) dataset is used to identify the main drivers of Laptev Sea interannual variability (Shiklomanov et al., 2021). Cumulative runoff until a certain Julian day of each year is calculated for spring (Julian day 150), autumn (Julian day 250) and the full year (Julian day 365). The spring peak in runoff has been shown to be shifting earlier with the rapidly warming Arctic (Melnikov et al., 2019; Yang et al., 2002) so a notable trend is present in the spring cumulative runoff timeseries with the shift to earlier permafrost thaw / river ice melt. To avoid spurious correlation and to be able to differentiate drivers of interannual variability from decadal/longer term trends, the trend in cumulative runoff timeseries (over the GLORYS time period of 1993-2022) is identified and removed. The de-trended spring runoff timeseries is used throughout this study.

3.2.1.2 Reanalyses

The same reanalysis products are used here as throughout the rest of the thesis, and include GLORYS12V1, GLORYS2V4, ORAS5 and CGLO.

3.2.1.3 Satellite data

To validate and identify strengths and weaknesses of satellite-based SSS measurements over the Laptev Sea, this chapter uses two SMOS and two SMAP monthly products which are described in more detail in section 2.3 (p14) and are detailed in the table below (Table 3.1).

Table 3.1: Satellite sea surface salinity products used in this Laptev Sea chapter and their start and end dates, and native and used temporal and grid resolutions

SSS Products	Start date used	End date used	Native temporal resolution	Temporal resolution used	Native grid resolution	Grid resolution used
L3 LOCEAN SMOS Artic v1.1	2010-06	2019-12	Monthly	Monthly	25km EASE	0.25°
L3 BEC SMOS ARCTIC+ v3.1	2011-01	2019-12	3day	Monthly	25km EASE	0.25°
L3 JPL SMAP v5 (where uncertainty < 1)	2015-04	2022-01	Monthly	Monthly	0.25°	0.25°
L3 RSS SMAP v4	2015-04	2022-01	Monthly	Monthly	0.25°	0.25°

SST measurements are taken from the gap-filled L4 CCI (Climate Change Initiative) SST CDR (Climate Data Record) v2.1 (Merchant et al., 2019). A monthly product of this data regridded at 0.1 ° resolution is used over the SSS satellite period (2010 to 2021).

3.2.2 Methods

Two Septembers are shown for comparison of how well interannual variability is captured in each satellite product: 2016, a year of predominant eastward wind and 2019, a year of predominant westward wind (Figure 3.2, Figure 3.3). This study does not consider variability in SSS below 20 pss due to the sparsity of in-situ observations with SSS values below this threshold. As is shown in Figure 3.2, JPL SMAP and LOCEAN SMOS are found to agree particularly well so are used for further analysis.

To investigate the contribution of key drivers to Laptev Sea interannual variability, correlations are calculated between GLORYS12V1 SSS and both spring Lena runoff and mean June to August eastward turbulent surface stress over the Laptev Sea shelf: 120-160 °E, 70-80 °N for each grid cell (Figure 3.4). The same correlations are calculated with GLORYS12V1 September SST and SIC at each grid cell (Figure 3.5, Figure 3.6).To identify years of anomalous eastward/westward wind over the shorter satellite timeseries, the mean ERA5 eastward and northward turbulent surface stress are calculated for June to August over the Laptev Sea shelf: 120-160 °E, 70-80 °N. The period of June to August is chosen because of the particularly strong correlations found in the lagged correlation analysis between eastward turbulent surface stress in June, July and August and GLORYS12V1 September SSS (Figure 3.4). A three-month mean is chosen to reduce the high temporal variability in wind stress (± 0.05 N m^{-2}) and only keep the lower frequency signal the ocean reacts to.

Correlations are calculated between spring Lena runoff and eastward turbulent surface stress over the satellite timeseries (2010-2022) and over a longer timeseries (1993-2022). Whilst this study focuses on the satellite timeseries (and hence this is the period shown in Figure 3.7), correlations are also calculated over a longer timescale (1993-2022) to ensure robustness and consistency of correlations found.

To be able to calculate “eastward” and “westward” SSS and SST composites, the 3 years of maximum and minimum eastward turbulent surface stress are identified for each of the two satellite periods (SMOS: 2011-2020 and SMAP: 2015-2022). The three years of maximum eastward turbulent surface stress are identified to be 2012, 2016 and 2017 over the SMOS timeseries, and identified to be 2016, 2017 and 2021 over the SMAP timeseries (Figure 3.7, Appendix Figure B.5). Conversely, the three years of westward (minimum eastward) turbulent surface stress are identified to be 2011, 2013 and 2019 over the SMOS timeseries, and 2015, 2019 and 2020 over the SMAP timeseries (Figure 3.7, Appendix Figure B.4).

The “eastward” SSS composite is then calculated as the September mean of the three most eastward years for GLORYS12V1 SSS and LOCEAN SMOS (2012, 2016, 2017), and for JPL SMAP (2016, 2017, 2021). The “westward” SSS composite is calculated as the September mean of the three most westward years for GLORYS12V1 SSS and LOCEAN SMOS (2011, 2013, 2019) and for JPL SMAP (2015, 2019, 2020). The same years are used to calculate “eastward” and “westward” September SST composites using GLORYS12V1 SST and L4 v2.1 CCI SST as well as for GLORYS12V1 September SIC.

The same years are also used to calculate "eastward" and "westward" current velocity composites (for both eastward and northward velocity components) from GLORYS12V1 mean June-August eastward and northward current velocity components.

The surface Ekman current expected from the wind stress is computed for this region according to Equations (1) and (2) (Price et al., 1987). Surface Ekman currents (for z=0 m) are calculated using an Ekman depth (d) of 10 m (roughly equivalent to the mixed layer depth found from in-situ data) and a surface density (ρ_0) of 1020 kg m^{-3} (roughly equivalent to an SSS of 25 pss and SST of 5 °C). The expected surface Ekman current under average eastward and westward wind forcing is then calculated from the mean June-August eastward and northward wind stress for identified most eastward and westward years. This surface current is calculated for each pixel over the Laptev Sea shelf: 120-160 °E, 70-80 °N. These expected Ekman surface currents under eastward and westward wind forcing are then compared with those observed in GLORYS12V1 to visualise the contribution of the Ekman component to the overall surface current (overlaid on Figure 3.8).

3.3 Results

3.3.1 Comparison of SSS products

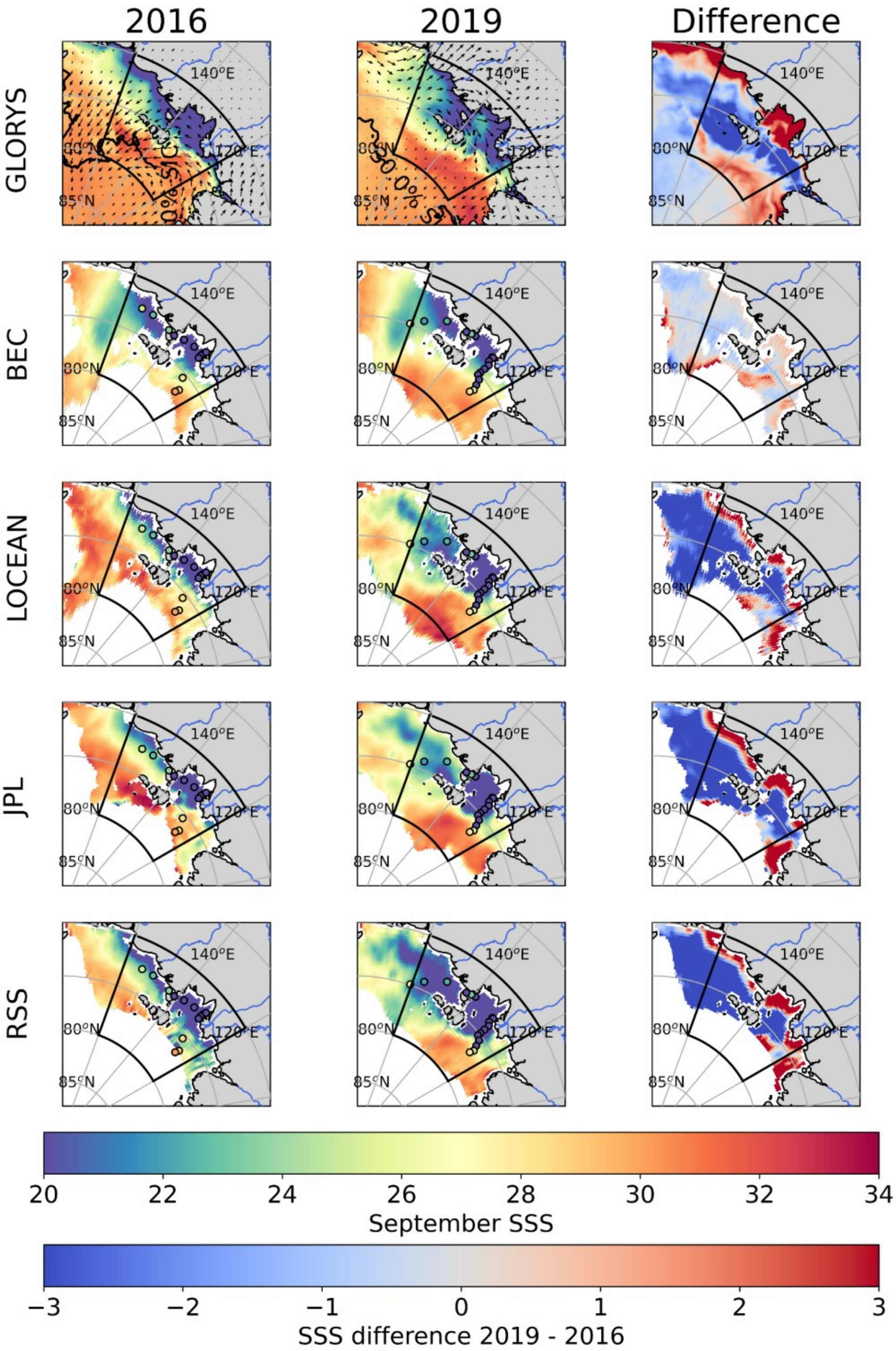

Figure 3.2: Laptev Sea sea surface salinity field in September 2016 (left) and 2019 (middle) and the difference between 2016 and 2019 (right) for the CMEMS GLORYS12V1 reanalysis (top) and for each of the 4 satellite products (RSS SMAP, JPL SMAP, LOCEAN SMOS, BEC SMOS) (top to bottom). ERA5 mean wind speed for June-August are overlaid on the GLORYS12V1 SSS field with a box over the region of interest (70-80°N, 120-160°E). The GLORYS12V1 30% sea ice concentration contour is also overlaid as a black line over the GLORYS12V1 SSS field. In-situ data for late September 2016 and early October 2019 are overlaid on satellite products using the same colour scale.

There is close agreement between the September SSS pattern in GLORYS12V1 and all satellite September SSS products in both years compared (Figure 3.2). The SSS off the continental shelf (> 100 m) or above 75 °N is typically > 28 pss in both years analysed and in both products. SSS generally decreases with proximity to shore, and is lowest near the outflow of the Lena River, around 130 °E, with salinity values as low as 10 pss nearshore. This low salinity area (< 20 pss) extends considerably to the East of the Lena River outflow throughout the southern Laptev Sea and past the New Siberian Islands into the East Siberian Sea, extending to over 160 °E in both years.

The years 2016 and 2019 stand out as having notably different patterns of Laptev SSS, with differences in SSS of over 3 pss between years in all satellite products (reasons for these differences will be further discussed in section 3.3.3). GLORYS12V1 SSS and all satellite products except BEC capture the same SSS patterns as in-situ data from cruises in all years of overlap (2016 and 2019 shown in Fig. 1). In 2016, the freshest salinities are coastally confined and do not travel far off the continental shelf. In 2019, the freshest salinities travel considerably further offshore and extend over most of the Western Laptev and East Siberian Sea.

Despite the strong overall similarity between gridded products, notable differences are visible between in-situ data and both the satellite products and GLORYS12V1 SSS. In 2019, the fresh layer appears to extend further offshore in in-situ data than in GLORYS12V1 (Figure 3.2). LOCEAN, JPL and RSS appear to capture this extended plume better, but still do not capture the full extent visible in in-situ data. This difference is likely primarily due to the temporal mismatch between the September monthly mean GLORYS12V1 and satellite products and in-situ data collected in late September 2016 and early October 2019. Both GLORYS12V1 and satellite SSS do show the plume extending further offshore by the following month (not shown), supporting this suggestion. However, the better representation of plume extent in LOCEAN, JPL and RSS, as compared to GLORYS12V1, suggests the temporal mismatch is not the only driver of this difference.

Most of the satellite products (LOCEAN SMOS and both SMAP products) and GLORYS12V1 manage to capture a consistent pattern of interannual variability and agree well with in-situ data (Figure 3.2, Appendix Figure A.1). However, notably different patterns are observed in the BEC product, which also has a lower correlation with in-situ data (r = 0.79, Appendix Table A.2). All other satellite products analysed appear to capture the SSS pattern described above for 2016 and 2019 and correlate strongly with in-situ data (r > 0.9, Appendix Table A.2). This difference in SSS pattern agrees well with the two modes of SSS variability previously observed in in-situ data and described by other studies in this region (Dmitrenko et al., 2005; Osadchiev et al., 2021a). Of the four products considered here, the LOCEAN SMOS Arctic and JPL SMAP products capture particularly consistent patterns of interannual variability and have strongest correlations with in-situ data (r=0.92 for LOCEAN, r=0.95 for JPL, Appendix Table A.2). This is notable given they originate from different satellites and are generated from different processing algorithms. These two products (LOCEAN SMOS and JPL SMAP) are further used in this study, for their strong similarity and good correlation values with in-situ data.

GLORYS12V1 and the two satellite products show similar areas of open water or of no retrievals (Figure 3.2). In 2019, the area of open water is particularly large in GLORYS12V1 and in all satellite products, with no regions of notable sea ice (where SIC > 30%) below 80 °N throughout the Laptev and East Siberian Sea. In 2016, there is more extensive sea ice and few satellite SSS retrievals in the Laptev Sea but a large area of open water in the East Siberian Sea, which extends considerably offshore to over 80 °N.

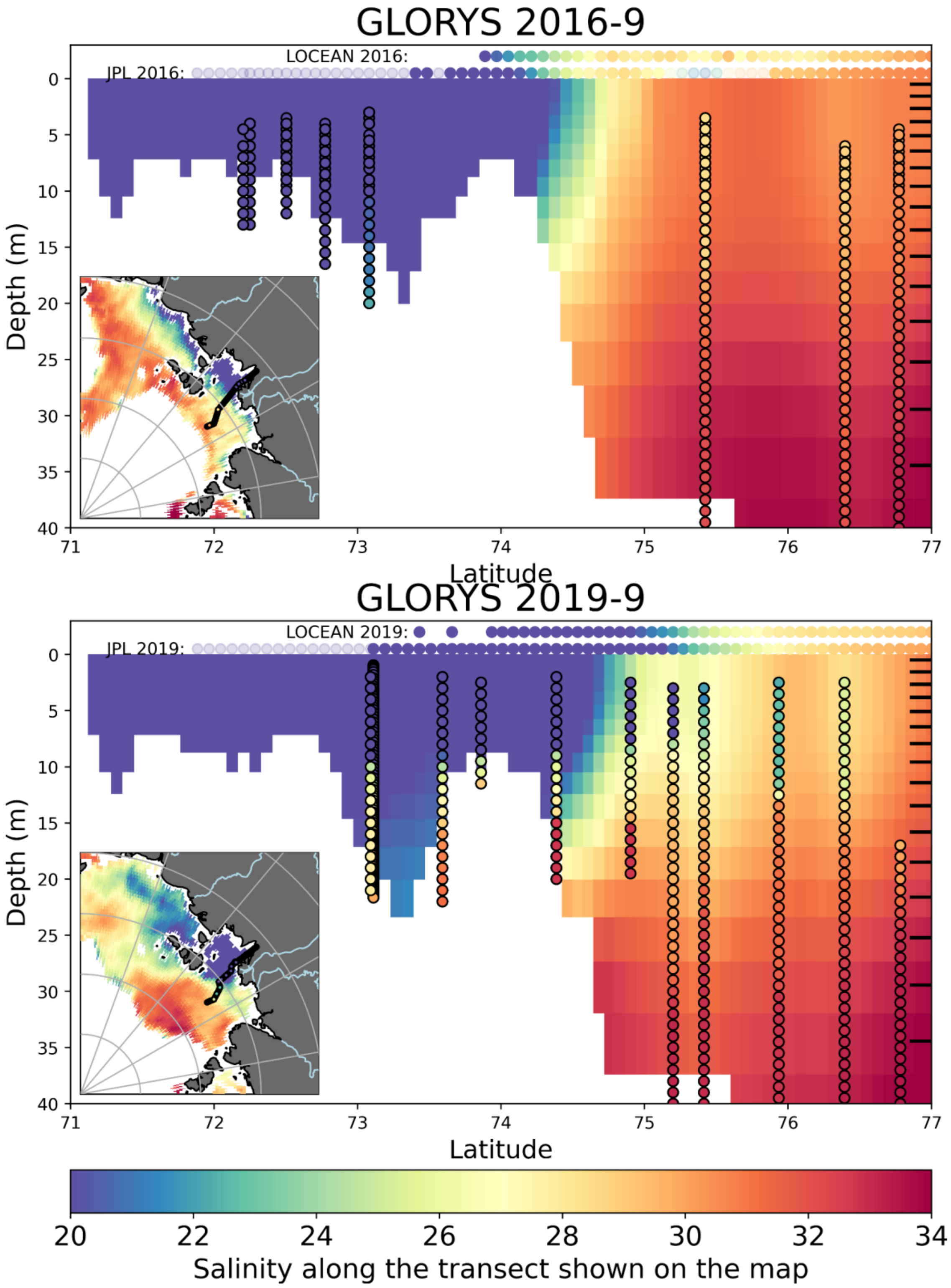

Figure 3.3: GLORYS12V1 salinity vertical transects for 2016 (top) and 2019 (bottom) as colour mesh with in-situ data overlaid with black rings and satellite data for that transect for JPL SMAP and LOCEAN SMOS SSS shown as a line of points (without black wings). JPL SMAP data is made semi-transparent where the provided SMAP SSS uncertainty is > 1 pss.). The location of these transects are shown in the inset in the bottom left by the black line which is interpolated through in-situ data (overlaid on a map of JPL SMAP SSS for each year) The GLORYS12V1 vertical levels are overlaid as black lines at 77 °N.

GLORYS12V1 features a well-mixed plume in the shallowest regions of the shelf in 2016 and 2019 (Figure 3.3), and in almost all other years considered. Hence, it agrees well with in-situ data in regions and years where the plume is well-mixed nearshore (e.g. 2016 shown above and 1994 and 2000 not shown) but fails to represent years with a stratified plume nearshore (e.g. 2019 shown above and 2008 and 2011 not shown). The variability of stratification dynamics, even just in the two years examined, suggests it is not appropriate to assume a constant mixed layer depth on the shallow shelf, as previously applied to estimate fresh water content (Umbert et al., 2021). In all years examined, in-situ data shows the fresh layer (< 15 pss) is relatively shallow and only extends between 5 and 10 m, shallower than Kara due to weaker tidal mixing (Osadchiev et al., 2021).

In 2019, differences in surface plume extent are visible between GLORYS12V1 and in-situ data. Some of these differences are due to spatio-temporal mismatch of September monthly 1/12 degree data with point in-situ data (in late September/early October), as vertical stratification is very seasonally and regionally variable (and bathymetrically controlled) in this region, and can vary considerably on a weekly timescale (Janout et al., 2020; Tarasenko et al., 2021). However, both satellite products more closely resemble the extended plume visible in in-situ data than GLORYS12V1, suggesting this is not the main reason for these differences. The reasons for these differences are discussed further in 3.4.3.

In addition, previous studies show considerable interannual variability in the lowest values of SSS at the outflow of the Lena River. Whilst in certain years, there are only very small regions of SSS below 20 pss (2014), in other years, notable regions of SSS as low as 6 pss have been observed (in 2013) (Janout et al., 2020). Within GLORYS12V1, the shallow surface layer is consistently more saline (between 15-20 pss) than in-situ data and salinities below 20 pss are typically very confined to the shelf. Although there are few satellite SSS retrievals near the coast (due to land contamination), nearshore SSS are notably lower and quite variable (10-20 pss) in LOCEAN SMOS and JPL SMAP and more consistent with in-situ data. Overall, within shallow shelf regions (< 20 m), the more saline surface waters, fresher subsurface waters and less extensive surface plumes suggest GLORYS12V1 is too well-mixed compared to in-situ data (discussed further in section 3.4.3). This is reinforced by the weak tidal influence in this region and as there is rarely sufficient wind-driven mixing to break up such strong stratification (Fofonova et al., 2014; Hölemann et al., 2011; Janout and Lenn, 2014; Shakhova et al., 2014).

Salinity stratification on the shelf is much stronger than that of temperature and is by far the dominant control on density in this region (Appendix Figure B.6, Osadchiev et al., 2021). SST, and stratification in temperature also vary considerably over the course of September, so a higher temporal resolution analysis would be needed for investigating temperature stratification dynamics. This is visible from the difference between in-situ data (from late September/early October) and September mean satellite/reanalysis SST data (Appendix Figure B.1). Therefore, this study focuses on salinity stratification in this region, which is more consistent over the course of September, and more appropriately represented by the monthly data used for analysis in this study.

3.3.2 Impact of runoff and wind stress on SSS, SST and SIC in GLORYS12V1

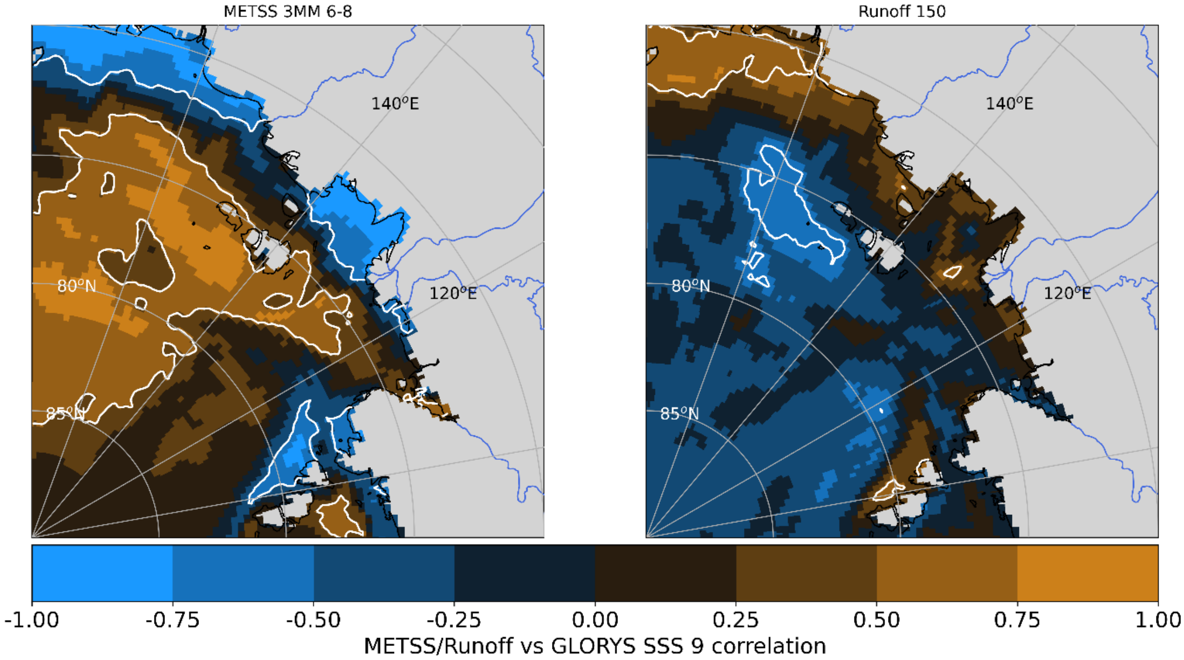

Figure 3.4: Correlation between GLORYS12V1 September SSS and the three-month mean ERA5 eastward turbulent surface stress (METSS) over June to August (6-8) (left) over 1993-2022. Correlation between GLORYS12V1 September SSS and cumulative Lena River runoff in spring (Julian day 150) (right) over 1993-2022. Regions where correlations are statistically significant ($p \leq 0.05$) are denoted by the white contour and brighter colours.

There is a significant spatial pattern in correlation between the three-month (June to August) mean eastward turbulent surface stress and GLORYS12V1 September SSS field for the 1993-2022 time period (Figure 3.4, left). This pattern consists of a strong negative correlation nearshore (< -0.75) and a strong positive correlation offshore (> 0.75), particularly in the East Siberian Sea. The negative correlation suggests strong eastward wind stress is consistent with fresher SSS nearshore. The strong positive correlations offshore are present, albeit in different regions, throughout June, July and August, as well as in the three-month mean (Appendix Figure B.2). However, extensive negative correlations nearshore are only present in July and August, suggesting eastward turbulent surface stress in these months is a stronger control on near shore SSS. A small region of negative correlation (< -0.75) is also present just East of the Vilkitsky Strait, and is visible in all three months. These strong correlations are statistically significant at $p < 0.05$ (highlighted by the white contour).

A weak, mostly non-significant spatial pattern in correlation is found between cumulative spring runoff and GLORYS12V1 SSS (Figure 3.4, right). This pattern suggests a positive correlation nearshore, particularly in the East Siberian Sea, and a negative correlation offshore. The weak positive correlation nearshore suggests increases in runoff are consistent with increases in SSS. This pattern is the opposite of what would be expected and what has previously been suggested: that an increase in runoff would drive nearshore freshening. However, there is almost nowhere that this correlation is statistically significant. Whilst there are some regions that yield significant p values, these regions are all relatively small and more confined to the East Siberian Sea. The spatial patterns of correlation between GLORYS12V1 September SSS and both cumulative autumn and total annual runoff show similar correlations but are even weaker and are not statistically significant at $p < 0.05$ (Appendix Figure B.2).

Similar correlation analyses conducted between runoff and eastward surface stress with SSS in the other reanalysis products yielded similar spatial correlation patterns to those visible here in GLORYS12V1.

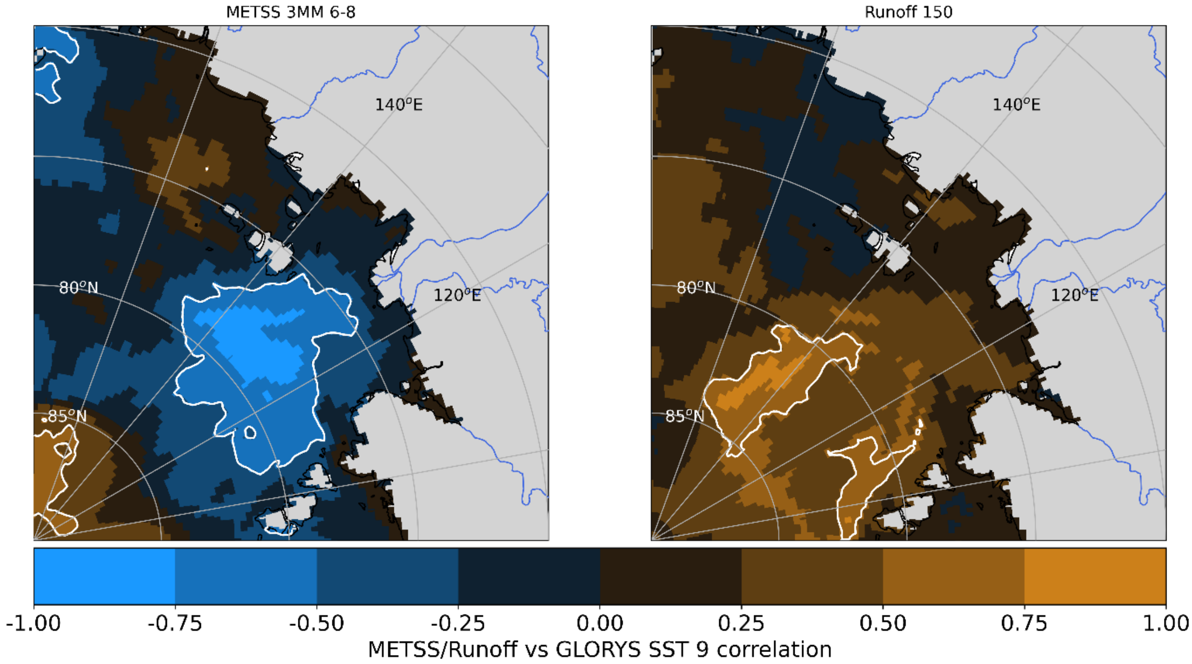

Figure 3.5: Correlation between GLORYS12V1 September SST and the three-month mean ERA5 eastward turbulent surface stress (METSS) over June to August (6-8) (left) over 1993-2022. Correlation between GLORYS12V1 September SST and cumulative Lena River runoff in spring (Julian day 150) (right) over 1993-2022. Regions where correlations are statistically significant ($p \leq 0.05$) are denoted by the white contour and brighter colours.

Figure 3.5 depicts the strong spatial pattern of correlation between the three-month (June to August) mean eastward turbulent surface stress and GLORYS12V1 SST. This spatial pattern consists of strong negative correlations (< -0.75) near the edge of the continental shelf. This negative correlation suggests eastward wind stress is consistent with cooler SSTs near the edge of the continental shelf (and that westward wind stress is consistent with warmer SSTs in this region). The region of negative correlation differs in region between June and August (Appendix Figure B.3). It is closest to shore in June and appears to move offshore over July and August. Whilst this negative correlation is mainly confined to the Laptev Sea in June and August, it extends into the East Siberian Sea in July. No significant correlation is present nearshore in any month.

A weak positive correlation is present between cumulative spring runoff and GLORYS12V1 SST throughout the Laptev Sea. This positively correlation is not statistically significant anywhere except in the central Arctic (> 80 °N). This positive correlation suggests increased spring runoff is consistent with warmer SSTs throughout the Laptev Sea. The spatial patterns of correlation between GLORYS12V1 September SST and both cumulative autumn and total annual runoff show similar correlations but are even weaker and are not statistically significant (Appendix Figure B.3).

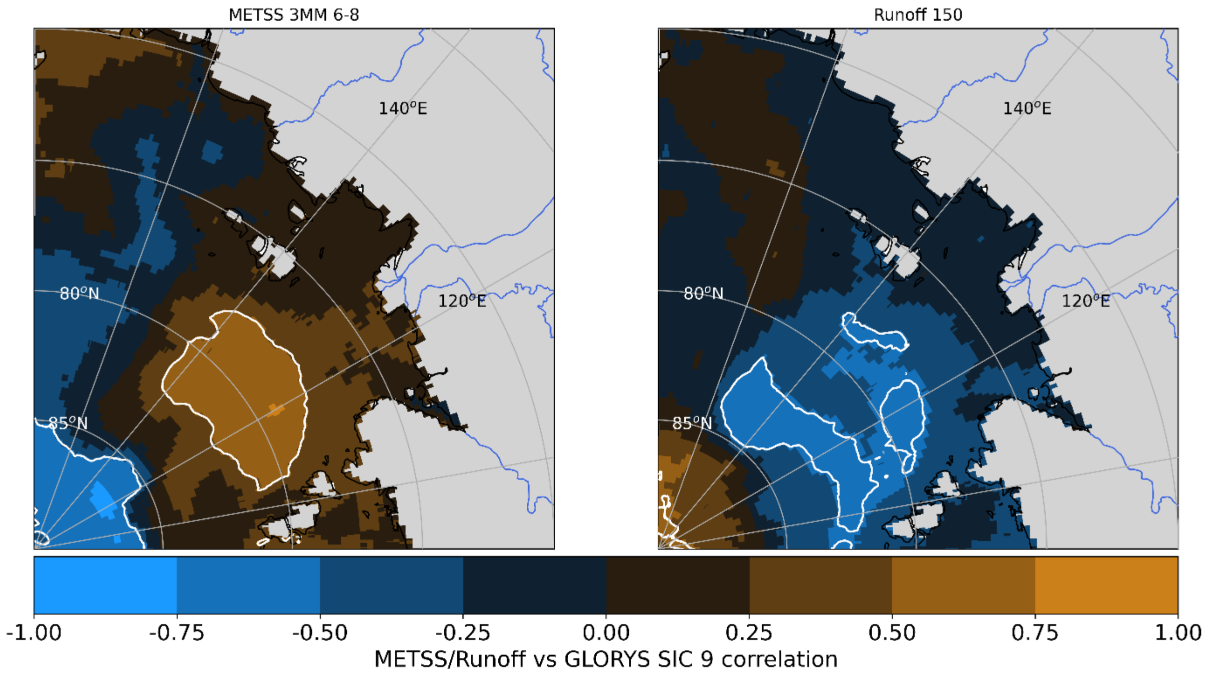

Figure 3.6: Correlation between GLORYS12V1 September SIC and the three-month mean ERA5 eastward turbulent surface stress (METSS) mean over June to August (6-8) (left). Correlation between GLORYS12V1 September SIC and spring cumulative Lena River runoff (to Julian day 150) (right) over 1993-2022. Regions where correlations are statistically significant ($p \leq 0.05$) are denoted by the white contour and brighter colours.

Figure 3.6 depicts the strong spatial pattern of correlation between the three-month (June to August) mean eastward turbulent surface stress and GLORYS12V1 SIC. This pattern suggests a large region of strong positive correlation is present just off the continental shelf in the Laptev Sea and a region of strong negative correlation is present in the central Arctic (> 85 °N). In turn, this implies that eastward wind stress is consistent with increased SIC in the northern Laptev Sea and lower SIC in the central Arctic (and that westward wind stress is consistent with decreased SIC in the northern Laptev Sea and increased SIC in the central Arctic).

A large region of weak negative correlation is present between cumulative spring runoff and GLORYS12V1, suggesting increased spring runoff is consistent with lower SIC. This negative correlation is present throughout almost all the Laptev Sea but is only significant ($p < 0.05$) near 84 °N. The relatively small regions of significant correlation with SIC may be due to the long-term decline in sea ice cover over this period, and hence the changing region of interannual variability in sea ice concentration. However, this hypothesis warrants further investigation.

3.3.3 Drivers of interannual variability in September SSS

The mean atmospheric circulation pattern, represented in Figure 3.7, is calculated as the mean surface stress over the box defined in Figure 3.2. Values are notably different in 2016 and 2019 (Figure 3.2). In 2016, there is predominantly cyclonic circulation, with strong Eastward winds over the Laptev Sea shelf, and Northward winds present over the region of the Laptev Sea just off the continental shelf. In 2019, there is predominantly anticyclonic circulation with North-westward winds dominant over the Laptev Sea shelf. The anticyclonic circulation visible in 2019 more closely resembles the mean circulation pattern visible over 2011-2020 (Figure 3.1).

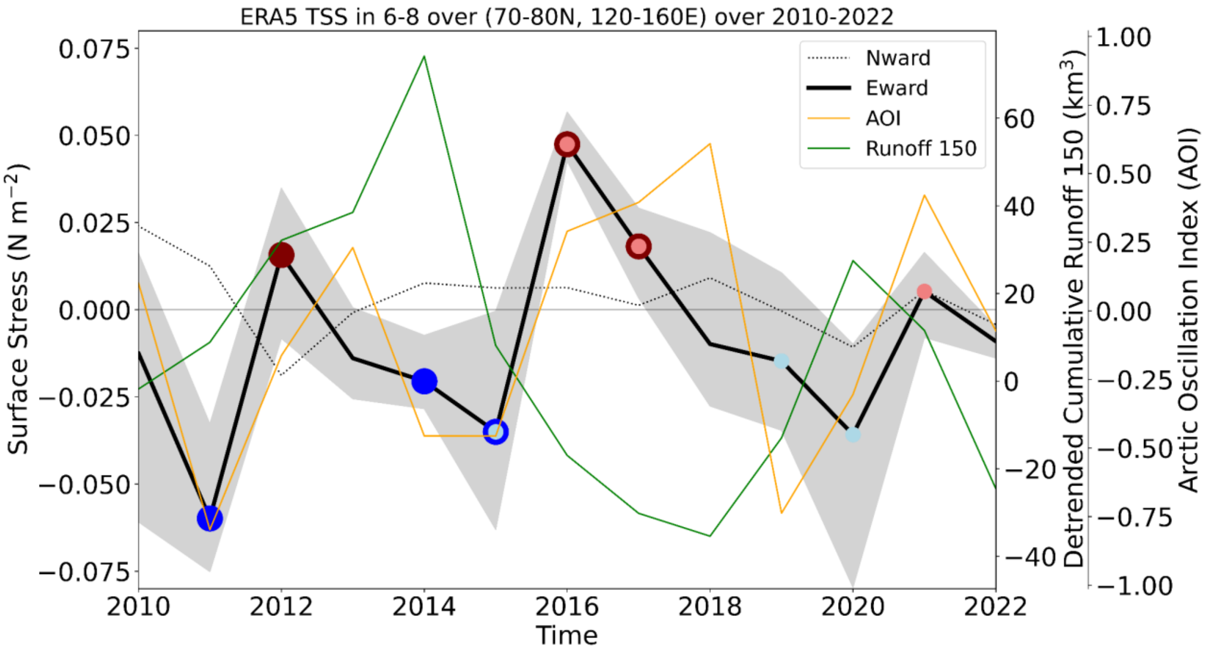

Figure 3.7: Three-month (June to August) mean ERA5 eastward (black solid) and northward (black dashed) turbulent surface stress over 70-80 North and 120-160 East. Overlaid are dots indicating the most eastward (red dots) and westward (blue dots) years chosen for analysis for both the longer SMOS/GLORYS12V1 timeseries (2011-2020) (darker red and blue dots) and the shorter SMAP timeseries (2015-2022) (lighter red and blue dots). The range of the maximum and minimum eastward turbulent surface stress between June and August is shaded in grey. Spring cumulative Lena River runoff (until the 150th Julian day) (green) is overlaid.

The magnitude of variability in mean eastward turbulent surface stress (± 0.05 N m^{-2}) across the entire timeseries is notably larger than that of northward turbulent surface stress, which remained within ± 0.02 N m^{-2}. The years of highest eastward turbulent wind stress are 2012, 2016, 2017 over the SMOS timeseries and 2016, 2017 and 2021 over the SMAP timeseries. The years of strongest westward turbulent wind stress are 2011, 2013 and 2019 over the SMOS timeseries and 2015, 2019 and 2020 over the SMAP timeseries. In years where the mean eastward turbulent surface stress is negative (denoting predominant westward turbulent surface stress), there is considerably more within-year variability (typically > 0.05 N m^{-2} in eastward turbulent surface stress in the months spanning June to August (denoted by the grey overlay in Figure 3.7).

Spring cumulative runoff does not significantly co-vary with turbulent surface stress over 2010-2022 (r=-0.30, p=0.31) or over 1993-2022 (r = -0.29, p = 0.11). Spring runoff is highest in 2012, 2013 and 2014 over the SMOS timeseries and 2015, 2020 and 2021 over the SMAP timeseries. Spring runoff is lowest in 2016, 2017 and 2018 over both the SMOS and SMAP timeseries. Interannual variability in runoff and turbulent surface stress over the short satellite period visible in Figure 3.7 are consistent with interannual variability over longer time periods (not shown).

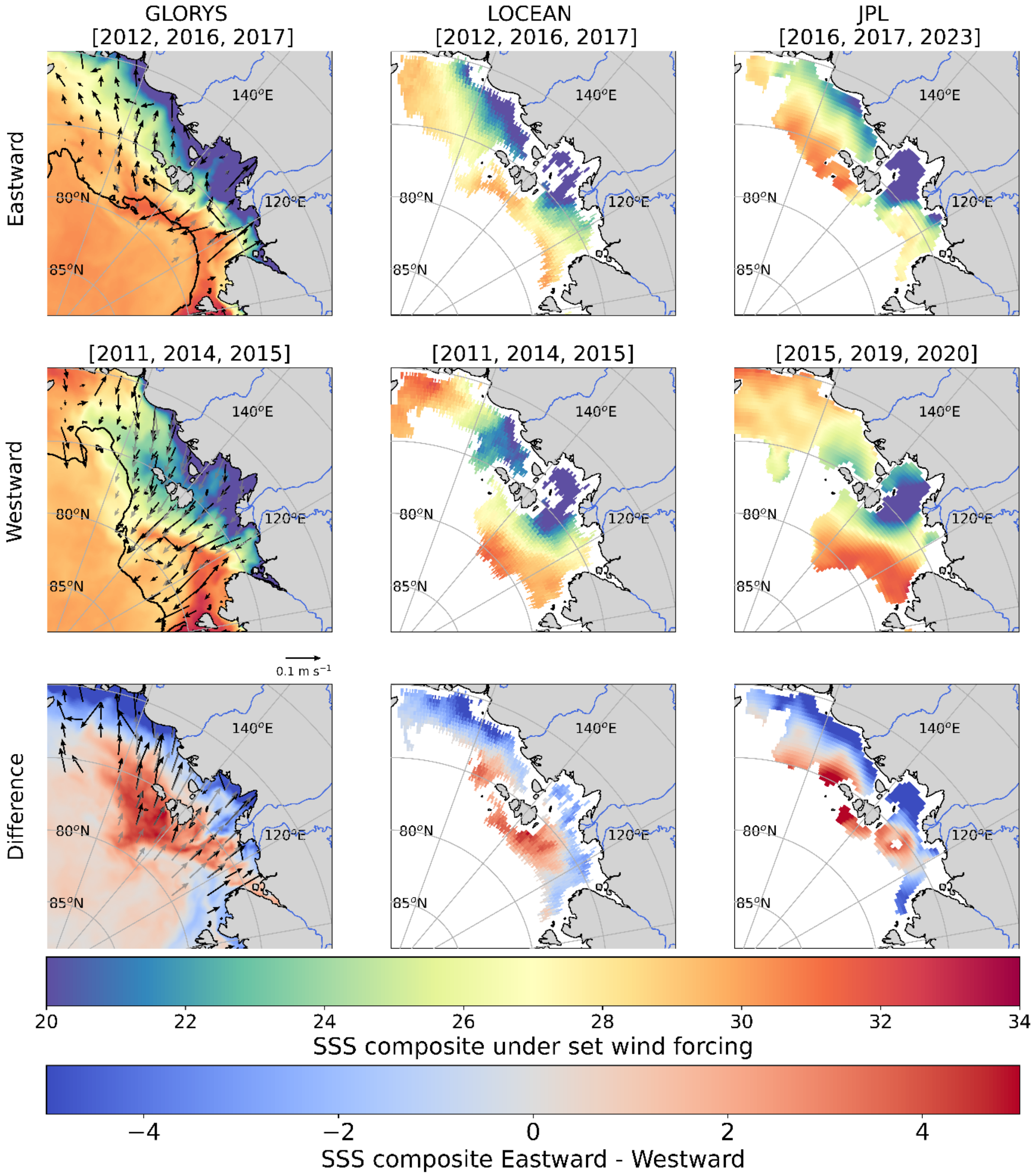

Figure 3.8: Eastward (E, top row) and westward (W, middle row) composites calculated for (left to right) GLORYS12V1 SSS, LOCEAN SMOS and JPL SMAP, from the identified three most eastward and westward years (over 2011-2020 for GLORYS12V1 and LOCEAN SMOS and over 2015-2022 for JPL SMAP). The difference composite (eastward – westward) for each product is shown on the bottom row. The GLORYS12V1 mean 30% sea ice concentration contour is overlaid on the respective composite plots. Eastward and westward GLORYS12V1 current velocity composites for June-August and the difference between them are overlaid as black arrows on the respective composite plots (masked by the region of mean sea ice concentration above 30%). Expected Ekman surface currents based on observed average eastward and westward wind stress (and their difference) are overlaid as grey arrows for comparison.

The eastward/westward composites of all three SSS products agree strongly, regardless of the differing years chosen for analysis (Figure 3.8). The composite analysis highlights the differing pattern of SSS under positive (eastward) and negative (westward) zonal wind. The eastward composite closely resembles the 2016 SSS pattern visible in Figure 3.2, and the westward composite closely resembles the 2019 SSS pattern. This strong resemblance between particularly anomalous individual years and the zonal wind composite plots supports that the zonal wind is the dominant driver of variability in this region.

GLORYS12V1 current velocity composites and expected surface Ekman transport calculated from ERA5 wind stress also agree well in direction and magnitude. Years with strong westward wind have considerable expected and observed offshore transport, and northward spreading of the plume, denoted by northward current velocities in GLORYS12V1 and by the presence of anomalous fresh water in the Northern Laptev Sea and relatively higher salinity water in the East Siberian Sea in all products. Alternatively, years of eastward wind are associated with onshore and alongshore transport, and a coastally confined plume, denoted by southward current velocities in GLORYS12V1 and by more saline waters in the Northern Laptev Sea and fresher waters in the Southern Laptev and East Siberian Sea.

The composite difference plots provide a clearer visualisation of the North/South (offshore/nearshore) dipole in current velocities and freshwater transport visible under eastward/westward wind forcing. The strong agreement between all three products strengthens the weighting of this finding, particularly as the difference plots appear to agree even more closely than the individual eastward/westward composites. This agreement suggests that although the three products have different mean SSS states, they capture very similar patterns of variability.

There is a notable difference in SIC in years of westward and eastward wind forcing in both GLORYS12V1 and the satellite data (indicated by the absence of SSS data). Under westward wind forcing, the Laptev SIC is smaller in the Laptev Sea and the 30% SIC contour is nearer shore in the East Siberian Sea. The opposite is true under eastward wind forcing, with a larger SIC in the Laptev Sea and the 30% SIC contour further offshore in the East Siberian Sea.

3.3.4 Impact of variability in wind forcing on SST

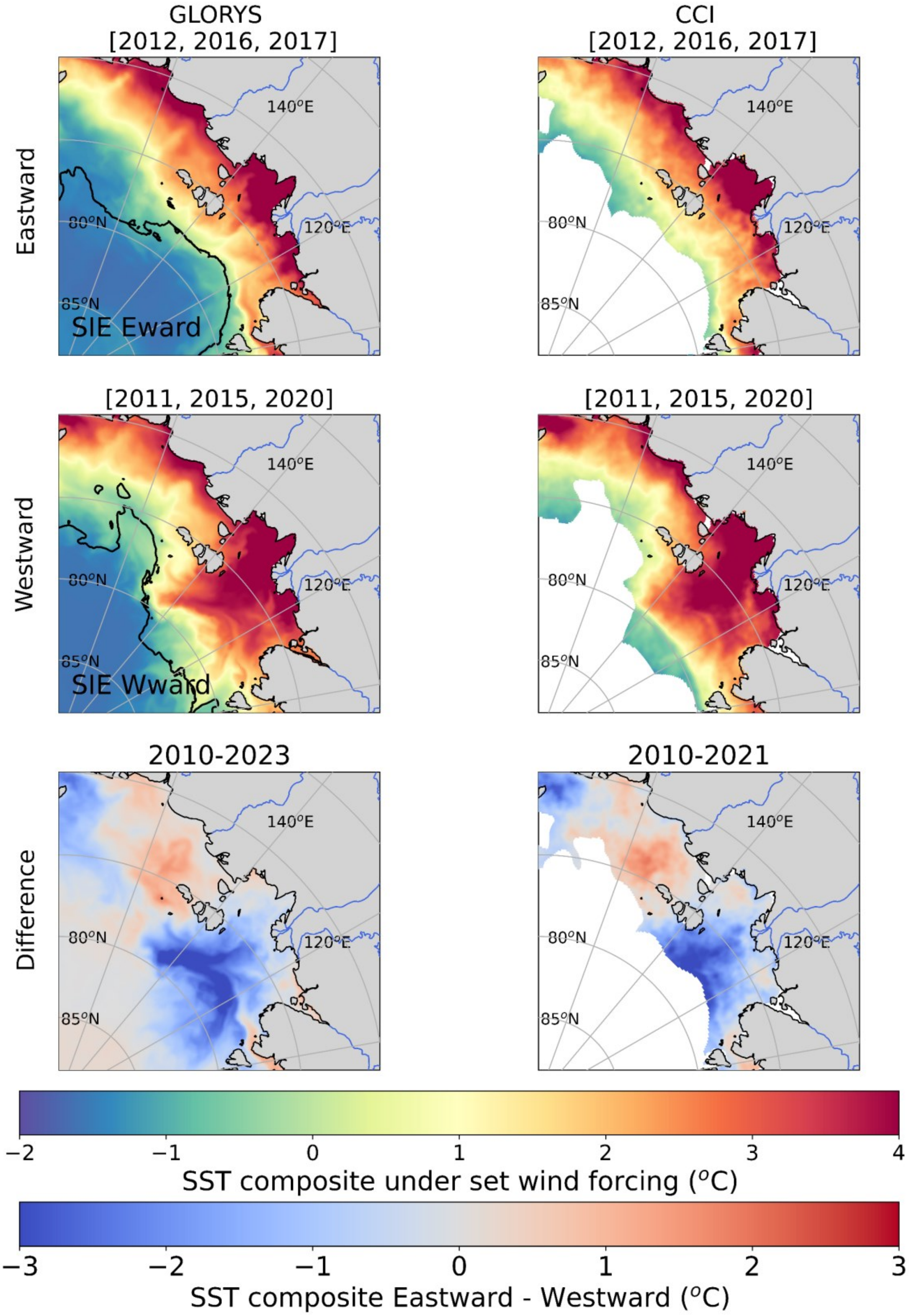

Figure 3.9: Eastward (E, top row) and westward (W, middle row) composites calculated from the identified three most eastward and westward years over 2011-2020 for (left to right) GLORYS12V1 SST and L4 CCI SST (masked by 30% sea ice concentration). The difference composite (eastward – westward) for each product is shown on the bottom row. The mean 30% sea ice concentration contour for eastward and westward years is used to mask L4 CCI data and is overlaid in GLORYS12V1 in black on both eastward and westward composite plots.

Similar to Figure 3.8, Figure 3.9 represents the eastward and westward composites of GLORYS12V1 and ESA CCI SST. Temperatures < 1 °C are typically present off the continental shelf in both composites (and all years analysed), with a rapid transition in temperature present at the 30% SIC margin (Figure 3.9). On the shelf, temperatures are typically warmer (> 1 °C) and riverine plume is typically > 2 °C, with large regions in excess of 4 °C. The presence of these two opposing water masses in GLORYS12V1 (i.e. the cold salty offshore water and the warm fresh river plume) and the mixing between them is clearly visible in GLORYS12V1 T-S plots (Appendix Figure B.6).

The eastward/westward composites of both products agree very well and suggest notable differences in SST pattern under differing zonal wind forcing. Under eastward wind forcing, both GLORYS12V1 and CCI SST composites show that warm SST anomalies are confined to the southern Laptev Sea and travel alongshore towards the East Siberian Sea. This eastward wind state is coincident with a larger SIC in the Laptev Sea and a 30% SIC contour nearer shore in the East Siberian Sea. Under westward wind forcing, both SST composites show warm SST anomalies are mostly advected offshore to the Northern Laptev Sea. The westward wind state is coincident with lower SIC in the Laptev Sea and a 30% SIC concentration contour further from shore in the East Siberian Sea. A dipole composite pattern is also visible in the SST difference composite, as is visible in the SSS difference composite. However, the difference composite between eastward and westward wind states presents in an East/West direction rather than a North/South direction. The differing relationship between SST and SSS under eastward and westward wind forcing is also denoted by the differing T-S plot patterns and correlation coefficients under years of eastward and westward wind forcing, characterized by the presence of warm salty and cold fresh water under westward wind forcing (Appendix Figure B.6).

3.4 Discussion

3.4.1 Runoff as a driver of SSS, SST and SIC variability

Spring, autumn and annual Lena River runoff do not appear to play a role in controlling GLORYS12V1 September SSS, SST or SIC in the Laptev or East Siberian shelf seas. Cumulative spring runoff is most strongly correlated to variability in SSS, SST and SIC, suggesting the timing of the initial peak in runoff has more of an impact on Laptev Sea dynamics than the cumulative runoff in autumn or the total runoff over the year. However, the correlations with spring cumulative runoff are almost entirely not significant.

It might be expected that years with the largest magnitude of cumulative spring / autumn / annual river discharge would have the largest fresh surface layer (< 20 pss) as previously suggested of cumulative annual discharge (Umbert et al., 2021). However, the GLORYS12V1 correlation analysis suggests no significant correlation near the outflow of the Lena River between SSS and cumulative runoff at any time of year. If anything, the opposite pattern appears true nearshore in the East Siberian Sea: with increases in spring runoff driving higher salinities near the coast and low salinities offshore. The differing result here, compared to Umbert et al. (2021) appears to be linked to differences in BEC and GLORYS SSS, and the variability in fresh surface layer area. No alternative mechanism to date explains the opposing behaviour observed here. It is possible there is some negative feedback whereby earlier spring runoff drives earlier sea ice retreat, and expands the region of wind influence and spreads the plume further offshore. However, this counterintuitive correlation warrants further investigation but this is outside the scope of this thesis.

The short nature of the satellite SSS timeseries prevents an in-depth correlation analysis with runoff as was done with GLORYS12V1 but visual comparison indicates no clear pattern between interannual variability in spring runoff and SSS over the SMOS or SMAP satellite periods. This comparison is also complicated by the interannually varying ice-free region, which determines the total area of SSS retrievals and any derived fresh surface layer areas. Over this period, spring runoff is lowest in 2016, 2017 and 2018. Whilst the fresh surface layer is extensive in 2018 (not shown), it is very small and coastally confined in 2016 and 2017 (Appendix Figure B.5). These two years were excluded from analysis in Umbert et al. (2021) due to lack of SSS data, which partially explains the differing results here. Whilst the area of satellite SSS retrievals is relatively small in these years compared to other years analysed, the edge of the plume is clearly visible in the area of open water. This suggests that the small plume observed in these two years is not just due to the relatively small area of open water and that there is no reason to exclude these years from analysis. Conversely, spring runoff is highest in 2012, 2013 and 2014. Again, there is no conclusive SSS pattern as the fresh surface layer is relatively average in all three of these years (Appendix Figure B.4, Appendix Figure B.5). The inconsistent response in satellite data suggests cumulative spring runoff is not a major driver of interannual variability in SSS pattern, as is suggested from GLORYS12V1 and as has previously been suggested by other studies (Osadchiev et al., 2021a).

3.4.2 Wind as driver of SSS variability

Previous studies using sparse in-situ data have suggested wind forcing appears to drive some variability in freshwater transport (Dmitrenko et al., 2005; Osadchiev et al., 2021a). Satellite SSS data shown here provides a picture of SSS variability and confirms what has previously only been suggested from in-situ data: that zonal wind forcing is the dominant driver of Laptev SSS. Satellite SSS data also provides a clear, complete visualization of differences in freshwater transport throughout the sea ice free Laptev and East Siberian Sea under different wind regimes, augmenting the scattered view available from in-situ data. Westward wind drives considerable offshore transport, and northward spreading of the plume toward the Northern Laptev Sea. Conversely, eastward wind is found to drive alongshore transport, resulting in a coastally confined river plume, denoted by more saline waters in the Northern Laptev Sea and fresher waters in the Southern East Siberian Sea. Given the different eastward and westward years chosen for composite analysis for SMOS and SMAP, the agreement in eastward/westward SSS composites between JPL SMAP and LOCEAN SMOS products solidifies this finding.

The composite analysis highlights the dominance of the zonal wind over the meridional wind in driving SSS patterns. Within regions with particularly shallow shelf bathymetry, such as in the South Laptev Sea, the Ekman current has been suggested to almost completely align with wind direction or to be transported ~60 ° to the right (Dmitrenko et al., 2005; Kubryakov et al., 2016; Zatsepin et al., 2015). The relatively good agreement in direction between the expected surface Ekman current and the observed surface current in GLORYS12V1 suggests the surface current appears to follow Ekman theory and is aligned ~45 ° to the right of the wind. However, the alignment between the expected Ekman surface currents and the observed strong North/South dipole in SSS composite difference plots suggests that mean transport is relatively well aligned with surface currents and therefore suggest that the full Ekman spiral does not manifest.

Meridional wind stress also does appear to play a role in plume transport but only in the absence of strong zonal wind stress. This has previously been shown to be true for both 2014 (Janout et al., 2020) and 2018 (Tarasenko et al., 2021), where the wind is primarily north-westward and fresh water is transported directly offshore. Both LOCEAN SMOS and JPL SMAP support this.

3.4.3 Vertical distribution of plume

Nearshore in-situ data suggests that the two modes of SSS variability, visible under eastward/westward wind forcing appear to be related to very different stratification dynamics (Figure 3.3). In 2016, in-situ and GLORYS12V1 SSS agree particularly well and show a well-mixed very fresh plume nearshore (Figure 3.3), likely driven by the strong consistent onshore Ekman transport driving downwelling (Osadchiev et al., 2021). This year (2016) stood out as having a particularly well mixed plume compared to all other in-situ data in this region, the extent of which had not previously been observed (Janout et al., 2020) . A similar dynamic appears to be visible in 1994, where strong eastward wind stress is coincident with a coastally confined and well-mixed plume (not shown but visible in in-situ data and GLORYS12V1 SSS and SST).

Conversely, in-situ data showed a strongly stratified fresh layer in 2008, 2011 and 2019, even in shallow regions on the shelf (Osadchiev et al., 2021), which is poorly represented nearshore in GLORYS12V1 (Figure 3.3). The strong stratification on the shelf, visible in in-situ data in these years, suggests that the fresh layer is more strongly stratified in years with considerable northward spreading. This phenomenon appeared true in 1994 and 2016, where strong onshore Ekman transport appeared to drive the well-mixed plume observed. Hence, despite that the shallow shelf is shallower in many regions than both the Ekman depth used here (10 m) and the previously calculated Ekman depth for this region (37 m) (Baumann et al., 2018; Tarasenko et al., 2021), Ekman transport plays a role in controlling vertical stratification, at least in years where eastward wind stress drives onshore transport and mixing / downwelling (Lentz and Helfrich, 2002). It is also possible that the magnitude of river discharge is a dominant control on the vertical distribution of SSS, given there is no conclusive evidence that the surface fresh layer varies with cumulative runoff.

This hypothesis was not tested as the constant well-mixed plume nearshore suggests GLORYS12V1 is not capable of fully representing plume stratification dynamics in this complex environment. Other model output was considered for use (including CMEMS TOPAZ, GLORYS2V4, ORAS5, GloSea5/FOAM, CGLORS), but all models considered show the shallow shelf to be well-mixed in all years considered. The challenge of accurately representing mixing/stratification dynamics in Arctic shallow shelf seas has been widely documented (Hordoir et al., 2022; Janout et al., 2020). Given all models used here have many vertical levels but are all (except CMEMS TOPAZ) on z-level grids, it is likely the overmixing issue is a result of z-level vertical grids, as previously suggested (Arpaia et al., 2023; Heuzé et al., 2023; Wise et al., 2022). Even in years with a mostly well-mixed plume (EG 2016), in-situ data typically shows a more saline layer at depth in certain regions on the shelf, which is almost never captured by GLORYS12V1. The challenge of accurately modelling stratification in Arctic shallow shelf seas and the very limited availability of in-situ data on the shelf prevents a more in-depth analysis of the representation of vertical plume structure within GLORYS12V1. Whilst GLORYS12V1 does assimilate some in situ observation in this region, incorporation of data on the shallow shelves (such as that used for comparison in this study) may help to improve representation of variability in stratification dynamics. It may be useful for future studies to consider if the inclusion of interannual runoff forcing would improve representation of stratification dynamics.

3.4.4 Sea surface temperature / sea ice concentration variability

SST is known to be a useful indicator of plume location in this region (Dmitrenko et al., 2005; Osadchiev et al., 2021a; Tarasenko et al., 2021). During the summer, Lena River water is typically at around 16 °C before entering the Laptev Sea, which is much warmer than the typical SST below sea ice of < 0 °C (Juhls et al., 2020). This sets up the gradient in SST that is present over the Laptev Sea (Appendix Figure B.1), with temperatures < 0 °C off the continental shelf and below sea ice and temperatures > 4 °C present over much of the shelf. Similar results have previously been shown from in-situ data, with offshore SSTs typically < 0 °C and SSTs near the mouth of the Lena River typically > 3 °C and up to 10 °C in the last 2 decades (Osadchiev et al., 2021a). This represents a significant increase in September near-shore SSTs over the last several decades (Kraineva and Golubeva, 2022; Polyakov et al., 2005).

Many studies have considered the dominant drivers of SSS interannual variability and of the seasonal and decadal variability in SST (Janout et al., 2020; Osadchiev et al., 2021a), but few have considered whether SSS and SST co-vary with distance from the mouth of the Lena and what drives interannual variability in SST in this region. The lagged-correlation and composite analyses shows that zonal wind component is a key driver of interannual variability in SST as well as of SSS. This finding highlights that correspondence between SSS and SST is not only driven by their common source but also by their common driver of interannual variability. This strong correspondence is also highlighted by the significant correlations between GLORYS12V1 SST and all SSS products shown under both eastward and westward wind forcing (Appendix Figure B.6). The strong correlation and correspondence between eastward/westward SSS and SST composites on the shallow Laptev shelf is unsurprising given that warm and fresh Lena River water dominates oceanic properties in this region.

Whilst the eastward/westward composites appear similar, considerable differences are observed between the SSS and SST composite difference and correlation plots. The SSS composite difference (eastward-westward) plots suggest a North/South dipole where eastward forcing appears to drive onshore / south-eastward transport of fresh SSS anomalies and westward wind forcing drives offshore / northward transport of fresh SSS anomalies. In the lagged-correlation analysis between mean eastward turbulent surface stress and SSS, this pattern is highlighted by the dipole between the strong negative correlation nearshore and strong positive correlation at the edge of the continental shelf. Conversely, the SST composite (eastward-westward) difference plots show an East/West dipole where eastward surface stress drives eastward transport of warm SST anomalies and westward surface stress drives north-westward transport of warm SST anomalies. The lagged-correlation analysis between June to

August eastward turbulent surface stress and SST consists predominantly of a strong negative correlation in the northern Laptev Sea. Whilst there is a weak region of positive correlation in the East Siberian Sea, which would create the East/West dipole described above, it is not significant. The difference in strength of correlation indicates that whilst westward wind stress drives a strong increase in SST (and/or eastward wind stress a strong decrease in SST) in the northern Laptev Sea, eastward/westward wind stress drives a much smaller change in SST in the East Siberian Sea. These differences in composite difference plots likely occur due to feedback cycles between SST, SIC, SSS and albedo.

Hence, whilst the zonal wind plays a key role in controlling both SSS and SST patterns, the differences between SSS and SST composite difference and correlation plots highlight that this warm and fresh water can be exposed to very different thermal and freshwater forcing after entering the Laptev Sea. This is reiterated by the difference in pattern in T-S diagrams under years of eastward and westward wind forcing, especially for GLORYS12V1 SSS and LOCEAN SMOS SSS (Appendix Figure B.6). Under eastward wind forcing, there is a very strong correlation between GLORYS12V1 SST and both GLORYS12V1 SSS and LOCEAN SMOS SSS. This strong correlation suggests that eastward wind is the primary driver of the pattern observed, with any thermal forcing predominantly warming the already warm, fresh river plume. Conversely, under westward wind forcing, the correlation between GLORYS12V1 SST and both GLORYS12V1 SSS and LOCEAN SMOS SSS is much weaker, and there is a much wider variation in SSS across the full range of SST. Comparing the responses of SSS and SST provides unique insight into understanding the contribution of the zonal wind in distributing warm riverine anomalies and the contribution of summer heating to the September SST pattern.

Regardless of differences in SSS and SST composite difference plots, the zonal wind clearly controls plume propagation. Under eastward wind forcing, it transports the fresh, warm plume along the coast to the East Siberian Sea, and otherwise, under westward wind forcing, it transports the plume offshore to the Northern Laptev Sea.

Zonal wind forcing is also a dominant control on the spatial distribution of September SIC in this region. The similarity in correlation patterns between eastward wind stress and GLORYS12V1 SST and SIC and the strong correlation between mean SST over the Laptev Sea and September SIC highlight the strongly coupled nature of SST and SIC in this region. The strong correlation previously found between river-water fraction and melt-water fraction suggests that early plume transport may drive sea ice melt in that region (Bauch et al., 2013). However, despite this strong correspondence, the initial heat brought by river runoff is only suggested to contribute ~10% to sea ice breakup in early spring (Dean et al., 1994). However, the initial loss of sea ice near the river mouth and the dark-coloured water that replaces it (high in dissolved and suspended particulate matter) alters surface albedo and increases heat absorption creating a strong positive feedback (Bauch et al., 2013; Park et al., 2020). As SSTs are cooler than atmospheric air temperature in summer, SSTs will continue to warm until atmospheric temperatures start to cool in autumn (Janout et al., 2016). The strongly stratified summer halocline also increases stability of the water column, making summer heating more effective (Osadchiev et al., 2021). Whilst warm summer air temperatures will drive a warming of SST in open water regions, freshwater input from precipitation has a negligible impact on SSS and sea ice melt only plays a small role in altering summer SSS (Dubinina et al., 2017). These processes drive the observed differences in composite difference and correlation plots.

The SSS composite difference plots represent just the direct response of SSS to the zonal wind (offshore/nearshore). The SST composite difference plots also highlight the importance of the SST/SIC positive feedback whereby warm river runoff drives sea ice melt, increasing the area of shallow open water exposed to the warm atmosphere, and further driving SST warming in newly open water regions. The much stronger correlation between zonal wind stress and SST and SIC in the northern Laptev Sea, compared to the East Siberian Sea, may be related to this SST/SIC positive feedback and the timing and/or region of sea ice retreat.

Under eastward wind forcing, the strong correlation between SST and SSS (Appendix Figure B.6) and the relatively smaller area of open water in the Laptev Sea suggests atmospheric thermal forcing either has little influence or only acts to strengthen the gradient between the warm, fresh plume and the cold, saltier waters offshore in years of eastward wind forcing. However, under westward wind forcing, it is possible that offshore transport drives earlier and/or more expansive sea ice melt, which would alter the area of open water exposed to the atmosphere and the length of time it is exposed to the warm summer atmosphere, driving more dramatic warming of SSTs. This process would explain the notably higher correlation between SSS and SST under westward wind forcing and can explain some of the difference in pattern in T-S diagrams under years of eastward and westward wind forcing. In particular, the warm, salty waters visible in westward T-S plots may be driven by enhanced warming of salty offshore waters that would otherwise be sea ice covered. Alternatively, these warm salty waters could be signatures of upwelling modified Lower Halocline Waters, with offshore Ekman transport. The northward plume expansion under westward wind forcing also explains the cold, fresh water visible in T-S diagrams, which is likely a product of mixing between the extended plume and the cold, salty water that typically sits offshore under sea ice. Whilst these hypotheses are consistent with results here, further work would be needed to confirm this. It is worth noting that the similarity between SSS and SST eastward/westward composites and the significant correlation between SSS and SST even under westward wind forcing highlight the importance of the zonal wind in modulating this SST/SIC warming positive feedback.

The difference in spatial pattern of SIC under eastward and westward wind forcing and the relationship between SST and SIC suggests zonal wind is not only a key driver of variability in SSS and SST but also of Laptev SIC.

Previous work in this region has suggested that variability in SSS is unrelated to sea ice dynamics (Osadchiev et al., 2021a). However, both the composite and correlation analysis here show that variability in zonal wind stress does play a role in controlling SST and SIC. Attributing interannual variability in SST and SIC to zonal wind stress is complex due to the SST/SIC warming positive feedback described above and the strong decline in SIC visible in the Laptev (Kraineva and Golubeva, 2022). Future work should be done to untangle the direct and indirect (via SST) influences of zonal wind on SIC in this region.

The spatial pattern of GLORYS12V1 eastward and westward SST composites is consistent regardless of time period chosen (the full GLORYS12V1 time period, the LOCEAN SMOS time period or the JPL SMAP time period), suggesting this variability is interannual in nature and does not only exist due to the SIC trend (i.e. if years of westward/eastward forcing are present earlier/later in the timeseries). In addition, the spatial pattern of variability visible in both SST composite difference plots and in eastward turbulent surface stress and SIC correlation plots is different from the long-term pattern of SST warming or SIC decline (between 1993-2002 and 2010-2019 in GLORYS12V1), which suggests a pattern of more rapid warming distributed across the continental shelf. The consistency of SST composites shown, the difference in spatial pattern of SST under differing wind forcing and the strength of correlation and similarity in correlation pattern between eastward turbulent surface stress and SST and SIC support that wind stress is a control on SST and in turn September SIC. The impacts of variability in SSS and SST on later sea ice formation and longer-term implications of these findings are explored further in section 6.6 (p123).

3.5 Conclusions

Satellite SSS agrees well with in-situ data ($r \geq 0.84$) and provides notable improvement compared to GLORYS12V1 SSS ($r \leq 0.80$) and the other reanalysis products ($r \leq 0.83$) considered in capturing patterns and variability observed by in-situ SSS data. Hence, satellite SSS provides a useful tool to strengthen our current understanding of Laptev Sea and wider Arctic SSS dynamics, particularly in regions with strong SSS gradients. Comparison between satellite and in-situ data in this region highlights the need for more near-surface in-situ data for validation in this region, particularly nearshore over the lowest salinities. The current lack of nearshore low salinity in-situ data limits the confidence in and ability to validate satellite data over regions of very low salinities (< 20 pss) and limits our understanding of vertical stratification over the shelf, particularly given its high spatial and temporal variability.

GLORYS12V1 and satellite SSS data confirms what in-situ data has previously suggested: that the zonal wind is the dominant driver of offshore/onshore Lena River plume transport, with strong consensus in SSS patterns under eastward and westward wind regimes in GLORYS12V1, LOCEAN SMOS and JPL SMAP. Annual, autumn and spring runoff do not appear to play a role in controlling interannual variability in SSS, SST or SIC in the Laptev and East Siberian Sea. The zonal wind also plays a key role in driving SST variability and appears to drive spatial variability in SIC across the Laptev and East Siberian Sea. The differences in spatial patterns of SSS and SST under eastward/westward wind forcing highlight the importance of the zonal wind for dispersing riverine heat and controlling the SST/SIC positive feedback, which plays a considerable role in driving further SST warming in shallow open water regions.

Chapter 4 Kara Sea

4.1 Introduction

The Kara Sea sits upstream and just to the west of the Laptev Sea and is partially enclosed by the Novaya Zemlya, to the west, and Severnaya Zemlya Archipelagos, to the east (Figure 4.1). Whilst the Laptev Sea has quite a shallow shelf (< 50m), with significant very shallow regions (< 20m), the Kara Sea is much deeper, as less than half the Kara Sea is < 50m. The enclosed nature of the Kara Sea limits transport from the Barents Sea and to the Laptev Sea, and the deeper bathymetry result in considerable differences in plume dynamics. The Kara Sea receives a third of the total fresh water to the Arctic, and almost double the volume of river runoff as the Laptev, primarily due to the contributions of both the Ob and Yenisei rivers. Despite this, the fresh layer generated by the Ob-Yenisei plume occupies a much smaller area than the fresh layer of the Lena plume (Osadchiev et al., 2023a). However, the Ob-Yenisei plume depth (15-30m) is typically deeper than that the Lena plume depth (5-15 m) (Hudson et al., 2024; Osadchiev et al., 2021; Osadchiev et al., 2023a; Osadchiev et al., 2020; Zatsepin et al., 2010). Differences in geography / bathymetry and the presence and interaction of both Ob and Yenisei river plumes cause significant differences in both the area and position of the plume and in its seasonal, interannual and decadal variability.

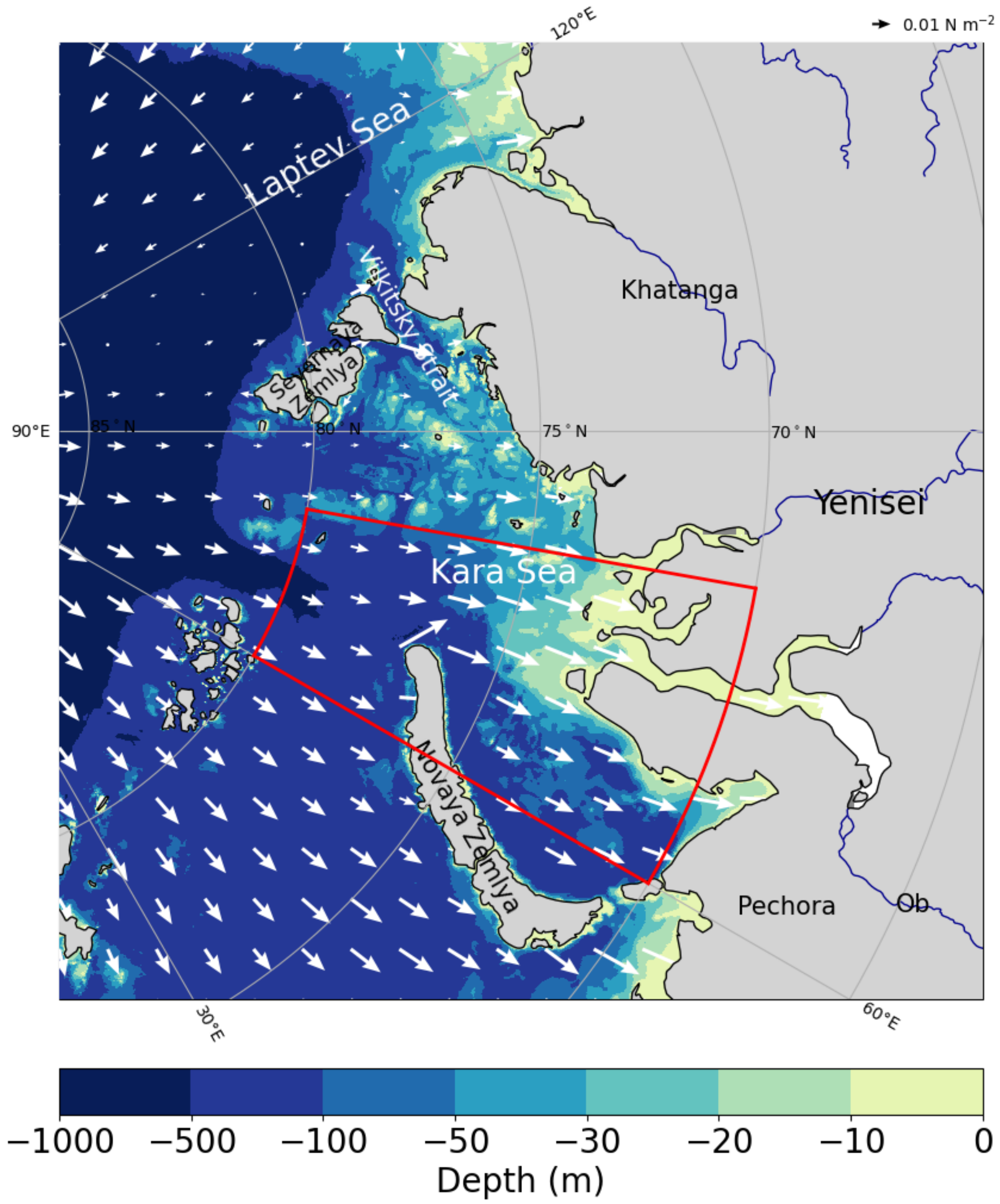

Figure 4.1: Map of Kara Sea and Vilkitsky Strait with bathymetry contours overlaid in shades of blue/yellow with mean 2010–2023 ERA5 June–August wind stress vectors overlaid over the ocean. The box used to calculate mean eastward/northward turbulent surface stress is overlaid in red.

The combined influence of both Ob and Yenisei runoff creates a large inflow of fresh water, concentrated over a short period in spring, which drives a strong seasonality in Kara Sea salinity, temperature and therefore stratification dynamics. Whilst runoff from both Ob and Yenisei rivers is relatively low in winter, the spring freshet transports almost three-quarters of the total freshwater input into the Kara Sea just over June to September (Pavlov and Pfirman, 1995). This considerable riverine input drives freshening of the Ob and Yenisei deltas, setting up an intense gradient in SSS between the plume nearshore and the offshore ambient sea. Over June and July, this gradient causes spreading of this very fresh plume (<15 pss) from the Ob and Yenisei deltas over the central Kara Sea. However, initially this plume is suggested to occupy only the very surface layer of the Kara Sea (to ~ 10m). Over August and September, the loss of sea ice allows increased wind driven vertical mixing of this surface fresh layer with sub-surface ambient sea water, deepening the mixed layer and increasing surface salinities (Osadchiev et al., 2021). Over winter, this fresh layer slowly dissipates, either transported into the Laptev Sea or becomes well-mixed with subsurface waters (Osadchiev et al., 2023a; Pavlov et al., 1996).

Interannual variability in SSS is relatively low in the Kara Sea, compared to the neighbouring Laptev Sea, but the vertical profile is suggested to vary considerably between years (Osadchiev et al., 2021). However, it receives a much larger riverine freshwater input, which equates to around 25% of the total river runoff into the Arctic Ocean. Previously, three different modes of variability in SSS have been suggested: western, eastern, central (Kubryakov et al., 2016; Pivovarov, 2001; Polukhin and Makkaveev, 2017). These three types denote the predominant region where the plume is located, which can be primarily along the coast of the southeastern Kara Sea (eastern type) or in the western Kara Sea between the Novaya Zemlya Archipelago and the continent to the south (western) or a mix of these two, where the plume is primarily located in the central/northern Kara Sea (central).

There is general agreement that wind forcing is the dominant driver of interannual variability, and appears to control geostrophic circulation (Kubryakov et al., 2016; Osadchiev et al., 2021). In the absence of strong wind forcing, the salinity gradient between plume and ambient sea water offshore and the impact of Coriolis drive eastward baroclinic transport along the coast (Garvine, 1987; Osadchiev et al., 2020). There is also general agreement that fresh water contributions from both sea ice and P-E are typically minimal over the summer period (Dubinina et al., 2017; Kazakova et al., 2024; Lambert et al., 2019; Makkaveev et al., 2010).

However, there remains debate as to whether interannual variability in Ob and Yenisei runoff play a role in driving interannual variability in SSS. A number of studies have suggested that variability in cumulative Ob-Yenisei river runoff controls the size of the area of the fresh surface layer (Lemeshko and Tsyganova, 2022; Osadchiev et al., 2017; Umbert et al., 2021). The ratio between Ob and Yenisei runoff has also been suggested to impact the position and interaction between the Ob and Yenisei plumes (Osadchiev et al., 2017). However, there has also been suggestion that variability in runoff plays little or no role in driving variability in SSS (Harms and Karcher, 2005; Zatsepin et al., 2010). Most of the previous studies, especially those using satellite SSS, only consider cumulative Ob and Yenisei runoff or the ratio between them and not the individual contributions of each river (Lemeshko and Tsyganova, 2022; Umbert et al., 2021).

In this chapter, I aim to identify the drivers of interannual variability in the Kara Sea and how these may resemble or differ from the Laptev Sea. To do so, in section 4.3.1, I first consider drivers of variability of GLORYS12V1 September SSS, including the influences of eastward and northward turbulent surface stress (section 4.3.1.1) and of the ratio of Ob/Yenisei runoff, as well as of the individual contributions of Ob and Yenisei runoff (section 4.3.1.2). The findings of this analysis are then tested using satellite SSS products in section 4.3.3 and discussed in sections 4.4.1, 4.4.2 and 4.4.3. A similar analysis is then conducted in sections 4.3.2, 4.3.4 and 4.4.4 for GLORYS12V1 and satellite September SST and SIC. The overall conclusions of drivers of interannual variability in SSS, SST and SIC are then in section 4.5.

4.2 Methods

Ob and Yenisei River runoff data from the Arctic Great Rivers Observatory (GRO) dataset are used to identify the main drivers of Kara Sea interannual variability (Hiklomanov et al., 2021). Cumulative runoff until a certain Julian day of each year is calculated for spring (Julian day 150), summer (Julian day 200) and autumn (Julian day 250). Neither Ob nor Yenisei runoff were detrended over any integration time. Whilst there do appear to be trends in some of the timeseries, none of them are significant over GLORYS12V1 period, as was true for spring Lena runoff. In addition, the Ob and Yenisei rivers are known to have notable anthropogenic influence (in the form of watershed management), which causes significant decadal variability and alters any expected long-term trend (Davidson, 2018). There has also been previous work about the complexity of trends in Ob/Yenisei runoff and the danger of poor trend analysis (Stadnyk et al., 2021; Yang et al., 2004). Where relevant, the same analysis was conducted with de-trended timeseries to ensure the presence of trends do not impact results.

As for the Laptev Sea, the key drivers of Kara Sea interannual variability are first assessed using a lagged-correlation analysis between Ob and Yenisei GRO runoff over different integration times (cumulative runoff until spring, summer, autumn and over the full-year), ERA5 eastward turbulent surface stress and GLORYS12V1 SSS, SST, and SIC over 1993–2023 . However, as might be expected given the lag time between changes in gauged runoff and changes in SSS, correlations are strongest with spring and summer runoff, so only correlations with spring and summer runoff are shown.

Pearson correlation coefficients are also calculated for the ratio of spring, summer and autumn Yenisei/Ob runoff. However, it has previously been suggested that there is a lag of ~50 days in the difference in the time it takes for Ob or Yenisei runoff to travel from the discharge station (Salekhard or Igarka) into the sea (Osadchiev et al., 2017). This lag is considered prior to calculating ratios. The ratio is calculated using cumulative Yenisei runoff on days 150, 200 and 250 and cumulative Ob runoff up to 50 days before these days (IE on Julian days 100/150/200). The same correlations are also calculated with the ratio of Yenisei/Ob runoff and GLORYS12V1 September SST and SIC at each grid cell.

Whilst there were small differences in correlation pattern with June, July and August ERA5 eastward turbulent surface stress, correlations shown are calculated between GLORYS12V1 SSS and mean June to August eastward turbulent surface stress over the Kara Sea shelf: 70-80 °N, 60-80 °E for each grid cell (Figure 3.4) to be consistent with other chapters. The same correlations are calculated with GLORYS12V1 September SST and SIC at each grid cell (Figure 3.5, Figure 3.6). Given the difference in correlation patterns with June, July and August eastward turbulent surface stress, pearson correlation coefficients between ERA5 eastward turbulent surface stress in June, July and August and GLORYS12V1 September SSS (over 1993–2023) in each grid cell are also included in Appendix Figure C.1.Similar correlations were calculated for varied (22.5°, 45°and 67.5°) wind directions rotated to be aligned with the coast (i.e. eastnortheast-ward and northnorthwest-ward for 22.5°, northeast-ward and northwest-ward for 45° and northnortheast-ward and westnorthwest-ward for 67.5°). However, similar patterns and no notable improvement in correlation strength were found with SSS so unrotated wind stress was used for consistency with the Laptev Sea (Chapter 3).

To identify years of anomalous eastward/westward wind over the shorter satellite time series, the mean ERA5 eastward and northward turbulent surface stress is calculated for June to

August over the Kara Sea shelf: 70-80 °N, 60-80 °E (region visible in the red box in Figure 4.1). The June-August averaging period was chosen to be consistent with Laptev Sea (Chapter 3) and given that previous studies have suggested wind over June-September is relevant for plume regime (Kubryakov et al., 2016).

The 3 years of maximum and minimum eastward turbulent surface stress are identified for each of the two satellite periods (SMOS: 2011–2022 and SMAP: 2015–2023), which happen to be the same years for both periods. Eastward wind stress is highest in 2016, 2018 and 2021 and lowest (most westward) in 2015, 2019 and 2020.

The eastward SSS composite is then calculated as the mean of the 3 most eastward years for GLORYS12V1 SSS, CCI, JPL SMAP and LOCEAN SMOS (2016, 2018, 2021). The westward SSS composite is calculated as the mean of the 3 most westward years for GLORYS12V1 SSS, CCI, JPL SMAP and LOCEAN SMOS (2015, 2019, 2020). The same years are used to calculate eastward and westward SST composites using GLORYS12V1 SST and L4 v2.1 CCI SST as well as for GLORYS12V1 SIC.

The same years are also used to calculate "eastward" and "westward" current velocity composites (for both eastward and northward velocity components) from GLORYS12V1 mean June-August eastward and northward current velocity components.

The surface Ekman current expected from the wind stress is computed for this region according to Equations (1) and (2) (Price et al., 1987). Surface Ekman currents (for z=0 m) are calculated using an Ekman depth (d) of 10 m (roughly equivalent to the mixed layer depth found from in-situ data) and a surface density (ρ_0) of 1020 kg m^{-3} (roughly equivalent to an SSS of 25 pss and SST of 5 °C). The expected surface Ekman current under average eastward and westward wind forcing is then calculated from the mean June-August eastward and northward wind stress for identified most eastward and westward years. This surface current is calculated for each pixel over the Kara Sea shelf: 70-80 °N, 60-80 °E. These expected Ekman surface currents under eastward and westward wind forcing are then compared with those observed in GLORYS12V1 to visualise the contribution of the Ekman component to the overall surface current (overlaid on Figure 4.7 and Figure 4.8).

Composites are also calculated for years of high and low ratios of summer Yenisei/Ob runoff. The 3 years of highest and lowest ratios of summer Yenisei/Ob runoff are identified for each of the two satellite periods (SMOS: 2011–2022 and SMAP: 2015–2023). The 3 years of highest runoff ratio are identified to be 2010, 2013, and 2018 over the SMOS time series and to be 2018, 2021 and 2023 for the SMAP time series. Conversely, the 3 years of lowest runoff ratio are identified to be 2011, 2012 and 2016 over the SMOS time and 2016, 2017 and 2020 over the SMAP time series.

The high Yenisei/Ob runoff ratio SSS composite is then calculated as the mean of the 3 years of highest runoff ratio for GLORYS12V1 SSS, CCI and LOCEAN SMOS (2010, 2013, 2018) and for JPL SMAP (2018, 2021, 2023). The low Yenisei/Ob runoff ratio SSS composite is calculated as the mean of the 3 years of lowest runoff ratio for GLORYS12V1 SSS and LOCEAN SMOS (2011, 2012, 2016) and for JPL SMAP (2016, 2017, 2020). The same years are used to calculate high and low SST composites using GLORYS12V1 SST and L4 v2.1 CCI SST as well as for GLORYS12V1 SIC.

As for wind, the same years are also used to calculate current velocity composites under high and low ratios of Yenisei/Ob runoff (for both eastward and northward velocity components) from GLORYS12V1 mean June-August eastward and northward current velocity components.

4.3 Results

4.3.1 Impact of runoff and wind stress on SSS in GLORYS12V1

4.3.1.1 Wind Stress

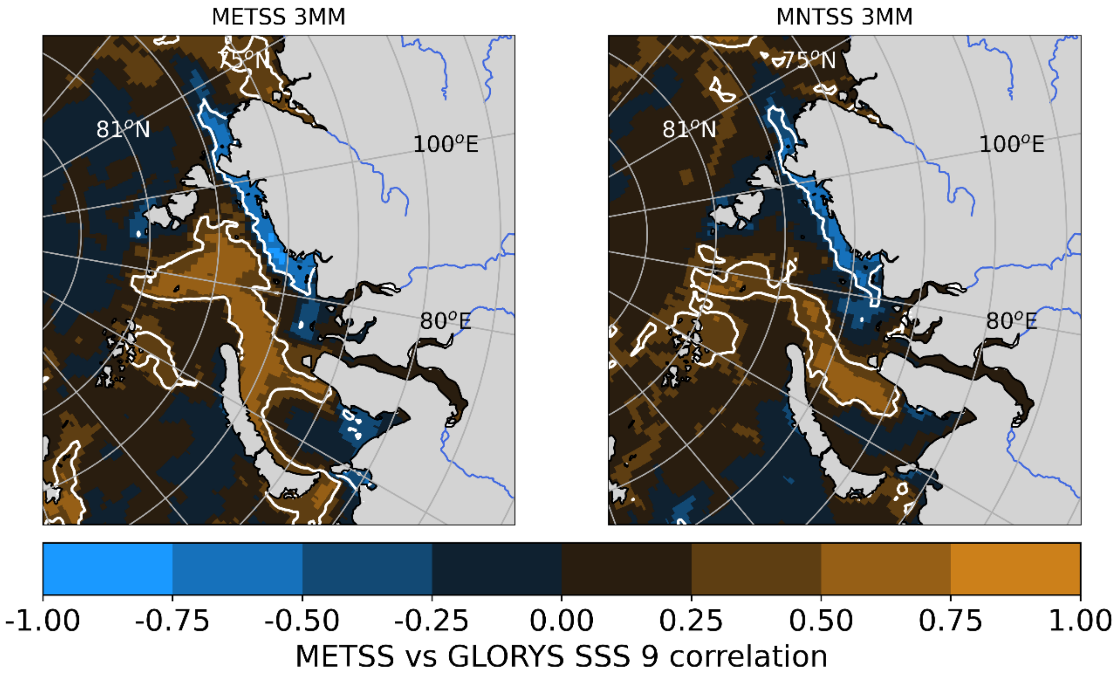

Figure 4.2: Correlation between GLORYS12V1 September SSS and ERA5 eastward and northward turbulent surface stress over June to August (6-8) over 1993-2023. Regions where correlations are statistically significant ($p \leq 0.05$) are denoted by the white contour and brighter colours.

In the Kara Sea, a strong correlation pattern is present with June-August eastward wind stress, which depicts a narrow band of negative correlation that extends nearest the coast, particularly east of the Ob and Yenisei deltas, and a wider band of positive correlation just offshore (Figure 4.2). However, whilst this pattern is relatively consistent across all months, the regions with significant correlations are often quite small and differ notably by month (Appendix Figure C.1).

The negative nearshore / positive offshore correlation pattern suggests that years of notable eastward wind forcing are consistent with particularly low SSS nearshore, particularly along the eastern coast of the Kara Sea, and higher SSS in the western Kara Sea and further offshore and vice versa under westward wind forcing (Figure 4.2). This suggests that eastward wind forcing is consistent with the Ob-Yenisei plume remaining nearshore and to the east of the initial Ob and Yenisei deltas. Conversely, westward wind forcing is consistent with the Ob-Yenisei plume being transported further offshore and spreading both east and west of the Ob and Yenisei deltas. Whilst the correlation pattern between eastward turbulent surface stress and

SSS in the Kara Sea is somewhat similar to that present in the Laptev Sea, the plume tends to travel further East under eastward forcing and further west under westward forcing in the Kara Sea, rather than traveling onshore or offshore as in the Laptev Sea.

The correlations between SSS and August eastward turbulent surface stress (Appendix Figure C.1) are notably stronger than correlations with eastward turbulent surface stress in other months. This has previously been explained by the sea ice covered nature of the Kara Sea leading up to June and the calm conditions typically present in July (Osadchiev et al., 2021b; Pavlov et al., 1996). The higher standard deviation of eastward turbulent surface stress over the Kara Sea in August (0.030 N m^{-2}), compared to in September (0.022 N m^{-2}), July (0.024 N m^{-2}) or June (0.023 N m^{-2}) also support this suggestion. In addition, Ob and Yenisei runoff must be transported down the Ob and Yenisei deltas before entering the central Kara Sea and being subject to wind forcing. This lag likely accounts for the lack of correlation with June and July wind forcing, as is present in the Laptev Sea.

In the Kara Sea, the spatial correlation patterns between GLORYS12V1 SSS and mean northward turbulent surface stress over 1993-2023 (Figure 4.2, right), resemble those with mean eastward turbulent surface stress but are generally weaker and smaller. The band of negative correlation near the coast, to the east of the Ob and Yenisei deltas, visible in correlation plots with eastward turbulent surface stress is also visible in July-August northward turbulent surface stress plots. The band of positive correlation in the central Kara Sea is also visible with northward turbulent surface stress but is considerably narrower, less extensive and is more confined to the western Kara Sea. As with eastward wind stress, the August northward turbulent surface stress pattern is the largest, and closely resembles that of eastward turbulent surface stress in August, but with less extensive regions of significant positive/negative correlations.

Overall, this suggests that both eastward and northward wind stress are consistent with a band of low SSS nearshore which extends from the mouths of the Ob and Yenisei deltas, through the Vilkitsky Strait. Conversely, westward or southward wind stress is coincident with lower SSS offshore, in the central Kara Sea. Whilst June and July eastward and northward wind stress seem to have some influence on SSS, August eastward and northward wind stress appear far more dominant.

4.3.1.2 Runoff

Spatial correlations between Ob, Yenisei and the ratio of Yenisei/Ob runoff and GLORYS12V1 September SSS are examined to understand the influence of runoff in controlling Kara Sea SSS. Correlations are strongest for spring (Julian day 150) Ob runoff and summer (Julian day 200) Yenisei runoff so these are shown below (Figure 4.3). The correlation with ratio between summer Yenisei and spring Ob runoff is also shown. The ratio is calculated using different integration times for Ob and Yenisei runoff to take into account the difference in lag time between the two rivers (of ~50 days).

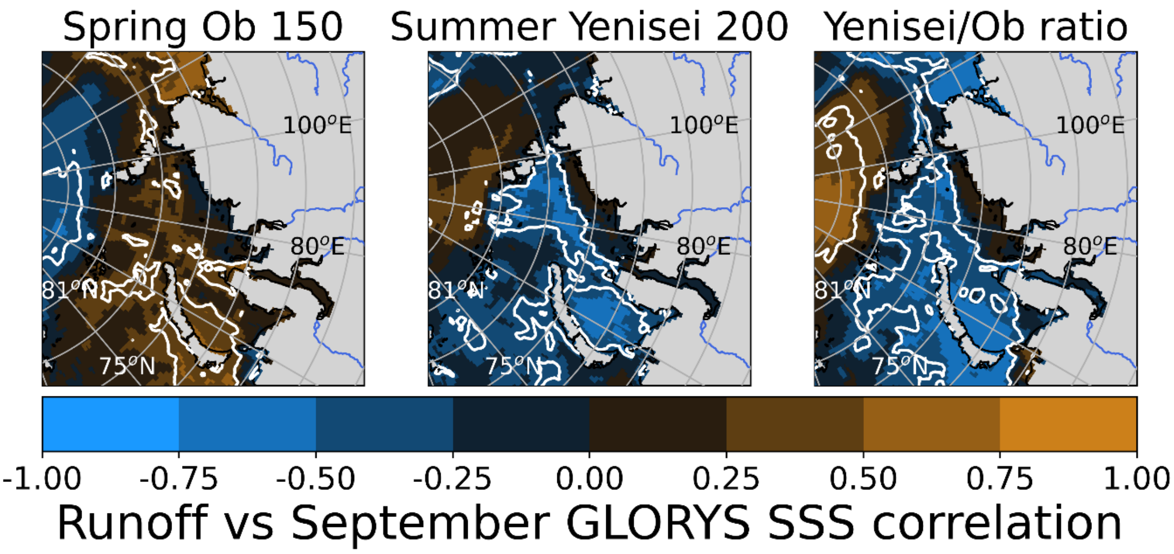

Figure 4.3: Correlation between GLORYS12V1 September SSS and cumulative Ob River runoff in spring (Julian day 150), cumulative Yenisei River runoff in summer (Julian day 200), and the ratio of summer Yenisei and spring Ob River runoff over 1993-2022. Regions where correlations are statistically significant ($p \leq 0.05$) are denoted by the white contour and brighter colours.

Only spring Ob runoff has a notable correlation pattern with GLORYS12V1 SSS over the 1993-2023 time period (Figure 4.3, first panel). This pattern consists of patches of positive correlation below 82 °N and a significant negative correlation pattern above this latitude, in the central Arctic. This positive correlation has multiple patches where it is significant, including at the outflow of the Ob delta, most of the way around the Novaya Zemlya Archipelago, in several patches of the northern Kara Sea and in the western Laptev Sea. No notable correlation patterns were present with cumulative runoff over other integration times. Hence, high spring Ob runoff appears to drive increased SSS in September right at the mouth of the Ob Delta. The reasoning for this counter-intuitive correlation will be further discussed in section 4.4.1.

Summer Yenisei runoff has a large region of negative correlation with GLORYS12V1 SSS over the 1993-2023 time period (Figure 4.3, middle panel). This significant negative correlation extends throughout most of the central Kara Sea and in multiple regions in the Barents Sea A similar, but weaker, correlation pattern is also visible with Yenisei runoff over other integration times. This strong negative correlation pattern suggests that increased summer Yenisei runoff is consistent with low SSS in September over most of the Kara Sea.

The cumulative Ob-Yenisei runoff (not shown) presents a similar spatial correlation to that of cumulative Yenisei runoff. This suggests that the strong negative correlation visible with summer Yenisei runoff dominates over the weaker positive correlation visible with spring Ob runoff. On average, the magnitude of Yenisei runoff is about 1.5 times larger than Ob runoff, supporting the more dominant role of Yenisei runoff. The magnitude of interannual variability in Yenisei runoff (standard deviation of 4.58×10^{10} m^3 $year^{-1}$) is also larger compared to that of Ob runoff (standard deviation of 2.05e10 m^3 $year^{-1}$). The stronger and larger area of significant correlation with Yenisei runoff and the larger magnitude of Yenisei runoff and of its variability, compared to Ob runoff, suggests Yenisei runoff is a dominant control on Kara Sea SSS.

Whilst Yenisei runoff appears to play a stronger role in controlling SSS variability than Ob runoff, previous studies have suggested a stronger role for the ratio of Yenisei/Ob runoff than of either individual contributor (Osadchiev et al., 2017). Here, the ratio of Yenisei/Ob runoff has a consistent correlation pattern with GLORYS12V1 SSS over 1993-2023 for all runoff integration times. However, the strongest correlation pattern is found with the ratio of spring Ob / summer Yenisei runoff (Figure 4.3, right panel). This pattern consists of a negative correlation in the central Kara Sea and a positive correlation in the central Arctic, above 80 °N. The large region of significant negative correlation with the summer runoff ratio resembles the region of negative correlation with summer Yenisei runoff, and covers the region of positive correlation with spring Ob runoff, so extends all the way from the edge of the Ob Delta, into the western Kara Sea and across to the Vilkitsky Strait. This correlation pattern suggests that high Yenisei runoff and/or low Ob runoff are consistent with decreased SSS over the central and western Kara Sea, and conversely that low Yenisei runoff and/or high Ob runoff are consistent with increased SSS over the central and western Kara Sea. Hence, opposing variability in Ob and Yenisei runoff has a stronger influence on SSS than either river's individual or their cumulative contribution.

4.3.2 Impact of runoff and wind stress on SST and SIC in GLORYS12V1

4.3.2.1 Wind stress

As for GLORYS12V1 SSS, spatial correlations between June, July and August eastward wind stress and GLORYS12V1 September SST are examined to understand the influence of zonal wind stress in controlling Kara Sea SST.

However, there are relatively few, small regions of significant correlation between eastward turbulent surface stress and GLORYS12V1 SST so results are summarized here (see Kara Sea additional figures for full results). Only August northward turbulent surface stress has regions of significant positive correlation with GLORYS12V1 SST nearshore (Appendix Figure C.2) and regions of significant negative correlation with GLORYS12V1 SIC (Appendix Figure C.3). The small regions of significant positive correlation with SST are located in the eastern coastal Kara Sea, in the offshore Kara Sea, and in the eastern Barents and western Laptev Sea. A negative correlation is also visible between August northward turbulent surface stress and GLORYS12V1 SIC but only extends throughout the western Laptev Sea. There are no notable regions of significant correlation between eastward turbulent surface stress in any month and GLORYS12V1 SST or SIC. There are no notable regions of significant correlation between northward turbulent surface stress in June and July and GLORYS12V1 SST or SIC. Hence, only August turbulent surface stress is consistent with increased SSTs, particularly in the eastern Kara Sea, and with decreased SIC in the western Laptev Sea.

The small regions of positive correlation nearshore between August northward turbulent surface stress and SST are consistent with the previous suggestion that eastward wind stress will drive increased eastward transport of the relatively warm water from the Barents Sea into the Kara Sea (Karcher et al., 2003; Mäkinen and Vanhatalo, 2016; Zhang et al., 1998). In addition, Barents Sea water is warmer under positive AOI, as intensified cyclonic flow drives increased Atlantic Water inflow, accelerating sea ice retreat and providing a longer period where the open ocean is exposed to atmospheric warming. Increased cyclonic flow, and the location of the positive correlation in August also support that the Pechora plume likely enters the Kara Sea under eastward wind forcing. This is consistent with the previous suggestion that (south/) eastward winds spread the Pechora plume along the coast and drive transport into the Kara Sea through the Kara Strait (Rogozhin et al., 2023). However, it is worth noting that the

Pechora plume rarely makes it far into the Kara Sea before being mixed with ambient sea water, due to the strong internal waves frequently present in this region (Morozov et al., 2017; Rogozhin et al., 2023).

There is no correlation between northward turbulent surface stress and either SST or SIC in July but there is a notable weak positive correlation in August (Appendix Figure C.2, Appendix Figure C.3). This is likely to be partly driven by the greater variability of August northward turbulent surface stress (STDV = 0.020 N m^{-2}) than of July (STDV = 0.018 N m^{-2}). As southward wind drives offshore transport and upwelling, it is likely that the southward wind dominant in this region, regularly drives upwelling from the southwestern Kara Sea onto the shelf and into the surface waters, lowering SST. Conversely, northward wind drives transport onto shore and downwelling, maintaining the warm SST present on the shallower region of the shelf. This would explain the positive correlation visible in this region, which appears coincident with the region where the Kara Sea is shallowest. This is consistent with previous work that has suggested bathymetry is positively correlated with SST in this region (Mäkinen and Vanhatalo, 2016). As might be expected, this causes loss of any sea ice still in the eastern Kara Sea and/or helps to slow late-September sea ice formation. This correlation pattern arises due to the southwest/northeast alignment of the coast, and the contrast of the deep western and the shallow southeastern Kara Sea. It also helps to explain the much stronger correlation with northward wind stress in the Kara Sea than is visible in the Laptev Sea.

4.3.2.2 Runoff

As with GLORYS12V1 SSS, spatial correlations between Ob, Yenisei and the ratio of Yenisei/Ob runoff and GLORYS12V1 September SST are examined to understand the influence of runoff in controlling Kara Sea SST. Correlations are shown for spring (Julian day 150) Ob runoff, summer (Julian day 200) Yenisei runoff (Figure 4.4). The correlation with the ratio between summer Yenisei and spring Ob runoff is also shown. The ratio is calculated using different integration times for Ob and Yenisei runoff to take into account the difference in lag time between the two rivers (of ~50 days).

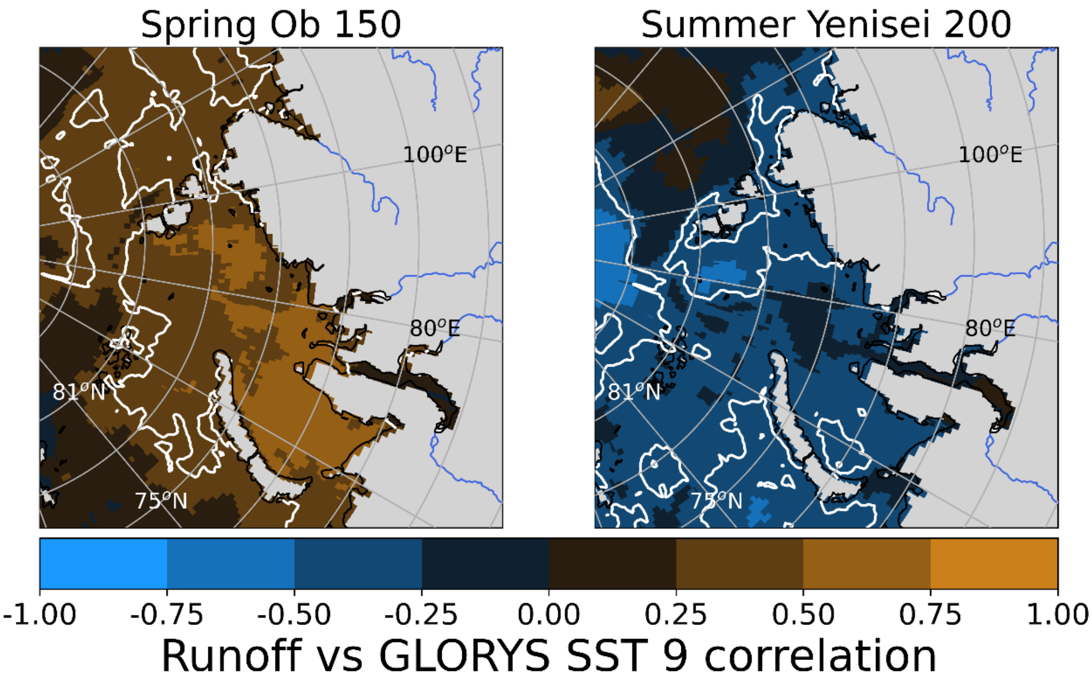

Figure 4.4: Correlation between GLORYS12V1 September SST and cumulative Ob River runoff in spring (Julian day 150) and cumulative Yenisei River runoff in summer (Julian day 200) over 1993-2022. Regions where correlations are statistically significant ($p \leq 0.05$) are denoted by the white contour and brighter colours.

Spring Ob runoff has a large region of significant positive correlation with GLORYS12V1 September SST that extends throughout most of the Barents, Kara and Laptev Sea (Figure 4.4, left panel). A similar but notably weaker and mostly non-significant pattern is also visible with summer Ob runoff. Hence, high spring Ob runoff is coincident with increased SST over all of the Kara Sea and in the western Laptev Sea.

The spatial pattern of correlation between cumulative summer Yenisei runoff and GLORYS12V1 September SST over the 1993-2023 time period (Figure 4.4) is the opposite of that with spring Ob runoff. Summer Yenisei runoff is negatively correlated with GLORYS12V1 SST over almost the entire region visible (Figure 4.4, middle panel). This negative correlation is significant over large regions of the Barents, Kara and Laptev Sea, except for a wide band in the central Kara Sea. Whilst high summer Yenisei runoff appears coincident with decreased September SSTs in the eastern Barents and western Kara Sea, it does not appear related to September SST in the central Kara Sea. This opposing correlation is likely due to interactions between Ob and Yenisei runoff, as discussed in section 4.4.1.

Given lack of significant correlation with Yenisei runoff in the central Kara Sea and the fact all regions of significant negative correlation with Yenisei runoff are also regions of significant positive correlation with Ob runoff, the correlation with the ratio of Yenisei/Ob runoff is omitted. The stronger correlations with Ob runoff, compared to Yenisei runoff suggest Ob runoff is the dominant control on Kara Sea SSTs, unlike with SSS, where Yenisei runoff is the dominant control.

As with GLORYS12V1 SSS and SST, spatial correlations between Ob, Yenisei and the ratio of Yenisei/Ob runoff and GLORYS12V1 September SIC are examined to understand the influence of runoff in controlling Kara Sea SIC. Correlations are shown for spring (Julian day 150) Ob runoff, summer (Julian day 200) Yenisei runoff (Figure 4.5). The correlation with the ratio between summer Yenisei and spring Ob runoff is also shown. The ratio is calculated using different integration times for Ob and Yenisei runoff to take into account the difference in lag time between the two rivers (of ~50 days).

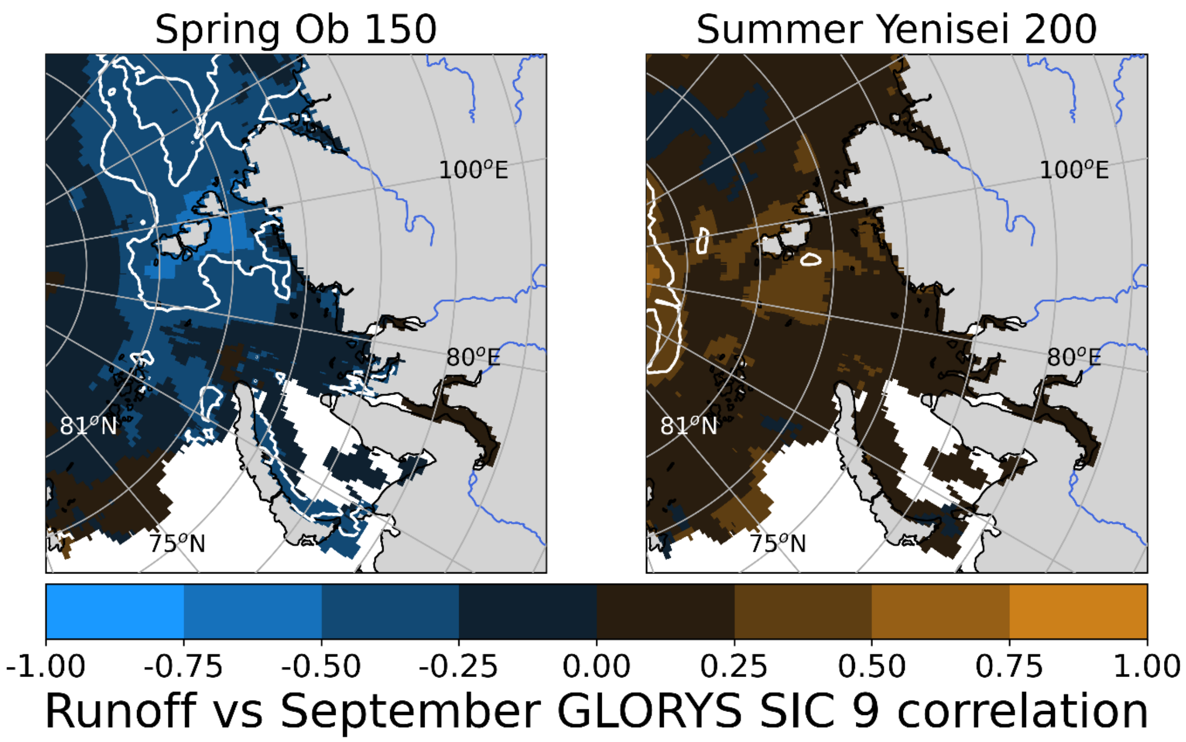

Figure 4.5: Correlation between GLORYS12V1 September SIC and cumulative Ob River runoff in spring (Julian day 150) and cumulative Yenisei River runoff in summer (Julian day 200) over 1993-2022. Regions where correlations are statistically significant ($p \leq 0.05$) are denoted by the white contour and brighter colours.

The correlation pattern between cumulative spring Ob runoff and GLORYS12V1 September SIC over the 1993-2023 time period (Figure 4.5, left) is somewhat opposite of those with GLORYS12V1 September SST. Spring Ob runoff is very weakly negatively correlated with SIC almost everywhere below 82 °N (Figure 4.5, left panel). This negative correlation is strongest, and only significant, in the eastern Kara and western Laptev Sea and extends over a large area from the coast to ~80 °N, both sides of the Vilkitsky Strait. This region of significant negative correlation suggests increased spring Ob runoff is consistent with decreased sea ice nearshore in the eastern Kara and western Laptev Sea.

The correlation pattern between Yenisei runoff and GLORYS12V1 September SIC over the 1993-2023 time period (Figure 4.5, middle) is almost exactly the opposite of those with GLORYS12V1 September SST but notably weaker. Summer Yenisei runoff is positively correlated with SIC. However, there are no regions of significant correlation with Yenisei runoff in the central Kara Sea. Given the lack of correlation with Yenisei runoff, the correlation with the ratio of Yenisei/Ob runoff is omitted as it is clear Yenisei runoff has no impact on Kara Sea SIC.

This correlation pattern suggests that low Ob runoff is consistent with increased SIC over the central and western Kara Sea, and conversely that high Ob runoff is consistent with decreased SIC over the central and western Kara Sea. Unlike with SSS, Yenisei runoff has no notable impact on Kara Sea SST.

4.3.3 Drivers of interannual variability in September SSS

A metric of eastward (and northward) wind stress is devised to identify anomalous years of wind forcing and calculate SSS composites for particularly anomalous years (shown in Figure 4.6). Given June, July and August eastward (and northward) turbulent surface stress appear dominant drivers of variability in GLORYS12V1 September Kara Sea SSS, and to be consistent with the Laptev Sea study, the mean of these three months is used for this metric.

The ratio of summer Yenisei / spring Ob runoff is also used as a metric to help identify the role of runoff in controlling variability in Kara Sea SSS, given the strong correlation found between the runoff ratio and GLORYS12V1 September SSS. The ratio of summer Yenisei / spring Ob, the variability of summer Yenisei runoff and spring Ob runoff are also overlaid in Figure 4.6.

To ensure no coverability exists between different variables, the Pearson correlation coefficient is calculated between each of the variables (June-August mean eastward turbulent surface stress, June-August northward turbulent surface stress, spring Ob runoff, summer Yenisei runoff and the ratio of summer Yenisei/spring Ob runoff).

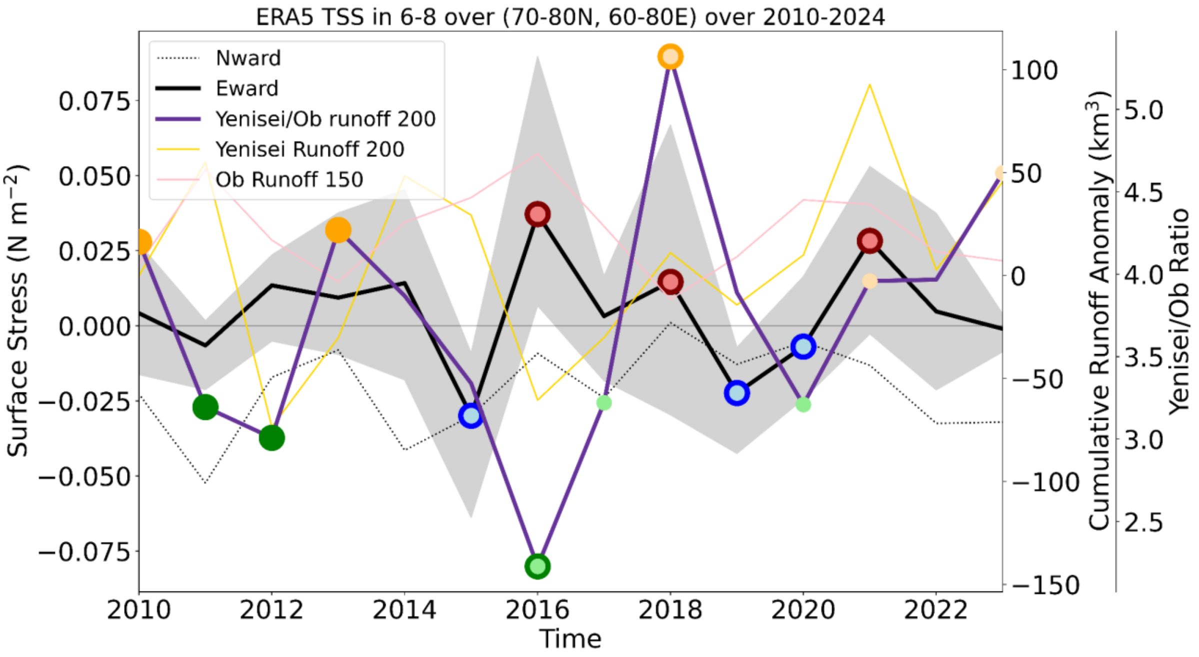

Figure 4.6: Three-month (June to August) mean ERA5 eastward (black solid) and northward (black dashed) turbulent surface stress over 70-80 °N and 60-80 °E. Overlaid are dots indicating the most eastward (red dots) and westward (blue dots) years chosen for analysis for both the longer SMOS/GLORYS12V1 timeseries (2011-2022) (darker red and blue dots) and the shorter SMAP timeseries (2015-2023) (lighter red and blue dots). The range of the maximum and minimum eastward turbulent surface stress between June and August is shaded in grey. The ratio of summer (until the 200th Julian day) Yenisei runoff to spring (until the 150th Julian day) Ob runoff is in purple with the highest (orange) and lowest (green) years chosen for analysis for both the longer SMOS/GLORYS12V1 timeseries (2011-2022) (darker orange and green dots) and the shorter SMAP timeseries (2015-2023) (lighter orange and green dots). Spring cumulative Ob River runoff (until the 150th Julian day) (pink), and summer cumulative Yenisei runoff (until the 200th Julian day) (light orange) anomalies from climatology are overlaid.

As with the Laptev Sea, the magnitude of variability in June to August mean eastward turbulent surface stress over the Kara Sea is larger (range of -0.03 to 0.04 N m^{-2}) than that of mean northward turbulent surface stress (range of -0.05 to 0 N m^{-2}) (Figure 4.6). However, unlike the Laptev Sea, northward turbulent surface stress was almost always negative over the Kara Sea, indicating persistent southward turbulent surface stress. This has previously been suggested to be the dominant wind forcing over this region (Osadchiev et al., 2021). The standard deviation of eastward turbulent surface stress over the Kara Sea (over 1993-2023) is also notably higher in August (0.030 N m^{-2}) than in September (0.022 N m^{-2}), July (0.024 N m^{-2}) or June (0.023 N m^{-2}). The standard deviation of northward turbulent surface stress over the Kara Sea (over 1993-2023) is also higher in September (0.028 N m^{-2}) than in August (0.020 N m^{-2}), July (0.018 N m^{-2}) or June (0.025 N m^{-2}). Eastward turbulent surface stress does not co-vary with northward turbulent surface stress over 2010-2022 ($r = 0.29$, $p = 0.31$) and is weakly, but significantly correlated over 1993-2023 ($r = 0.37$, $p = 0.04$). The years of highest eastward turbulent surface stress were 2016, 2018 and 2021 over both the SMOS timeseries and SMAP timeseries. The years of strongest westward turbulent surface stress were 2015, 2019 and 2020 over both the SMOS and SMAP timeseries.

The ratio of summer Yenisei/Ob runoff varies between 0.18 and 0.45 over the SMOS time period. The average magnitude of cumulative summer Yenisei runoff (3.86e11 m^3 $year^{-1}$) is over three times greater than that of cumulative summer Ob runoff (1.09e11 m^3 $year^{-1}$) over 2010-2023, which explains the consistently low ratio of summer Ob/Yenisei runoff. In addition, the standard deviation of cumulative summer Yenisei runoff (4.47e10 m^3 $year^{-1}$) is around double that of cumulative spring Ob runoff (2.03e10 m^3 $year^{-1}$) over 2010-2023. Both the mean and standard deviation of summer Yenisei runoff are also much greater than that of spring Ob runoff over the GLORYS12V1 time period (1993-2023). It is also worth noting that both the magnitude and standard deviation of cumulative Yenisei runoff are larger than cumulative Ob runoff regardless of integration time chosen. The years of highest Yenisei/Ob runoff ratio were 2010, 2013 and 2018 over the SMOS timeseries and 2018, 2021 and 2023 over SMAP timeseries. The years of strongest westward turbulent surface stress were 2011, 2012 and 2016 over the SMOS timeseries and 2016, 2017 and 2021 over SMAP timeseries.

There is no co-variability between the ratio of summer Yenisei runoff / spring Ob runoff and either eastward or northward turbulent surface stress. Summer Yenisei/Ob runoff does not co-vary with eastward turbulent surface stress over 2010-2023 ($r = -0.07$, $p = 0.80$) or over 1993-2023 ($r = -0.25$, $p = 0.17$). Summer Yenisei/Ob runoff also does not co-vary with northward turbulent surface stress over 2010-2023 ($r = 0.15$, $p = 0.62$) or over 1993-2023 ($r = 0.11$, $p = 0.54$).

Conversely, both spring Ob and summer Yenisei runoff co-vary with the ratio of Yenisei/Ob runoff. Summer Yenisei/Ob runoff is significantly negatively correlated with spring Ob runoff over both 2010-2023 ($r = -0.84$, $p < 0.01$) and 1993-2023 ($r = -0.90$, $p < 0.01$). Summer Yenisei/Ob runoff is also positively correlated with summer Yenisei runoff over both 2010-2023 ($r = 0.39$, $p = 0.17$) and over 1993-2023 ($r = 0.30$, $p = 0.09$). Summer Yenisei runoff does not co-vary with spring Ob runoff over 2010-2023 ($r = 0.10$, $p = 0.73$) or 1993-2023 ($r = -0.04$, $p = 0.84$).

4.3.3.1 Wind composite

The identified three most eastward and westward years are then used to calculate eastward and westward composites for GLORYS12V1, LOCEAN SMOS, JPL SMAP and CCI SSS (Figure 4.7, Figure 4.8).

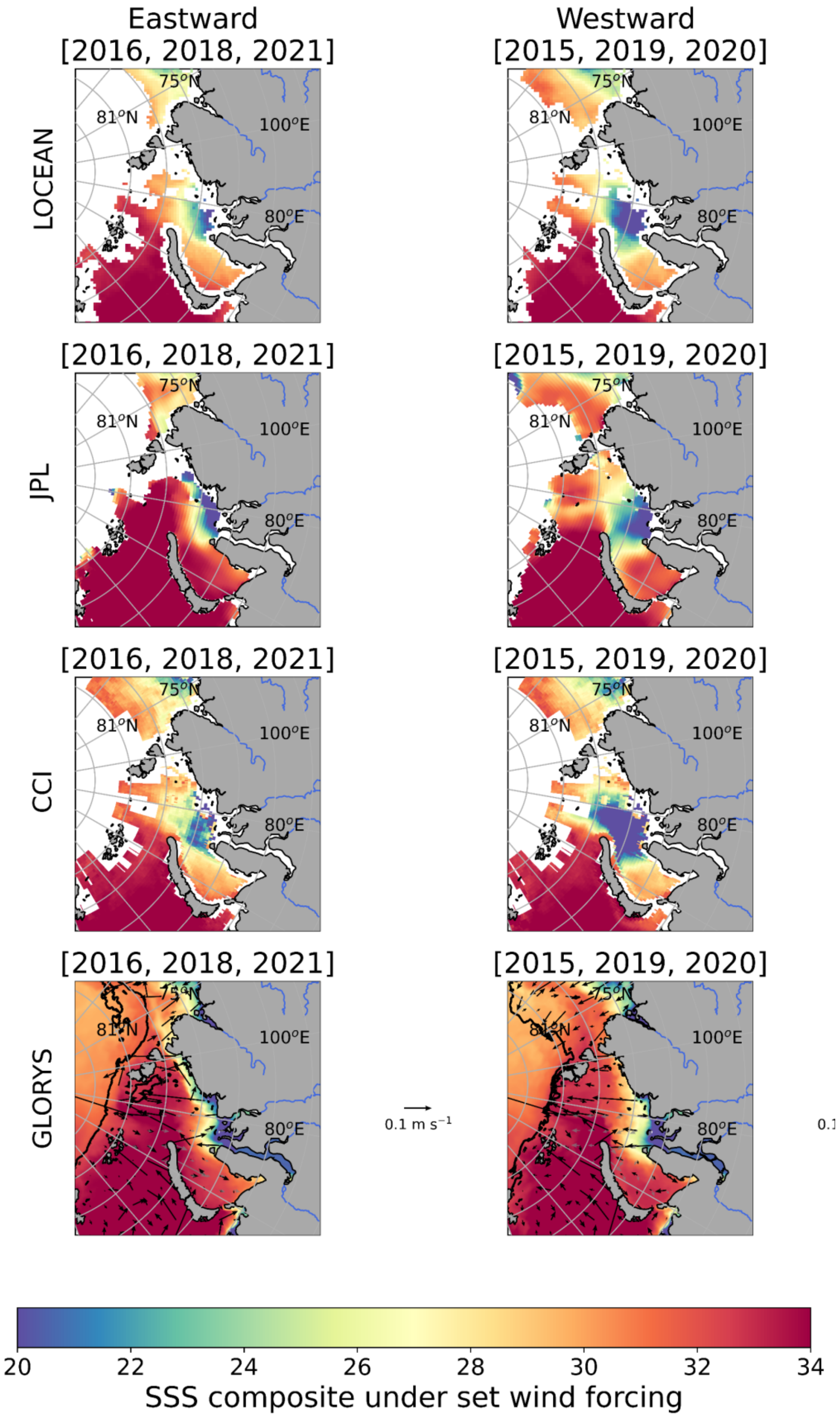

Figure 4.7: Eastward (E, left column) and westward (W, right column) composites calculated for (top to bottom) LOCEAN SMOS, JPL SMAP, CCI and GLORYS12V1 SSS, from the identified three most eastward and westward years (over 2011-2023 for GLORYS12V1 and LOCEAN SMOS and over 2015-2023 for JPL SMAP). The GLORYS12V1 mean 30% sea ice concentration contour is overlaid on the respective composite plots. Eastward and westward GLORYS12V1 current velocity composites for June-August are overlaid as black arrows on the respective composite plots (masked by the region of mean sea ice concentration above 30%).

All products suggest relatively consistent SSS patterns under both positive (eastward) and negative (westward) zonal wind forcing. Under eastward wind forcing, the freshest salinities (<24 pss) are mostly coastally confined and extend further eastward along the coast. Conversely, under westward wind forcing, all four products suggest these freshest salinities travel further offshore and occupy most of the central Kara Sea. A mid-composite (composite of three years without strong eastward or westward wind forcing) was also calculated, but is not shown, which closely resembles the westward composites, suggesting years with no strong east/westward wind forcing tend to spread offshore and resemble the westward wind SSS composite. However, years with westward wind forcing do appear to spread further into the western Kara Sea than those with more moderate/low zonal wind forcing, which appear to remain in the central Kara Sea and not extend as far westward.

The eastward/westward composites of the satellite SSS products agree strongly (Figure 4.7). GLORYS12V1 broadly agrees with the satellite products, but the freshest salinities are notably more coastally confined in both GLORYS12V1 composites than in the satellite products. Whilst this difference is visible in eastward composites, it is much clearer in westward composites, where low salinities (< 25 pss) in satellite products extend up to 77 °N, compared to barely extending above 75 °N in the GLORYS12V1 westward composite.

A weak pattern is visible in GLORYS12V1 surface current velocity composites with more onshore or southward transport under eastward wind forcing and more offshore or northward transport under westward wind forcing. However, surface current velocities are much more variable and complex in the Kara Sea, compared to the Laptev Sea, so the general circulation pattern dominates over this difference. Therefore, whilst the expected surface Ekman current does match the observed circulation in some nearshore regions, the expected and observed currents do not agree as well as in the Laptev Sea. This difference may be due to the more complex bathymetry in this region.

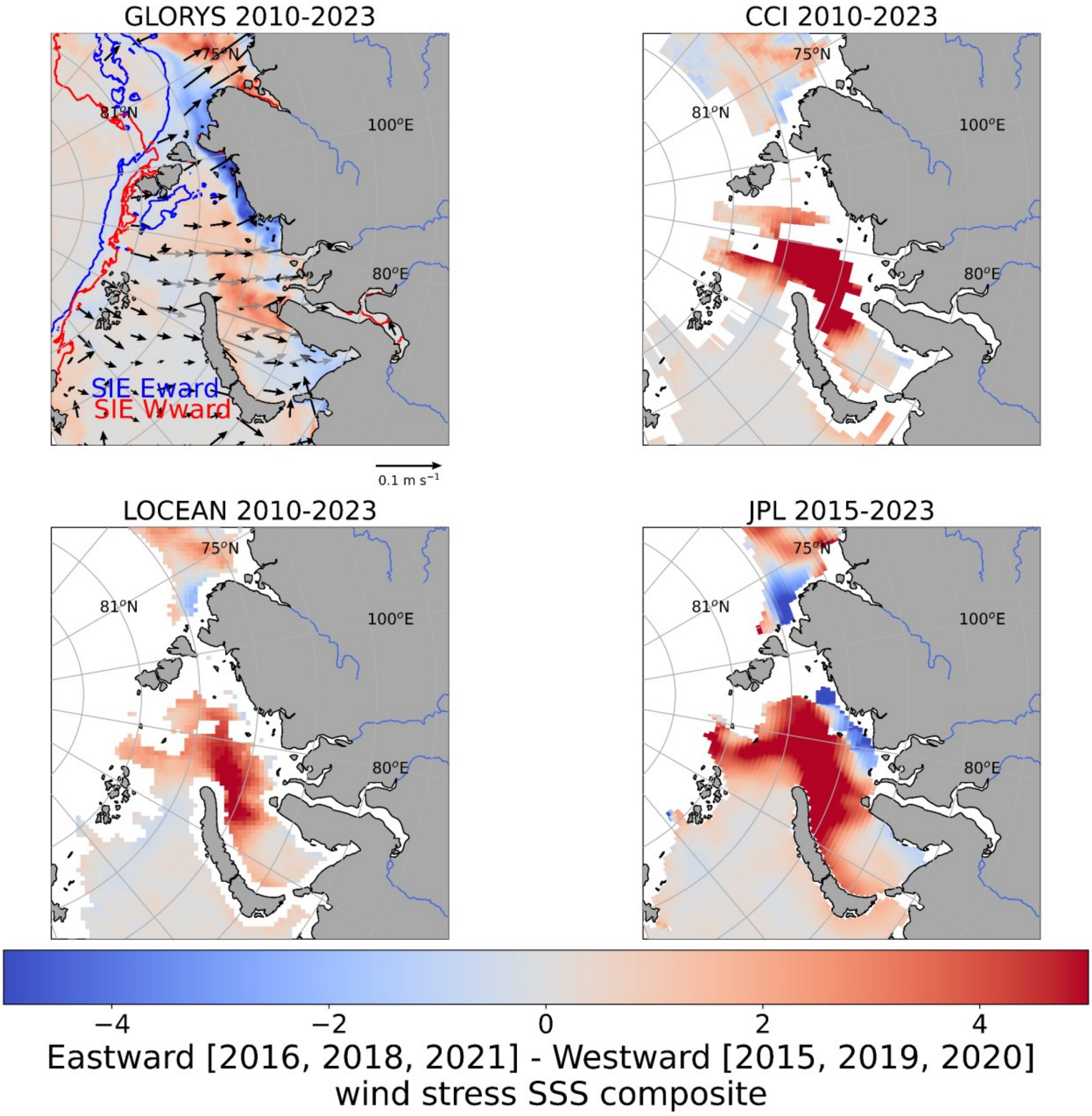

Figure 4.8: The difference between eastward and westward composites calculated for GLORYS12V1 SSS, CCI SSS, LOCEAN SMOS, and JPL SMAP, from the identified three most eastward and westward years (over 2010-2023 for GLORYS12V1, CCI and LOCEAN SMOS and over 2015-2023 for JPL SMAP). Regions in blue represent regions with lower salinities under eastward wind forcing and regions in red represent lower salinities under westward wind forcing. The GLORYS12V1 mean 30% sea ice concentration contour under eastward (blue) and westward (red) wind forcing is overlaid. The difference between eastward and westward GLORYS12V1 current velocity composites for June-August are overlaid as black arrows on the composite difference plot (masked by the region of mean sea ice concentration above 30%). The difference in expected Ekman surface currents based on observed average eastward and westward wind stress are overlaid as grey arrows for comparison.

The differences in SSS under eastward and westward wind forcing are re-iterated by the composite difference plots (Figure 4.8). All composite difference plots clearly depict a notable onshore/offshore dipole of freshwater transport. This dipole pattern consists of a thin negative SSS anomaly along the eastern coast of the Kara Sea, which extends from the Ob delta through to the western Laptev Sea. A large positive SSS anomaly is present throughout almost all of the offshore Kara Sea. Hence, all products show a consistent pattern of lower SSS nearshore and higher SSS offshore under eastward wind forcing.

Whilst all composite difference plots depict the same pattern of difference in SSS, the magnitude of offshore SSS transport in GLORYS12V1 is much smaller than that in satellite products. The satellite products depict notably larger freshwater transport northwards under westward wind forcing compared to under eastward wind forcing. This larger northward freshwater transport is visible both from the magnitude of the SSS difference in this region (> 5 pss) and the large area of the positive anomaly, which extends throughout most of the central Kara Sea, and over regions of the western Kara Sea. The much lower SSS in the central Kara Sea under westward wind forcing is much more clearly visible than the lower SSS nearshore under eastward wind forcing. Whilst satellite products do have some evidence of eastward/alongshore plume transport under eastward wind forcing, sea ice and land contamination contribute to a notable lack of observations near the coast, and mean there is no data where you would expect the negative SSS anomaly. The reasons for these differences are discussed further in section 4.4.1 (p70).

Despite that a clear difference in surface currents is not particularly visible from individual eastward and westward composites (Figure 4.7), the GLORYS12V1 surface current velocity composite difference plot suggests a clear difference in current velocity under eastward and westward wind forcing (Figure 4.8). This pattern indicates much more southward current velocities under eastward wind forcing than westward wind forcing, indicating onshore transport. Observed differences in surface current closely match both the magnitude and direction of the expected difference in Ekman surface current calculated from wind stress.

4.3.3.2 Runoff Composite

The identified years of highest and lowest ratio of summer Yenisei / spring Ob runoff are then used to calculate eastward and westward composites for GLORYS12V1, LOCEAN SMOS, JPL SMAP and CCI SSS (Figure 4.9, Figure 4.10).

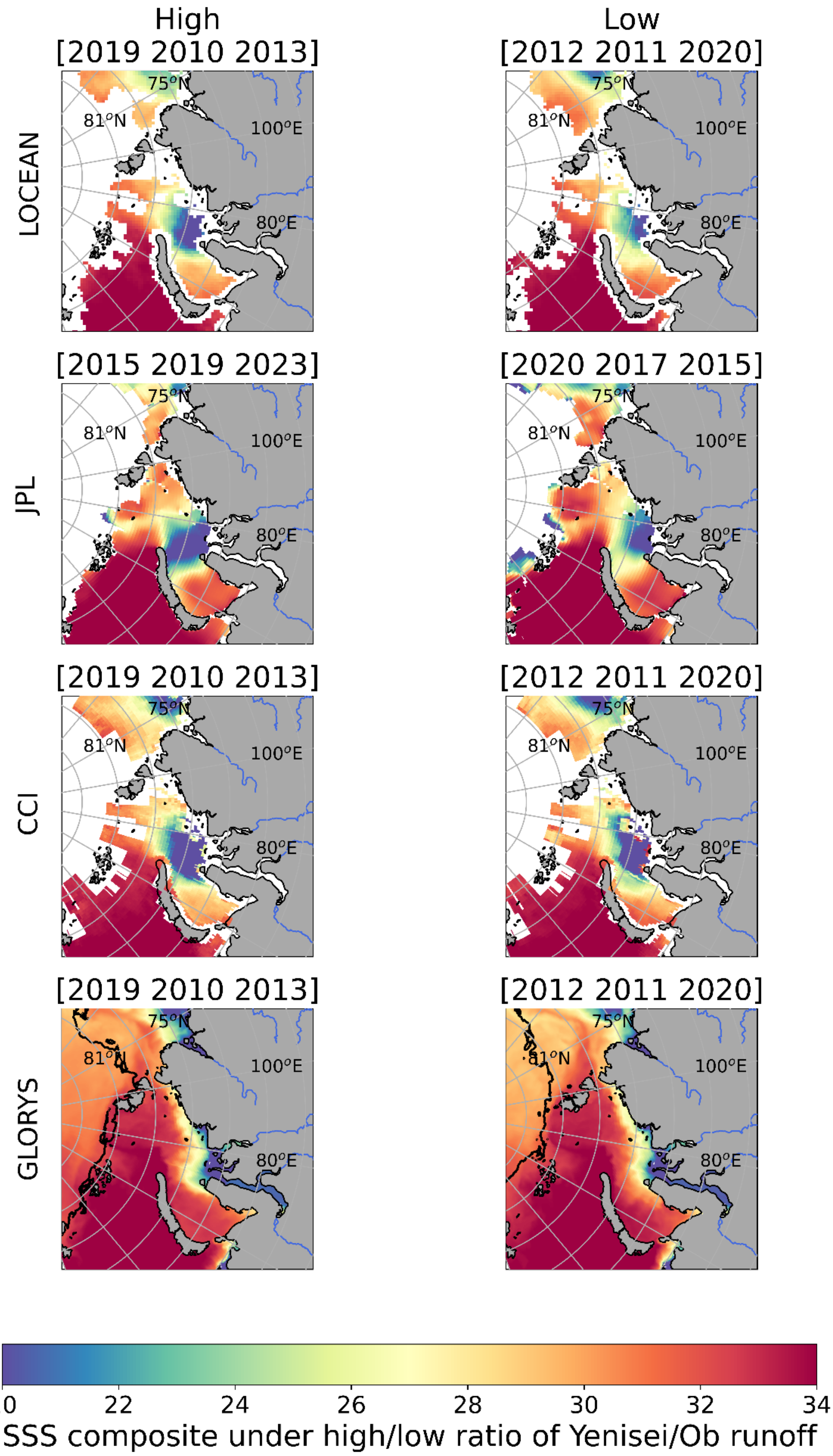

Figure 4.9: High (H, left column) and low (L, right column) Yenisei/Ob runoff composites calculated for (top to bottom) LOCEAN SMOS, JPL SMAP, CCI and GLORYS12V1 SSS, from the identified three years of highest and lowest ratio between summer (Julian day 200) Yenisei and spring (Julian day 150) Ob runoff (over 2011-2023 for GLORYS12V1 and LOCEAN SMOS and over 2015-2023 for JPL SMAP). The GLORYS12V1 mean 30% sea ice concentration contour is overlaid on the respective composite plots.

The high and low Yenisei/Ob runoff ratio composites somewhat resemble the east/west-ward wind composites, despite the different years used to calculate them (Figure 4.9). However, the low Yenisei/Ob runoff ratio composites extend much further offshore than the eastward wind composites, particularly in LOCEAN and JPL. In addition, the high Yenisei/Ob runoff ratio composites appear to not extend as far westward, into the western Kara Sea, compared to the westward wind composites. Despite this, it is clear that a low ratio of Yenisei/Ob runoff is coincident with the plume remaining more coastally confined and extending into the eastern Kara Sea and that a high ratio of Yenisei/Ob runoff is coincident with the plume extending further offshore into the central Kara Sea.

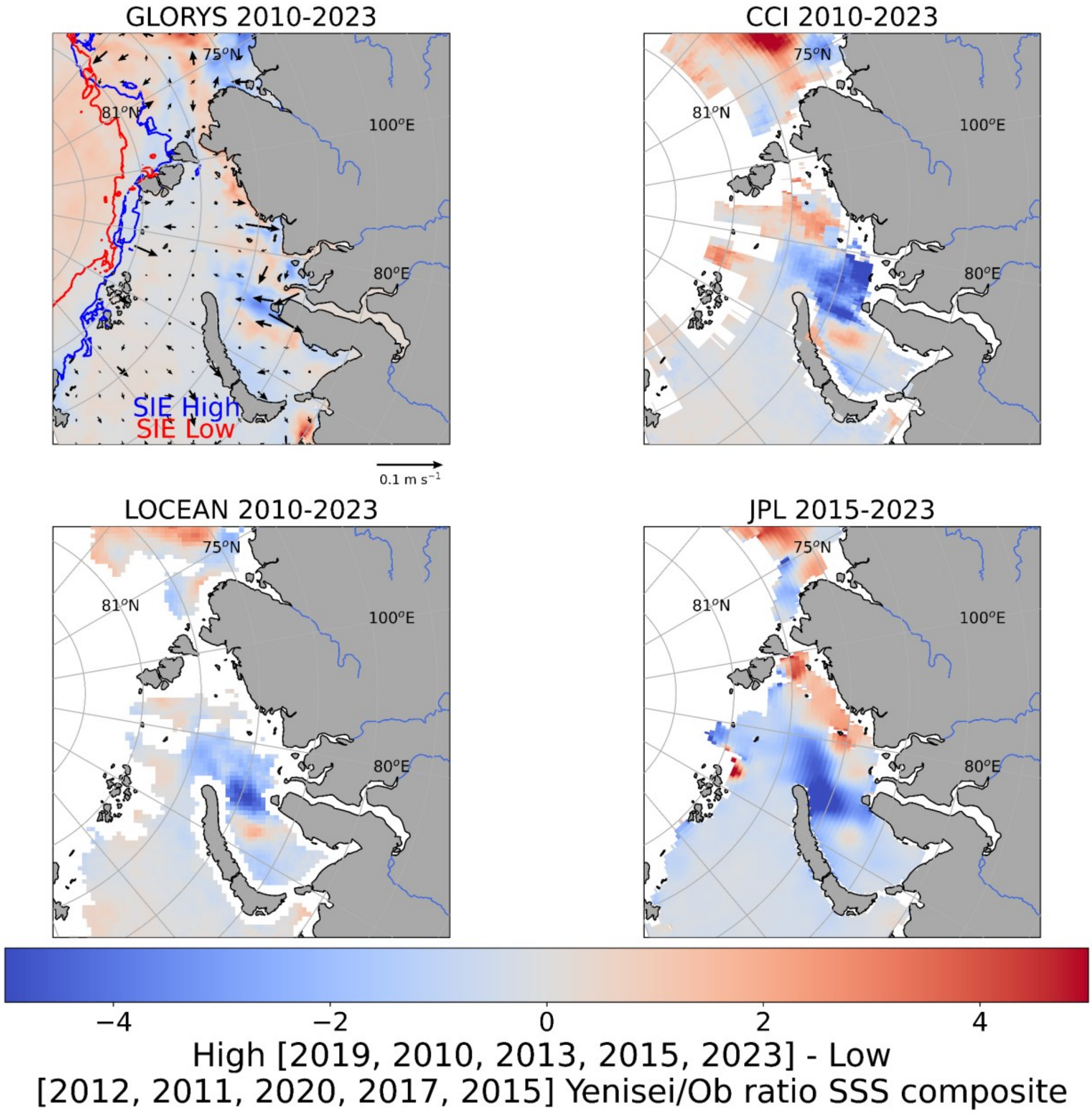

Figure 4.10: The difference between high and low composites calculated for GLORYS12V1 SSS, CCI SSS, LOCEAN SMOS, and JPL SMAP, from the identified three years of highest and lowest ratio between spring (Julian day 150) Ob and Yenisei runoff (over 2010-2023 for GLORYS12V1, CCI and LOCEAN SMOS and over 2015-2023 for JPL SMAP). Regions in blue represent regions with lower salinities under eastward wind forcing and regions in red represent lower salinities under westward wind forcing. The GLORYS12V1 mean 30% sea ice concentration contour under high (blue) and low (red) ratios of Yenisei/Ob runoff is overlaid. The difference in GLORYS12V1 current velocity for June-August in years of high and low ratios of Yenisei/Ob runoff is also overlaid as black arrows (masked by the region of mean sea ice concentration above 30%).

The satellite runoff ratio composite difference plots all have much more notable negative anomalies than positive anomalies (Figure 4.10). However, the location of these negative anomalies differs between products. In GLORYS12V1, the spatial pattern of runoff composite difference plots is very different from the wind composite difference plots, which appear to have alternating bands of positive and negative anomalies along the coast. These bands consist of a negative anomaly in the very western Kara Sea, then alternating positive and negative anomalies which extend offshore from the coast until a positive anomaly extends through the Vilkitsky Strait. In the satellite products, the composite difference plots generally resemble zonal wind composite difference plots (Figure 4.8) but the negative anomaly is predominantly positioned over the central Kara Sea in runoff composite difference plots, covers a smaller area and does not extend into the western Kara Sea as the positive anomaly does in wind composite difference plots. In both CCI and LOCEAN products, there is a positive anomaly in the western Kara Sea, as there is in GLORYS12V1. The JPL composite difference plot is the only satellite product that has a notable region of positive anomaly in the eastern Kara Sea, which appears to extend into the Laptev Sea. Both LOCEAN and CCI have no clear positive anomaly nearshore. Differences between GLORYS12V1 and satellite products may occur as GLORYS12V1 is forced with climatological, rather than interannually varying Ob and Yenisei runoff. This may also account for the smaller, patchier pattern observed.

The negative anomaly visible in runoff ratio composite difference plots, particularly those for satellite products, somewhat resemble the wind composite difference plots (Figure 4.8) as several of the years of high runoff ratio were also years of strong eastward wind. Hence, the composites for high and low years of Ob/Yenisei runoff ratios were also re-calculated excluding the three most eastward years (2016, 2018, 2021). Whilst the high runoff composites did appear to extend notably further offshore when these years were excluded, the composite difference pattern remained consistent (but was weaker in all products). This reiterates that high and low ratios of Ob/Yenisei do also drive the onshore/offshore dipole in plume location visible in composite difference plots and that the consistency between wind and runoff composites is not because similar years are chosen for both composites.

Only a very weak pattern is visible in the GLORYS12V1 current velocity composite difference plot, which suggests no notable differences over most of the Kara Sea. This suggests that observed differences in SSS are not due to differences in wind forcing (or associated current velocities) that happen to be present in the years chosen. However, there are several small differences right at the outflow of the Ob and Yenisei rivers. This difference suggests that high Yenisei and/or low Ob runoff drive increased offshore transport at the outflow of the Yenisei delta, which likely drive the lower SSS under high Yenisei / low Ob runoff in this region.

4.3.4 Impact of variability in wind forcing on SST

As with SSS, the identified most eastward and westward years are then used to calculate eastward and westward composites for GLORYS12V1 and CCI SST (Figure 4.11).

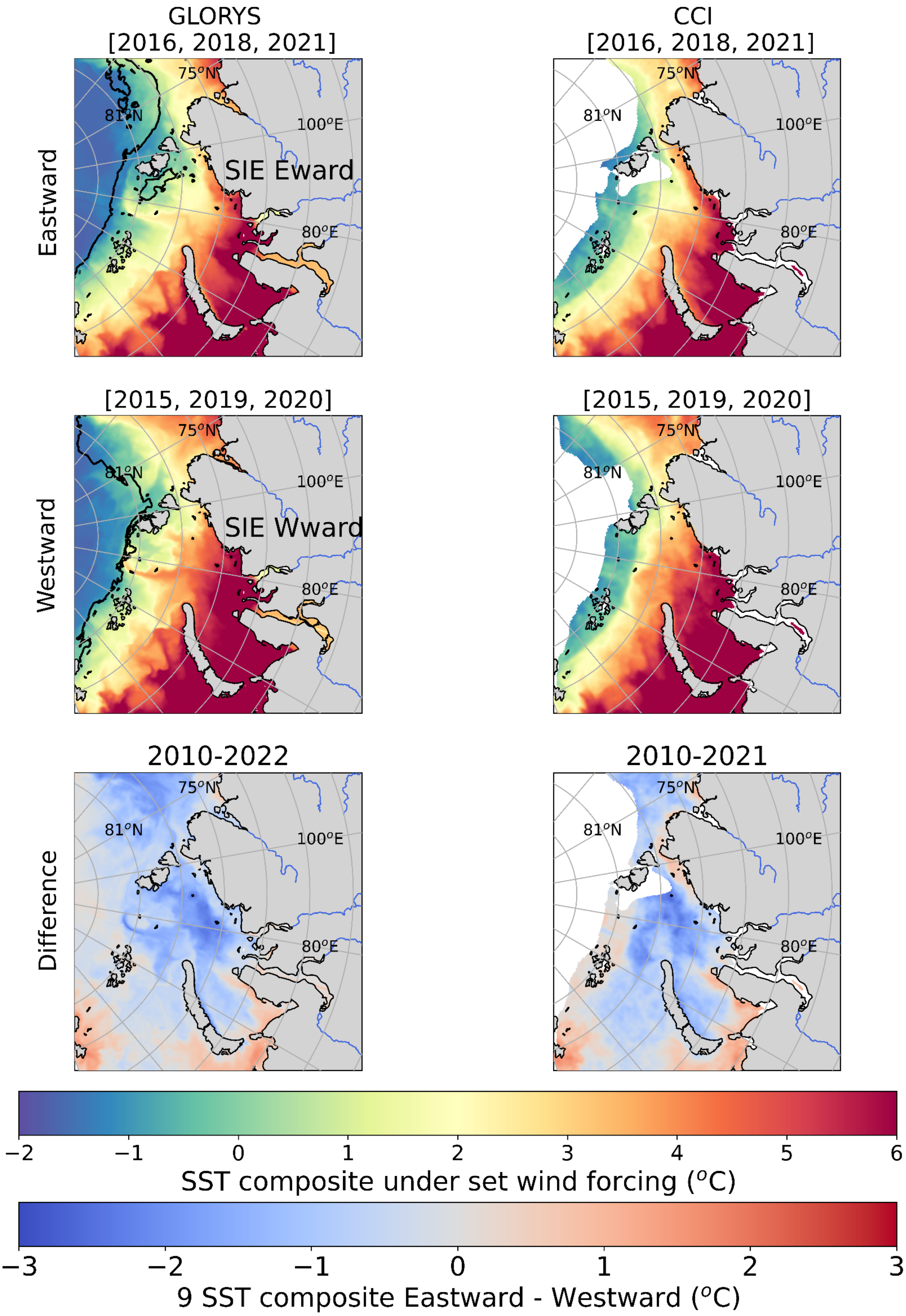

Figure 4.11: Eastward (E, top row) and westward (W, middle row) composites calculated from the identified three most eastward and westward years over 2010-2020 for (left to right) GLORYS12V1 SST and L4 CCI SST (masked by 30% sea ice concentration). The difference composite (eastward – westward) for each product is shown on the bottom row. The mean 30% sea ice concentration contour for eastward and westward years is used to mask L4 CCI data and is overlaid in GLORYS12V1 in black on both eastward and westward composite plots.

The eastward/westward CCI composite plots closely resemble GLORYS12V1 composite plots (Figure 4.11). In both products, SST varies in a strong gradient, with the warmest SSTs nearshore and in the southern Barents and southwestern Kara Sea (> 6 °C) and much cooler SSTs (< 1 °C) offshore. SSTs in the Barents and Kara Sea are notably warmer (often > 4 °C) than in the north-western Laptev Sea (-1.5 to 2 °C) (Figure 3.9). In addition, the region of warmest SSTs extends throughout the eastern Barents Sea and western Kara Sea as well as along the coast of the Kara Sea, which make it difficult to differentiate the Ob-Yenisei plume from background warm SSTs present here (Figure 4.11). This represents a notable difference from the Laptev Sea, where the Lena River plume is clearly identifiable by the it's SST signature (Figure 3.9). Whilst the SST pattern is similar in CCI and GLORYS12V1 products, the CCI product suggests that warm SSTs extend further into the Vilkitsky Strait under eastward wind forcing than GLORYS12V1, which causes a notable difference in composite difference pattern between the two products (Figure 4.11, bottom row).

Whilst it is difficult to differentiate the Ob-Yenisei plume from background SSTs, there is still a notable difference in SST under eastward and westward forcing. Under eastward wind forcing, the warmest SST appear somewhat more coastally confined, particularly in CCI in the eastern Kara Sea and these warmest SSTs are particularly warm (> 6 °C). Conversely, under westward wind forcing, relatively warm SSTs (> 4 °C) propagate further offshore and occupy a larger region of the Kara Sea. This difference is again highlighted by the composite difference plots, which show a weak onshore / offshore dipole. This dipole clearly re-iterates that under westward wind forcing, the warm SSTs propagate offshore and occupy the central Kara Sea. However, this dipole also suggests there is relatively little difference in SST nearshore in the central Kara Sea, suggesting plume transport has little impact on nearshore SST. The presence of this pattern in the SST composite difference plots is particularly notable given the same pattern is not visible in GLORYS12V1 SST correlation plots with eastward wind stress.

4.3.4.1 Ob and Yenisei runoff as a driver of GLORYS12V1 SST and SIC

Spring Ob runoff has large significant correlations with GLORYS12V1 September SST and SIC (Figure 4.4, Figure 4.5). Spring Ob runoff is coincident with warmer SSTs over most of the central Kara Sea. It is likely that this correlation is at least partly a result of auto-correlation with atmospheric forcing. Spring Ob runoff is relatively strongly positively correlated to March AOI (Appendix Figure C.4). Positive March AOI has previously been suggested to be coincident with warm surface air temperatures and anomalously warm springs drive both an increase in spring Ob runoff and earlier sea ice melt, which drive warmer summer SSTs throughout the Kara Sea (Kryjov, 2002; Lim et al., 2022). This autocorrelation may also drive increased Atlantic Water inflows, which would explain why this positive correlation extends from the Barents Sea and through the St Anna Trough. This positive correlation could also suggest that spring Ob runoff timing (IE freshet timing) plays a role in controlling central Kara Sea September SSTs. However, the very extensive region of significant correlation between Ob runoff and SST is more indicative of autocorrelation with atmospheric forcing. The direct and indirect relationship between runoff and larger-scale atmospheric forcing should be better assessed (for example by further investigating relationships with large-scale atmospheric forcing in the previous winter / spring and precipitation patterns over the continent).

Summer Yenisei runoff is significantly negatively correlated to GLORYS12V1 SST over most of the Barents Sea and in the very western and eastern Kara Sea (Figure 4.4). A negative correlation between Yenisei runoff and SST has previously been suggested, but only offshore (Mäkinen and Vanhatalo, 2016). It is worth noting that when the negative trend in Yenisei runoff (over the GLORYS12V1 time period) is removed, there are much smaller regions where this negative correlation remains significant, and none of these are within the central Kara Sea. Hence, it is likely that this correlation is strengthened because of coincident trends in both SST and in summer Yenisei runoff.

The consistently opposing correlation patterns (between Ob or Yenisei runoff) with SST and SIC highlights a level of coupling between SST and SIC in this region. However, significant correlations with SIC are only present in the eastern Kara Sea and around the Vilkitsky Strait. It is likely that correlations with SIC are only significant in this region as this is one of the few regions of the Kara Sea that still has sea ice at this time of year. Hence, whilst there is a weak level of coupling between SST and SIC throughout the Kara Sea and Vilkitsky Strait, this coupling is notably stronger in the eastern Kara Sea and Vilkitsky Strait. Therefore, this region currently represents a transition zone between the seasonally sea ice free Kara Sea and the consistent partial sea ice covered Laptev Sea.

In addition, the very different spatial correlation pattern of Ob/Yenisei runoff with SSS and SST highlights that SSS and SST/SIC are controlled by notably different processes in this region. Unlike with SSS, where both Ob and Yenisei runoff appear to interact to play a stronger role in controlling variability, spring Ob runoff appears to play a notably stronger role in controlling SST/SIC variability over the Kara Sea, with Yenisei runoff only playing a role in the eastern Kara Sea. This depicts another key difference from the Laptev Sea and suggests a lack of co-variability between SSS and SST in this region. This has previously been suggested for the Vilkitsky Strait (Tarasenko et al., 2021) and suggests SST should not be used alone, in the place of SSS, to infer variability in plume transport.

4.4 Discussion

4.4.1 Ob and Yenisei runoff as joint and individual drivers of SSS variability

Previous studies have predominantly investigated the impact of cumulative Ob-Yenisei runoff on interannual variability in SSS (Lemeshko and Tsyganova, 2022; Umbert et al., 2021). However, there has also been suggestions that the ratio of Yenisei/Ob runoff can influence the resulting interaction between the Ob and Yenisei plumes, in addition to wind forcing, and contribute to the differing patterns of SSS observed (Osadchiev et al., 2017). The strong (significant) negative correlation between the ratio of summer Yenisei/Ob runoff and GLORYS12V1 SSS supports the influence of this ratio (Figure 4.3), highlighting that a high ratio of Yenisei/Ob runoff drives decreased SSS over most of the offshore Kara Sea. This negative correlation is consistent with the suggestion that under low Ob runoff and high Yenisei runoff, the Ob and Yenisei plumes spread further offshore and occupy the western and central Kara Sea (Osadchiev et al., 2017). The dominant role of the ratio of summer Ob/Yenisei runoff in this region is also nicely highlighted in runoff composite difference plots (Figure 4.10) by the strong negative anomaly in the central Kara Sea, which is consistently present for all products, and by the offshore surface current velocities nearshore in the GLORYS12V1 composite difference plot.

Whilst previous studies typically focus on the joint impacts of both Ob and Yenisei runoff, here I also try to identify the individual contributions of Ob and Yenisei runoff on Kara Sea dynamics. Understanding the individual contributions is only becoming increasingly important given the strong differences in hydrography of the two watersheds (Osadchiev et al., 2019) and their likely differing responses to climate change. This is particularly pertinent given the very different impacts of upstream watershed regulation and of the differing seasonal cycle between the two rivers (Shiklomanov and Lammers, 2009; Stadnyk et al., 2021; Yang et al., 2004). This choice to focus on the individual contributions is also due to the challenge of calculating and interpreting cumulative Ob/Yenisei runoff given the differing locations and lag-times, of runoff observation stations at Salekhard (Ob) and Igarka (Yenisei) stations (Dianskii et al., 2015; Dolgopolova, 2015; Osadchiev et al., 2021; Osadchiev et al., 2017; Semizhon et al., 2010).

This challenge, and the importance of correct consideration of this lag, is nicely highlighted by the notable difference in the runoff integration times with the strongest correlations to Ob and Yenisei runoff (Figure 4.3). GLORYS12V1 SSS is most strongly correlated with spring Ob runoff but is most strongly correlated with summer Yenisei runoff. This difference may be partially due to the differing lag-times caused by the greater distance between the Ob observation station, Salekhard, and where the Ob River discharges into the sea, which is suggested to be ~80 days (compared to the distance between the Yenisei observation station, Igarka, and where the Yenisei River is discharged into the sea, which is suggested to cause a lag of 30 days). This difference in lag times, of ~50 days, explains the stronger correlation of GLORYS12V1 September SSS with cumulative summer Yenisei runoff (up to Julian day 200) and cumulative spring Ob runoff (up to Julian day 150). However, this difference is also likely due to the difference in seasonal discharge between the two rivers. Ob runoff is relatively consistent interannually; it typically peaks slightly earlier than Yenisei runoff but has a very low prolonged peak in discharge (Yang et al., 2003). Conversely, Yenisei runoff has a substantial peak between May and June, the timing of which varies considerably interannually, but has very low discharge after this.

The GLORYS12V1 correlation analysis clearly shows that variability in Yenisei runoff appears to play a dominant role in controlling SSS, especially in the central and western Kara Sea (Figure 4.3). The strong negative correlation with summer cumulative Yenisei runoff follows expectation given a larger volume of runoff provides a greater freshwater input to the Kara Sea, and therefore lowers salinities. Conversely, an opposite pattern is visible with Ob runoff as there are small patches of positive correlation with spring Ob runoff (Figure 4.3). This positive correlation suggests increased Ob runoff is consistent with increased salinity at the outflow of the Ob delta. This opposing correlation is consistent with the previous suggestion that high Ob runoff / low Yenisei runoff drive higher salinities at the edge of the delta by causing an "isolated" plume configuration (Osadchiev et al., 2017). This isolated plume configuration is suggested to only occur when there is sufficient Ob runoff to surround the Yenisei plume, confining it to the coast and isolating it from the saline ambient sea water, minimizing mixing. This manifests with higher salinities offshore, indicative of the Ob plume, and fresh salinities nearshore, indicative of the fresher Yenisei plume. Conversely, low Ob runoff / high Yenisei runoff allows the Yenisei plume to occupy more of the central and western Kara Sea and lowers salinities in this region. The presence of increased (decreased) freshwater offshore following low (high) Ob runoff and/or high (low) Yenisei runoff is clearly visible from the negative correlation in Yenisei/Ob ratio correlation plots and the negative anomaly in composite difference plots. However, no positive correlation is visible nearshore, which would denote the presence of the very fresh “isolated” Yenisei plume. Despite this, small regions of positive anomaly are visible in the GLORYS12V1 runoff ratio composite (Figure 4.10), which may indicate the presence of this fresh isolated plume. No similar positive anomaly is visible in satellite runoff ratio composites (Figure 4.10). However, the absence of this positive anomaly may be simply due to the lack of satellite SSS data nearshore. Hence, whilst high (/low) Yenisei runoff and low (/high) Ob runoff both clearly contribute to driving the low (/high) SSS visible throughout the central Kara Sea (Figure 4.3, Figure 4.10), there is insufficient evidence here to suggest that low Yenisei runoff and high Ob runoff drive an isolated plume configuration and low SSS nearshore, as has previously been suggested (Osadchiev et al., 2017). The interactions between these two rivers should be explored further (such as with a particle tracking study to isolate the interactions between rivers).

However, the much larger and stronger (significant) correlation patterns with cumulative Yenisei runoff, compared to those with Ob runoff, suggests variability in Yenisei runoff plays a stronger role in controlling SSS over most of the offshore Kara Sea. High and low Yenisei runoff composites (not shown here) also suggest high Yenisei runoff is consistent with lower SSS over the central and western Kara Sea, which also supports this suggestion. Whilst the Yenisei’s individual contribution has not previously been widely established, it has previously been suggested to be correlated with low SSS in the western Kara Sea (Mäkinen and Vanhatalo, 2016). The dominant role of Yenisei runoff is also unsurprising given the larger magnitude of Yenisei runoff and of its variability, compared to Ob runoff, and therefore its larger fresh water contribution (Zatsepin et al., 2010). It is also worth noting that Yenisei runoff composites closely resemble Yenisei/Ob ratio composites, supporting the suggestion that Yenisei runoff plays a dominant role in driving low SSS over the central Kara Sea. Whilst there is clearly strong evidence that variability in Yenisei runoff plays a dominant role in controlling SSS over the central and western Kara Sea, it is not possible to discount the role of spring Ob runoff.

It is also worth noting that there is a negative trend in the summer Yenisei timeseries over the GLORYS12V1 time period (1993-2023). However, this trend is not consistent over longer time-periods, and appeared to indicate a shift to a different mode of decadal variability, so was not removed. In addition, whilst there is a trend in summer Yenisei runoff, there are no significant trends in autumn or full year runoff, which present the same negative correlation pattern in the western Kara Sea. The same correlation pattern also remains regardless of if you detrend or of the time period used to calculate the trend. Hence, it does not appear that the decadal variability present impact correlation patterns.

Whilst there are very few regions of significant correlation between Ob runoff and GLORYS12V1 September SSS (Figure 4.3), a notable (significant) positive correlation is present right at the outflow of the Ob delta, suggesting an increase in spring Ob runoff drives higher SSS in this region. This correlation pattern is consistent with the previous suggestion that the ratio of Ob/Yenisei runoff can influence the resulting interaction between the Ob and Yenisei plumes, and cause an isolated or non-isolated plume configurations (Osadchiev et al., 2017). However, whilst previous work suggests that both high Ob runoff and low Yenisei runoff are needed to cause the non-isolated plume configuration, the correlation here with GLORYS12V1 SSS suggests Ob runoff is the dominant driver of differences in SSS at the outflow of the Ob delta. It is possible that increased Ob runoff prevents/slows the westward transport of Yenisei runoff into the edge of the Ob delta, which would drive the high salinities observed in this region.

An attempt is made here to identify the individual contributions of Ob and Yenisei runoff. However, the highly correlated nature of the ratio of spring (and summer) Yenisei/Ob runoff with both spring (and summer) Ob and Yenisei runoff prevents complete isolation of the contributions of Ob and Yenisei runoff. Regardless, whilst it is difficult to untangle the individual contributions of Ob and Yenisei runoff, it is clear that a low (/high) ratio of spring Yenisei/Ob runoff does drive higher (/lower) SSS in the central and western Kara Sea.

4.4.2 Wind as driver of SSS variability

As is true in the Laptev Sea, the zonal wind is a clear driver of Kara Sea SSS. This is visible from the consistent eastward/westward composite (Figure 4.7) and composite difference (Figure 4.8) plots for both GLORYS12V1 and satellite SSS, and from the consistency in eastward turbulent surface stress correlation patterns (Figure 4.2). The key role of wind forcing has also been highlighted by many previous papers (Kubryakov et al., 2016; Osadchiev et al., 2017). However, the dominant role of zonal wind forcing is emphasized here. Eastward wind forcing drives onshore transport, resulting in a very coastally confined Ob-Yenisei plume, which appears to extend all the way along the coast, through the Vilkitsky Strait and into the Laptev Sea. Conversely, westward wind forcing appears to drive offshore plume transport into the central, and western Kara Sea. The spatial extent and magnitude of this pattern are notably larger than that in the Laptev Sea, particularly under westward wind forcing, likely due to the much larger magnitude of runoff entering the Kara Sea from both Ob and Yenisei rivers.

Whilst eastward/westward wind components drive southeast/northwestward plume transport, there is a suggestion that there is a third central type of plume propagation, when the wind is relatively symmetrical (Kazakova et al., 2024; Kubryakov et al., 2016; Lemeshko and Tsyganova, 2022). Whilst there was relatively close similarity between the westward wind composite and the “mid” wind composite, calculated from years with no strong east/westward wind component, there was some evidence that the plume appeared to propagate further into the western Kara Sea in the westward composite. However, there are greater differences between “mid” composites for each of the satellite products, than between westward and mid composites, which complicate interpretation of the drivers of these differences. Analysis of westward plume propagation is further complicated by the poor representation of GLORYS12V1 Ob-Yenisei surface plume propagation, particularly as it does not appear to propagate into the western Kara Sea, which prevents analysis of this third plume type.

Kara Sea SSS is significantly correlated with northward as well as eastward turbulent surface stress (Figure 4.2). This may be partly due to the (weak) correlation between eastward and northward turbulent surface stress over this region over the GLORYS12V1 time period (1993-2020). The autocorrelation between eastward and northward wind stress complicates interpreting their individual contributions. However, previous studies have suggested that northward wind is required to drive zonal Ekman transport and downwelling of the Yenisei plume and formation of a deep and narrow alongshore current which propagates along the Tamyr Peninsula (Osadchiev et al., 2017). This represents a notable difference from the Laptev Sea, where zonal wind stress clearly drives eastward transport of the Lena plume, and where the correlation pattern is notably different between SSS and eastward and northward wind stress. The differing role of meridional wind stress in the Kara Sea, and the coherence between correlation patterns of SSS with eastward and northward wind stress, may be primarily due to geographical differences between the deltas/coastlines of the two regions. Whilst the coastline of the Laptev Sea runs almost exactly East/West, the Kara Sea coastline runs Southeast/Northwest. The differing coastline orientation suggests more northward transport may be needed to drive the alongshore plume structure in the Kara Sea, compared to in the Laptev Sea. In addition, runoff from the Ob and Yenisei must travel a considerable distance northward to make it out of their respective deltas, compared to Lena runoff which outflows directly into the central Laptev Sea. The climatological circulation in these two regions may also contribute to these differences. Southward wind forcing dominates circulation in the Kara Sea in July and August, which limits northward plume transport and lowers interannual variability in Kara Sea SSS (Osadchiev et al., 2021b). Hence, a weakening of this southward wind may be required to help promote earlier / more rapid transport out of the Ob and Yenisei deltas.

Whilst the composite difference plot patterns are the same in GLORYS12V1 and satellite products (Figure 4.8), composite difference plots also suggest GLORYS12V1 SSS varies much less than satellite SSS. This is particularly visible in the offshore Kara Sea, where satellite products all have an extensive region of high (/low) SSS under eastward (/westward) wind forcing with differences of > 5 pss but GLORYS12V1 only has differences of ~2 pss. These differences may originate partly because GLORYS12V1 is forced using climatological runoff. This has previously been suggested to be true of other reanalyses, particularly given reanalyses likely assimilate little or no in-situ data in this region (Tang et al., 2018). This hypothesis is particularly interesting given that the region where GLORYS12V1 tends to be too saline is coincident with the region of strongest correlation with Yenisei runoff and where there is the greatest difference in satellite SSS composite difference plots between years of high and low Yenisei runoff. Therefore, it is possible that whilst GLORYS12V1 manages to capture at least a component of the relationship between interannual variability in runoff and SSS by assimilating in-situ data, the lack of interannual variability in the climatological runoff used as forcing means this relationship is too weak, which drives the lower variability observed in SSS.

4.4.3 Combined influence of wind and runoff on SSS variability

In the Laptev Sea, cumulative Lena runoff for all integration times has little influence on interannual variability in the spatial pattern of SSS. The same is not true of Ob and/or Yenisei discharge in the Kara Sea. The key role of the ratio of Yenisei/Ob runoff is clear from both the significant negative correlation with GLORYS12V1 SSS (Figure 4.3) and the consistent runoff composite difference pattern visible in all satellite products (Figure 4.10). These findings are also supported by the lack of correlation between the timeseries of eastward (or northward) wind stress with the ratio of Yenisei/Ob runoff or with summer Yenisei or spring Ob runoff. This contradicts previous work suggesting runoff plays little to no role in controlling interannual variability in river plume transport (Harms and Karcher, 2005; Zatsepin et al., 2010). This highlights the significant difference in key controls of interannual variability in SSS in the Kara and Laptev Sea. These differences are not surprising given the dramatic differences in geography/bathymetry of the two regions and the much larger magnitude of fresh water that enters the Kara Sea. It is also likely that the presence of two large rivers, and in particular their interactions, also help to drive the notable differences in dynamics in this region (Osadchiev et al., 2017).

There is a notable difference between eastward and westward wind and runoff composites from GLORYS12V1 SSS and those from the other satellite products (Figure 4.7). In particular, the fresh layer extends much further offshore in the satellite products than in GLORYS12V1 SSS. These differences complicate untangling the effects of wind and runoff. The stronger horizontal gradient in salinity offshore visible in GLORYS12V1, which is present regardless of wind forcing, may occur due to overmixing in GLORYS12V1. The challenges of accurately representing mixing and stratification dynamics is well established and is discussed more extensively in the Laptev Sea Chapter (3) (Hordoir et al., 2022; Janout et al., 2020). Overmixing is observed in GLORYS12V1 in the Laptev Sea and causes a similar difference between GLORYS12V1 and satellite SSS (Hudson et al., 2024). However, this difference is more dramatic in the Kara Sea, possibly as the western Kara Sea, where the greatest differences from satellite SSS are present, is much deeper than the Laptev Sea (>100m rather than <50m). However, this difference also may be as GLORYS12V1 is forced with climatological Ob and Yenisei runoff. The ratio of Yenisei/Ob runoff has previously been suggested to divert the plume offshore/ keep the plume nearshore (Osadchiev et al., 2017). Whilst GLORYS12V1 appears to capture a similar pattern as satellite runoff composite difference plots, the pattern observed is notably weaker and patchier in this central Kara Sea region, supporting that the lack of interannually varying runoff may drive these differences. Regardless, improved representation of the Ob-Yenisei plume is needed to accurately represent Kara Sea dynamics, and Russian Arctic freshwater transport.

Both runoff ratio composite and correlation plots (Figure 4.3, Figure 4.10) suggest that runoff does influence Kara SSS. This is also supported by the consistency of runoff composites even when the years of strongest eastward wind forcing are removed. However, whilst both wind and runoff influence Kara SSS, untangling the effects of wind from those of runoff is a challenge. This is particularly true given the weak similarity between wind and Yenisei/Ob runoff composites (Figure 4.7, Figure 4.9). Regardless, the strong pattern in runoff ratio composites suggests a notable role for runoff regardless of wind forcing, and suggests that both westward wind forcing and low Ob / high Yenisei runoff both contribute to northward plume transport into the central Kara Sea (Osadchiev et al., 2017). This contradicts previous suggestions that runoff only controls the position of the plume edge when there is minimal/similar wind forcing (Lemeshko and Tsyganova, 2022). However, the lack of positive correlation or anomaly nearshore in runoff correlation and composite plots, in comparison to the strong negative correlation and anomaly in wind correlation and composite plots suggests wind forcing is the dominant driver of alongshore transport regardless of runoff conditions. Therefore, it seems that whilst eastward wind confines the plume to the coast and drives eastward transport regardless of the magnitude of Ob and/or Yenisei runoff, low Ob runoff and high Yenisei runoff help to strengthen offshore plume transport under westward wind forcing.

4.4.4 Wind as driver of SST/SIC variability

Whilst there are only small regions of significant correlation pattern between eastward/northward turbulent surface stress and SST in GLORYS12V1, the SST wind composites suggest a notable difference in SST pattern under differing eastward/westward wind forcing. This pattern suggests westward wind forcing drives increased SSTs offshore, which is consistent in both CCI and GLORYS12V1. CCI composites also suggest that eastward wind forcing drives warm SSTs nearshore, particularly in the Vilkitsky Strait, but this is not visible in GLORYS12V1. The lack of consistency between SST correlation and composite plots suggests that whilst interannual variability in plume dynamics do have an impact on driving SST variability, this is just one component of interannual variability in SST and is not the dominant component.

Despite wind being a common driver of SST as well as of SSS, zonal wind is not the dominant driver of SST in the central Kara Sea. The difference in dominant drivers of SSS and SST suggests a lack of co-variability between SSS and SST. This difference in dominant driver is highlighted by the considerable differences between SSS and SST zonal wind stress correlation plots, particularly the lack of strong correlation between wind stress and SST in the central Kara Sea. This lack of co-variability is consistent with previous findings for the Vilkitsky Strait (Tarasenko et al., 2021) but represents a key difference from the Laptev Sea. This lack of co-variability may also help to explain the relatively weak correlations with turbulent surface stress, especially in August, due to competing impacts of zonal wind driving increased warm Atlantic Water inflows but also eastward plume transport, which favours cooler temperatures over the central Kara Sea.

The opposite correlation pattern is visible between GLORYS12V1 SIC and eastward turbulent surface stress in July, August and September (Appendix Figure C.3) (as was visible with GLORYS12V1 SST). These opposing correlation patterns with eastward turbulent surface stress highlight the strong correspondence between SST and SIC in this region. This suggests zonal wind differences, and associated changes in SST are also associated with changes in SIC, as was true in the Laptev Sea. However, the lack of notable correlation patterns with eastward turbulent surface stress suggests this does not dominate SIC variability. This is also reiterated by the lack of notable difference in the position of the 30% sea ice concentration contour under eastward and westward wind forcing.

This minimal difference suggests interannual variability in plume dynamics have little to no impact on SIC in the Kara Sea. This may contribute to the notable difference in the SST composite difference plots in the Kara and Laptev Sea. The Laptev SST composite difference plots suggest an East/West dipole, as eastward (/westward) plume transport drives sea ice loss in the eastern Laptev and western East Siberian Sea (western Laptev Sea), and allowing increased ocean warming in this region. Conversely, Kara Sea SST composite suggests an onshore/offshore dipole. The majority of the Kara Sea remains sea ice free in all Septembers, so there is a much less interannual variability in sea ice cover, which prevents the positive feedback cycle that occurs in the Laptev from occurring in the Kara Sea. The deeper Kara Sea is also less prone to the dramatic shallow-shelf warming that occurs in the southern Laptev Sea.

However, wind stress does appear a more dominant driver of SST (and SIC) in the eastern Kara and western Laptev Sea. Meridional wind, particularly in August, also appears to be a more dominant control on SST, by controlling Ekman transport and the associated upwelling/downwelling on/off the shallow shelf in the eastern Kara Sea. Whilst there are no notable differences in the 30% SIC contour (Figure 4.8), there is a very small difference in position of the 0% SIC contours (not shown), particularly in the eastern Kara Sea, which are slightly further offshore under westward wind forcing than eastward wind forcing. This suggests that the zonal wind may promotes transport and accumulation of sea ice in the eastern Kara Sea (Yang et al., 2024). This provides an explanation for the notable area of no SSS retrievals / region with sea ice contamination in the eastern Kara Sea in eastward SSS composite plots, which is not present in westward SSS plots (Figure 4.8). This region, and this relationship is explored further in the Vilkitsky Strait (Chapter 5, p79).

4.5 Conclusions

As for the Laptev Sea, the zonal wind appears to be the main driver of whether the fresh plume is transported offshore or alongshore. This is highlighted by the strong agreement between GLORYS12V1 and satellite eastward and westward wind composites. However, unlike the Laptev Sea, the zonal wind in August appears to play a notably larger role than June or July, likely due to the large freshwater volume discharged by this time and the larger ice-free area and higher variability in zonal wind stress in August. Meridional wind, particularly in August, also appears to play a role in controlling this variability but the correlation between northward and eastward wind stress complicates determining their respective roles.

The ratio of summer Yenisei/Ob runoff also plays a role in controlling how fresh the plume is, but primarily only when the plume travels offshore, into the central and western Kara Sea. It appears that variability in summer cumulative Yenisei runoff is the dominant control on this ratio, and on SSS in the central Kara Sea. However, spring Ob runoff also appears to play a role in controlling this interaction, by hindering or promoting transport of the Yenisei plume offshore, and controlling SSS at the outflow of the Ob Delta.

Zonal wind forcing also has a clear influence on SST. However, the difference between correlation and composite difference plots highlights that the zonal wind is not the dominant control on SST, and that SSS and SST are notably less closely coupled in the Kara Sea than in the Laptev Sea. Whilst it is clear that there is coupling between SST and SIC, the persistent sea ice free nature of the central Kara Sea in September drives notably lower interannual variability in SIC. This has knock on effects on SST, as the positive feedback cycle that strongly couples SST and SIC in the Laptev, is not present in the Kara Sea.

Chapter 5 Vilkitsky Strait

5.1 Introduction to Vilkitsky Strait

The Vilkitsky Strait sits between the Kara and Laptev Sea and connects the Russian Arctic shelf seas (Figure 5.1). Whilst very narrow (~ 50km wide), the Vilkitsky Strait facilitates freshwater transport from the Kara to the Laptev Sea, and is a primary component in the pathway of Arctic freshwater transport. Whilst other freshwater pathways have previously been suggested by modelling studies, including eastward advection through Shokalsky Strait (100-150k northwest of the Vilkitsky Strait) and northward advection to central Arctic, transport throughout these pathways has never yet been observed in-situ (Kelly et al., 2018; McClimans et al., 2000; Osadchiev et al., 2023a; Panteleev et al., 2007). Transport through Vilkitsky Strait, whilst initially suggested by a numerical circulation study (Aksenov et al., 2011), has now been widely confirmed by in-situ data (Osadchiev et al., 2023a, 2020b). As the only confirmed observed pathway of freshwater transport, it is crucial to understand Vilkitsky Strait processes, and particularly drivers of variability in freshwater transport, to predict changes to future Arctic freshwater storage.

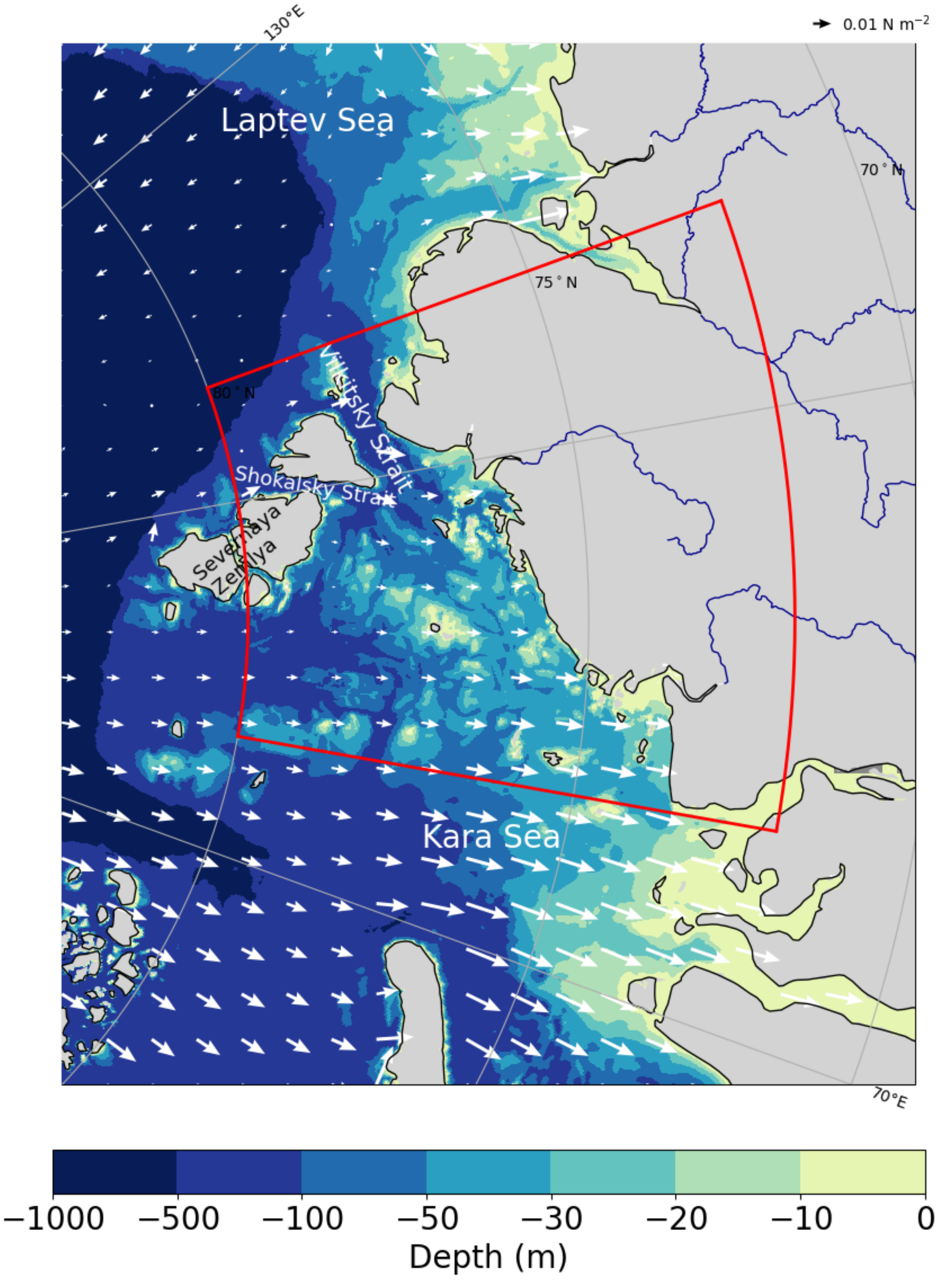

Figure 5.1: Map of Vilkitsky Strait with bathymetry contours overlaid in shades of blue/yellow with mean 2010-2023 ERA5 June-August turbulent surface stress vectors overlaid over the ocean. The box used to calculate Vilkitsky Strait mean eastward/northward turbulent surface stress is overlaid in red.

Hydrographic observations suggest the Ob-Yenisei plume propagates as a narrow (20km) but deep (20 m) plume, with a sharp gradient between the well-mixed fresh plume (< 25 pss) and the adjacent sea water (> 30 pss) (Osadchiev et al., 2020). This sharp salinity gradient is suggested to almost always promote buoyancy driven baroclinic eastward plume transport (Fong and Geyer, 2002; Garvine, 1987). Model simulations suggest this transport is strongest in October to March, with velocities over 0.5 m s^{-1} in winter (Janout et al., 2015).

However, whilst there is almost always some eastward plume transport, the strength of this transport is suggested to be controlled by local wind forcing. It has previously been suggested that northward winds are needed to promote plume propagation, but that alongshore wind over the eastern, rather than central, Kara Sea is most strongly correlated to propagation along the coast (Osadchiev et al., 2020). Whilst there is considerable locally-forced interannual variability in Vilkitsky Strait transport, previous modelling studies have suggested no direct relationship to the AOI or large-scale atmospheric circulation (Bauch et al., 2010; Janout et al., 2015; Rabe et al., 2014).

It was previously suggested that strong, sustained (> 25 days) northeastward winds are required for the plume to reach the Vilkitsky Strait (Osadchiev et al., 2020). Lack of evidence of northward plume transport to the central Arctic Ocean in turn suggests freshwater accumulation in Kara Sea under weaker or westward wind forcing (Osadchiev et al., 2020; Pavlov et al., 1996; Zatsepin et al., 2010). However, seafloor sediments in the region suggest that the plume does not remain in the central Kara Sea long-term (Osadchiev et al., 2023a). It has recently been shown that eastward plume transport can occur over winter regardless of wind forcing (below sea ice), and hence suggested that the plume may be transported into the Laptev Sea over winter each year (Osadchiev et al., 2023a). Whilst this will not be extensively tested here as there are no satellite observations under sea ice, the implications are discussed.

The role of wind stress in controlling transport through the strait has previously been widely suggested from model output and in-situ data. Transport through the strait has also been observed from satellite data (Tarasenko et al., 2021). However, the role of wind stress as a driver of plume transport through the strait has not previously been shown from satellite data. The Vilkitsky Strait is too narrow for non-land contaminated satellite retrievals, SSS just to the east/west of the Strait can provide insight into transport through the strait. Hence, I here use a combination of in-situ, satellite and reanalysis data from this region to investigate if satellite SSS supports the current understanding that wind stress controls the transport of the Ob-Yenisei plume through the Vilkitsky Strait. I first investigate the variability in spatial pattern of SSS in and around the Vilkitsky Strait, particularly under varying zonal wind forcing. I then compare the distribution of SSS across the strait in in-situ, satellite and reanalysis products under eastward and westward wind forcing. I also comment on the roles of Ekman transport and buoyancy forcing in driving this transport and on the representation of transport through the Vilkitsky Strait by reanalyses as compared to satellite and in-situ data.

5.2 Methods

As in the Laptev Sea Chapter, lagged correlations are calculated between GLORYS12V1 SSS and mean June to August eastward and northward turbulent surface stress over the Vilkitsky Strait: 80-110 °E, 72-80 °N for each grid cell (Figure 5.2).

Given the lack of notable correlation patterns found with GLORYS12V1 SST and SIC in the Kara Sea, and to not duplicate analysis unnecessarily, discussion in this chapter of variability in SST and SIC refers to the results from the correlation analysis conducted for the Kara Sea Chapter (section 4.3.2).

Whilst a relatively consistent pattern is visible in the Vilkitsky Strait under Kara and Laptev Sea eastward or westward wind stress, to be consistent with the Laptev Sea and Kara Sea Chapters a new metric is devised for identifying years as eastward / westward (northward/southward) for the Vilkitsky Strait, based on the previous suggestion that transport through the strait does not vary with wind around the central Kara Sea and at the edge of the Ob and Yenisei deltas, but rather that it depends on wind in the eastern Kara Sea, over the Tamyr Peninsula (Osadchiev et al., 2020). This metric is calculated as the mean ERA5 eastward and northward turbulent surface stress over June-August over 72-80 °N and 80-110 °E (red rectangle in Figure 5.1). Using this metric, eastward wind stress is found to be strongest in 2012, 2016 and 2021 and westward wind stress is found to be strongest for 2011, 2015 and 2020 (Figure 5.3). I then calculate eastward (and westward) September SSS composites from the identified three most eastward and westward years, for CCI, LOCEAN SMOS and JPL SMAP and for all four reanalysis products. Individual eastward and westward composites are not shown here as they closely resemble those in both the Laptev and Kara Sea chapters. However, the difference between these composites is then calculated and shown for satellite products (Figure 5.4), for GLORYS12V1 (Figure 5.5, left panel) and for the other reanalyses (Appendix Figure D.1). The same is done for SST for GLORYS12V1 (Figure 5.5, middle panel) and the other reanalyses (Appendix Figure D.2).

The same years are also used to calculate "eastward" and "westward" current velocity composites (for both eastward and northward velocity components) from GLORYS12V1 mean June-August eastward and northward current velocity components.

The surface Ekman current expected from the wind stress is computed for this region according to Equations (1) and (2) (Price et al., 1987). Surface Ekman currents (for z=0 m) are calculated using an Ekman depth (d) of 10 m (roughly equivalent to the mixed layer depth found from in-situ data) and a surface density (ρ_0) of 1020 kg m^{-3} (roughly equivalent to an SSS of 25 pss and SST of 5 °C). The expected surface Ekman current under average eastward and westward wind forcing is then calculated from the mean June-August eastward and northward wind stress for identified most eastward and westward years. This surface current is calculated for each pixel over the Vilkitsky Strait: 80-110 °E, 72-80 °N. These expected Ekman surface currents under eastward and westward wind forcing are then compared with those observed in GLORYS12V1 to visualise the contribution of the Ekman component to the overall surface current (overlaid on Figure 5.5).

Transport of the plume through the Vilkitsky Strait has recently been suggested to occur over winter even after summers of westward (/weak eastward) wind forcing (Osadchiev et al., 2023a). To test this suggestion and determine the impact of summer zonal wind on SSS in the following spring, SSS composites are also calculated for March of the years following the previously identified most eastward / westward years, for all four reanalysis products. Again, the difference between these composites is calculated and shown for GLORYS12V1 (Figure 5.5, right panel) and for all four reanalyses (Appendix Figure D.3).

The same years are also used to calculate "eastward" and "westward" current velocity composites (for both eastward and northward velocity components) from GLORYS12V1 mean September-February eastward and northward current velocity components to estimate the difference in transport between September and March following summers of particularly eastward or westward wind forcing.

September SSS distributions are calculated over the Vilkitsky Strait for both satellite and reanalysis products. To be consistent between satellite and reanalysis products, distributions are only calculated over a region that is sea ice free in all satellite products in all years (region in black in Figure 5.6). This masking is done to ensure sea ice cover variability does not impact the SSS distributions. These distributions are calculated for 1 pss salinity bins and shown as the percentage of the total (sea ice free) area that falls within that salinity bin. To clearly identify the presence of different water masses in this region, the 28 pss and 25 pss isohalines are used to differentiate spreading and non-spreading regimes. These isohalines were chosen as the 28 pss isohaline has previously been used as a threshold for the minimum salinity expected under non-spreading regimes (Osadchiev et al., 2020b). Similarly, the 25 pss isohaline has been used previously in the Kara Sea to denote the presence of the Ob-Yenisei plume (Osadchiev et al., 2020; Tarasenko et al., 2021). Only years with strong eastward (>0.02 N m^{-2}) or westward wind stress (<-0.02 N m^{-2}) are included on plots. This threshold was chosen given the previous suggestion that only strong eastward wind has sufficient force to drive transport all the way through the strait in one summer season (Osadchiev et al., 2020), and as this was around the lowest wind stress that was coincident with low salinities in the strait. The distributions were also calculated for unmasked products (not shown) and are very similar regardless of if products are masked or unmasked, and regardless of whether the products are masked by where that satellite product is sea ice free in all years or where all products are sea ice free in all years.

A similar distribution is also calculated and shown for all in-situ data in the strait (100-115 °E, 77-78.5 °N, red box in Figure 5.6). In-situ data was not masked (to include only the sea-ice free region) prior to plotting to maximise the amount of data used due to the limited amount of in-situ data. Hence, the regional coverage of in-situ data is not consistent across different years shown. However, only in-situ data in the red box is used to try and ensure similar coverage in eastward and westward years. In addition, the similarity in reanalysis distributions when masked (by only where satellite products have data) and not masked suggests water in the central strait is of similar composition to that in the very western Laptev Sea, in the (persistently sea-ice free) masked region.

5.3 Results

5.3.1 Spatial patterns of freshwater transport through Vilkitsky Strait: Findings from Kara and Laptev Sea wind forcing

Both Kara and Laptev Sea spatial correlation plots (in chapters 3 and 4) suggest a significant correlation between June, July and August eastward and northward turbulent surface stress and SSS. Hence, spatial correlations between mean June-August eastward (and northward) wind stress in the Vilkitsky Strait and GLORYS12V1 September SSS are examined to understand the influence of Vilkitsky Strait zonal (and meridional) wind stress in controlling SSS in the Vilkitsky Strait and in the western Laptev.

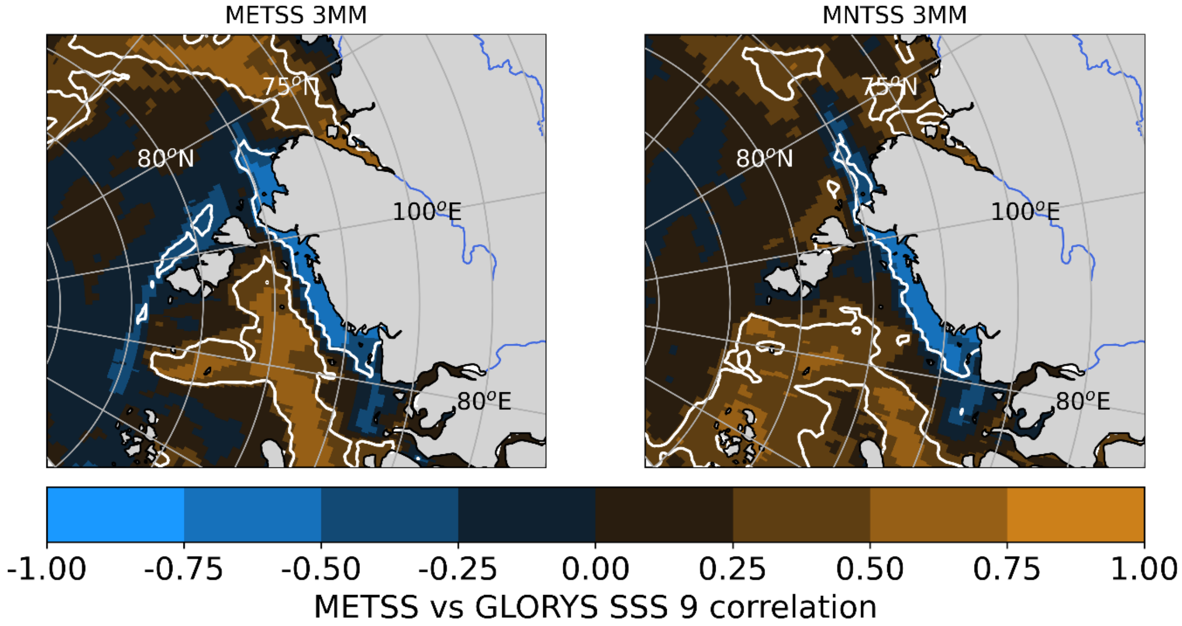

Figure 5.2: Correlation between GLORYS12V1 September SSS and the three-month mean ERA5 eastward turbulent surface stress (METSS) and northward turbulent surface stress (MNTSS) over June to August (6-8) (left) over 1993-2022. Regions where correlations are statistically significant ($p \leq 0.05$) are denoted by the white contour and brighter colours.

A significant correlation pattern is visible between June to August eastward mean wind stress and GLORYS12V1 September SSS over 1993-2023 (Figure 5.2, left). This pattern consists of a dipole correlation pattern with a negative correlation nearshore and a positive correlation offshore. The negative correlation nearshore is very coastally confined and extends from the eastern Kara Sea, through the Vilkitsky Strait and into the western Laptev Sea. The region where this correlation is significant differs with June, July and August eastward wind stress (Kara Sea Chapter 4 Figure 4.2). This significant correlation pattern suggests that mean June to August eastward wind stress is consistent with fresher salinities in the Vilkitsky Strait and western Laptev Sea in September, and higher salinities offshore, particularly in the offshore Kara Sea. Very similar significant negative correlation patterns are also present with Laptev and Kara Sea eastward turbulent surface stress in the southern Vilkitsky Strait (Kara Sea Chapter 4 Figure 4.2, Laptev Sea Chapter 3 Appendix Figure B.2). A small band of negative correlation is also present in a thin band just east of the Severnaya Zemlya Islands, suggesting eastward wind stress is also consistent with lower SSS in this region. Overall, this suggests that eastward wind stress over the Vilkitsky Strait, as well as over the Kara and Laptev Sea, is coincident with fresher SSS in the Vilkitsky Strait and western Laptev Sea. This process will be discussed further in section 5.4.1.

A very similar significant correlation pattern is also visible between June to August northward wind stress and GLORYS12V1 SSS (Figure 5.2, right panel). This pattern consists of a similar thin band of negative correlation which extends along the coast, and a larger region of positive correlation in the offshore eastern Kara Sea. As with eastward wind stress, the band of negative correlation with August northward surface stress extends almost all the way from the mouth of the Ob delta but covers a much thinner region in the Laptev Sea. This correlation pattern suggests that both Kara and Laptev Sea northward wind stress in July and August is consistent with fresher SSS in the Vilkitsky Strait in September, but that northward wind stress is not coincident with fresh SSS in the western Laptev Sea.

No notable correlation patterns are visible between Ob, Yenisei or the ratio of Ob/Yenisei runoff and GLORYS12V1 September SSS in the Vilkitsky Strait. Hence, there is nowhere along the Kara Sea coast that has a significant correlation with runoff. There are also no notable correlation patterns between Lena runoff and GLORYS12V1 September SSS in the Vilkitsky Strait. This suggests Ob, Yenisei and Lena river runoff do not play any role in controlling freshwater transport through the Vilkitsky Strait.

No notable significant correlation patterns are visible between Kara or Laptev Sea eastward turbulent surface stress in June, July or August and GLORYS12V1 September SST in the Vilkitsky Strait. However, a significant positive correlation is present between Kara Sea August northward turbulent surface stress and GLORYS12V1 SST, both along the coast of the eastern Kara Sea and in the western Laptev Sea (Appendix Figure C.2). A notable correlation also appears present between Ob and Yenisei runoff and GLORYS12V1 SST in the Vilkitsky Strait (Kara Sea Chapter Figure 4.4). However, these correlations are expected to be due to autocorrelation with atmospheric forcing (as discussed in section 3.4.1), given the overly extensive region of correlation with Ob runoff and the spatial disparity between the Yenisei delta and the region of significant correlation with Yenisei runoff.

Hence, Ob, Yenisei and Lena runoff have no impact on SSS in the Vilkitsky Strait or western Laptev Sea. Conversely, June to August mean eastward and northward turbulent surface stress are consistent with fresher SSS in the Vilkitsky Strait. However, eastward wind stress is consistent with a larger region of fresh salinities in the western Laptev Sea (as well as through the strait). Only northward wind stress is consistent with increased SST in the Vilkistky Strait and western Laptev Sea.

5.3.2 Spatial patterns of freshwater transport through Vilkitsky Strait: Reanalysis comparison under Vilkitsky Strait wind forcing

A metric of eastward (and northward) wind stress is devised to identify anomalous years of wind forcing and calculate SSS composites for particularly anomalous years. Given June, July and August eastward (and northward) turbulent surface stress appear dominant drivers of variability in GLORYS12V1 September SSS in the Vilkitsky Strait, and to be consistent with the Laptev and Kara Sea Chapters (3 and 4), the mean of these three months is used for this metric (Figure 5.3). The Arctic Oscillation Index (AOI) mean for June-August is also overlaid for comparison. Given the lack of correlation between Lena or Ob/Yenisei runoff and GLORYS12V1 September SSS in this region, no further comparison is made with runoff.

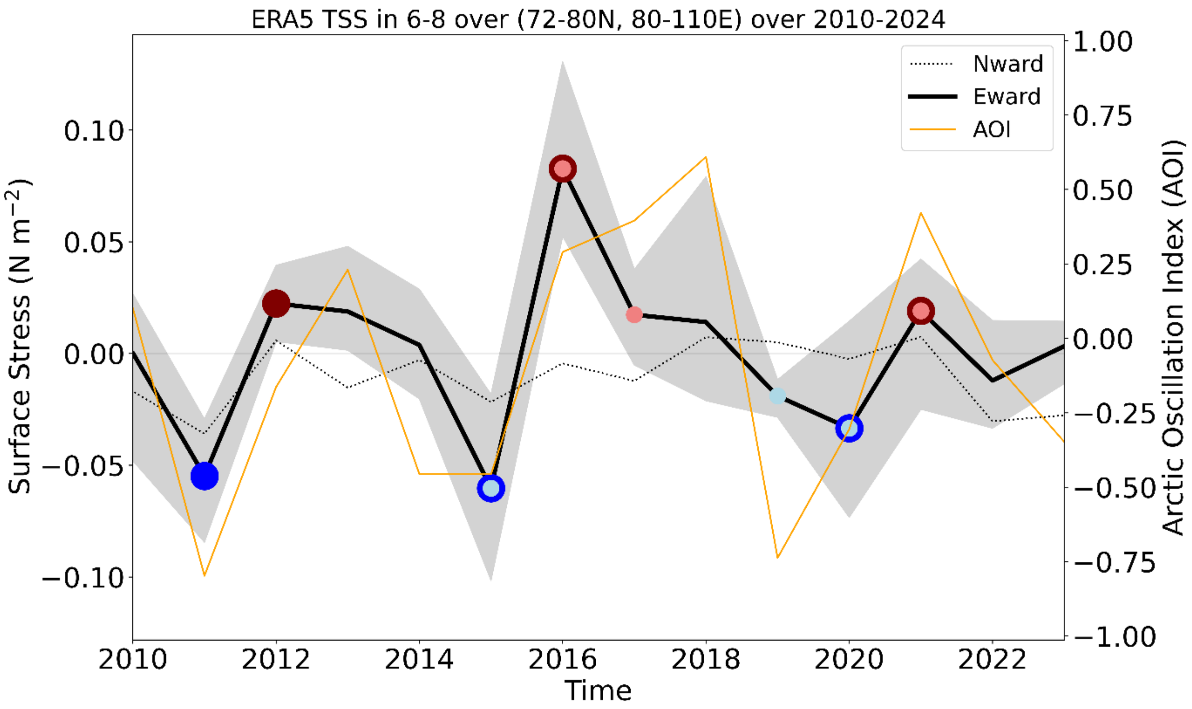

Figure 5.3: Three-month (June to August) mean ERA5 eastward (black solid) and northward (black dashed) turbulent surface stress over 72-80 °N and 80-110 °E. Overlaid are dots indicating the most eastward (red dots) and westward (blue dots) years chosen for analysis for the longer SMOS/GLORYS12V1 timeseries (2010-2023) (darker red and blue dots) and for the shorter SMAP timeseries (2015-2023) (lighter red and blue dots). The range of the maximum and minimum eastward turbulent surface stress between June and August is shaded in grey.

As with the Laptev and Kara Sea, the magnitude of variability in June to August mean eastward turbulent surface stress over the Vilkitsky Strait is larger (range of -0.05 to 0.1 N m^{-2}) than that of mean northward turbulent surface stress (range of -0.03 to 0.01 N m^{-2}) (Figure 5.3). As was true for the Kara Sea, northward turbulent surface stress is almost always negative over the Kara Sea, indicating persistent southward turbulent surface stress. This has previously been suggested to be the dominant wind forcing over this region (Osadchiev et al., 2021b). Eastward turbulent surface stress is weakly, but not significantly, correlated with northward turbulent surface stress over 2010-2022 ($r = 0.44$, $p = 0.11$) and is weakly, significantly correlated over 1993-2023 ($r = 0.38$, $p = 0.03$). Correlations between eastward wind stress and the AOI will be further discussed in the Eurasian Shelf Seas Chapter (section 6.3, p109). The years of highest eastward turbulent surface stress were 2012, 2016 and 2021 over the SMOS period and 2016, 2017 and 2021 over the SMAP period. The years of strongest westward turbulent surface stress were 2011, 2015 and 2020 over the SMOS period and 2015, 2019 and 2020 over the SMAP period.

5.3.2.1 Kara and Laptev Sea composite plots

The identified three most eastward and westward years are then used to calculate eastward and westward composites for LOCEAN SMOS, JPL SMAP and CCI SSS. Individual eastward and westward composites for the Vilkitsky Strait closely resemble those calculated for the Laptev and Kara Sea so to not replicate analysis, discussion of initial eastward/westward composites refers to Kara and Laptev Sea zonal wind composite plots. However, the difference between Vilkitsky Strait composites is shown in Figure 5.4 and discussed below.

Due to the lack of correlation with eastward turbulent surface stress and SST, composites are not re-calculated for the Vilkitsky Strait but the SST composites from the Kara and Laptev Sea chapters are discussed.

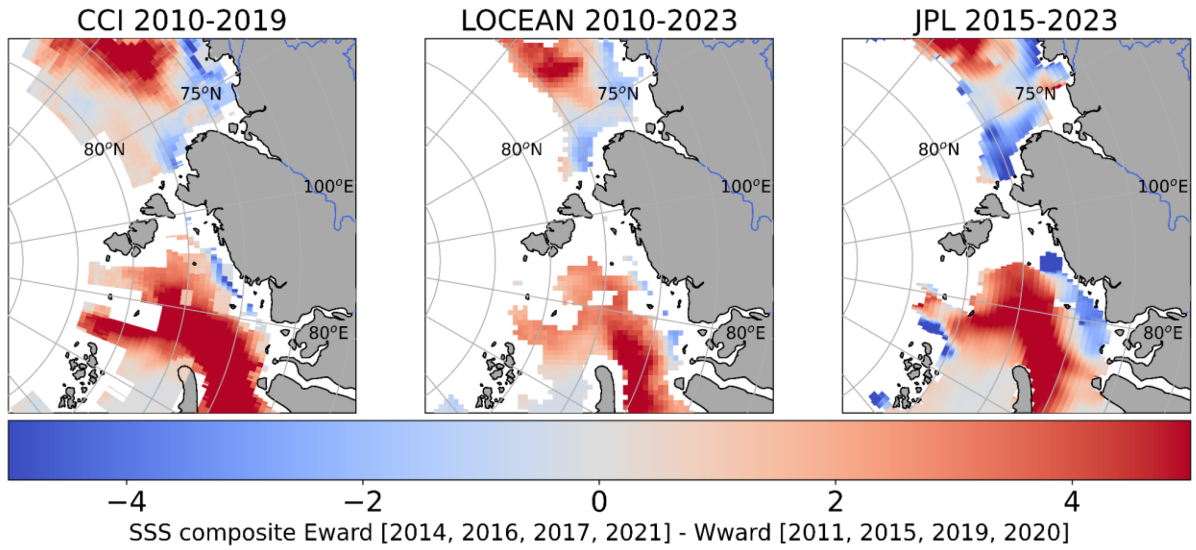

Figure 5.4: The difference between eastward and westward SSS composites calculated for CCI SSS, LOCEAN SMOS, and JPL SMAP, from the identified three most eastward and westward years (over 2010-2023 for CCI and LOCEAN SMOS and over 2015-2023 for JPL SMAP). Regions in blue represent regions with lower salinities under eastward wind forcing and regions in red represent lower salinities under westward wind forcing.

A difference in SSS is visible in the Vilkitsky Strait and western Laptev Sea in Kara Sea eastward and westward SSS composites (Kara Sea Chapter 4 Figure 4.6). In the western Laptev Sea, westward SSS composites suggest almost solely SSS values > 28 pss. In all products, there is also a region of increased salinity (>29 pss) in the eastern Kara Sea, which appears to distinguish the eastern edge of the Ob-Yenisei plume. However, whilst this is clearly visible in most products, including in JPL, CCI and GLORYS12V1, this region of higher salinity is confined to only a few pixels in LOCEAN, due to more extensive masking. Conversely, Kara Sea eastward SSS composites for all products show notable regions of SSS <28 pss in the western Laptev Sea. In some products, including in JPL and GLORYS12V1, the region of low salinity in the western Kara Sea appears clearly separated from the low salinities of the Lena plume. In LOCEAN and CCI, there also appears to be a small separation between the two plumes but this is much less clear. Whilst there is a clear difference in eastward and westward composites in all products, the lack of retrievals in this region, due to land and sea ice contamination, complicate interpretation.

The difference between eastward and westward composites is more clearly visible in Vilkitsky Strait composite difference plots (Figure 5.4). All three products highlight a strong negative anomaly in SSS (of < -2 pss) in the western Laptev Sea, indicating lower values of SSS under eastward wind forcing. Whilst the difference between low SSS values associated with the Ob-Yenisei and Lena plumes are not clearly visible in the eastward composite plots for all products, the composite difference plots for all products show a clear separation between the fresher anomalies associated with the Ob-Yenisei plume in the northwestern Laptev Sea and more saline anomalies in the southwestern Laptev Sea. In JPL, the negative anomaly pattern in the northwestern Laptev Sea appears to extend throughout most of the coastal Kara Sea, through the Vilkitsky Strait and into the western Laptev Sea, although there is a data gap around the

Vilkitsky Strait. The same negative anomaly along the coast is also visible in CCI and LOCEAN products but only very weakly. However, it is worth noting that this signal is clearly visible in the CCI product when the land contamination mask is not applied. A similar pattern in also visible in Kara and Laptev Sea composite and composite difference plots (Laptev Sea Chapter 3 Figure 3.8, Kara Sea Chapter 4 Figure 4.6). In Laptev Sea composite plots, LOCEAN and JPL eastward composites clearly show notable regions of SSS <28 in the western Laptev Sea, and westward plots show a large region of SSS >29 that extends throughout most of the offshore western Laptev Sea. Very similar findings are also visible in Laptev Sea composite difference plots, which also suggest a clear negative anomaly which extends throughout the western Laptev Sea, indicating lower SSS under eastward wind forcing.

Kara Sea SST composites suggest a large negative anomaly over most of the central and eastern Kara Sea and western Laptev Sea. This suggests eastward wind forcing over the Kara Sea is coincident with cool SSTs across almost all the offshore Kara Sea. However, in both GLORYS12V1 and CCI, there is a weaker negative anomaly nearshore in the southern Kara Sea, and a weak positive anomaly in the Vilkitsky Strait. In CCI, this weak positive anomaly is much stronger and larger than in GLORYS12V1, and extends from the eastern Kara Sea, through the Vilkitsky Strait and into the western Laptev Sea. A similar, but stronger positive SST anomaly is also visible in Laptev Sea composite difference plots in the Vilkitsky Strait and very western Laptev Sea. Hence, eastward wind forcing over the Kara or Laptev Sea is consistent with low SSS and high SST in the Vilkitsky Strait and western Laptev Sea.

September eastward and westward SSS and SST composites are then calculated for all four reanalyses, using the previously identified years of most eastward and westward turbulent surface stress. The difference between eastward and westward composites is then calculated and shown for GLORYS12V1 (Figure 5.5 left and middle panels) and for all four reanalyses (Appendix Figure D.1, Appendix Figure D.2). Similar eastward and westward SSS composites are also calculated for all reanalyses for March of the year following the previously identified years of eastward and westward summer wind forcing. The difference between eastward and westward March composites is then calculated and shown for GLORYS12V1 (Figure 5.5 right panel) and for all four reanalyses (Appendix Figure D.3).

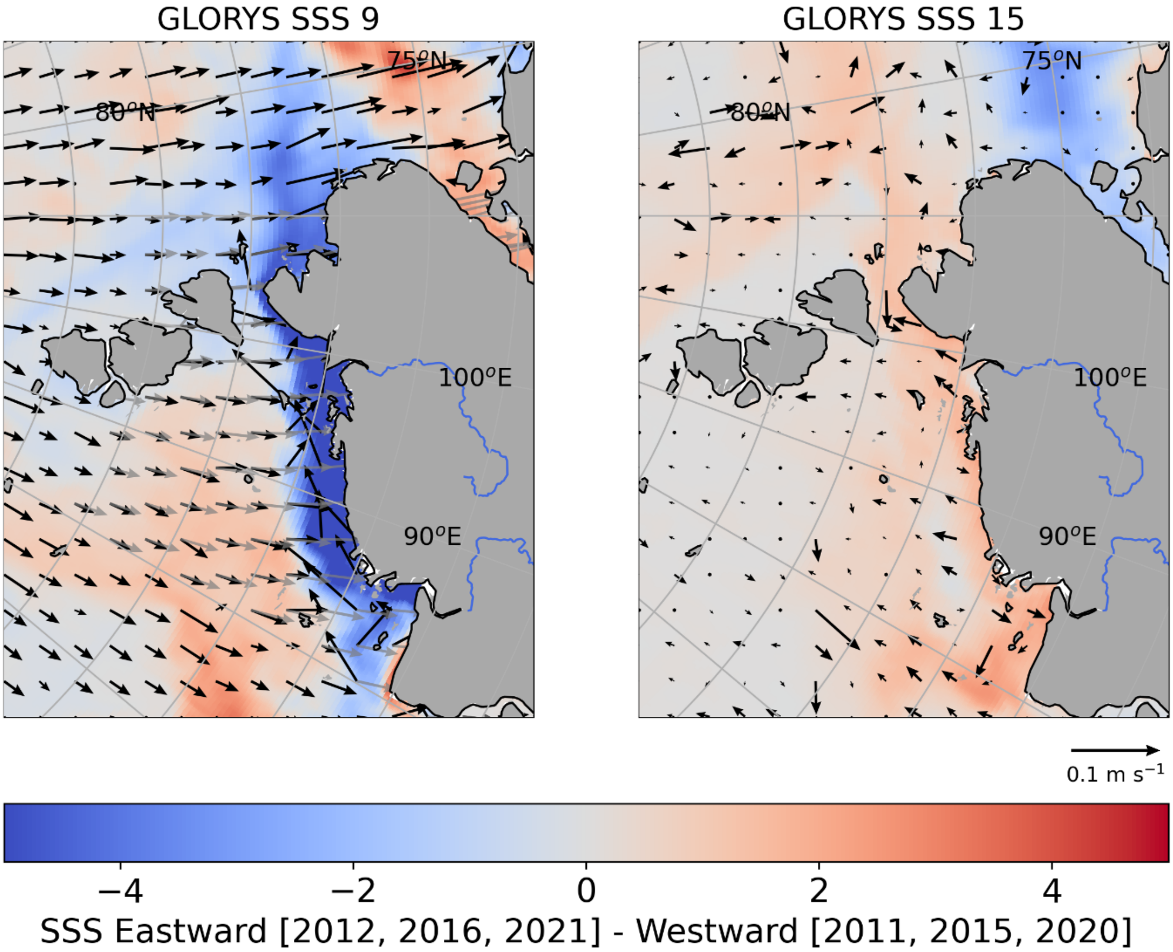

Figure 5.5: The difference between eastward and westward SSS composites calculated for September GLORYS12V1 SSS (left) from the identified three years of most eastward and westward wind forcing (over 2011-2023). The difference between eastward and westward SSS composites for the following March (15) calculated for GLORYS12V1 SSS is then shown (left). Regions in blue represent regions with lower salinities under eastward wind forcing and regions in red represent lower salinities under westward wind forcing. The difference between eastward and westward GLORYS12V1 current velocity composites for June-August are overlaid as black arrows on the September composite difference plot. The difference in expected Ekman surface currents based on observed average eastward and westward wind stress are overlaid as grey arrows for comparison. The difference between eastward and westward GLORYS12V1 current velocity composites for September-February are overlaid as black arrows on the March composite difference plot.

Under eastward wind stress over the Vilkitsky Strait, all reanalyses show a very consistent pattern of fresh anomalies all the way along the Kara Sea coast which extend into the western Laptev Sea (Figure 5.5 left panel, Appendix Figure D.1). The SSS anomalies appears strongest in GLORYS12V1 (and in ORAS), which have large regions with anomalies < -5 pss. The negative anomaly is relatively similar in CGLO and GLOR but is weaker and less extensive. This negative anomaly pattern is consistent with the difference in SSS pattern observed under eastward wind forcing in both the Kara and Laptev Sea. This anomaly pattern suggests that eastward wind stress is consistent with alongshore transport of the Ob-Yenisei plume along the south coast of the Kara Sea and through the Vilkitsky Strait. A positive anomaly pattern is visible offshore in all products, suggesting offshore freshwater transport under westward wind forcing, although this is much weaker than the negative pattern nearshore.

Whilst there is relatively strong agreement between anomalies through the Kara Sea, there is notably different behaviour upon entering the western Laptev Sea. In GLORYS12V1, the negative anomaly extends considerably further eastward than the other products, to above 120 °E. This fresh anomaly is clearly isolated from fresh anomalies along the coast of the Laptev Sea by a salty anomaly that extends from the mouth of the Khatanga River. This salty anomaly is visible in all four reanalysis products both right at the mouth of the Khatanga River and over the southwestern Kara Sea, and is bounded to the south by a fresh anomaly along the coast. These two salty anomalies are connected in both GLORYS products, and extend considerably far offshore. However, in both CGLO and ORAS, these two sections are separated by the fresh anomaly that propagates southward upon entering the Laptev Sea, leaving a small section of salty anomaly right in the mouth of the Khatanga River, and another region in the southwestern Kara Sea. These differences are discussed further in section 5.4.1.2 (p99).

A strong pattern is also visible in the GLORYS12V1 current velocity composite difference plot. This pattern indicates much more southward current velocities over most of the Kara and eastern Laptev Sea under eastward wind forcing than westward wind forcing, indicating onshore transport. These observed differences in surface current closely match the direction of the expected difference in Ekman surface current calculated from wind stress over most of the Kara and eastern Laptev Sea. Whilst they also agree relatively well in magnitude, expected currents tend to be stronger than those observed, potentially suggesting the 10m Ekman depth used to calculate expected currents may be too shallow for much of this region.

However, notable differences in both magnitude and direction of current velocities are present in the nearshore Kara Sea and through the Vilkitsky Strait. The expected Ekman surface current in this region is similar to that further offshore, and suggests onshore current velocities. However, the observed surface current in GLORYS12V1 is much stronger and more eastward or alongshore in direction. These differences suggest that GLORYS12V1 nearshore current velocities are not only driven by the expected differences in Ekman transport.

GLORYS12V1, and all three other reanalyses, suggest a very consistent SST composite difference pattern (Appendix Figure D.2), which is almost exactly the reverse pattern of that visible in SSS composite difference plots. This dipole pattern contains a positive anomaly that is visible all the way along the coast, from the edge of the Ob and Yenisei deltas, through the Vilkitsky Strait and in the western Laptev Sea. This positive anomaly suggests eastward wind forcing is consistent with warm SSTs in the Vilkitsky Strait and western Laptev Sea. Conversely, a negative anomaly is visible offshore in the central and northern Kara Sea, suggesting westward wind forcing is coincident with warmer SSTs offshore.

All reanalysis products suggest there is a difference in the 30% SIC contour under eastward and westward wind forcing, which is relatively consistent across all products. However, this difference is relatively minimal. Under eastward wind forcing, the 30% SIC contour roughly follows the 83 °N parallel north of the Kara Sea but is notably further south in the offshore Laptev Sea, around 80 °N. Under westward wind forcing, the 30% SIC contour is further south (compared to the eastward 30% SIC contour) offshore of the Kara Sea but further north offshore of the Laptev Sea. All reanalyses suggest the 30% SIC contour never reaches the strait, regardless of wind forcing, but also suggest the 30% SIC contour is nearer the Severnaya Zemlya Archipelago under westward wind forcing.

March composite difference plots for GLORYS12V1, and all three other reanalyses, suggest a weak but consistent pattern is visible (Figure 5.5 left panel, Appendix Figure D.3). This pattern is nearly opposite of that visible in September SSS composite difference plots (Figure 5.5) but is notably weaker (differences of ~ 1-2 pss rather than up to 5 pss). This pattern consists of a positive anomaly along most of the coast of the Kara Sea, which extends from the Ob and Yenisei deltas, through the Vilkitsky Strait and into the western Kara Sea. However, whilst the negative anomaly in September composite difference plots is bounded by a positive anomaly offshore, the positive anomaly nearshore in March composite difference plots spreads further offshore and there are almost no regions of negative anomaly over the Kara Sea. This suggests that in the March following a year of westward summer transport, there is anomalous fresh SSS which occupies much of the southern Kara Sea, but also extends through the Vilkitsky Strait. A negative anomaly is also visible in the southwestern Laptev Sea, suggesting the fresh transport visible in September after a summer of strong eastward wind forcing, persists until at least March.

Only very weak patterns are visible in March current composite difference plots, indicating there is no notable difference in current velocities in the September to February after a summer of particularly eastward or westward wind forcing. The notable difference in SSS composite difference despite the lack of notable difference in current velocity composites suggests that the observed difference in SSS is simply due to differences in initial September SSS not differences in surface circulation over winter.

5.3.3 SSS distribution in the Vilkitsky Strait in in-situ, satellite and reanalyses

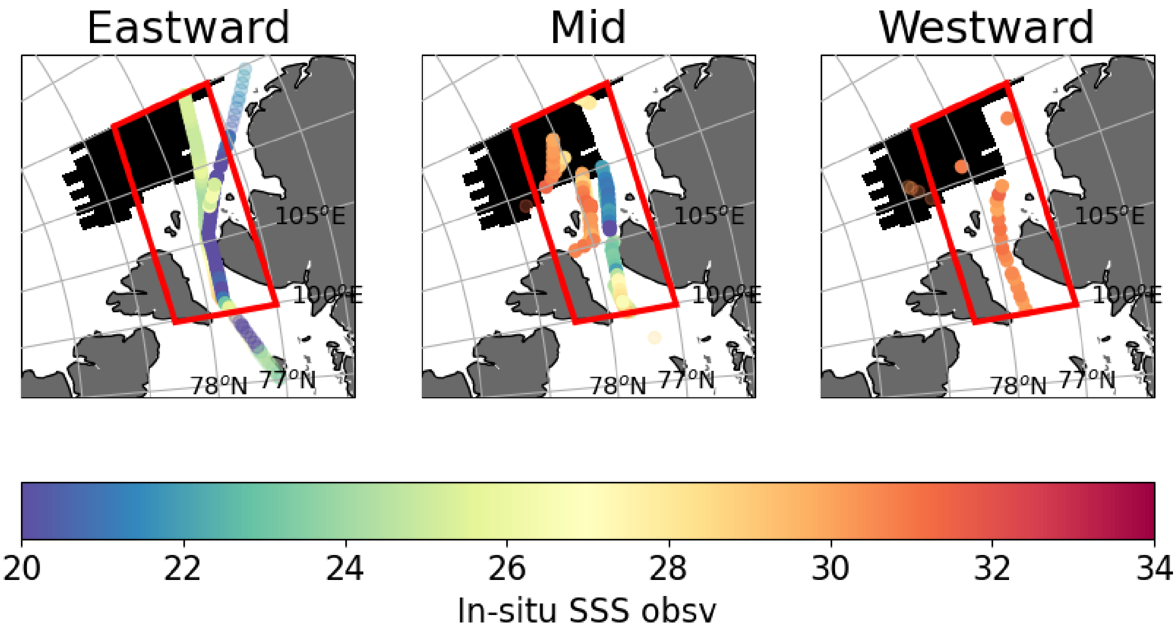

Figure 5.6: Map of available in-situ data present in years of eastward (left), mid (middle) and westward (right) wind forcing. Eastward (/westward) years are identified as having mean zonal wind above (/below) the 0.02 (/-0.02) N m^{-2} threshold. Only in-situ data located in the red box (100-115 °E, 77-78.5 °N) are used for distributions. The masked region of common satellite retrievals is also included and is shaded in black.

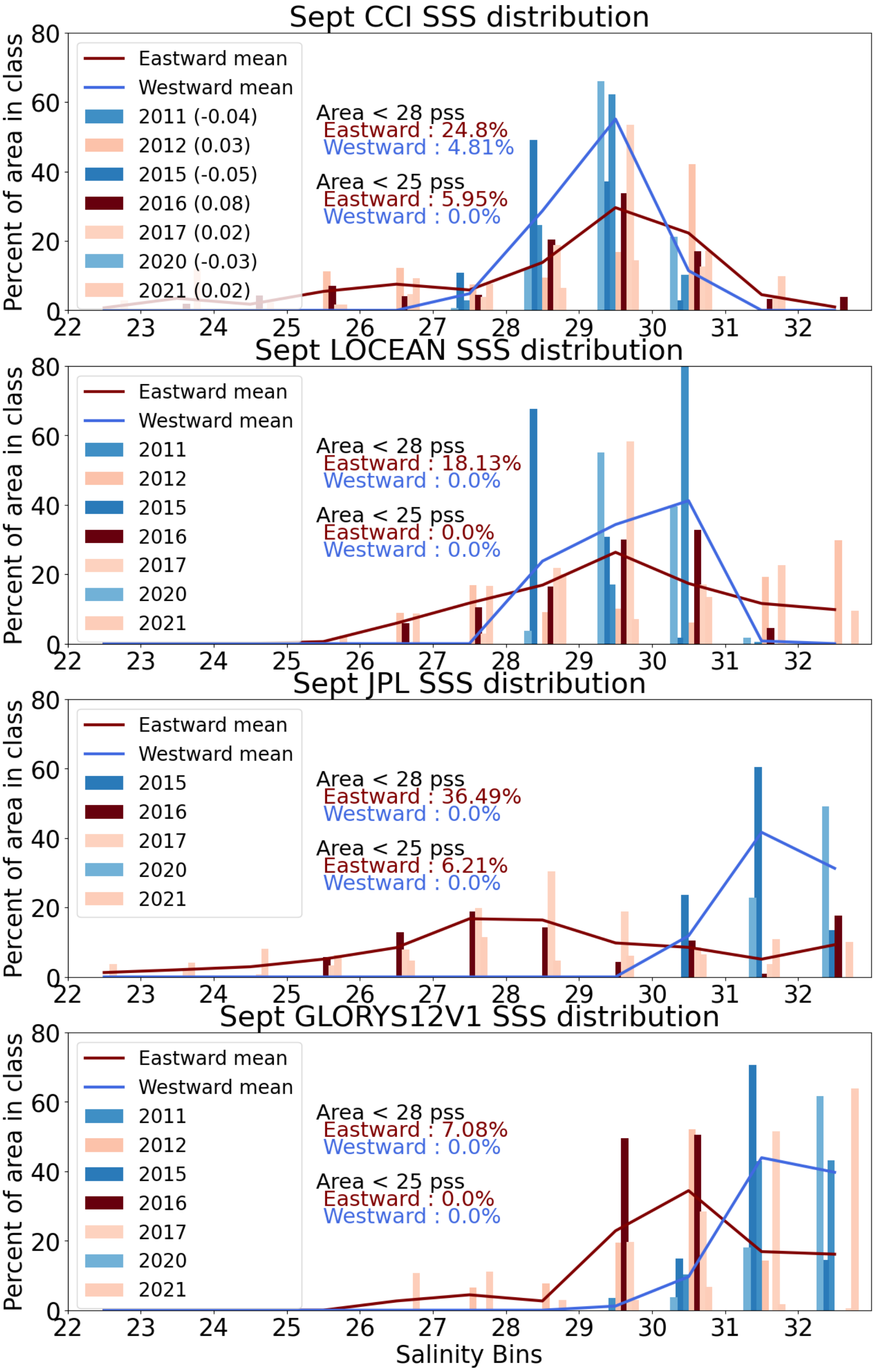

Figure 5.7: Satellite SSS distribution in the Vilkitsky Strait for CCI, LOCEAN SMOS and JPL SMAP and GLORYS12V1 SSS distribution for years of strong (> 0.02 N m^{-2}) eastward (red) and westward (blue) wind stress. The distribution is shown as the percentage of total area in each 1 pss salinity bin over the 22 to 33 pss range. The total area used is the common area where all satellite products have retrievals in all years (shown in black in Figure 5.6). Darker red and blue bar colours indicate years of stronger eastward/westward wind stress. The mean values for all eastward (red) and westward (blue) years are overlaid as lines across all bins. The total percentage of cells below 28 pss and 26 pss in the eastward and westward means are overlaid as text.

There is a notable difference in the distribution of SSS in the Vilkitsky Strait under eastward and westward wind stress, which is relatively consistent across all three satellite products (Figure 5.7, top three panels). The same difference under eastward and westward wind forcing can also be seen in T-S plots for this region (Appendix Figure D.5). Under westward years (including 2011, 2015 and 2020), SSS was above 28 pss across almost all of the Vilkitsky Strait, and was confined to a relatively small number of salinity bins. Conversely, under eastward years (2012, 2016, 2017, 2021), SSS was distributed across the full range of values, from 22 to 33 pss. On average under eastward wind forcing, a significant proportion of SSS is below 28 pss (25% for CCI, 18% for LOCEAN and 36% for JPL). This compares to 5% for CCI, 0% for LOCEAN and 0% for JPL on average under westward wind forcing. On average under eastward wind forcing, a significant proportion of SSS is also below 25 pss (6% for CCI, 0% for LOCEAN and 6% for JPL). This compares to 0% for CCI, LOCEAN and JPL under westward wind forcing.

Whilst there is a consistent shift in distribution between eastward and westward wind forcing between all products, notable differences in distribution were present between satellite products. In CCI, under westward wind forcing, all SSS values were between 27 and 31. On average in CCI, over half (55%) of the total area had SSS values between 29 and 30 pss, with 29% between 28 and 29 pss and 11% between 30 and 31 pss. In LOCEAN, under westward wind forcing, all SSS values over the region were between 28 and 31. On average in LOCEAN, the percent of the total area was highest between 30 and 31 pss (41%), with significant proportions also between 29 and 30 pss (34%) and between 28 to 29 pss (24%) and with almost no years/regions with SSS values outside this range. In JPL, under westward wind forcing, SSS was distributed across notably higher SSS bins, with no values below 30 pss. On average in JPL, the majority (42%) of the total area was between 31 and 32 pss with a significant proportion (31%) above 32 pss and 12% between 30 and 31 pss.

In both CCI and LOCEAN, under eastward wind forcing, the majority of SSS was still in relatively high salinity bins, with the majority of SSS for both products between 29 and 30 pss (30% in CCI and 26% in LOCEAN), and a significant proportion between 30 and 31 pss (22% in CCI and 17% in LOCEAN). In JPL, under eastward wind forcing, 17% of the total area had SSS values between 27 and 28 pss, with 16% between 28 and 29 pss.

The SSS distribution in GLORYS12V1 (Figure 5.7) and the other reanalyses (Appendix Figure D.4) is similar to that in satellite products, and there is a similar level of variability in the distribution pattern between reanalysis products as there is between satellite products. However, whilst all satellite products (Figure 5.7) and the in-situ data (Figure 5.8) show a clear difference in the average SSS distribution under eastward and westward wind stress, this distinction is less clear, or not apparent in the reanalysis products. In addition, most of the reanalyses tend to be biased to higher SSS values than the satellite products or the in-situ data.

Under westward wind forcing (2011, 2015, 2020), all reanalysis products have the highest percentage of the region in high SSS bins. For GLORYS12V1, on average under westward wind forcing, most (84%) of the total area was above 31 pss, with 44% between 31 and 32 pss, and 40% above 32 pss. Under eastward wind forcing (2012, 2016, 2017, 2021), the GLORYS12V1 distribution is shifted to lower SSS values (IE the largest proportions of the total area in lower SSS bins). On average under eastward wind, the majority (34%) of the area has SSS values between 30 and 31 pss, with a significant portion (23%) between 29 and 30 pss, 17% between 31 and 32 pss and 16% over 32 pss.

Whilst the distinction between SSS distribution under eastward and westward wind forcing is less clear in reanalysis products, GLORYS12V1 and most other products still show a difference. Under westward wind forcing, most reanalyses only have SSS values above 28 pss (0% of the total area is below 28 pss for GLORYS12V1), consistent with satellite products and in-situ data. Conversely, under eastward wind forcing, GLORYS12V1 and most other products have a higher percentage of area below 28 pss (7% for GLORYS12V1) than under westward wind forcing. This pattern is consistent with that observed in satellite products. However, whilst satellite products suggest notable regions with SSS < 26 pss under eastward wind, GLORYS12V1 has no regions of SSS < 26 pss. Only the ORAS reanalysis has SSS values < 26 pss under eastward wind forcing and has notably less area in this bin (2%) than most of the satellite products, and the in-situ data.

A very similar pattern of distribution was also visible (in both satellite and reanalyses) when the total area was not restricted to only where all products were sea ice free in all years (and when each product was masked by where that product was sea ice free in all years). A very similar pattern is also visible when SSS distributions are calculated from years of high and low AOI.

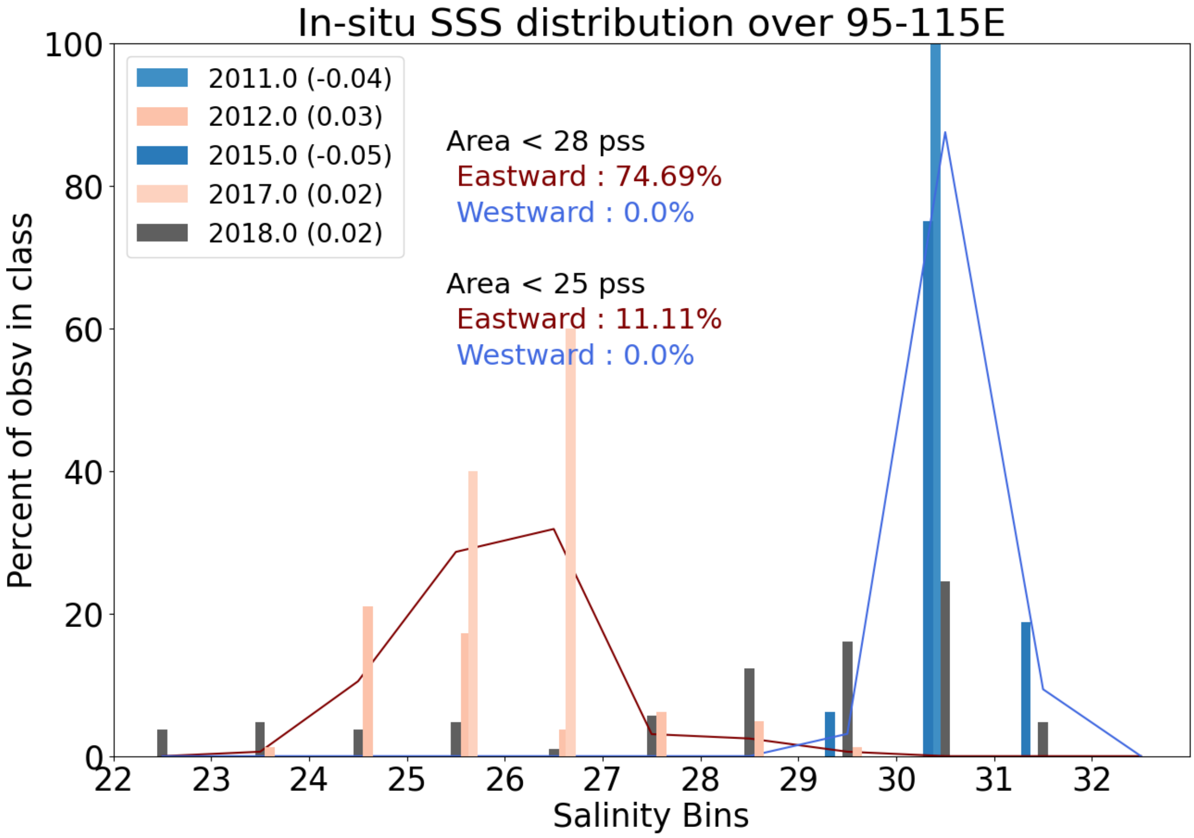

Figure 5.8: In-situ SSS distribution in the Vilkitsky Strait for years of strong (> 0.02 N m^{-2}) eastward (red) and westward (blue) wind stress. Years of mid wind stress (< 0.02 N m^{-2} and > -0.02 N m^{-2}) are shown in grey. The distribution is shown as the percentage of retrievals in each 1 pss salinity bin over the 22 to 33 pss range. Darker red and blue bar colours indicate years of stronger eastward/westward wind stress. The mean values for all eastward (red) and westward (blue) years are overlaid as lines across all bins.

There is a notable difference in the SSS distribution of in-situ data under eastward and westward wind forcing (Figure 5.8). Under westward wind forcing (2011, 2015), all SSS values are above 29 pss (and below 32 pss), with the majority of values between 30 and 31 pss in both years. Conversely under eastward wind forcing (2012, 2017), almost all values are below 29 pss, with the majority of values between 25 and 26 pss. Under eastward wind forcing on average 95% of SSS is below 28 pss and 65% is below 26 pss. Conversely, under westward wind forcing on average 0% of SSS is below 28 (or 26) pss.

The same threshold (of ± 0.02 N m^{-2}) was used to identify years of eastward/westward wind stress in Figure 5.8, for consistency with satellite and reanalysis distributions. However, 2018 is also included and overlaid. In 2018 (wind forcing of ~ 0.02 but below the threshold used), SSS values are widely spread across all salinity bins from 22 to 32 pss. Overall, this suggests that under negative or even weak positive zonal wind stress, no low SSS values < 28 pss are present in this region, suggesting low SSS anomalies are not transported this far east over the summer season. Conversely, under strong positive zonal wind stress, all years have regions of SSS < 26 pss, implying transport of low SSS anomalies through the Vilkitsky Strait. Whilst this pattern is very clear, it is worth noting that there is notably more data in years of strong eastward wind forcing than in years of strong westward wind forcing, which may impact these results. However, the regional coverage of in situ data under eastward and westward wind forcing is relatively consistent (Figure 5.6).

There is relatively good similarity between in-situ and satellite SSS distributions despite the differences in data location, as in-situ data is primarily in the Vilkitsky Strait, compared to satellite data in the western Laptev Sea. The similarity in distribution suggests SSS in western Laptev Sea is a good proxy for transport through the strait. This confirms that differences in SSS observed in satellite data in the Laptev Sea are indicative of changes in SSS in the Vilkisky Strait.

5.4 Discussion

5.4.1 The Vilkitsky Strait as an enabler of freshwater transport / Drivers of transport through the Vilkitsky Strait

The strong role of wind forcing in driving transport through the Vilkitsky Strait has been widely suggested (Janout et al., 2015; Lentz and Fewings, 2012; Osadchiev et al., 2020; Pimenta and Kirwan Jr., 2014). These previous findings are consistent with the strong negative correlation pattern visible in the Kara Sea (Chapter 4) between GLORYS12V1 September SSS and June to August eastward and northward wind stress. The similarity between correlation patterns with both northward and eastward wind stress are unsurprising given their autocorrelation and are consistent with findings in the Kara Sea (Chapter 4) and with previous work (Osadchiev et al., 2020).

Satellite data suggests a clear spatial difference in SSS in both the eastern Kara Sea and western Laptev Sea under eastward/westward wind stress, supporting the dominant role of zonal turbulent surface stress. This is visible from both Kara and Laptev Sea composite and composite difference plots (Chapter 3 and 4), which all have a consistent negative anomaly in the western Laptev Sea under eastward wind stress. All products also suggest this negative anomaly extends almost all the way from the mouth of the Ob delta, through the Vilkitsky Strait and into the western Laptev Sea. Whilst this pattern is most clearly visible in JPL, which has a clear strong negative anomaly most of the way along the coast, more extensive sea ice and land masking in CCI and LOCEAN mean this anomaly is much less clear. Regardless, all products suggest a negative anomaly in the western Laptev Sea.

Whilst data gaps in satellite SSS maps due to land and sea ice contamination complicate interpretation of the spatial pattern of SSS, all satellite SSS products clearly suggest that there is a distinct difference in SSS distribution in the Vilkitsky Strait under eastward and westward wind forcing. The difference in distribution is consistent with that visible from in-situ transects across the region. Eastward wind forcing is consistent with the presence of fresh water (< 28 pss) in the Vilkitsky Strait, implying freshwater transport from the Kara into the Laptev Sea. Conversely under westward wind forcing, almost no fresh water is present in the Vilkitsky Strait, and a larger proportion of higher salinities waters (> 28 pss) are present. This consistent pattern is particularly notable given the considerable differences in average SSS distribution between satellite products. All products, particularly JPL and CCI (along with in-situ data) suggest a considerable percentage of SSS is below 26 pss under eastward wind forcing. The presence of this water with this very fresh signature supports that this is likely Ob-Yenisei plume water, rather than water of other origin (Osadchiev et al., 2020b), and represents a distinct difference from all four reanalysis SSS distributions.

5.4.1.1 Scale of transport and relationship with large-scale atmospheric circulation

The difference in distribution under eastward and westward wind forcing is particularly interesting given the region considered is in the western Laptev Sea, rather than within the strait itself. Transport from the Ob-Yenisei deltas all the way into the Vilkitsky Strait has previously suggested to be possible, although only under strong, sustained alongshore wind forcing (Osadchiev et al., 2020). The very fresh signature of water in this region (the western Laptev Sea) suggests that the Ob-Yenisei plume can propagate all the way through the Vilkitsky Strait and into the Laptev Sea. This very fresh signature also suggests this water to be of Kara Sea origin, rather than from sea-ice or glaciers on the Severnaya Zemlya Archipelago. This water is currently understood to be of Kara Sea origin but the contribution of freshwater from different sources is also discussed further in (section 6.2, p104) (Osadchiev et al., 2023a; Tarasenko et al., 2021).

Whilst the fresh salinities are expected to be of Kara Sea origin, there remains some debate as to if this magnitude of transport can occur over one summer season. It is worth noting that transport all the way through the Vilkitsky Strait and into the Laptev Sea is only shown here to occur in years with average wind stress > 0.02 N m^{-2} over June to August. This strong eastward wind stress is expected to drive onshore Ekman transport. The expected difference in surface Ekman current, visible in the left panel of Figure 5.5, supports this nicely. This difference in surface Ekman current is also in relatively good agreement with the GLORYS12V1 surface current velocity composite difference in most of the Kara and eastern Laptev Sea.

However, in the nearshore Kara Sea, GLORYS12V1 surface current velocities do not agree well with the expected surface Ekman current. In addition, the distance of travel that would occur from the surface Ekman current under this wind stress cannot account for the scale of transport observed (given the ~1200 km distance between the Ob delta to the western Laptev Sea).

Equations (1) and (2) are used here to calculate Ekman surface currents using a latitude of 75 °N and a surface density of 1020 kg m^{-3}. Assuming an Ekman Depth of 20 m (previously suggested as a plume mixed layer depth in this region (Osadchiev et al., 2020)), an eastward wind stress of 0.02 N m^{-2} would equate to a surface velocity of ~ 0.007 m s^{-1} or ~ 50 km of distance traveled over the three-month period)[1]. This Ekman depth was chosen for use here both due to prior use in literature and as expected surface Ekman currents calculated from ERA5 wind stress (using an Ekman depth of 10m) appeared stronger than GLORYS12V1 surface currents (Figure 5.5). Even if the Ekman depth was assumed to be much shallower (5 m), the same wind stress would only equate to a surface velocity of ~ 0.03 m s^{-1} or ~ 200 km of distance travelled over the three-month period, still only 1/5 of the distance observed. Even using a stronger mean eastward wind stress of 0.08 N m^{-2} (as observed in 2016, the year of maximum summer eastward turbulent surface stress) and the shallower Ekman depth of 5m only gives a surface velocity of ~ 0.1 m s^{-1} or ~ 850 km of distance traveled over the three-month period.

$$u_s = -\frac{g}{f\rho_0}\int_{z_0}^{z_s}\frac{\partial\rho}{\partial y}dz \tag{3}$$

The alongshore component of the surface buoyancy current (u_s) was then calculated using Equation (3), given gravitational acceleration (g = 9.81 m s^{-2}) and the meridional density gradient $\left(\frac{\partial p}{\partial y}\right)$. The buoyancy current was calculated for the surface assuming there is no horizontal transport at the base of the mixed layer (using a mixed layer depth of 20m as above). A density difference (∂p) between the freshest bit of the plume under eastward wind forcing (density of ~ 1015 kg m^{-3} for SST of 6 °C and SSS of 20 pss) and the edge of the plume (density of ~ 1021 kg m^{-3} for SST of 4 °C and SSS of 26 pss) of 6 kg m^{-3} occurs over a distance (∂y) of 50 km (or ~2 JPL gridcells in latitude where 1 degree of latitude equates to ~110 km), would result in a buoyancy current of 0.17 m s^{-1}, which would equate to ~ 1300 km of distance traveled over the three-month period. This compares to the buoyancy current under westward wind forcing, where the plume is spread further out (i.e. where a similar density gradient occurs over a distance of ~150 m (or ~6 JPL gridcells in latitude) would give a buoyancy current of 0.05 m s^{-1}, equating to a distance of 400 km over the 3-month period.

Whilst the strength of salinity gradients under eastward and westward wind forcing differ by product, the buoyancy current driven by the difference in meridional salinity gradient is the only thing capable of generating the considerable magnitude of plume movement observed. This finding is consistent with previous suggestions (Osadchiev et al., 2020).The significance of this buoyancy current also explains the much stronger relationship with zonal (rather than meridional) wind stress, which facilitates the horizontal across-shore density gradient observed and drives this buoyancy current. The presence and significance of this buoyancy current (in addition to the surface Ekman current) is also supported by the strong alongshore surface currents visible in the GLORYS12V1 September composite difference plot, and their misalignment with expected difference in Ekman surface current (Figure 5.5).

Freshwater transport through the Vilkitsky Strait is visible under eastward wind stress in the Kara Sea, Laptev Sea and in the Vilkitsky Strait. This pattern is consistent in Kara and Laptev

---

Sea correlation plots and composite and composite difference plots calculated from satellite and reanalysis products using Kara, Laptev and Vilkitsky Strait zonal wind stress metrics. The consistency of this pattern is particularly notable given the different forcing and years chosen for composites in each region. This consistency suggests a level of co-variability in local wind forcing, and fresh water transport, over the Eurasian shelf seas. This suggests a potential role of large-scale atmospheric circulation / the Arctic Oscillation Index (AOI) in controlling Vilkitsky Strait transport. This will be discussed further in the following chapter (p103).

5.4.1.2 Challenges of studying the Vilkitsky Strait

Whilst all reanalyses suggest a notable difference in SSS under eastward/westward wind forcing, which is relatively consistent with that suggested by satellite products, there are several notable differences. The most notable is a considerable disparity in the proportion of SSS above 32 pss which varies between satellite products (Figure 5.7) as well as between reanalysis products (Appendix Figure D.4). This bias is present under both eastward and westward wind forcing but it is more evident under westward wind forcing, when there is a larger area in high SSS bins. Under westward wind forcing, JPL and both GLORYS products suggest the majority of SSS values are greater than 31 pss, with a considerable proportion above 32 pss. Conversely, none of the in-situ data in this region suggests SSS values above 32 pss. For satellite and in-situ data, some of this difference may be related to the location of observations. JPL has observations closer to the ice edge than any of the other products, which might be expected to have the highest salinities. This is supported by the presence of SSS > 32 in LOCEAN and JPL in some years when no sea-ice mask is applied. However, this does not entirely explain the difference, as these more saline anomalies are visible in Kara and Laptev Sea westward composite plots. These more saline anomalies are known to be present both offshore and at depth in this region (Janout et al., 2015) so differences in reanalyses are likely due to circulation differences. However, the presence of these saline anomalies on the shelf warrants further investigation and suggests a need for additional in-situ data in this region to understand what drives this saline water onto the shelf.

The other notable differences between satellite /in-situ and reanalysis SSS distributions is the absence of any very fresh plume waters (< 26 pss) in any of the reanalyses or in LOCEAN SMOS. The lack of low SSS values in LOCEAN may be due to the lack of validation data available and therefore used at very low SSS values (< 25 pss) (Boutin et al., 2024; Supply et al., 2020b). For the reanalyses, both of these differences may be due to overmixing in this region, as has been suggested in both the Laptev and Kara Sea and the wider Arctic (Chapter 3 and 4) (Heuzé et al., 2023; Hudson et al., 2024; Wise et al., 2022). The challenge of accurately representing Arctic freshwater transport is well-known and much work is underway to improve vertical mixing parameterization (Allende et al., 2024; Arpaia et al., 2023). Nevertheless, the poor representation of waters with SSS < 25 pss represents a considerable flaw in reanalysis products' ability to accurately represent freshwater transport around the Eurasian shelf seas. In addition, this may cause the reanalyses to dissipate anomalies in freshwater transport too rapidly, and underestimate the influence of these differences. This will likely only become increasingly important with the additional freshwater input the Arctic is receiving and will continue to receive.

There is some disagreement between reanalyses in the direction of plume transport upon entering the Laptev Sea. Previous transects in this region suggest some mixing of plume towards the Laptev Sea shelf but mostly spreading directly eastward, offshore and over the St Anna Trough. (Janout et al., 2015). This pattern appears to be true in both GLORYS products, as the fresh anomaly extends directly eastward (rather than southeastward along the coast). The fresh anomaly also extends much further east in GLORYS12V1. In both CGLO and ORAS, this fresh anomaly extends to the southeast and remains near the coast. High resolution models and those with an unstructured mesh with ~1/10 ° resolution nearest the coast have been suggested to be needed to accurately resolve transport through the Vilkitsky Strait (Aksenov et al., 2016; Chen et al., 2020; Janout et al., 2015; Proshutinsky et al., 2016). Therefore, it is possible that the better representation by the 1/12 degree GLORYS12V1 reanalysis allows better representation of the Strait's bathymetry and in turn better surface transport because of its higher resolution.

5.4.2 Implications of variability in Vilkitsky Strait transport

Satellite SST has previously been used (often as a proxy for SSS) to study plume propagation, and the warm signature of the plume has been observed to travel through the Vilkitsky Strait (Osadchiev et al., 2020). A very similar composite difference pattern is visible in SST as in SSS, suggesting eastward wind forcing drives a notable increase in coastal SSTs, as well as a decrease in SSS and suggesting co-variability between SSS and SST in the eastern Kara Sea and Vilkisky Strait. This similarity in pattern represents a notable difference from dynamics in the western/central Kara Sea, where SSS and SST did not appear to co-vary (Chapter 4). This highlights the importance of wind forcing in the eastern, rather than central/western Kara Sea in driving alongshore plume transport through the Vilkitsky Strait. This also denotes a considerable difference in regime between the western/central Kara Sea, which is most strongly influenced by inflowing Atlantic Water, and the eastern Kara Sea and Laptev Sea, where differences in plume transport appear to be more of a dominant control on SST.

Whilst there is a level of co-variability between SSS and SST over the Vilkitsky Strait in September, the impact this has on sea ice is minimal and varies between reanalyses. However, it is notable that all the analysed reanalyses products suggest no sea ice in almost any of the strait under eastward wind forcing, suggesting no solid freshwater transport into the Laptev Sea. Whilst there is some variability between reanalyses in very low SIC under westward wind forcing, there is good agreement in sea ice concentration in all reanalyses in the location of the 30% SIC contour. Therefore, despite the notable differences in SST under eastward and westward wind stress, there is no clear difference in sea ice concentration in the Vilkitsky Strait. This represents a notable difference from the Laptev Sea, and likely occurs as there is very little sea ice in the Vilkitsky Strait in September (typically < 15% sea ice concentration), compared to the Laptev Sea where there is a considerable portion of sea ice that remains even in September.

The lack of sea ice in September in this region means there is no sea-ice albedo feedback to intensify/alter the pattern of warming. This may explain the strong consistency between the impact of zonal wind on SSS and SST observed here, and their strong co-variability, which appears even stronger here than that in the Laptev Sea. These differences likely have notable impacts on later winter stratification and sea ice dynamics. This is considered further in (Chapter 4).

Thus far, most of the discussion has revolved around transport under years of particularly strong eastward and westward wind stress. However, freshwater transport through the Vilkitsky Strait has recently been suggested to occur more frequently than previously thought. The presence of fresh water in the eastern Kara Sea in September has been suggested to play a key preconditioning role in winter freshwater transport into the Laptev Sea, as transport in the Vilkitsky Strait is strongest over October to March (Janout et al., 2015). The lack of alternative observed fate of this freshwater (i.e. the lack of observed northward transport to the central Arctic and the lack of sediment evidence that the plume remains in the Kara Sea) has even led to the suggestion that transport through the Vilkitsky Strait may occur most winters (Osadchiev et al., 2023a). The strong role of buoyancy forcing in driving alongshore transport over summer also supports the existence of this winter transport, which cannot be wind driven due to the persistent sea-ice cover in this area over winter. The presence of increased freshwater transport over winter is visible in March in all reanalyses under westward wind forcing. There is also some evidence of additional freshwater in the western Laptev Sea in satellite (and reanalysis) data in early summer of the year following a westward event, which would support the suggestion of winter transport. However, the extensive sea ice and land contamination in this region prevents more thorough investigation in satellite data.

The existence of this winter transport may make these strong summer transport events seem less significant. However, this fresh anomaly appears to clearly persist over winter in the southwestern Laptev Sea and is visible in March in all reanalysis products. This persistence is particularly notable given the lack of representation of low salinities (< 25 pss) and overmixing tendencies of reanalyses, which if anything would imply these anomalies would be even stronger than observed in reanalyses. Whilst these transport events have little impact on September SIC given the lack of sea ice cover in this region, the difference in timing of these transport events appear to have impacts on later sea ice formation (see Chapter 6).

5.5 Conclusion

Satellite, reanalysis and in-situ SSS all support that strong eastward wind sets up a strong meridional density gradient which promotes buoyancy driven transport of the Ob-Yenisei plume through Vilkitsky Strait and into the western Laptev Sea, over one summer season. Whilst GLORYS12V1 and other reanalyses appear to adequately capture freshwater transport dynamics through the Vilkitsky Strait, the poor representation of very low salinities and the overmixing tendencies need addressing for accurate representation of Arctic freshwater transport. Differences in plume transport also have a notable SST signature, which closely resembles that of SSS, suggesting strong co-variability between SSS and SST in this region in September. Despite the co-variability between SSS and SST in this region, zonal wind dynamics do not appear to have a notable impact on September SIC.

Although the zonal wind clearly plays a dominant role in controlling summer freshwater transport through the Vilkistky Strait, plume transport through the strait still appears to occur over winter even in years with no strong eastward wind forcing. However, differences in timing drive very different SSS/SST patterns and in turn stratification dynamics, which appear to persist through much of winter and may impact later winter sea ice formation or melt the following summer.

Chapter 6 Eurasian Shelf Seas

6.1 Introduction to wider Eurasian shelf seas

The Artic Oscillation Index (AOI) is a mode of large-scale atmospheric variability, defined by the sea level pressure difference between the Arctic and mid-latitudes. A low sea level pressure over the Arctic results in a positive AOI, a strengthening of the jet stream and more cyclonic Arctic Ocean circulation resulting in an expanded Eurasian gyre, and a contracted Beaufort Gyre. The influence of the AOI on surface geostrophic circulation is relatively well established (Armitage et al., 2018; Morison et al., 2012). Under positive AOI, the Transpolar Drift is shifted towards the Amerasian Basin, resulting in an expanded cyclonic gyre over the Eurasian Arctic and a contracted Beaufort Gyre (Steele et al., 2004). This is suggested to drive increased Atlantic Water (AW) inflows, decreased Pacific Water inflows and increased freshwater export through the Fram Strait (Armitage et al., 2018; Dickson et al., 2000).

However, there remains debate as to whether this translates to changes in freshwater transport, and to longer term freshwater storage (Cornish et al., 2020; Rabe et al., 2014). This is complicated by the positive phase of the AOI driving increased Atlantic Water inflows and by driving increased sea ice export out of the Fram Strait, which both act to lower the overall Arctic freshwater content (Morison et al., 2021). There is, however, a suggestion that the AOI is not the dominant control over large-scale long-term Arctic-wide freshwater storage (Rabe et al., 2014; Thibodeau et al., 2014). Nevertheless, there is general agreement that the AOI is a strong influence on local wind stress and controls many aspects of Eurasian fresh water transport (Armitage et al., 2018; Lemeshko and Tsyganova, 2022; Morison et al., 2012; Tarasenko et al., 2021). There is also general agreement that positive AOI drives freshwater transport to the Amerasian Arctic where it either increases the freshwater content of Beaufort Gyre or is transported to Canadian Arctic (Morison et al., 2021, 2012; Q. Wang et al., 2021). There is also debate about pathway of freshwater transport under negative AOI. Whilst there is agreement that freshwater first enters Transpolar Drift, it is not confirmed if it's then exported east of Greenland or if it is transported to the Canadian Arctic and exported via Nares Strait (Morison et al., 2012; Q. Wang et al., 2021). There is also discussion as to the role of the AOI over individual regions. There have been multiple studies which suggest the AOI is not correlated with SSS variability in the Kara and Laptev Sea (Dmitrenko et al., 2005; Janout et al., 2015). However, most studies which consider regional and large-scale freshwater transport have been modelling focused or using relatively sparse in-situ data. Hence the relationships over local regions, and over the Eurasian Arctic as a whole will be re-examined here using satellite (and reanalysis) data.

The relationship between the AOI and freshwater transport is becoming increasingly important as the AOI is suggested to be increasingly positive with climate change (Cai et al., 2018; Houssais et al., 2007). These changes have already been linked to increased drought over Siberia and increased risk of Russian wildfires (Churakova Sidorova et al., 2021; Lapenis and Yurganov, 2023). In addition, the Eurasian shelf seas consist of 16% of the total freshwater volume in the Arctic Ocean and there are suggestions this proportion could be decreasing (Hall et al., 2023). It is crucial to better understand the large-scale controls on freshwater transport, and how they appear to be changing, in order to predict future changes and their implications.

The recent SASSIE (Salinity and Stratification at the Sea Ice Edge) field campaign is aiming to test if salinity (in the Beaufort Sea) can be a useful local predictor of sea ice anomalies (Drushka et al., 2024). However, the influence of variability in freshwater transport on sea ice formation (and sea ice melt the following season) has not previously been considered over the Eurasian Arctic. Hence, the potential implications on interannual differences in freshwater transport on sea ice growth (and melt) will be assessed over the Eurasian shelf seas. Previously a link has been made between September SIC in the Russian shelf seas and Eurasian winter air temperature and precipitation, so changes in SIC in this region may have impacts on Eurasian winter climate (Ding et al., 2021; Ding and Wu, 2021; Li and Wang, 2012; Wu et al., 2011).

This chapter will first assess the relationship between local and large-scale circulation in each of the three regions previously examined, as well as how this relationship appears to have been changing in recent decades. The implications of this large-scale coherence on initial freshwater transport will then be identified, as well as the persistence of these freshwater anomalies in the following year. The implications of differences in freshwater transport on sea ice persistence in autumn and in the following spring will be considered. Finally, changes in large scale circulation with climate change will be discussed as well as their implications on freshwater transport and sea ice.

6.2 Freshwater contributions to the Eurasian shelf seas

Over the entire Arctic, annual mean freshwater input is dominated by river runoff (38% or ~3200 km^3), inflow from the Pacific through the Bering Strait (30% or ~2500 km^3) and net precipitation (24% or ~2000 km^3) (Serreze et al., 2006). Whilst Bering Strait inflows to the Arctic does not show a significant seasonal cycle (Jonsson, 1989), a strong seasonal cycle is present in both river runoff and net precipitation. Runoff peaks in spring and 60% of river runoff is discharged between April and July (Lammers et al., 2001). Net precipitation peaks in late summer or early autumn due to seasonality in atmospheric circulation (Walsh et al., 1994). The strong seasonal cycle in sea ice also supplies a considerable volume of freshwater to the surface Arctic in spring and summer (of around 13400 km^3) (Haine et al., 2015). The timing of these inputs plays a crucial role in controlling surface ocean stratification and transport.

The spatial pattern of input also varies considerably by source and equally plays a notable role in controlling the eventual fate of freshwater inputs. Over the central Arctic, fresh water from sea ice melt dominates as the sea ice covered nature means there is no notable direct meteoric water source (other than via transport from other regions) (Alkire et al., 2015). Whilst river runoff is a very localised source of freshwater which forms a very stable water mass and very slowly mixes with ambient seawater, precipitation and sea ice melt contribute freshwater over much larger regions and have larger spatial variability (Osadchiev et al., 2024).

6.2.1 Methods

To understand the respective roles of fresh water inputs, the contribution of different fresh water sources to the overall fresh water content is assessed over the Russian shelf seas. Whilst Pacific Water is typically considered as a freshwater source to the Arctic, it primarily enters into the Amerasian Basin (Bluhm et al., 2015) so will not be considered here. In addition, Russian glaciers are another freshwater source. However, their contribution is only suggested to be ~ 30 km^3 a year (<.004%), and only negligible in comparison to contributions from runoff, sea ice and precipitation (Jakob and Gourmelen, 2023) so they are also not considered here.

The cumulative sum of Arctic Great Rivers Observatory (GRO) runoff of the 12 largest Russian Arctic Rivers (Ob, Yenisei, Lena, Kolyma, Onega, Norther Dvina, Mezen, Pechora, Nadym, Olenek, Yana, Indigirka) is used to estimate the riverine freshwater contribution. The contribution from just the Ob, Yenisei and Lena runoff is also calculated and shown to demonstrate the dominant role of just these three rivers. The drainage area that is covered by gauged rivers only accounts for 61–81% of the total area draining into the Arctic Ocean (excluding the Canadian Arctic Archipelago) (Serreze et al., 2006). Therefore, about a third (19-39%) of the freshwater discharge from land to the Arctic Ocean is not directly measured. Hence, if anything the freshwater contribution estimate from river runoff here is an underestimate of the total freshwater contribution from runoff.

Monthly ERA5 evaporation and total precipitation are used to obtain an estimate of the atmospheric freshwater contribution. The difference between precipitation and evaporation is then calculated for each pixel and each month to obtain the net precipitation. The net precipitation is scaled by the sea ice concentration in each pixel to account for the precipitation that falls on sea ice (rather than directly into the ocean). The cumulative difference is then calculated by summing the difference in each month.

GLORYS12V1 SIC and sea ice thickness are used to calculate the volume change in sea ice and the freshwater contribution from sea ice. First, the sea ice volume in March and September is calculated from GLORYS12V1 sea ice concentration and thickness. The volume change in sea ice is then calculated by differencing sea ice volume in September from that in March. The freshwater equivalent is then calculated from this volume change considering a sea ice density of 900 kg m^{-3} and salinity of 4 pss (Andersen et al., 2019; Mensah et al., 2023; Serreze et al., 2006).

The freshwater equivalent contribution from net precipitation and sea-ice is calculated for all pixels in GLORYS12V1 / ERA5 and then summed over the fresh surface layer and over the plume (see Figure 6.1 for location). The fresh surface layer is defined to be anywhere where GLORYS12V1 SSS is less than 28 pss in September of any year. The plume is defined to be anywhere where GLORYS12V1 SSS is less than 25 pss in September of any year. These two regions were chosen to assess the magnitude of contributors in both the central plume region as well as the wider shelf seas and were intentionally chosen to cover the widest area and include all regions that can be influenced by the fresh surface layer / plume.

6.2.2 Results

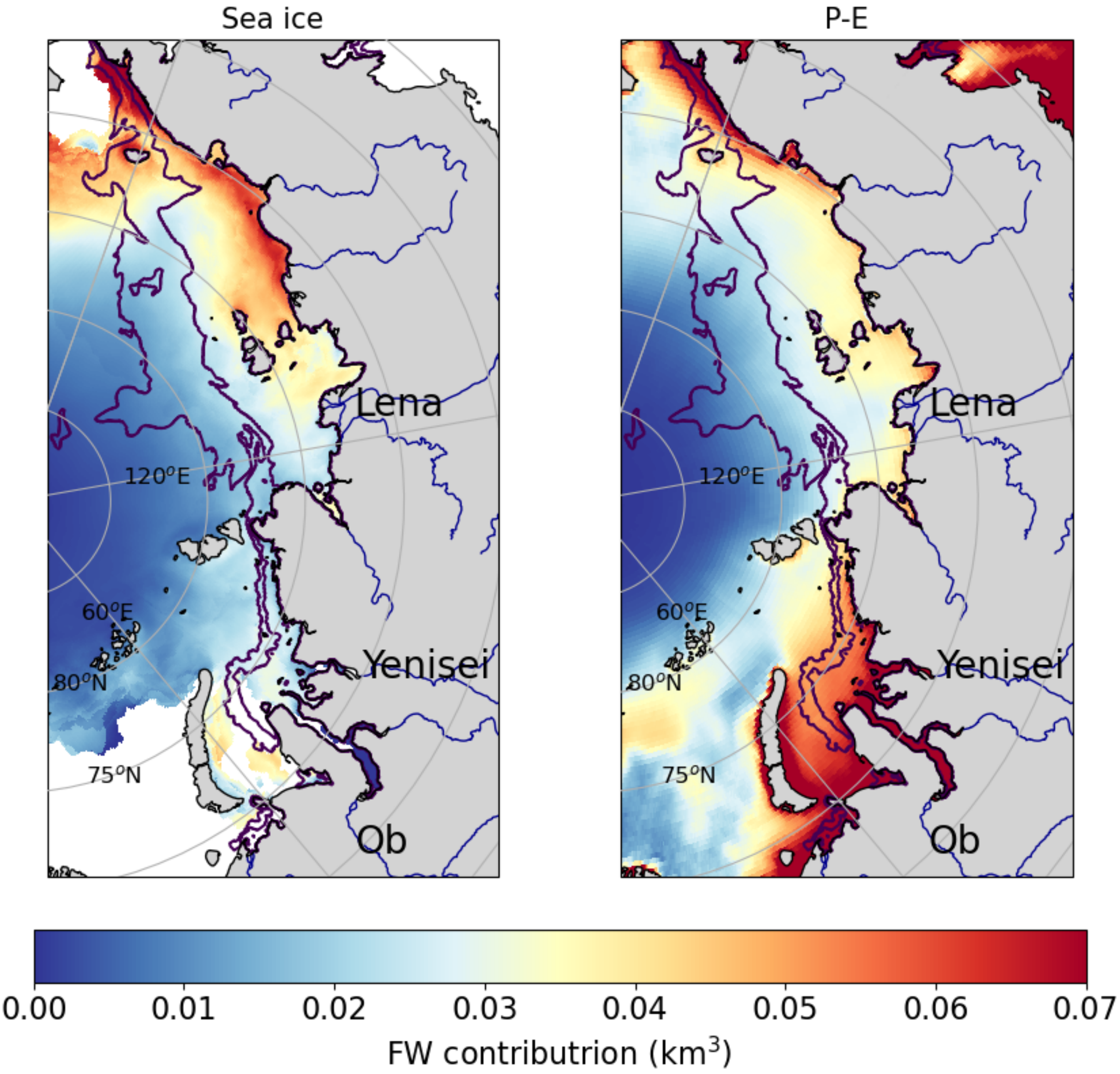

Figure 6.1: Spatial map of the freshwater contribution from sea ice (left) and of net precipitation-evaporation (P-E) (right) over the Russian Arctic. The fresh surface layer and plume regions are designated by the purple contour lines, with the nearer shore contour representing the plume.

Both sea ice and net precipitation provide the largest freshwater contribution to the coast and a much lower contribution to the central Arctic (Figure 6.1). The smaller contribution over the central Arctic likely occurs as persistent sea ice cover prevents a direct freshwater flux from precipitation. Sea ice has a particularly high freshwater contribution in the Laptev and East Siberian Sea (> 0.05 km^3). This contribution is much larger in the Laptev Sea than the Kara Sea, where there is no notable coastal increase in freshwater flux from ice melt. Net precipitation also has a very high freshwater contribution near the coast, but primarily over the southern Kara Sea. When net precipitation is not scaled by sea ice concentration, the pattern remains largely the same but net precipitation values are higher over the central Arctic.

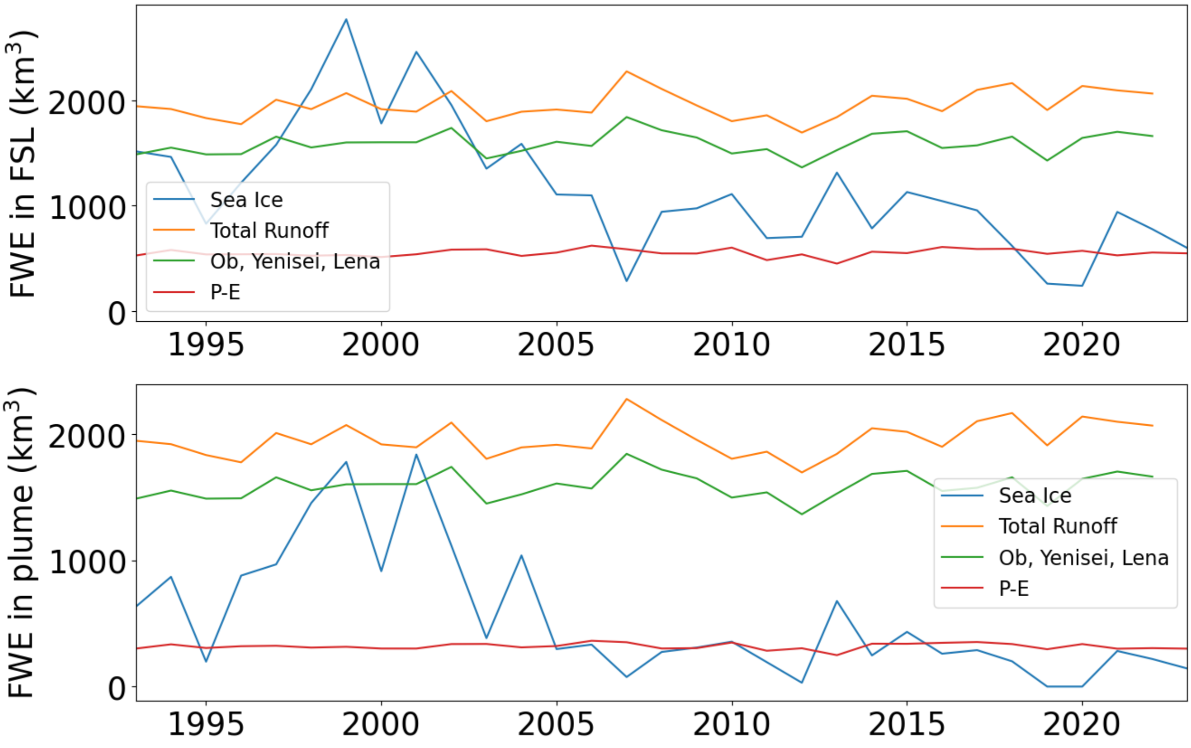

Figure 6.2: Timeseries of the freshwater equivalent from sea ice, runoff from the largest 13 Russian rivers, runoff from the Ob, Yenisei and Lena river and evaporation-precipitation over the Russian shelf seas (top) (where GLORYS12V1 SSS < 28 pss) and over the plume region (bottom) (where GLORYS12V1 SSS < 25 pss)

Over both the fresh surface layer and over the plume area, the freshwater contribution from river runoff generally dominates over other freshwater sources (Figure 6.2). The majority of this runoff comes from Ob, Yenisei and Lena runoff, which make up over 75% of all river runoff to this region. Sea ice also provides a notable contribution to the fresh surface layer but its contribution is notably smaller when confined to just the plume area. The freshwater flux from sea ice also has a notable decrease in contribution over the time period shown. The contribution from sea ice is much larger prior to 2005 at which point the freshwater contribution decreases notably. However, throughout the timeseries, the freshwater contribution from sea ice has a considerable magnitude of variability (STDV = 491 km^3 over the GLORYS12V1 time period, STDV = 173 km^3 over the SMOS period), which is notably larger than that of runoff (STDV = 102 km^3 over the GLORYS12V1 time period, STDV = 104 km^3 over the SMOS period). Interannual variability in net precipitation is very low and notably smaller than that of sea ice or runoff (STDV = 57 km^3 over the GLORYS12V1 time period, STDV = 79 km^3 over the SMOS time period). Net precipitation has a more notable role over the fresh surface layer than over the plume, but this role is relatively minimal in comparison to sea ice and runoff.

6.2.3 Comparison of freshwater contribution to Russian shelf seas and entire Arctic

The area of the fresh surface layer (2.5x10^6 km^2) occupies roughly a quarter of the Arctic Ocean and the plume (1.5x10^6 km^2) around 15% compared to the Serreze et al. (2006) definition of Arctic Ocean area (9.58x10^6 km^2). The relatively small region that constitutes the plume receives around 2/3 of the total river runoff to the Arctic (~2000 km^3 compared to ~3200 km^3 for full Arctic (Serreze et al., 2006)). Conversely, the fresh surface layer receives around 1/4 of total Arctic oceanic net precipitation (~500 km^3 vs ~2000 km^3 (Haine et al., 2015; Serreze et al., 2006)). The fresh surface layer also receives around 15% of Arctic sea ice (2400 km^3 compared to 13400 km^3 over the full Arctic (Haine et al., 2015; Sumata et al., 2023)).

Here, only direct sea ice melt is considered not sea ice transport into / out of the region, as this component of the study is intended as a preliminary comparison of the magnitudes of various freshwater sources. However, sea ice transport has previously been suggested as a significant component of ice thickness change in the Eurasian Basin (Polyakov et al., 2022). This is likely particularly true in the Laptev Sea, where sea ice is likely to be transported offshore by offshore wind, which is typically present over the region in summer (Steele et al., 2004). Whilst there may be some transport of solid ice transport out of the Laptev or East Siberian Sea to the central Arctic, it is unlikely that there will be much transport of solid ice into the Eurasian shelf seas, as the warm inflowing Atlantic Water would likely drive strong melt before it reaches the Kara Sea. However, there may be some import of sea ice meltwater into the Kara Sea, which is not visible here. Regardless, this would likely predominantly influence the offshore Kara Sea, rather than the fresh coastal surface layer.

Little focus is placed here on differentiating the magnitude of contribution each source has to the different regions considered in this thesis (i.e. the Laptev, Kara Sea and the Vilkitsky Strait), as transport between these regions likely represents a considerable source of freshwater, particularly to the Vilkitsky Strait and Laptev Sea. However, the differing contributions to the Laptev and Kara Sea have previously been investigated (Osadchiev et al., 2024). Findings suggest that the contribution from both sea ice melt and runoff are strong in Laptev (up to 30% from sea ice). Conversely, sea ice is suggested to play a much weaker role in the Kara Sea, and runoff is by far the dominant source of freshwater to the Kara Sea. This is consistent with results shown here, which suggest a much stronger contribution from sea ice in the Laptev Sea than the Kara Sea (Figure 6.1). This difference is likely primarily due to the later sea ice melt in the Laptev Sea, causing the peak in river discharge to occur prior to that of sea ice melt, which plays a key role in controlling the larger contribution of sea ice to the plume (Osadchiev et al., 2024). This is particularly true as sea ice melt is only suggested to contribute to the plume if the plume has already spread below sea ice before melt (otherwise sea ice meltwater subducts under river plume rather than mixing with it (Osadchiev et al., 2024). Hence, the freshwater flux to the plume from sea ice melt is (oppositely) correlated with the sea ice state in early summer (Osadchiev et al., 2024). Variability in initial early summer sea ice state may also explain the considerable interannual variability in the contribution of sea ice to the plume region. The current Kara Sea ice contribution may therefore forecast what the future Laptev contribution may be with the loss of the summer sea ice cover.

There is a clear decrease in the freshwater contribution from sea ice melt over the GLORYS12V1 time period (Figure 6.2). A regime shift in sea ice was suggested to occur in 2007 with slowed ice growth in the offshore Laptev Sea following this shift (Sumata et al., 2023). This shift is visible in the freshwater contribution timeseries (Figure 6.2). This may suggest that with the expected ice retreat, sea ice will provide a smaller fresh water contribution to the Russian shelf seas. In addition, sea ice melt is only suggested to contribute to river plumes when the plume has spread under sea ice prior to melt. Hence, earlier sea ice retreat may also minimise the direct freshwater contribution to river plumes, which may result in increased prevalence of a multilayer halocline with a surface plume and subsurface sea ice melt. The complexity of these dynamics and their interactions highlight that it is key to understand changes to timings of sea ice melt and runoff to understand future halocline dynamics.

6.3 Relationship between local and large-scale atmospheric dynamics

6.3.1 Regional correspondence between local and large-scale circulation

The relationship between the June-August AOI and local wind in the three regions analysed (the Laptev and Kara Sea, and the Vilkitsky Strait) is analysed to understand whether or not large-scale circulation is the dominant driver of local wind metrics used in the previous three chapters. Correlation coefficients are calculated for multiple time periods to infer how this relationship appears to be changing over time. These time periods include: the full ERA5 time-period (1950-2023), the start of the ERA5 time-period (1950-1980), the GLORYS12V1 time-period (1993-2023), the start of the GLORYS12V1 time-period (1993-2006) and the satellite period (2010-2023). Scatterplots, and the relevant correlation coefficients, are shown for the Laptev Sea (Figure 6.3), Kara Sea (Figure 6.4), and Vilkitsky Strait (Figure 6.5).

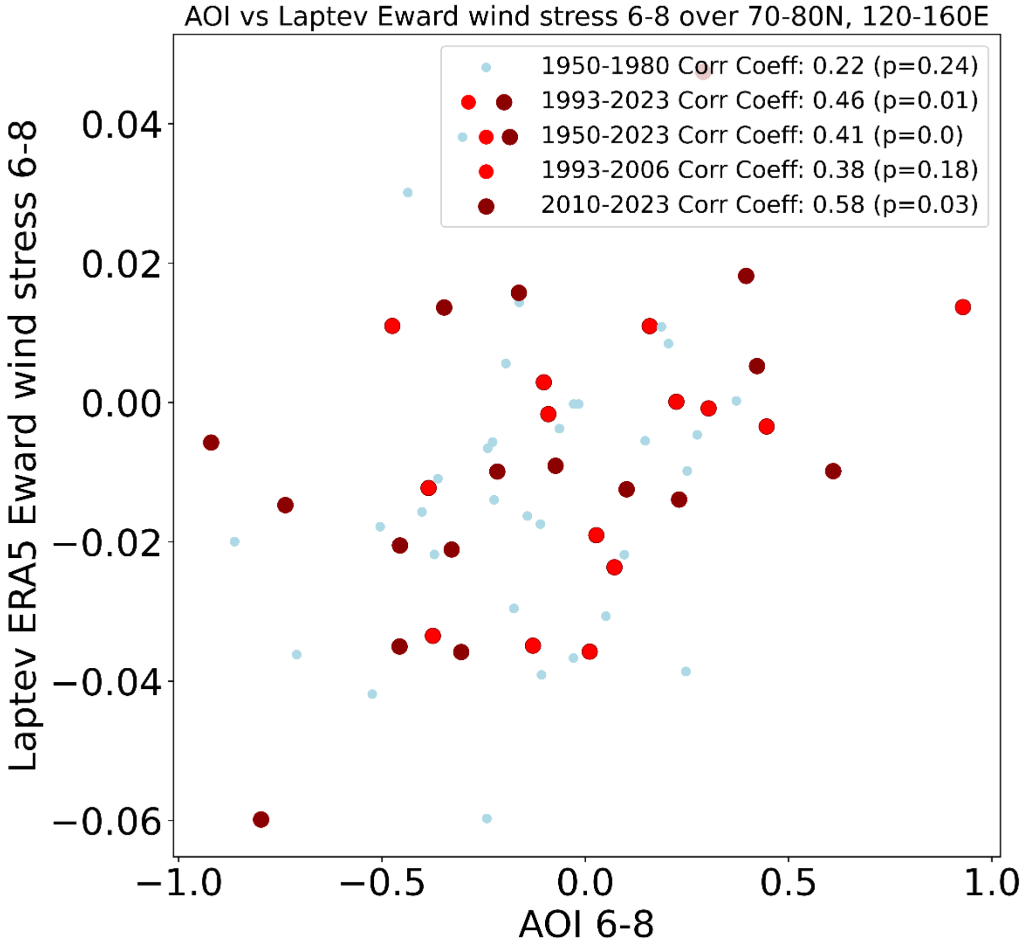

Figure 6.3: ERA5 eastward turbulent surface stress over the Laptev Sea (70-80 °N, 120-160 °E) mean over June to August (6-8) vs Arctic Oscillation Index mean over June to August (6-8). Dots are coloured by year with the smaller blue dots representing the pre-GLORYS period (1950-1980) and the larger red/brown dots representing the GLORYS12V1 period, with the light red dots representing the pre-satellite period (1993-2006) and the maroon dots representing the satellite period (2010-2023). The Pearson correlation coefficients (and their p-values) for the pre-GLORYS12V1 period (1950-1980), the GLORYS12V1 period (1993-2023), the full timeseries (1950-2023), the pre-satellite period (1993-2006) and the satellite period (2010-2023) are shown in the bottom right.

There is a linear positive correlation between the AOI and zonal wind stress in the Laptev Sea over almost all time periods analysed. However, this correlation is only significant ($p < 0.05$) over the full timeseries (1950-2023), over the GLORYS12V1 time period (1993-2023) and over the satellite time period (2010-2023). The Pearson correlation coefficient was higher for the GLORYS12V1 time period (r = 0.46, p = 0.01 over 1993-2023) than over the full ERA5 time period (r = 0.41, $p < 0.01$ over 1950-2023) or over the start of the ERA5 time period (r = 0.22, p = 0.24 over 1950-1980). The Person correlation coefficient was also much higher over the satellite time period (r = 0.58, p = 0.03 over 2010-2023) than over the start of the GLORYS12V1 time period (r = 0.38, p = 0.18 over 1993-2006). Overall, this implies a significant positive correlation between June to August AOI and eastward wind stress in the Laptev Sea, which appears to be strengthening in correlation in recent decades.

No notable correlation is present between AOI and Laptev Sea northward turbulent surface stress over any time period (not shown). There is also no increase in Pearson correlation coefficient over different time periods.

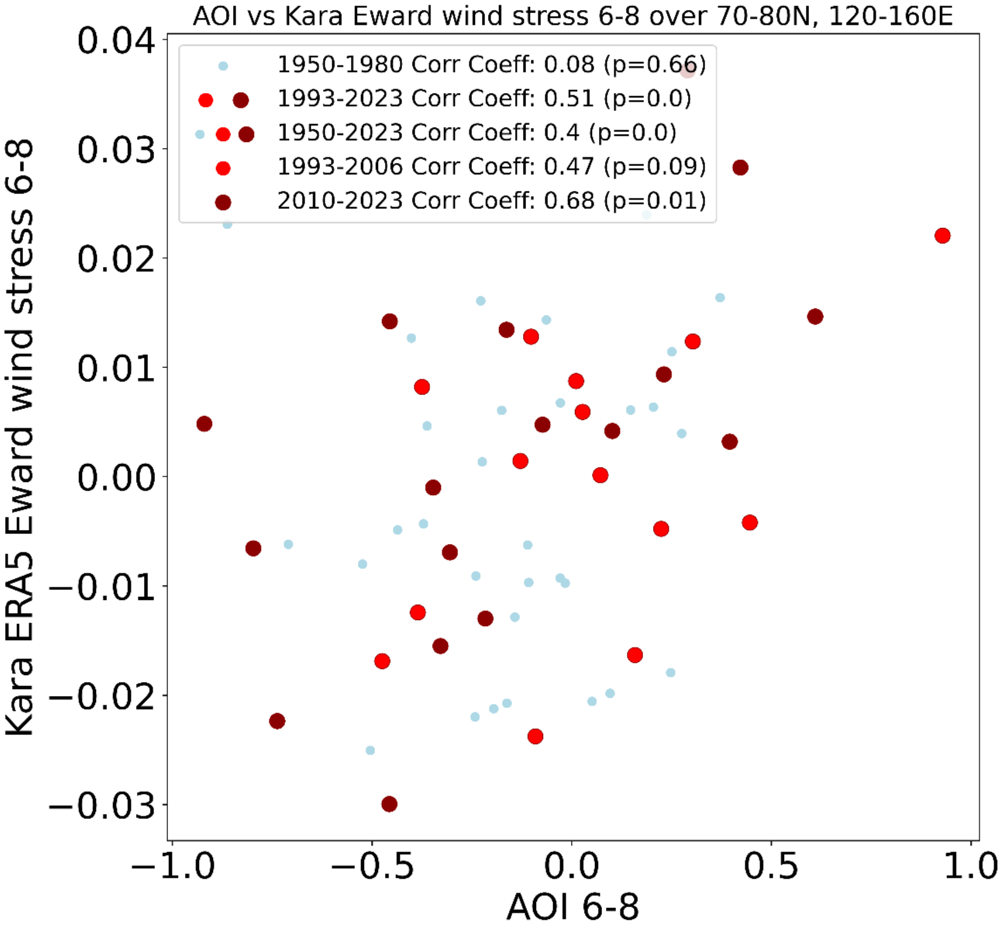

Figure 6.4: ERA5 eastward turbulent surface stress over the Kara Sea (70-80 °N, 60-80 °E) mean over June to August (6-8) vs Arctic Oscillation Index mean over June to August (6-8). Dots are coloured by year with the smaller blue dots representing the pre-GLORYS period (1950-1980) and the larger red/brown dots representing the GLORYS12V1 period, with the light red dots representing the pre-satellite period (1993-2006) and the maroon dots representing the satellite period (2010-2023). The Pearson correlation coefficients (and their p-values) for the pre-GLORYS12V1 period (1950-1980), the GLORYS12V1 period (1993-2023), the full timeseries (1950-2023), the pre-satellite period (1993-2006) and the satellite period (2010-2023) are shown in the bottom right.

There is a linear positive correlation between the AOI and eastward wind stress in the Kara Sea over all time periods analysed (Figure 6.4), consistent with that found with Laptev eastward wind stress. This linear positive correlation is also only significant over the full timeseries (1950-2023), over the GLORYS12V1 time period (1993-2023) and over the satellite period

(2010-2023). The Pearson correlation coefficient was notably higher for the GLORYS12V1 time period (r = 0.51, p < 0.01 over 1993-2023) than over the full ERA5 time period (r = 0.40, p < 0.01 over 1950-2023) or over the start of the ERA5 time period (r = 0.08, p = 0.67 over 1950-1980). The Person correlation coefficient is notably higher over the satellite time period (r = 0.68, p = 0.01 over 2010-2023) than over the start of the GLORYS12V1 time period (r = 0.47, p = 0.09 over 1993-2006). Overall, this implies a significant positive correlation between June to August AOI and eastward wind stress in the Kara Sea, which appears to be strengthening in recent decades.

It is notable that unlike in the Laptev Sea, this same increase in correlation is somewhat visible in the Kara Sea with northward wind stress. The Pearson correlation coefficient was notably higher for the GLORYS12V1 time period (r = 0.51, p < 0.01 over 1993-2023) than over the full ERA5 time period (r = 0.40, p < 0.01 over 1950-2023) or over the start of the ERA5 time period (r = 0.22, p = 0.23 over 1950-1980). The Person correlation coefficient was the similar over the satellite time period (r = 0.61, p = 0.02 over 2010-2023) and over the start of the GLORYS12V1 time period (r = 0.61, p = 0.02 over 1993-2006).

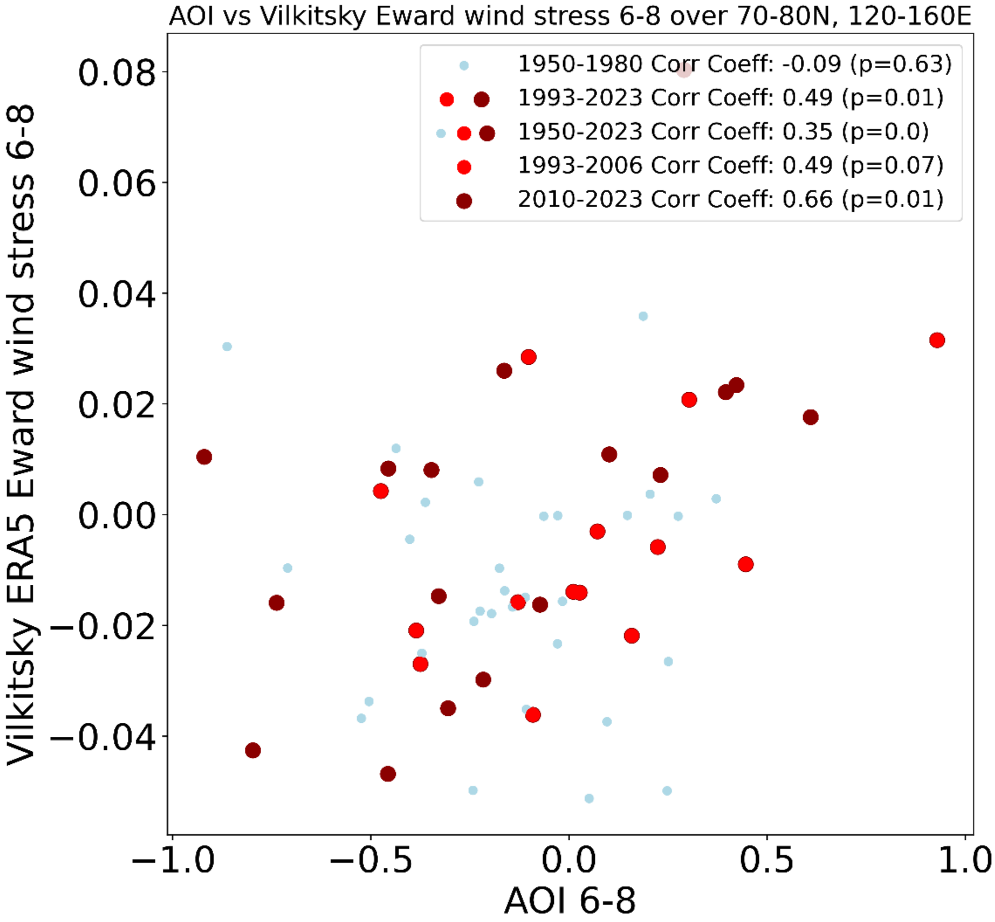

Figure 6.5: ERA5 eastward turbulent surface stress over the Vilkitsky Strait (70-80 °N, 120-160 °E) mean over June to August (6-8) vs Arctic Oscillation Index mean over June to August (6-8). Dots are coloured by year with the smaller blue dots representing the pre-GLORYS period (1950-1980) and the larger red/brown dots representing the GLORYS12V1 period, with the light red dots representing the pre-satellite period (1993-2006) and the maroon dots representing the satellite period (2010-2023). The Pearson correlation coefficients (and their p-values) for the pre-GLORYS12V1 period (1950-1980), the GLORYS12V1 period (1993-2023), the full timeseries (1950-2023), the pre-satellite period (1993-2006) and the satellite period (2010-2023) are shown in the bottom right.

There is a linear positive correlation between the AOI and eastward wind stress in the Vilkitsky Strait for almost all time periods analysed (all except 1950-1980). As for eastward wind stress over the Laptev and Kara Sea, this linear positive correlation is only significant over the full timeseries (1950-2023), over the GLORYS12V1 time period (1993-2023) and over the satellite period (2010-2023). The Pearson correlation coefficient was notably higher for the GLORYS12V1 time period ($r = 0.49$, $p = 0.01$ over 1993-2023) than over the full ERA5 time period ($r = 0.35$, $p < 0.01$ over 1950-2023) or over the start of the ERA5 time period ($r = -0.091$, $p = 0.63$ over 1950-1980). The Pearson correlation coefficient is notably higher over the satellite time period ($r = 0.66$, $p = 0.01$ over 2010-2023) than over the start of the GLORYS12V1 time period ($r = 0.49$, $p = 0.08$ over 1993-2006). Overall, this implies a significant positive correlation between June to August AOI and eastward wind stress in the Vilkitsky Strait, implying positive AOI is associated with more eastward wind forcing. This correlation appears to be strengthening in recent decades.

A weak positive correlation is also visible between the AOI and northward wind stress in the Vilkitsky Strait. However, unlike in the Kara Sea, this correlation appears strongest over the start of the GLORYS12V1 time period ($r = 0.60$, $p = 0.03$, over 1993-2006), and is notably weaker over the satellite period ($r = 0.29$, $p = 32$, over 2010-2023). It is also stronger over the GLORYS12V1 period ($r = 0.39$, $p = 0.03$, over 1993-2023) than over the start of the ERA5 timeseries ($r = 0.23$, $p = 0.22$, over 1950-1980) or over the full ERA5 time period ($r = 0.31$, $p = 0.01$, over 1950-2023).

In summary, a significant positive correlation is present between the AOI and eastward turbulent surface stress in the Laptev and Kara Sea and in the Vilkitsky Strait, suggesting strong correspondence between local and large-scale circulation in all three regions. This correlation also appears to be strengthening in all regions in recent decades. The cause of this strengthening is further discussed in the following section.

6.3.2 Increasing correspondence between local and large-scale wind stress over Eurasian shelf seas

The standard deviation of the AOI increases considerably over the full time period, roughly in line with this increase in correlation strength. The standard deviation of the AOI was higher for the GLORYS12V1 time period (0.42 over 1993-2023) than over the full ERA5 time period (0.36 over 1950-2023) or over the start of the ERA5 time period (0.29 over 1950-1980). This increase in standard deviation suggests the AOI may be getting more variable. A shift to more positive AOI has previously been reported (Cai et al., 2018; Morison et al., 2021) and is likely responsible for this increase in variability.

The standard deviation of eastward turbulent surface stress is also higher over the full GLORYS12V1 timeseries (0.021 for the Laptev, 0.015 for the Kara, 0.026 for the Vilkitsky, over 1993-2023) than over the start of the ERA5 timeseries (0.019 for the Laptev and 0.014 for the Kara, 0.021 for the Vilkitsky, over 1950-1980). The standard deviation of eastward turbulent surface stress is also higher in the satellite time period (0.026 for the Laptev and 0.017 for the Kara, 0.032 for the Vilkitsky, over 2010-2023) than over any other time period. A similar pattern is also present with northward turbulent surface stress in the Kara Sea. The satellite period stands out as having notably higher variability in eastward turbulent surface stress in all three regions than any other time period. However, the very low variability at the start of the GLORYS12V1 timeseries and the similarity in standard deviation over the ERA5 and GLORYS12V1 time periods suggests that there is minimal, if any, increase in variability prior to the satellite time period.

The significant correlation between the AOI and zonal wind stress suggests that the AOI clearly plays a dominant role in controlling local eastward turbulent surface stress in the Kara and Laptev Sea and through the Vilkitsky Strait. This implies large-scale atmospheric dynamics are the dominant control on local wind in the Kara, Laptev and over the Vilkitsky Strait. This follows with the strong correlation between local sea level pressure (SLP) variability and the AOI, which is suggested to be > 0.7 over most of the Eurasian Arctic, and above 0.5 over the whole region (Zhao et al., 2006). This relationship also appears to be strengthening in all these regions in recent decades. The increase in variability in both the AOI and in eastward turbulent surface stress may be partially responsible for the increase in correlation between local wind stress and the AOI. The cause and implications of this increase are discussed further in section 6.7.

6.4 AOI as a common driver of Eurasian Runoff transport

The coherence found here between the AOI and zonal wind implies variability in freshwater transport should be consistent across all three regions. As in previous chapters, for the individual regions considered, composites are calculated from the three identified years of most positive and negative AOI for satellite and reanalysis products to obtain a holistic view of freshwater transport under different modes of the AOI. The three years of most positive AOI were chosen to be 2016, 2017 and 2018 for both the SMOS and SMAP period. Whilst 2021 has a more positive AOI value than 2016, 2016 was chosen in order to use a consistent set of positive AOI years for both SMOS and SMAP products and to be able to calculate lagged composites for the following year (in the following section) as SMAP has no data in September 2022. The use of 2016 rather than 2021 has almost no impact on composite difference pattern. The three years of most negative AOI were identified to be 2011, 2014 and 2019 for the SMOS period and 2015, 2019 and 2020 for the SMAP period. The difference between these composites is then calculated and shown in Figure 6.6 for satellite products and Figure 6.7 for reanalysis products. The same years are also used to calculate positive and negative AOI current velocity composites (for both eastward and northward velocity components) from mean June-August eastward and northward current velocity components for all four reanalyses. Again, the difference between these composites is calculated (overlaid on Figure 6.7). These composite difference plots are then compared with composite difference plots for the Laptev and Kara Sea and over the Vilkitsky Strait to understand differences in freshwater transport under local and large-scale wind forcing.

A principal component analysis is also conducted on GLORYS12V1 SSS in September over the GLORYS12V1 time period (1993-2023). This is compared with the composite difference plots obtained from GLORYS12V1 to investigate whether the interannual variability discussed here relates to a dominant mode of variability in salinity.

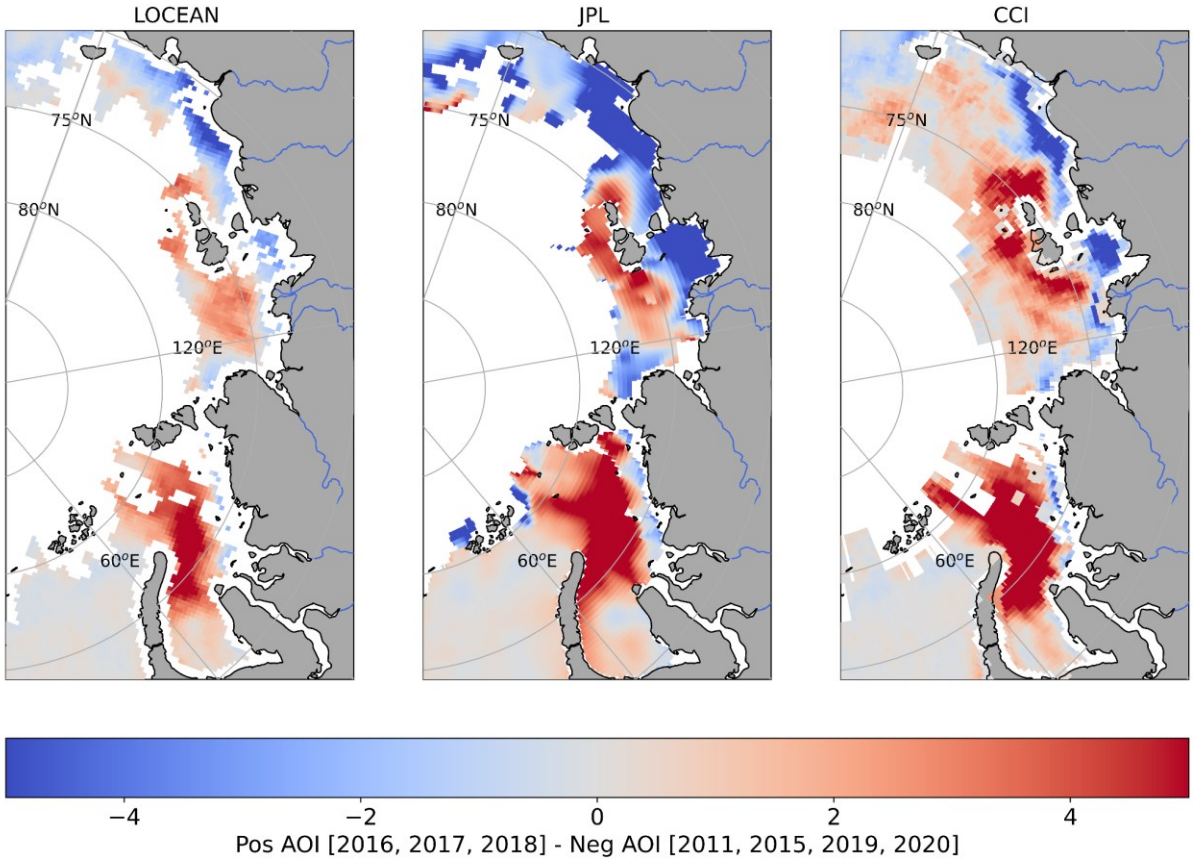

Figure 6.6: The difference between positive AOI (POS) and negative (NEG) AOI composites of September SSS calculated for (left to right) LOCEAN SMOS, JPL SMAP and CCI SSS from the identified three years of highest and lowest June-August AOI (over 2010-2023 for LOCEAN SMOS and CCI SSS and over 2015-2023 for JPL SMAP SSS).

The three satellite SSS AOI composite difference patterns suggest a large region of strong positive anomaly in the central and western Kara Sea and in the offshore Laptev Sea (Figure 6.6). They also all suggest an extensive region of negative anomaly throughout the nearshore Kara, Laptev and East Siberian Sea. The region of positive anomaly is much stronger (> 5 pss) in the central and western Kara Sea than in the Laptev and East Siberian Sea in all three products. Conversely, the region of negative correlation is stronger in the Laptev and East Siberian Sea, particularly in JPL SMAP. This suggests years of high AOI are coincident with alongshore transport of low SSS anomalies and that years of low AOI are coincident with offshore transport of low SSS anomalies, across the entire Eurasian shelf. This constitutes a considerable difference in the locations of Arctic freshwater under positive / negative AOI.

The AOI composite difference plots also resemble the Laptev, Kara and Vilkitsky Strait composite difference plots calculated from Kara / Laptev Sea / Vilkitsky Strait eastward and westward wind. Consistent with the local wind composites, the AOI composites all capture the clear onshore/offshore dipole in the Kara and Laptev Sea and clearly have a negative anomaly in the western Laptev Sea, indicative of transport through the Vilkitsky Strait. Whilst the general pattern of positive and negative anomalies is the same, the patterns visible in local wind composites are notably stronger, particularly in the Laptev and East Siberian Sea. In the Kara Sea, the positive anomaly offshore is also slightly larger in local wind composites, but the negative anomaly nearshore is more visible in the AOI composites. The consistency between local and AOI composites supports that large-scale atmospheric dynamics appear to be the dominant driver of variability in the Laptev and Kara Sea and in the Vilkitsky Strait. However, the weaker patterns in AOI composites suggest that whilst the AOI is a dominant driver of freshwater transport, it does not cause the full range of variability in transport observed.

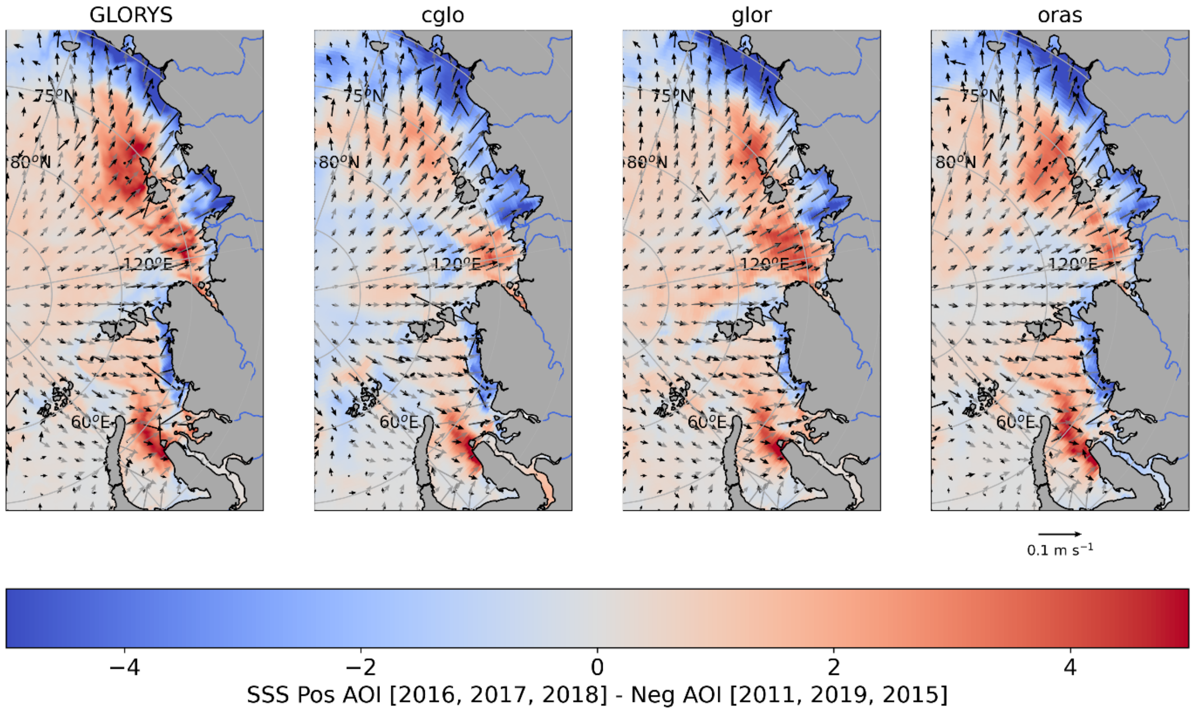

Figure 6.7: The difference between positive AOI (POS) and negative (NEG) AOI composites of September SSS calculated for (left to right) GLORYS12V1, CGLO, GLOR and ORAS from the identified three years of highest and lowest June-August AOI (over 2010-2023 for LOCEAN SMOS and CCI SSS and over 2015-2023 for JPL SMAP SSS). The difference between positive and negative AOI current velocity composites for June-August are overlaid as black arrows on the respective composite difference plots for each reanalysis. The difference in expected Ekman surface currents based on observed average June-August eastward and westward wind stress under positive / negative AOI are overlaid as grey arrows for comparison.

There is relatively good resemblance between AOI composite difference plots in all 4 reanalyses (Figure 6.7). All four products suggest a large region of strong positive anomaly in the central and western Kara Sea and in the offshore Laptev Sea. In the Laptev Sea, there is considerable variability in the magnitude and position of positive anomalies, particularly in the western Laptev Sea and around the New Siberian Islands. Conversely, there is close resemblance between all reanalysis products in the position and magnitude of the positive anomaly in the Kara Sea, which is much smaller and less extensive than that visible in satellite SSS composite difference plots.

All four products also show extensive regions of negative correlation nearshore throughout the Kara, Laptev and East Siberian Sea (Figure 6.7). In all reanalyses, this negative anomaly is by far the strongest (< -5 pss) in the East Siberian Sea. However, unlike in satellite products, this negative anomaly does not continuously extend throughout this region. In particular, transport through the Vilkitsky Strait is only clearly visible in GLORYS12V1. Just south of this, in the western Laptev Sea, all 4 products suggest a positive anomaly nearshore, located at the outflow of the Khatanga River.

All four reanalyses also clearly suggest more southward (or onshore) current velocities under eastward wind forcing than under westward wind forcing throughout the central and offshore Eurasian shelf seas. Nearshore, a strong pattern of eastward (or alongshore) current velocities in the eastern Kara Sea and Vilkitsky Strait and in the East Siberian Sea.

Very similar spatial patterns are found when calculating composites from the three years of maximum and minimum (June-August) AOI (Figure 6.6, Figure 6.7) as when calculating composites from years of maximum and minimum (June-August) zonal surface stress in the Laptev and Kara Sea and over the Vilkitsky Strait (Figure 3.8, Figure 4.7, Figure 5.5). The similar spatial patterns, and strong correlations between AOI and local wind stress reiterate that large-scale dynamics predominantly govern local wind variability and freshwater transport in this region.

The EOFs and principal components obtained from the GLORYS12V1 September SSS are then calculated and shown below (Figure 6.8 and Figure 6.9).

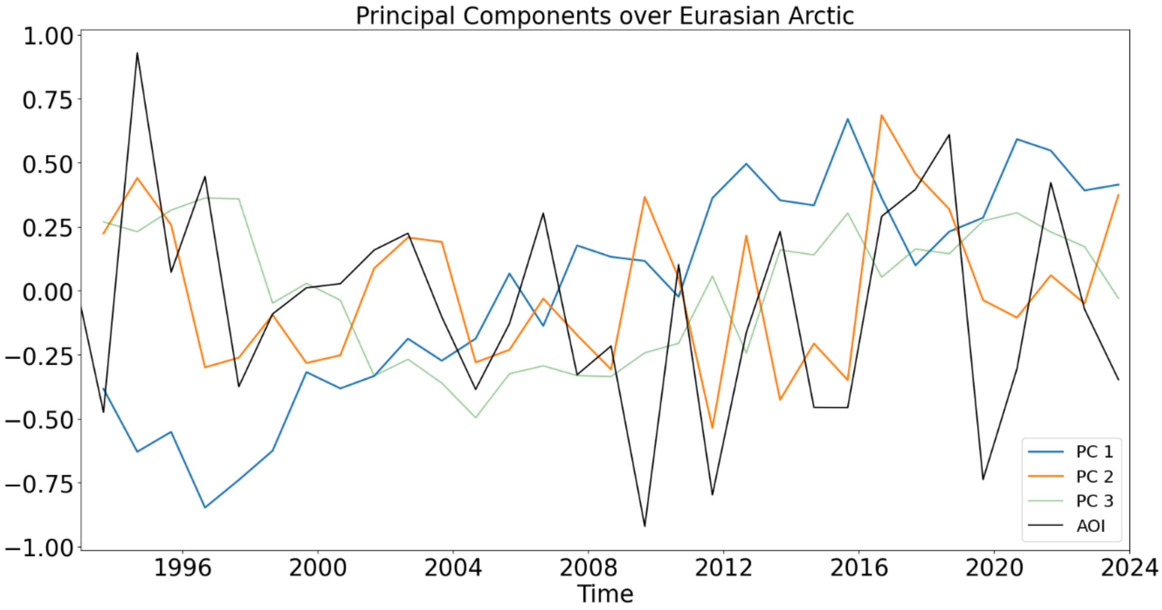

Figure 6.8: Principal components obtained from a principal component analysis (PCA) of GLORYS12V1 September SSS over the Eurasian Arctic (60-90 °N, 0-180 °E). The mean Arctic Oscillation Index (AOI) in June-August is overlaid in black for comparison. The AOI is weakly correlated with PC2 over the full GLORYS12V1 timeseries (over 1993-2023, r = 0.35, p = 0.05) and strongly correlated over the satellite period (over 2010-2023, r = 0.55, p = 0.04).

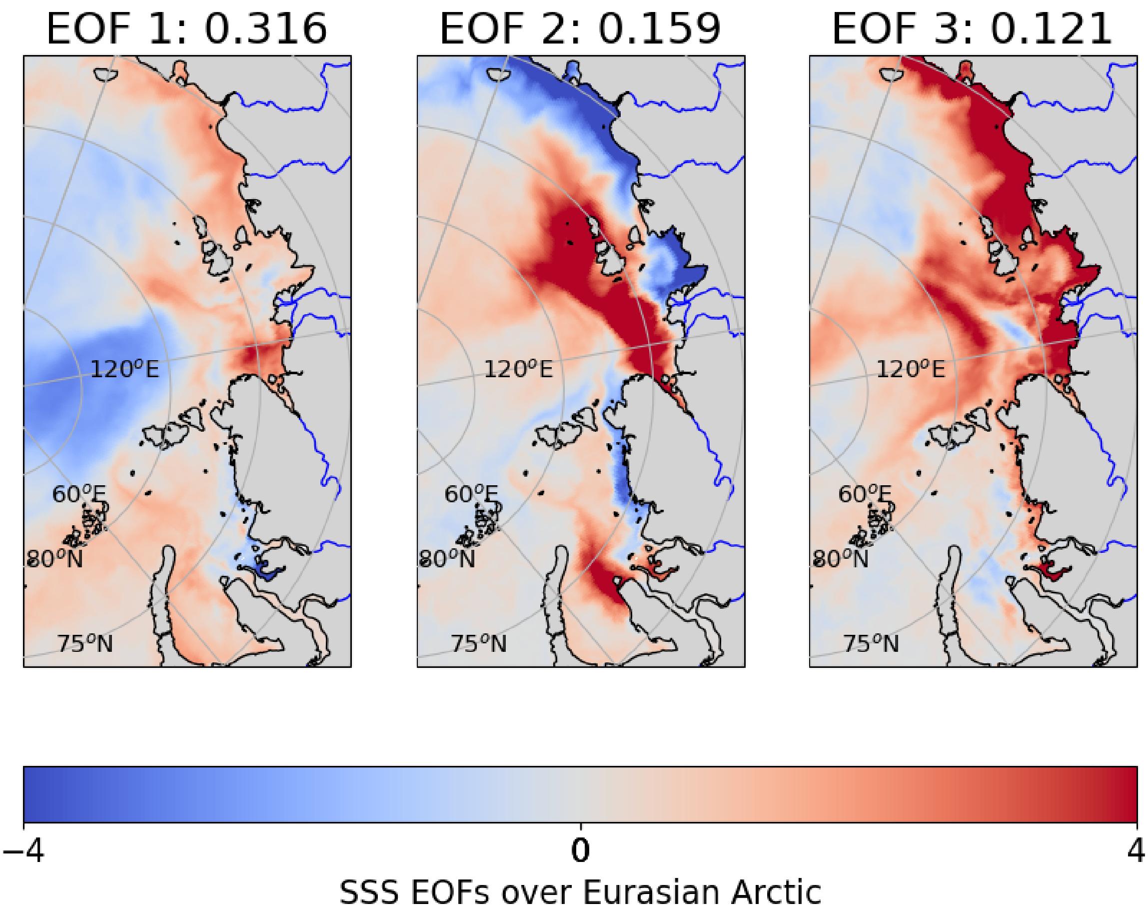

Figure 6.9: EOFs obtained from a principal component analysis (PCA) of GLORYS12V1 September SSS over the Eurasian Arctic (60-90 °N, 0-180 °E) with the percentage of explained variance included in the respective plot title.

The first principal component and EOF suggest a long-term trend in salinity, with increases in salinity over most of the shallow shelves and a decrease in salinity over the central Arctic. The second principal component and EOF represent interannual variability with a strong onshore/offshore dipole pattern in the Kara, Laptev and East Siberian Sea. The third principal component and EOF represent a form of decadal variability, with a strong positive anomaly across most of the nearshore Eurasian shelf seas, but is particularly strong in the Laptev and East Siberian Sea.

The long term trend in salinity on the Russian Shelf, indicated by the first principal component and EOF, has previously been widely reported as Arctic Atlantification / Borealization (Bertosio et al., 2022; Polyakov et al., 2020a, 2017b; Wang et al., 2024). The decreasing salinity on the Russian shelves and the freshening offshore suggests there is long-term redistribution of freshwater around the Arctic. This is consistent with suggestions that there is ongoing change in Arctic freshwater storage causing a decrease in freshwater content of the Russian Arctic and an increase in freshwater content of the Amerasian Arctic (Hall et al., 2023; S. Wang et al., 2021).

The second EOF pattern also closely matches the large-scale AOI difference pattern in GLORYS12V1 (and other satellite and reanalysis) SSS composite difference plots over the Eurasian Arctic (Figure 6.6, Figure 6.7) and in individual regions (Figure 3.8, Figure 4.8, Figure 5.4, Figure 5.5). The spatial patterns of the SSS composite difference pattern and the second EOF are also strongly correlated (r = 0.82, p = 0). Overall, this supports that this SSS difference pattern is the dominant mode of interannual variability in Eurasian Arctic SSS.

The June-August AOI is also weakly correlated to the second principal component over the full GLORYS12V1 timeseries (over 1993-2023, r = 0.35, p = 0.05) and strongly correlated over the satellite period (over 2010-2023, r = 0.55, p = 0.04). This correlation supports that the summer AOI is a dominant driver of this mode of interannual variability.

The key role of the AOI in controlling local eastward wind stress and the dominant role of eastward wind stress in controlling surface current velocities and freshwater transport in both the Kara and Laptev Sea has key implications for large-scale Arctic (short-term) freshwater transport. The composite difference pattern visible here is consistent with the current understanding of the variability in geostrophic transport under positive/negative AOI (Armitage et al., 2018; Morison et al., 2012). Under positive AOI, the cyclonic circulation in the Eurasian Arctic is expanded, driving freshwater transport along the coast of the Eurasian shelf seas (Morison et al., 2021). This promotes transport of the Ob-Yenisei plume through the Vilkitsky Strait and transport of the Lena plume towards the East Siberian Sea, so freshwater at least initially remains in the Eurasian Arctic. Conversely under negative AOI, the cyclonic circulation is contracted and the start of the Transpolar Drift is shifted to start in the offshore Laptev Sea, which promotes offshore/northward freshwater transport. This freshwater from the Laptev and East Siberian Sea then enters the Transpolar Drift, and is more rapidly exported from the Eurasian Arctic.

There is little to no observational (in-situ or satellite) evidence that suggests Ob-Yenisei plume derived waters can be directly transported northwards into the Transpolar Drift, despite this being inferred from modelling studies (Aksenov et al., 2011; Nummelin et al., 2016; Rabe et al., 2014). However, there is evidence of Ob-Yenisei derived waters underneath Lena-derived waters in the Transpolar Drift (Paffrath et al., 2021). Ob-Yenisei derived waters are suggested to enter the Transpolar Drift from the northwestern Laptev Sea (under low AOI conditions), the year after traveling through the Vilkitsky Strait. This emphasises the vital role of the Vilkitsky Strait in controlling freshwater exchange along the Eurasian shelf seas, and in particular the timing of transport into the western Laptev Sea, which will impact the plume's location the following year. This mechanism also highlights transport in the Laptev Sea as a key pathway controlling riverine freshwater exchange (of Ob, Yenisei and Lena runoff) between the Eurasian and central / Amerasian Arctic. This also explains the stronger and/or more extensive coastal negative freshwater anomaly in the Laptev Sea (Figure 3.8) (compared to the Kara Sea (Figure 4.7)) in composite difference plots, which may be due to the cumulative effects of eastward transport of the Ob-Yenisei plume (from previous year(s)) into the Laptev Sea as well as of the Lena plume.

This pathway emphasises the vital role of the Vilkitsky Strait as the only known pathway of freshwater transport from the Kara Sea. Whilst a relationship between basin-scale freshwater transport and local wind has been suggested, previous studies have suggested no relation between the AOI and transport through the Vilkitsky Strait (Bauch et al., 2010; Janout et al., 2015). However, the difference in both surface current velocities and in salinity distribution under eastward and westward wind stress (Chapter 5 Figure 5.5) is highly consistent with that visible under positive and negative AOI. This suggests a clear difference in freshwater transport. These results suggest the AOI causes a notable difference in the salinity of transport through the Vilkitsky Strait, even if the magnitude of transport itself remains relatively consistent. This contradicts the previous suggestion that regional conditions dominate Siberian freshwater pathways given the Vilkitsky Strait regulates freshwater transport between the west and eastern Eurasian Arctic (Bauch et al., 2010). However, whilst pattern of freshwater/heat transport is relatively consistent under positive/negative AOI and eastward/westward wind stress (over the Vilkitsky Strait), it does appear notably stronger when considering the relevant local wind metric.

Whilst the representation of individual regions in reanalyses is discussed more extensively in the relevant individual chapter, it is worth re-iterating here that the analysed reanalyses products do not seem to represent Kara Sea plume appropriately, which appears too small and too confined to the western Kara region. This may be partially due to the lack of interannually varying river runoff forcing, which has been suggested to play a role in controlling the extent of the Ob-Yenisei plume, particularly when it is transported into the central/western Kara Sea (section 4.4.3, p74). In addition, whilst reanalyses appear to be able to replicate transport through the Vilkitsky Strait, there are considerable differences in the western Laptev Sea, which may relate to reanalysis resolution. Given the demonstrated importance of this region in controlling freshwater storage/export from the Eurasian Arctic, poor representation of this region presents a major flaw in the ability to accurately represent Arctic wide freshwater transport. Improved representation of both the Kara Sea plume and of circulation in the western Laptev Sea are needed for accurate portrayal of current and predictions of future freshwater transport.

6.5 Longer term freshwater storage

To investigate the impacts that this difference in freshwater transport has on longer term freshwater storage, composites were also calculated for September of the year following the previously identified years of positive and negative AOI. The difference between the positive and negative composite is shown in Figure 6.10 for satellite products and Figure 6.11 for reanalysis products. Current velocity composites (for both eastward and northward velocity components) are also calculated for the period between these two Septembers from mean September-August eastward and northward current velocity components for all four reanalyses. Again, the difference between these composites is calculated (overlaid on Figure 6.11).

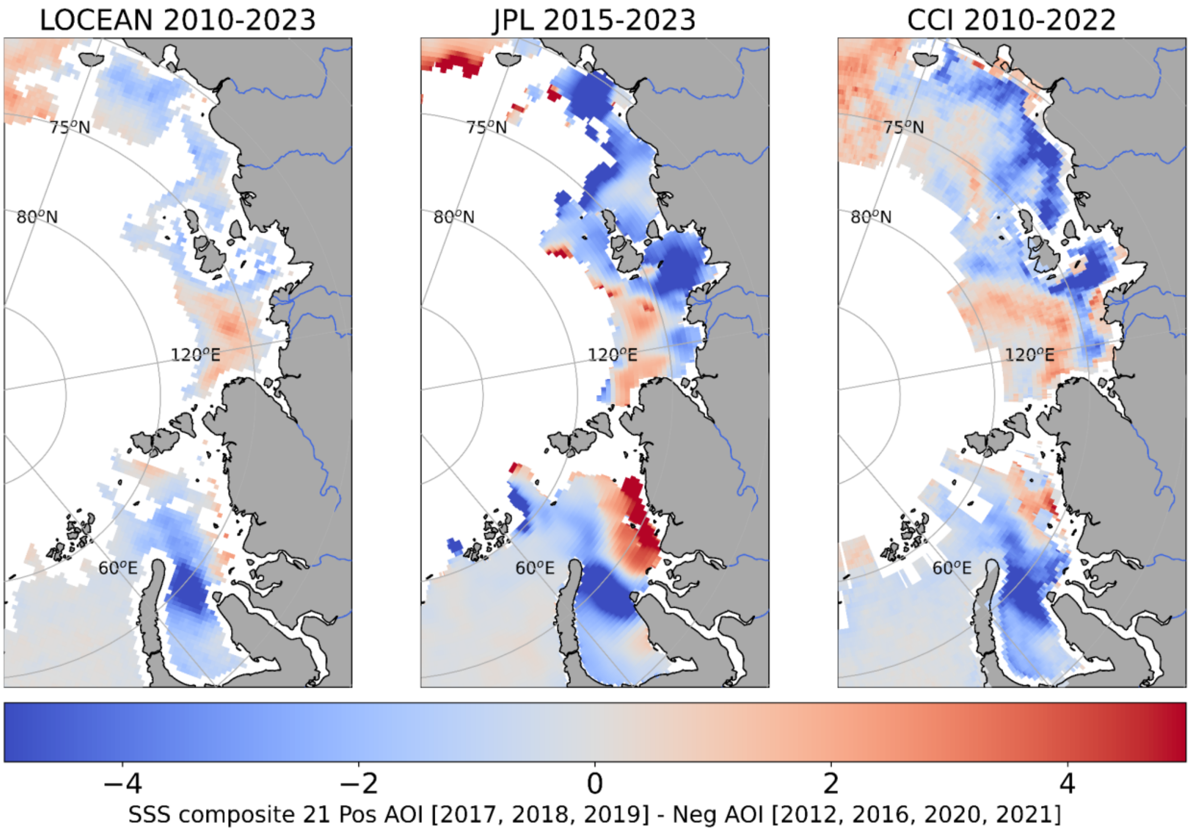

Figure 6.10: The difference between positive (POS) and negative (NEG) AOI composites calculated for (left to right) LOCEAN SMOS, JPL SMAP and CCI SSS for September of the year following the identified three years of highest and lowest June-August AOI (over 2010-2023 for LOCEAN SMOS and CCI SSS and over 2015-2023 for JPL SMAP SSS).

All three satellite products show a relatively consistent pattern in lagged composite difference plots for the year following the years of highest and lowest AOI (Figure 6.10). This pattern is similar but weaker than the pattern visible in the non-lagged composite difference plots (Figure 6.7). This pattern consists of a strong region of negative correlation in the eastern Laptev and East Siberian Sea, particularly nearest the coast. They then have a positive anomaly in the eastern Kara Sea and in the offshore western and central Laptev Sea. Just west of this, there is a notable region of negative anomaly in the western Kara Sea. Whilst this pattern is visible in all satellite products, the magnitude of these positive and negative anomalies differs by product. Both positive and negative anomalies tend to be much stronger in JPL and CCI compared to in LOCEAN, particularly the positive anomaly in the nearshore eastern Kara Sea and the negative anomalies in the southern Laptev Sea and western Kara Sea.

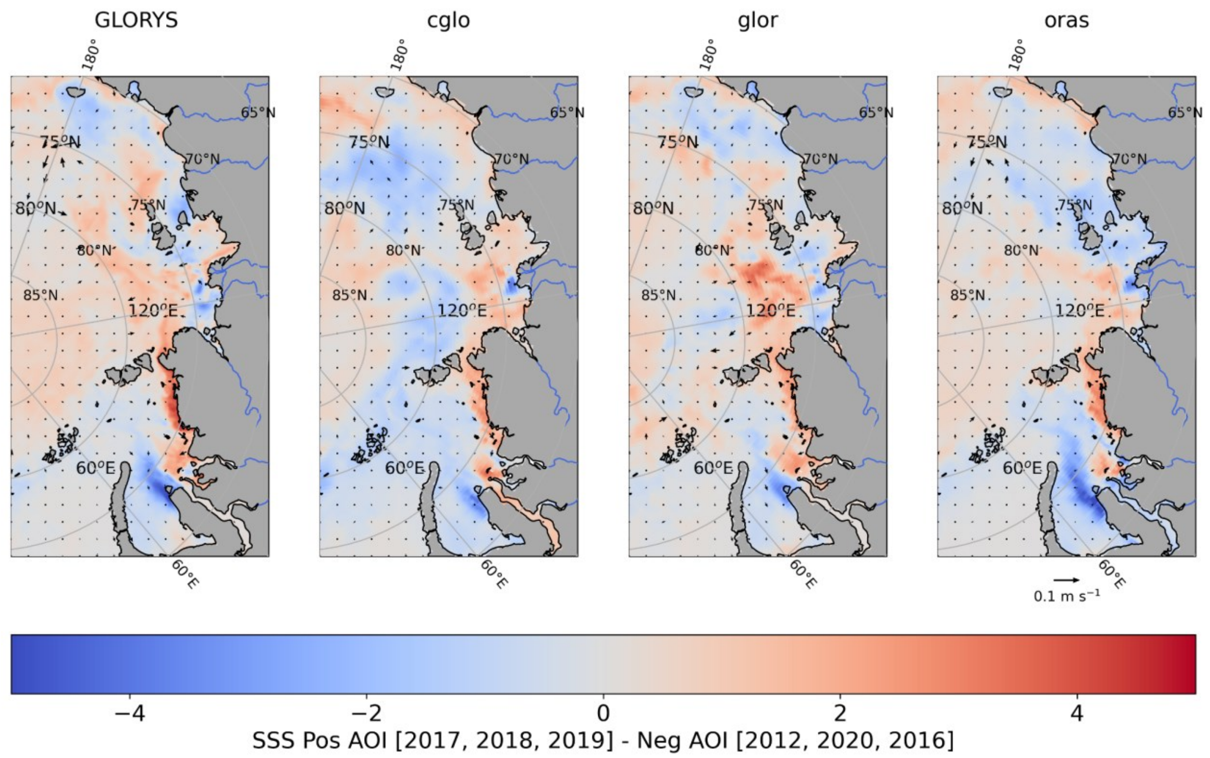

Figure 6.11: The difference between positive (POS) and negative (NEG) AOI composites calculated for (left to right) GLORYS12V1, CGLO, GLOR and ORAS for September of the year following the identified three years of highest and lowest June-August AOI (over 2010-2023). The difference between positive and negative AOI current velocity composites for each reanalysis for September-August are overlaid as black arrows on the respective composite difference plots.

A relatively similar but weaker pattern is visible in the reanalysis composite difference plots (Figure 6.11). As with the satellite products, this pattern suggests a positive anomaly over most of the central Arctic, and in the eastern Kara and Laptev Sea, and a negative anomaly over most of the nearshore Laptev and East Siberian Sea. A small negative anomaly is also visible in the western Kara Sea. Whilst this pattern is generally consistent, the magnitude and extent of these anomalies differs from that in satellite products. Both the positive and negative anomalies in the Kara Sea are much smaller and patchier in reanalyses than in the satellite products. The negative anomaly in the East Siberian Sea is also much weaker than in satellite products. In CGLO and ORAS, it also appears to extend further offshore in a wider band. The pattern present in satellite composite difference plots is much weaker in reanalysis composite difference plots, consistent with the previous suggestion of reanalyses overmixing. No notable difference is visible in surface currents following a summer of eastward or westward wind forcing.

A consistent pattern of positive and negative anomalies is present in satellite and reanalysis composite difference plots for the year following years of positive and negative AOI. These lagged composites suggest that the anomalies that originate in years of particularly high or low AOI appear to persist until at least the following year. In particular, the negative anomaly in the nearshore Laptev and East Siberian Sea suggests the fresh anomalies transported eastward in the previous summer under positive AOI are still present the following year. Alongshore transport of fresh anomalies under positive AOI is consistent with previous work which suggests this water is transported around the Eurasian and then eventually to the Beaufort Gyre over a 3-year period (Morison et al., 2021). This hypothesis provides a mechanism that explains the balance between the increase in Beaufort Gyre freshwater content and decrease in Eurasian freshwater content which has been observed numerous times in the last decades (Solomon et al., 2021; Steele and Ermold, 2004). However, the magnitude of contribution of Eurasian runoff to the Beaufort Gyre is still subject to some debate (Wang et al., 2021). Conversely, the positive anomalies in the offshore Laptev and East Siberian Sea may be indicative of salty Atlantic Water upwelling under positive AOI conditions. Negative AOI conditions promote offshore transport which helps to strengthen and maintain the Arctic halocline and prevent Atlantic Water upwelling (Rudels et al., 1996; Steele and Boyd, 1998). However, positive AOI conditions and alongshore transport result in a weakened halocline offshore, which allows Atlantic Water to upwell.

Both satellite and reanalysis products also suggest a positive anomaly in the eastern Kara Sea, Vilkitsky Strait and offshore Laptev Sea. This positive anomaly indicates that fresh anomalies, which remain largely in the offshore Kara and Laptev Sea under negative AOI conditions, which slowly migrate eastward over winter, are still present in the eastern Kara Sea, Vilkitsky Strait and offshore Laptev Sea the following summer. The presence of these fresh anomalies in the Vilkitsky Strait and western Laptev Sea under negative AOI supports the role of the Vilkitsky Strait as a key pathway of winter freshwater transport as previously suggested (Chapter 5, (Osadchiev et al., 2023a)). The considerable freshwater transport through the Vilkitsky Strait in winter after a summer of negative AOI implies very little riverine freshwater remains in the western and central Kara Sea by the following summer. This also helps to explain the dipole in anomalies between the eastern/nearshore Eurasian (with primarily negative anomalies) from the western/offshore Eurasian (with primarily positive anomalies) which is likely due to the combined input of Kara and Laptev freshwater persisting in eastern Arctic. This represents a notable difference in multi-year salinity controls in the western Arctic which appears partially driven by Atlantic Water inflow, and the eastern Arctic which appears primarily controlled by the magnitude of riverine freshwater transport in the previous summer and whether this remains near the coast or is transported offshore.

However, untangling the salinity signature that remains from previous years from those of interannual variability is a challenge, as winter sea ice cover hides changes that occur over winter. This is particularly true as for the initial positive/negative AOI years chosen, the lagged years used have the same (but much weaker) positive/negative AOI signature, so the same pattern might be expected. However, when the composite difference plots are calculated from 5 years (rather than 3 as above), a very similar (but weaker) pattern emerges. It is also notable that the lagged composite patterns are visible despite that there is no clear difference in surface current velocities, suggesting the differences in lagged composites only exist due to differences in end of summer SSS, rather than differences in winter advection. This supports that fresh anomalies do persist in the following year, and that the initial difference in transport does impact freshwater storage in at least the following year. Very preliminary particle tracking work in the Laptev Sea, placing particles in the nearshore and offshore plume locations, also supports this hypothesis (not shown). However, further work is needed to confirm the different controls between the eastern and western Arctic, and to better understand the longer-term differences in freshwater storage/transport and their implications.

6.6 River plumes as a driver of sea ice persistence

There are also suggestions that current statistical relationships used to predict SIC anomalies will break down with the changing climate, suggesting an increasing need for more physically based sea ice forecasts, which have already been shown to have good predictive skill (Holland and Stroeve, 2011; Mu et al., 2022; Serreze and Stroeve, 2015). This is only emphasised by the predicted loss of summer sea ice in the coming decades. Summer (and previous winter) surface air temperature historically have also been used as main predictor of sea ice anomalies (Holland and Stroeve, 2011). However, the key role of a strong halocline, and of salinity, in sea ice formation has long been understood (Carmack, 2007). In addition, processes controlling sea ice variability are numerous and complex, can be atmospheric or oceanic in origin and include dynamic, thermodynamic and combined influences (Ding et al., 2017; Graversen, 2006; Graversen and Burtu, 2016; Kay et al., 2008; L'Heureux et al., 2008; Ogi and Wallace, 2007; Rigor et al., 2002; Smedsrud et al., 2017; Wang et al., 2009). The lack of understanding of processes driving sea ice decline is exemplified by the ongoing debate as to if the anthropogenically driven loss of sea ice occurs due to vertical heat exchange with atmosphere or through meridional heat flux or combination of both (Stroeve and Notz, 2018b).

It is known that variance in summer (positive) AOI accounts for almost half of variance in (positive) ice anomalies in September with lag of 1-3 months (Ogi and Wallace, 2007). It has also been shown in the previous chapters that differences in SSS/SST associated with summer local wind anomalies (and therefore positive and negative AOI) have implications on Laptev September SIC, but do not have a clear impact on September SIC in the Kara Sea or Vilkitsky Strait.

The influence of fresh surface layers for preconditioning increased autumn sea ice growth, by suppressing mixing and upward heat transfer and enhancing surface cooling, has recently been suggested by the SASSIE campaign (Crews et al., 2022, Drushka et al., 2024). There have been studies that have considered and established the influence of riverine heat on sea ice melt (Dean et al., 1994; Griffin et al., 2018; Nghiem et al., 2014). However, the impact that these differences in SSS and SST appear to have Arctic-wide implications on mixed layer depth (MLD) and on longer term sea ice persistence, including sea ice growth in the following autumn and on sea ice melt in spring, has not previously been studied at large scales, but will be considered here.

To investigate the impacts of differences in freshwater transport on autumn sea ice persistence, composites were calculated for September, October and November of the previously identified years of positive and negative AOI (Figure 6.12). Composites were then calculated for May, June and July of the years following the previously identified years of positive and negative AOI to investigate the impacts on sea ice in the following spring (Figure 6.13). The difference between the positive and negative composite for each of these months is shown in Figure 6.10.

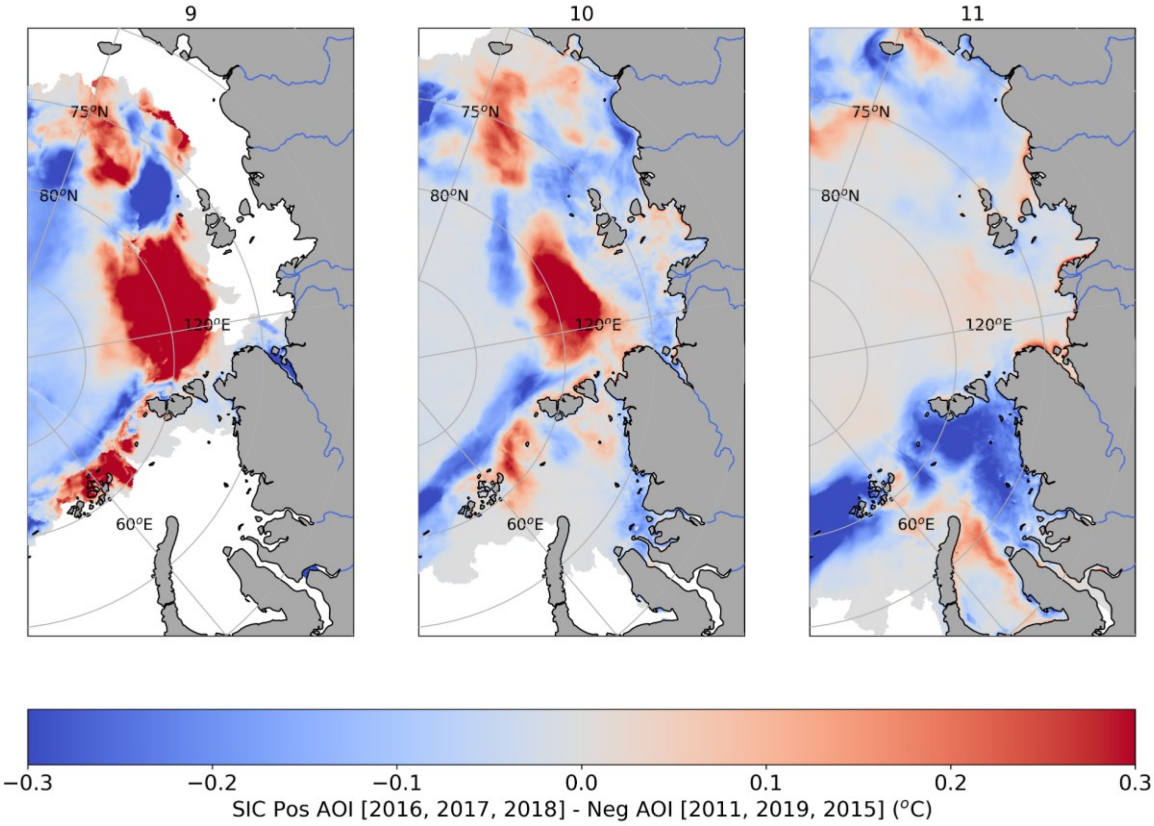

Figure 6.12: The difference between positive (POS) and negative (NEG) AOI composites calculated for GLORYS12V1 sea ice concentration for (left to right) September (9), October (10), November (11) after the identified five years of highest and lowest June-August AOI (over 2010-2023).

In September, a positive anomaly is visible in the offshore Kara, Laptev and East Siberian Sea, suggesting increased sea ice under positive AOI (Figure 6.12). However, just off of the New Siberian islands in the East Siberian Sea, there is a strong negative anomaly suggesting decreased sea ice under positive AOI in this region. Offshore of these positive anomalies, there is a negative anomaly in the central Arctic. This anomaly is strongest in a band offshore of the Barents Sea and in a small patch offshore of the East Siberian Sea, but is relatively weak elsewhere. Most of these anomalies persist in October but generally weaken, expand and migrate nearer shore as the sea ice cover expands. The negative anomalies offshore weaken considerable and are only visible offshore of the Barents and Kara Sea. By November, all of the anomalies in the Laptev and East Siberian Sea have weakened considerably and have a meridional pattern with a positive anomaly over the Laptev Sea, a negative anomaly over the western East Siberian Sea and a positive anomaly over the eastern East Siberian Sea. Most of the Barents and Kara Sea have a negative anomaly in November, except for the central Kara Sea which has a small positive anomaly. Overall, positive AOI drives a strong meridional pattern with primarily low sea ice anomalies in the Kara and East Siberian Sea and a positive sea ice anomaly in the Laptev Sea. Anomalies in the Laptev and East Siberian Sea slowly weaken until November in the Laptev and East Siberian Sea but expand and strengthen in the Kara Sea.

6.6.1 Autumn

Findings in the Kara Sea Chapter (p47) suggest plume transport does have an impact on SST but has little impact on the 30% sea ice concentration contour. Here, a small positive anomaly in sea ice concentration is visible in September (after a summer of positive AOI) in the offshore Kara Sea. Positive autumn anomalies in the Barents and Kara Sea have previously been linked to positive AOI, which is suggested to drive stratospheric warming and warm winter weather over Europe (Cai et al., 2024). This response is suggested to last until spring of following year (Zhang et al., 2022). However, the anomaly in the Kara Sea is very sensitive to the years chosen for composites, and is surrounded by a negative anomaly. This negative anomaly is particularly large in the composite shown and expands and migrates south and is visible until November, where it appears to occupy most of the Barents and Kara Sea. This negative anomaly is likely due to increased warm air intrusions and Atlantic Water inflow under positive AOI (Muilwijk et al., 2019; Nost and Isachsen, 2003) and the related increase in temperature (Dickson et al., 2000; Dörr et al., 2024; Swift et al., 1997), which drives sea ice melt. In addition, the eastward plume transport under positive AOI weakens stratification offshore allowing more Atlantic Water to reach the surface and driving sea ice melt (Morison et al., 2012; Rudels et al., 1996; Steele and Boyd, 1998). Conversely, under negative AOI, offshore transport helps maintain the Arctic halocline and prevent Atlantic Water upwelling (Rudels et al., 1996; Steele and Boyd, 1998). The impact of increased Atlantic Water inflows under positive AOI conditions is likely only increasing with Atlantification, and with the tendency to more positive AOI (Morison et al., 2021; Polyakov et al., 2020b, 2017b).

The positive anomaly in the offshore Kara and Laptev Sea in September and October suggests increased sea ice after a summer of positive AOI in both Kara and Laptev Sea. The positive anomaly in the Laptev Sea is consistent with Laptev Sea Chapter findings of increased sea ice under eastward wind stress (/ positive AOI) (Figure 3.9). The strong positive anomaly in the Laptev Sea appears to originate from decreased offshore transport of warm SSTs (as well as of SSS) under positive AOI (/ eastward wind stress) which minimizes sea ice retreat. The lack of offshore transport minimizes the area of open water and the albedo, decreasing further heat uptake. This is nicely visible in SST AOI composites (not shown) and Laptev Sea Chapter SST zonal wind composites (Figure 3.9), which clearly show a dipole pattern of cool SSTs over the Laptev Sea and warm SSTs over the western East Siberian Sea (Hudson et al., 2024).

One of the most notable anomalies in September is the negative anomaly just off the New Siberian Islands. This negative anomaly is likely linked to the strong positive anomaly in the Laptev Sea. Positive AOI drives alongshore transport of warm SSTs causing a warm SST anomaly in the western East Siberian Sea, visible in SST AOI composites (not shown) and Laptev Sea Chapter SST zonal wind composites (Figure 3.9) (Hudson et al., 2024). In turn these warm SSTs drive sea ice melt. Whilst this negative anomaly is clearly visible regardless of years used in composite analysis, the persistence of this anomaly depends slightly on the years used. However, by November, anomalies in the Laptev and East Siberian Sea have mostly dissipated and only a very weak dipole remains of positive sea ice anomalies in the Laptev Sea and negative sea ice anomalies in the East Siberian Sea.

6.6.2 Following spring

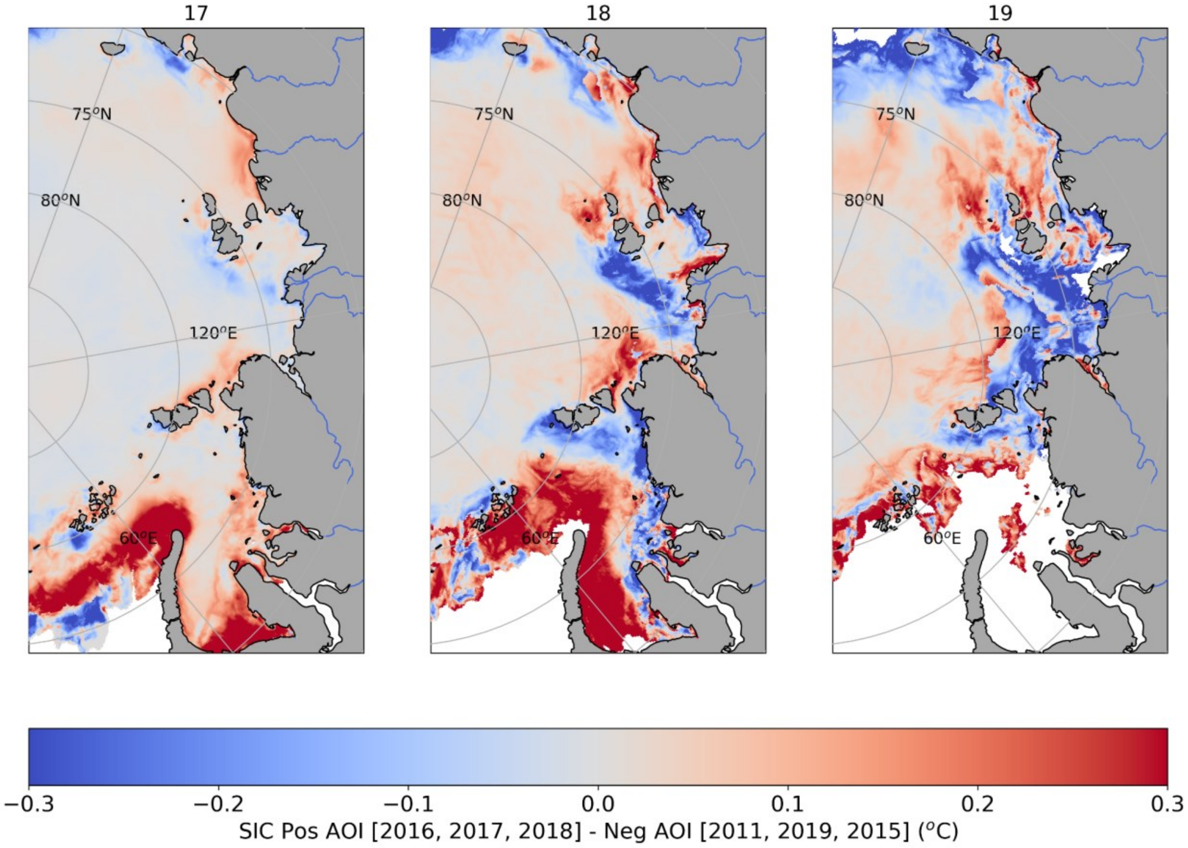

Figure 6.13: The difference between positive (POS) and negative (NEG) AOI composites calculated for GLORYS12V1 sea ice concentration for (left to right) May (17), June (18) and July (19) after the identified five years of highest and lowest June-August AOI (over 2010-2023).

By the following spring, a meridional pattern of positive and negative anomalies appears throughout the Eurasian shelf seas (Figure 6.13). This pattern is very consistent between composites regardless of the years chosen for analysis. To the west, this pattern consists of a positive anomaly, which emerges in the Barents and southern Kara Sea and migrates eastward as the sea ice cover contracts. A negative anomaly is then present in the nearshore Kara Sea, but is only clearly visible from June. A small positive anomaly is then present in the very eastern Laptev Sea, just east of the Severnaya Zemlya Archipelago. Further east, a negative anomaly emerges in May which spans from the southwestern Laptev Sea to the New Siberian Islands, and expands and strengthens through July. A positive anomaly is present across most of the northern Laptev Sea and the western East Siberian Sea but is bounded to the east by a negative anomaly in the eastern East Siberian Sea. These anomalies are relatively small and localized to the coast in May but expand offshore and increase until August.

One of the most pronounced features in spring is the negative anomaly in the central Laptev Sea, which is clearly visible in May through July. It has previously been suggested that September sea ice extent (and positive summer AOI) is linked to strong offshore sea ice transport away from Eurasian coast in winter (Krumpen et al., 2013; Nielsen et al., 2020; Rigor et al., 2002; Williams et al., 2016). Ice export from the Laptev Sea has previously been suggested to be linked to SLP gradient, with high pressure over the ESS driving anticyclonic circulation and offshore wind which increases ice export from the northern Laptev Sea (Krumpen et al., 2013). This ice export drives the negative sea ice anomaly in the southern

Laptev and more sea ice offshore, in the Transpolar Drift, and potentially in the Beaufort and Chukchi seas (Stroeve et al., 2008). The strong ice export decreases the spring sea ice concentration in the southern Laptev Sea, accelerating fast ice breakup and triggering enhanced summer melt (Babb et al., 2019; Itkin and Krumpen, 2017). In addition, positive summer AOI drives both increased Atlantic Water inflows and alongshore plume transport. The lack of offshore transport of fresh riverine anomalies weakens the offshore halocline, allowing Atlantic Water upwelling, which may also contribute to the negative sea ice anomaly observed. Whilst winter ice export has previously been linked to sea level pressure anomalies in the East Siberian Sea and whilst winter leads have previously been suggested to be related to early summer sea ice cover (Krumpen et al., 2013; Zhang et al., 2018), the link between summer AOI and winter sea ice export as a predictor of spring Laptev Sea ice cover has not previously been discussed.

Negative anomalies in Barents and Kara Sea, as are present in autumn after a summer of positive AOI, are suggested to be followed by negative AOI pattern from January to March (Delhaye et al., 2024). Negative AOI drives weaker Atlantic Water inflows and a more extensive sea ice cover. The sub-seasonal reversal in atmospheric pattern, and the role of sea ice in helping control this pattern, has been widely discussed and linked with weather over Eurasia (Xu et al., 2022; Yin et al., 2023; Zhang et al., 2023). However, the opposing pattern between sea ice anomalies in autumn that help generate this reversal in atmospheric circulation, and those in spring that result from this have not previously been widely discussed and warrants further investigation.

Numerous other patterns are also clearly present in spring composite plots, including a negative anomaly in the eastern Kara Sea, a positive anomaly in the Vilkitsky Strait and western Laptev Sea and a positive anomaly in the East Siberian Sea. It is likely that some of these patterns are linked to salinity stratification, particularly as temperature anomalies in spring appear to lag rather than lead sea ice changes in all regions other than Barents/Kara Sea, suggesting sea ice differences are likely either due to salinity stratification or differences in dynamics (or both). In particular, eastward transport under positive AOI yields strong salinity stratification in both the western Laptev Sea, from transport of the Ob-Yenisei plume through the Vilkitsky Strait, and in the East Siberian Sea, from transport of the Lena River plume. This strong stratification would prevent warm Atlantic Water from reaching the surface layer, and delay sea ice melt. Conversely, this would leave an absence of fresh water in the in eastern Kara Sea, which would allow warm Atlantic Water to upwell onto the shelf and drive sea ice melt. The consistent, strong nature of this pattern indicates a level of predictability to spring sea ice. However, this pattern warrants further investigation.

6.6.3 Sea ice persistence discussion

Sea ice concentrations in autumn in the Barents and Kara Sea appear to be primarily dependent on Atlantic Water inflows into the region. Conversely, the strong SIC anomalies that emerge with differences in plume transport in the Laptev and East Siberian Sea in September persist in October but are mostly gone by December. The rapid disappearance of these anomalies likely occurs as they are primarily driven by SST differences. Autumn and winter heat loss has a strong stabilizing effect, minimizing the persistence of summer sea ice anomalies. Large negative anomalies in September result in large ocean heat loss in autumn and winter and large ice production (Stroeve et al., 2012; Tietsche et al., 2011). Ice formed later in season also has a thinner snow cover so can grow more effectively in winter (Notz, 2009). However, September sea ice is weakly but significantly correlated with the previous September SIC, meaning that autumn heat loss is insufficient to counteract interannual anomalies (Holland and Stroeve, 2011). In turn, a strong meridional pattern emerges in the following spring. Elements of this pattern, such as the negative sea ice anomaly in the Laptev Sea which emerges after a winter of increased sea ice production and export, have previously reported mechanisms. Patterns such as this provide a partial explanation to the suggestion that incorporating surface heat flux into forecasts is suggested to improve spring sea ice predictability (Zeng et al., 2023). This is particularly true as spring sea ice anomalies the impact amount of open water that develops in summer (Perovich et al., 2008; Stroeve et al., 2016, 2014). However, many elements of this pattern have not previously been reported and are relatively poorly understood, but could hold key to improving spring sea ice predictability. In particular, the impacts of differences in freshwater transport and their impacts on mixed layer dynamics and spring sea ice melt, requires further investigation.

It is all the more important to better understand the physical relationships governing sea ice cover anomalies as the statistical relationships used to predict sea ice anomalies break down with the regime shifts climate change will bring (Holland and Stroeve, 2011; Mu et al., 2022; Serreze and Stroeve, 2015). The Kara Sea has already been suggested to be transitioning from a "summer mode" to a "winter mode" as it loses its summer sea ice and has increased winter ice loss (Stroeve and Notz, 2018b). It is possible that as sea ice cover retreats in Laptev Sea, and there is a longer period of open water, there may be a switch in regime similar to the one present in the Kara Sea whereby Atlantic Water inflows play a stronger role in controlling surface sea ice cover. The stabilizing feedback which minimizes the influence of summer anomalies on the following summer has also been suggested to be weakening as Arctic winters become warmer and with increased winter cloud cover after summer sea ice loss (Liu et al., 2012; Stroeve and Notz, 2018b). This may cause the spatial variability in stratification (due to salinity) to play a stronger role on ice re-growth than the anomalies initially observed by differences in plume transport (due to plume temperature). In addition, the correlation between the AOI and sea ice extent has been suggested to be strengthening in recent decades as the sea ice cover thins and the ocean is increasingly more exposed to atmospheric circulation changes (Williams et al., 2016). However, this relationship has also been predicted to weaken in future with climate change (Holland and Stroeve, 2011). A better understanding of sea ice relationships, particularly that with salinity stratification, is needed to be able to accurately predict future sea ice changes.

6.7 Implications of increase in large-scale/local correlation

The considerable variability in correlation strength between eastward wind stress and the AOI (depending on time period analysed) suggests there may be some decadal variability in the extent to which the AOI controls local wind forcing in this region. The decline in summer sea ice is likely at least partially responsible for this increase in correlation strength as the increased area of open water allows increased atmosphere-ocean momentum transfer, which increases in wind stress and may play a role in altering how strongly coupled the AOI is to local wind stress in each of these regions.

To analyse the changes in freshwater transport in recent decades, salinity composites for September over the reanalysis pre-satellite-period (1993-2006) are calculated for comparison with those calculated for the satellite period in all four reanalyses (GLORYS12V2, CGLO, GLOR and ORAS). Positive and negative AOI composites are calculated from the three years of highest AOI (1994, 1996, 2006) and lowest AOI (1993, 1997, 2004) over 1993-2006. The composite difference is then calculated between the high and low AOI composites (Figure 6.14). The difference between the pre-satellite period and the satellite period composite difference plots is then calculated (Figure 6.15).

The same years are also used to calculate positive and negative AOI current velocity composites (for both eastward and northward velocity components) from mean June-August eastward and northward current velocity components for all four reanalyses. Again, the difference between these composites is calculated (overlaid on Figure 6.14) as well as the difference between the pre-satellite period and the satellite period composite difference plots (overlaid on Figure 6.15).

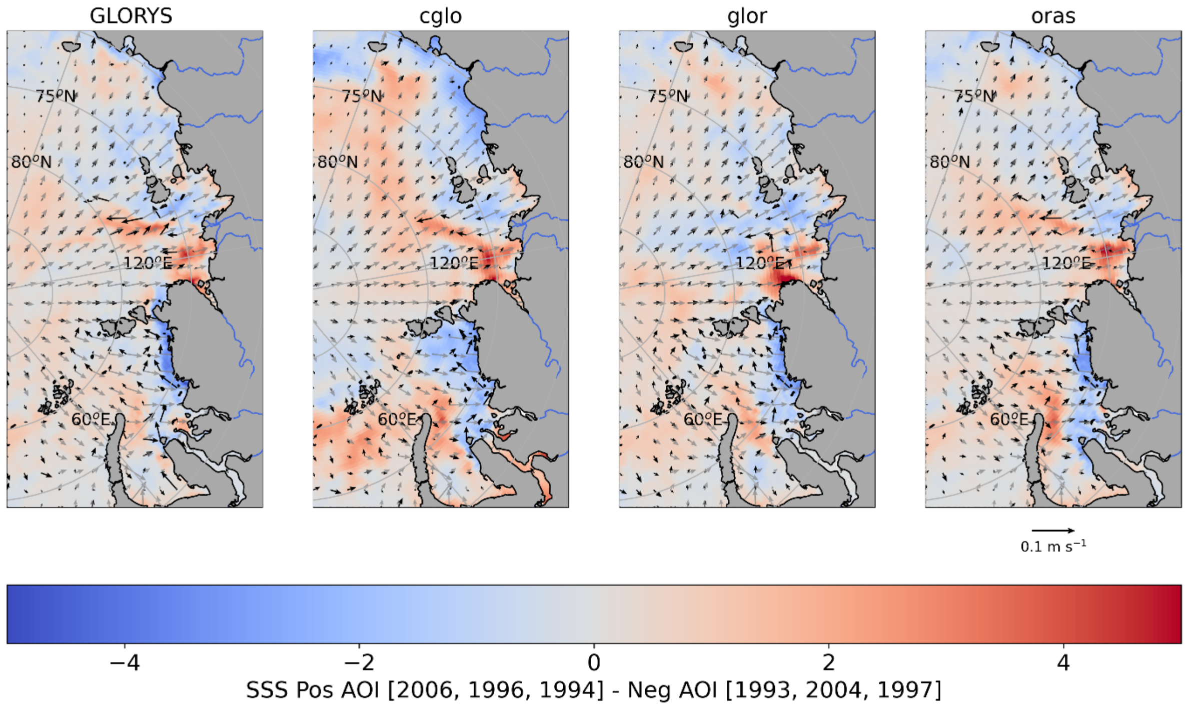

Figure 6.14: The difference between positive (POS) and negative (NEG) AOI composites of September SSS calculated for (left to right) GLORYS12V1, CGLO, GLOR and ORAS from the identified three years of highest and lowest June-August AOI (over the start of the GLORYS12V1 pre-satellite period (1993-2006)). The difference between positive and negative AOI current velocity composites for June-August are overlaid as black arrows on the respective composite difference plots for each reanalysis. The difference in expected Ekman surface currents based on observed average June-August eastward and westward wind stress under positive / negative AOI are overlaid as grey arrows for comparison.

A somewhat consistent composite difference pattern is visible from pre-satellite (start of the GLORYS12V1 period (1993-2006)) years of high and low AOI in all four reanalyses. This pattern is somewhat similar but much weaker than that visible from the composite calculated over the satellite period. This pattern consists of a negative anomaly nearshore and positive anomaly offshore in the Kara Sea. Whilst this resembles the composite calculated over the satellite period, the positive anomaly offshore in much weaker, especially just offshore of the Ob delta. The negative anomaly nearshore is also much wider, and extends further offshore, in the pre-satellite composite. The anomalies in the Laptev and East Siberian Sea in the pre-satellite composite, however, are different to those in the satellite composite. In both, there is a notable positive anomaly in the southwestern Laptev and a negative anomaly in the southern Laptev and East Siberian Sea. However, a negative anomaly is present in the eastern Laptev and western East Siberian Sea in the pre-satellite composite but a strong positive anomaly is present in this region in the satellite composite. This suggests the plume was much less coastally confined over this period, and further extended offshore under positive AOI.

A somewhat consistent pattern is also visible in surface velocity composite difference plots over the pre-satellite period (compared to the satellite period), of more southward (or onshore) transport under eastward wind forcing. However, this pattern is much weaker in the pre-satellite period and the surface current velocity difference is less directly southward, with more zonal variation and clearer alongshore transport in the Kara Sea.

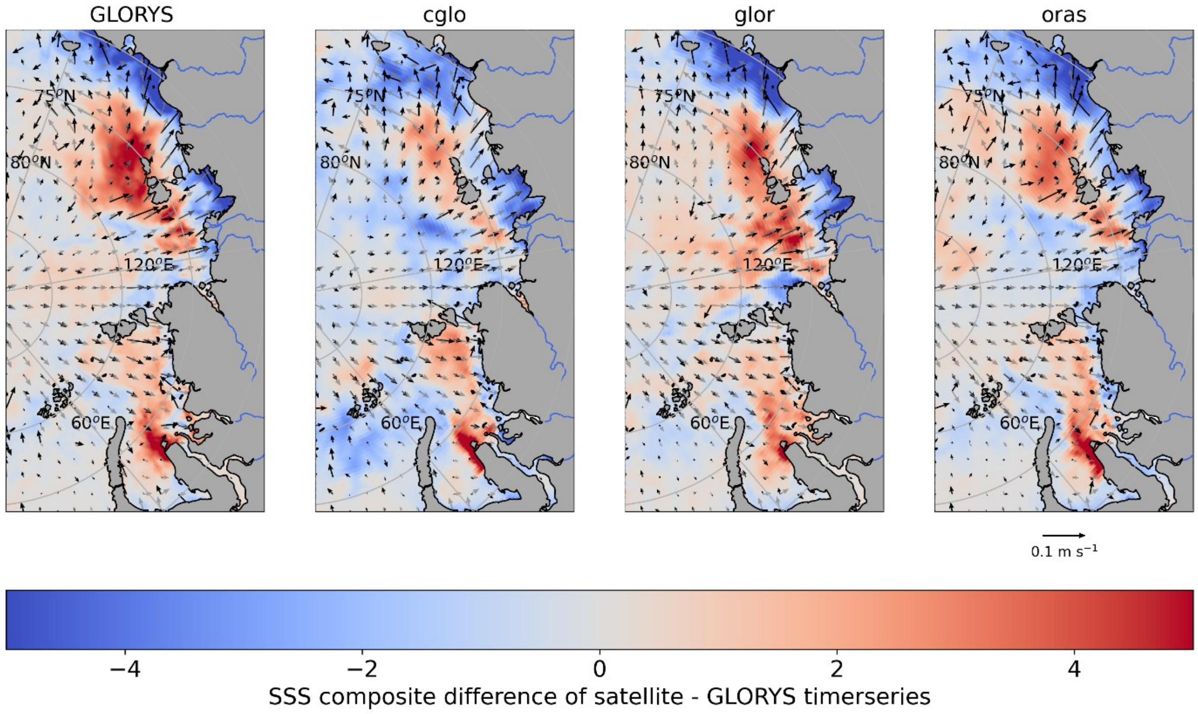

Figure 6.15: The difference between the composite difference of September SSS calculated over the satellite time-period (2010-2023) and that calculated over the start of the GLORYS12V1 time-period (1993-2006) for (left to right) GLORYS12V1, CGLO, GLOR and ORAS from the identified three years of highest and lowest June-August AOI (over the GLORYS12V1 pre-satellite period (1993-2006)). The correlation coefficients between the satellite time-period composite difference plots and the difference between the composite difference plots (shown here) are included in the title. The difference between the composite difference of June-August current velocities calculated over the satellite time-period (2010-2023) and calculated over the start of the GLORYS12V1 time-period (1993-2006) are overlaid as black arrows on the respective composite difference plots for each reanalysis. The difference in expected Ekman surface currents based on the difference in observed average June-August eastward and westward wind stress under positive / negative AOI over the satellite time-period (2010-2023) and calculated over the start of the GLORYS12V1 time-period (1993-2006) are overlaid as grey arrows for comparison.

The difference between composite difference plots (for the satellite period (2010-2023) and for the GLORYS12V1 pre-satellite time period (1993-2006)) (Figure 6.15) has a very similar pattern to both the reanalysis and satellite composite difference plots calculated for the satellite period (2010-2023) (Figure 6.10, Figure 6.11). All four reanalyses suggest large regions of positive anomalies offshore in both the Kara and Laptev Sea. All four reanalyses also suggest extensive regions of negative anomalies nearshore throughout the Laptev and East Siberian

Sea. However, nearshore negative anomalies are not apparent in the Kara Sea, likely as nearshore negative anomalies are present in both pre-satellite and satellite composites. The similar pattern in composite difference plots indicates stronger variability in SSS between positive and negative AOI states over the satellite period, than over the start of the GLORYS12V1 time period. However, whilst all reanalyses clearly show an amplification in SSS variability, the increase in available in-situ data (assimilated / used to constrain the models) could also drive this difference.

A similar amplification also appears visible in the difference in surface current composite difference between the satellite and pre-satellite period. This amplification suggests notably stronger variability in surface currents (under positive/negative AOI) over most of the Eurasian shelf seas in the satellite period compared to the pre-satellite period, with eastward wind forcing driving stronger southward surface currents. This difference appears to be mostly north/southward in the Kara and Laptev Sea but has a much stronger eastward component in the East Siberian Sea. This supports the previous suggestion that the shift to a more positive AOI, and the associated enhanced cyclonic circulation this brings, drives eastward alongshore flow and freshwater transport along Russian coast, which then ends up in the Beaufort Gyre (Alkire et al., 2015; Morison et al., 2021).

This implies that the variability in the magnitude of freshwater transport appears to be increased over the satellite period, compared to the GLORYS12V1 pre-satellite era. It has been suggested that modes of surface circulation have changed since 1990s, associated with shift to more variable and more positive AOI, which has resulted in increasingly cyclonic circulation in Eurasian Basin (Morison et al., 2021). Alternatively, it has also been suggested that an increase in runoff could contribute to increased eastward (baroclinic) transport around the Eurasian shelf seas (Hordoir et al., 2022). This explanation might be expected to be consistent with a less strongly wind driven system, and less transport directly offshore (Hordoir et al., 2022). However, the strengthening response to the AOI suggests an increasingly wind driven system as there is larger variability in SSS nearshore and offshore over the satellite time period than the initial GLORYS12V1 period. This is particularly visible in the Laptev Sea, where there is very strong resemblance between reanalysis composite difference plots for the satellite period and the difference between satellite and pre-satellite composite difference plots. This increase in SSS variability is coincident with the increased standard deviation of the AOI, and the increase in correlation between large-scale and local wind stress in both the Laptev and Kara Sea. However, this increase in variability, particularly nearshore, could also be a function of the increased freshwater present in the Eurasian shelf seas and increased baroclinic transport.

As well as the increase in salinity variability visible, there also appears to be an acceleration of freshwater transport around the Eurasian Arctic. Whilst there is no clear negative anomaly in the nearshore Kara Sea in composite difference plots, all four products have a clear, significant region of negative anomaly in the western Laptev Sea, coincident with where you would expect to find the Ob-Yenisei plume to enter the Laptev Sea after transport through the Vilkitsky Strait. The extension of this negative anomaly suggests there could be an increase in the distance the plume travels under positive AOI in more recent time periods. This could be a feature of the longer sea ice free period and period of open water, which allows increased atmosphere-ocean momentum flux and drives a stronger ocean response to wind forcing (Holland and Stroeve, 2011; Morison et al., 2021). It likely also reflects the stronger, more variable and more positive AOI signal visible in recent decades or the increase freshwater input, and the associated stronger baroclinic transport (Hordoir et al., 2022; Morison et al., 2021). This acceleration helps to explain the positive anomaly in the difference between composite difference plots, which likely does not suggest a notable increase in the SSS of the Ob-Yenisei plume under high AOI / eastward wind transport but suggests more saline waters are present in this region as more of the central plume gets transported out of the western and central Kara Sea under positive AOI.

6.8 Conclusions and implications with climate change

A strong correlation is present between the AOI and local zonal wind stress in the Laptev and Kara Sea and over the Vilkitsky Strait, which suggests that the AOI clearly plays a dominant role in controlling local eastward turbulent surface stress throughout the Eurasian shelf seas. A notable correlation is also present with meridional wind stress in the Kara Sea. The strength of these correlations appears to be increasing as the AOI becomes more positive (and more variable).

The strong correlation between local and large-scale atmospheric forcing implies the AOI drives a consistent pattern of freshwater transport across all Eurasian shelf seas. Under positive AOI, the cyclonic circulation in the Eurasian Arctic is expanded, promoting transport of the Ob-Yenisei plume through the Vilkitsky Strait and transport of the Lena plume towards the East Siberian Sea. Conversely under negative AOI, the cyclonic circulation is contracted, and the start of the Transpolar Drift is shifted to start in the offshore Laptev Sea, which promotes offshore/northward freshwater transport. This pattern illustrates the vital role of Vilkitsky Strait as a pathway for freshwater transport around Eurasian shelf seas and of the Laptev Sea as a key pathway controlling riverine freshwater exchange between the Eurasian and central / Amerasian Arctic. Whilst variability in freshwater transport through the Vilkitsky Strait is clearly visible in all reanalyses, inconsistencies with satellite data denote poor representation in the reanalysis products of the Kara Sea plume and in the western Laptev Sea, suggesting a poor representation of at least some processes controlling freshwater transport.

Anomalies that originate in years of particularly high or low AOI appear to persist until at least the following year. Following a summer of positive AOI, freshwater at least initially remains in the nearshore Eurasian Arctic. This is particularly strongly visible in the eastern Eurasian Arctic due to the combined influence of the Lena and Ob-Yenisei plumes. Conversely, following a summer of negative AOI, freshwater appears to be transported offshore from the Laptev and East Siberian Sea, suggesting more export of freshwater to the central Arctic.

Currently, differences in the AOI, and freshwater transport, appear to drive sea ice persistence (and in turn predictability), especially in the Laptev and East Siberian Sea. This persistence appears linked to both SST differences and MLD differences driven by differences in freshwater transport. However, more work is needed to untangle the competing feedbacks between SSS/SST/MLD and SIC. The Kara Sea currently appears to exhibit a notably different regime, which is more strongly controlled by Atlantic Water inflows, and has stronger anomalies which persist longer, likely due to the longer sea ice free period. This regime may forecast how future changes in the Laptev/East Siberian Sea will manifest.

In recent decades, there appears to be an increase in variability and an acceleration of freshwater transport around the Eurasian Arctic. Multiple mechanisms may contribute to this including the shift to more positive (and more variable) AOI, the loss of ice cover and increase in atmosphere-ocean momentum transfer or increases in coastal freshwater contribution driving increased baroclinic transport. The contribution of each of these mechanisms needs to be better understood, if these constitute decadal changes or climatic changes, to accurately predict future change.

The increase in riverine heat has already contributed to a regional loss of sea ice, and it has been suggested that warming river discharge is a key control on basin-wide SIC (Dong et al., 2022; Park et al., 2020). It is also clear that the increase in river runoff will increase the freshwater supply to the Eurasian shelf seas and have implications for local and Arctic-wide stratification dynamics as well as for local biogeochemistry. However, the dominance of zonal wind and the AOI as a key driver of SSS and SST interannual variability suggests that understanding variability in wind stress, and whether this is likely to change, is the key to predicting future freshwater transport from the Eurasian shelf seas.

This is all the more relevant as the dominance of wind stress variability is only likely to increase further with the loss of sea ice cover. Prior to the mid-2000s, the Lena and Ob-Yenisei plumes typically remained strongly-stratified and confined to the shallow shelf, constrained by the extensive sea ice cover and small region of atmospheric influence (Janout et al., 2020). The loss of sea ice cover is enlarging the area in contact with the atmosphere and increasing the time of atmosphere-ocean exposure.

The strong influence of the AOI on local wind stress in this region, and the increase in correlation strength over the more recent time period, highlights the need to investigate how large-scale atmospheric circulation has and will change over the Arctic to predict future changes in freshwater storage and transport from the Eurasian shelf seas. This relationship is only likely to become stronger given the AOI is suggested to have increased in variability in recent decades (Armitage et al., 2018; Morison et al., 2021), and as future sea ice loss will only strengthen coupling between large-scale and local wind dynamics. These changes have already and will likely continue to expand the region of potential riverine freshwater influence (Janout et al., 2020; Johnson and Polyakov, 2001; Zhuk and Kubryakov, 2021). In turn, these have the potential to speed up transport between the shelf seas and central Arctic (Charette et al., 2020). Whilst the dominant role of the AOI in controlling geostrophic circulation, and Eurasian runoff transport, has been widely suggested, there remains debate with respect to the longer-term pathway of this transport (Morison et al., 2012; Q. Wang et al., 2021). The longer-term fate of this transport is key for predicting future Arctic freshwater storage or export, and may hold vital clues to variability in the AMOC; therefore, further work into understand these feedbacks is required.

However, the impact this will have on the wider Arctic will strongly depend on changes in stratification dynamics. Whilst it is likely that stratification dynamics will change as the region of potential freshwater influence expands, it remains uncertain what the dominant drivers of this change will be, and how this change will manifest. On the one hand, having a larger open water region exposed to wind-driven mixing for longer periods could deepen stratification, increasing the tendency of a well-mixed plume (Janout et al., 2020). This appeared to occur in 2016 in the Laptev Sea and seems likely under strong eastward wind forcing (/ positive AOI), where the fresh water is transported eastwards, driving downwelling and mixing and creating a coastally confined well-mixed plume. Alternatively, the increase in river runoff to the Arctic could strengthen surface stratification (Nicolì et al., 2020; Nummelin et al., 2016) and increase the likelihood of a very shallow plume that extends out northwards towards the central Arctic. It is also possible that the likelihood of both of these alternating states could become more frequent, with the increased influence of wind variability with the loss of sea ice cover (Janout and Lenn, 2014). Changes in stratification will be strongly coupled to changes in sea ice dynamics and persistence, and will have implications for the timing, magnitude and region of water mass formation / transformation in the Laptev (Preußer et al., 2019). The interconnected nature of SSS, SST and SIC, especially in the Laptev and East Siberian Sea, highlights the challenge but also the need to understand this region as a system rather than trying to understand drivers of individual components in isolation. This will prove vital to be able to predict how the conflicting changes in this region will impact both individual regions and wider Arctic sea ice dynamics and freshwater transport.

Chapter 7 Conclusions

This thesis set out to address one aim through four main research questions. The key findings related to each of these research questions, their implications and suggested future work related to these findings are presented below.

This thesis aimed to improve our understanding of the common and isolated drivers of interannual variability in sea surface salinity, temperature and sea ice in the Laptev and Kara seas and through the Vilkitsky Strait. The differences in dynamics between these regions was then explored as well as the implications of these findings for how climate change will impact the Eurasian Arctic.

1. Demonstrate the value and potential of applying satellite SSS data to Arctic based process studies

Satellite SSS is a useful tool to strengthen our understanding of Arctic SSS dynamics. Satellite SSS agrees well with in situ data ($r \geq 0.81$) and provides notable improvement compared to reanalysis products ($r \leq 0.76$) (section 2.4). There is strong consensus in SSS patterns under eastward and westward wind regimes (and under positive / negative AOI) in the Laptev and Kara Sea and in the Vilkitsky Strait (and over the Eurasian Shelf Seas) in LOCEAN SMOS, JPL SMAP and CCI. Satellite SSS products typically agree well with GLORYS12V1, providing trustworthy conclusions but also provide a baseline that allows us to identify shortcomings in reanalyses.

Implications of these findings:

- Given the demonstrated value, satellite SSS needs to be further exploited, both for process-based studies and to improve models (and forecasts).
- Continued improvement to satellite SSS processing will help to increase confidence and usage of satellite SSS in the Arctic.

Future work - to improve representation of satellite and reanalysis products in this region:

1. Validation efforts highlight the need for more near-surface in situ data and more near-shore profiles for improved product validation over the Russian Arctic shelf and for better understanding of vertical stratification processes, particularly over the

shelf. In particular, there is a need for additional efforts for common widespread usage of accessible Arctic data portals.

2. Whilst variability in freshwater transport through the Vilkitsky Strait is clearly visible in all the reanalyses products analysed in this work, inconsistencies with satellite data denote poor reanalysis representation of the Kara Sea plume and in the western Laptev Sea and suggest poor representation of at least some processes controlling freshwater transport. The poor representation of very low salinities and the overmixing tendencies need addressing for accurate representation of Arctic freshwater transport. The incorporation of more shallow vertical levels (especially with high performance computing advancements) would likely help improve this. In addition, the impacts of interannually varying runoff forcing (compared to climatological) should be examined further.
3. Data assimilation, as well as conventional comparison approaches, should be further explored to improve model representation of Arctic salinity (Xie et al., 2023). This may help to address some of the identified issues with the reanalyses used here.

2. What are the processes controlling the interannual variability of summer salinity, temperature and sea ice variability and how do they interact in the Laptev and Kara Sea and in the Vilkitsky Strait?

In the Laptev Sea, zonal wind is the dominant driver of offshore/alongshore Lena River plume transport, with eastward wind driving alongshore transport (and westward wind driving offshore transport) (Laptev Sea Chapter 3). The zonal wind plays a key role in driving SSS and SST variability and appears to drive spatial variability in SIC across the Laptev and East Siberian Sea. The differences in spatial patterns of SSS and SST under eastward/westward wind forcing highlight the importance of the zonal wind for dispersing riverine heat and in turn controlling the SST/SIC positive feedback, which plays a considerable role in driving further SST warming in shallow open-water regions. Annual, summer, and spring Lena runoff does not appear to play a role in controlling interannual variability in SSS, SST, or SIC in the Laptev and East Siberian Sea.

Kara Sea zonal wind and runoff both appear to be key drivers of whether the fresh plume is transported offshore or alongshore, again with eastward wind driving alongshore transport, as was true in the Laptev Sea (Kara Sea Chapter 4). In the Kara Sea, unlike the Laptev Sea, the zonal wind in August plays a notably larger role than June or July and meridional wind, particularly in August and September, also plays a role in controlling this variability. The ratio of summer Yenisei runoff/ spring Ob runoff also plays a role in controlling salinity variability in the Kara Sea. However, this ratio has the strongest impact under westward wind forcing, where a high ratio (high summer Yenisei runoff and low spring Ob runoff) acts to further freshen the central and western Kara Sea. Summer cumulative Yenisei runoff is the dominant control on this ratio, and on SSS in the central Kara Sea. However, spring Ob runoff also appears to play a role in controlling this interaction, by preventing/allowing transport of the Yenisei plume offshore and controlling SSS at the outflow of the Ob Delta.

Zonal wind forcing also has an influence on SST but is not the dominant driver of variability in SST. Meridional wind also appears to have a dominant impact on SST, by controlling Ekman transport and the associated upwelling/downwelling on/off the shallow shelf in the eastern Kara Sea. Therefore, SSS and SST/SIC are notably less closely coupled in the Kara Sea and appear to be controlled by differing processes. Whilst it is still clear that there is coupling between SST and SIC, the consistent sea ice free nature of the Kara Sea in September drives notably lower interannual variability in SIC. In turn, this has knock-on effects on SST, as the positive feedback cycle that strongly couples SST and SIC in the Laptev is not present in the Kara Sea.

Strong eastward wind drives buoyancy driven transport of the Ob-Yenisei plume through Vilkitsky Strait and into the western Laptev Sea and can occur over one summer season (Vilkitsky Strait, Chapter 5). Differences in plume transport also have a notable SST signature, which closely resembles that of SSS, suggesting strong co-variability between SSS and SST in this region in September. Despite the co-variability between SSS and SST in this region, zonal wind dynamics do not appear to have a notable impact on September SIC. Despite the dominant influence of zonal wind in controlling summer freshwater transport through the Vilkitsky Strait, plume transport through the strait still appears to occur over winter even in years with no strong eastward wind forcing. However, differences in timing drive very different SSS/SST patterns and stratification dynamics, which appear to persist through much of winter and may impact later winter sea ice formation or melt the following summer.

Implications of these findings:

- Despite zonal wind being a dominant driver of SSS interannual variability in all three regions, the notable differences in key controls between regions suggests they should not be expected to respond to changes in the same way, and need to be studied independently.

Future work:

1. Differences, particularly in SSS/SST/SIC coherence between Kara, Vilkitsky Strait and Laptev Sea dynamics should be used to forecast potential future changes in downstream regions.

3. What are the dominant controls on Eurasian-wide interannual variability and what implications do these have on sea ice persistence and Arctic-wide freshwater storage?

The similar spatial patterns, and strong correlations between AOI and local wind stress reiterate that large-scale dynamics predominantly govern local wind variability and freshwater transport in this region. A strong correlation is present between the AOI and local zonal wind stress in the Laptev Sea, Kara Sea and over the Vilkitsky Strait suggesting the AOI clearly plays a dominant role in controlling local eastward turbulent surface stress throughout the Eurasian shelf seas (section 6.3). A notable correlation is also present with meridional wind stress in the

Kara Sea. The strength of these correlations appears to be increasing as the AOI becomes more positive (and more variable).

The AOI drives a consistent pattern of freshwater transport across all Eurasian shelf seas, as might be expected from the strong correlation between local and large-scale atmospheric forcing (section 6.4). Under positive AOI, the cyclonic circulation in the Eurasian Arctic is expanded, promoting transport of the Ob-Yenisei plume through the Vilkitsky Strait and transport of the Lena plume towards the East Siberian Sea. Conversely, under negative AOI, the cyclonic circulation is contracted, and the start of the Transpolar Drift is shifted to start in the offshore Laptev Sea, which promotes offshore/northward freshwater transport. This pattern illustrates the vital role of Vilkitsky Strait as a pathway for freshwater transport around Eurasian shelf seas. This pattern also highlights transport in the Laptev Sea as a key pathway controlling riverine freshwater exchange between the Eurasian and central / Amerasian Arctic. However, whilst the AOI is a dominant control on freshwater transport around the Eurasian Shelf Seas, the relevant local wind metric drives greater variability in the three regions studied.

Anomalies that originate in years of particularly high or low AOI appear to persist until at least the following year (section 6.5). Following a summer of positive AOI, freshwater at least initially remains in the nearshore Eurasian Arctic. This is particularly visible in the eastern Eurasian Arctic due to the combined influence of the Lena and Ob-Yenisei plumes. Conversely, following a summer of negative AOI, freshwater appears to be transported offshore from the Laptev and East Siberian Sea, suggesting more export of freshwater to the central Arctic.

Currently, differences in the AOI, and in freshwater transport, appear to drive sea ice persistence (and predictability) until at least the following spring, especially in the Laptev and East Siberian Sea (section 6.6). This persistence appears linked to both SST differences and MLD differences driven by differences in freshwater transport. Kara Sea SST currently appears to exhibit a notably different regime, which is more strongly controlled by Atlantic Water inflows, and has stronger anomalies which persist longer, likely due to the longer sea ice free period. This sea ice free regime in the Kara Sea may be useful to forecast how future changes in the Laptev/East Siberian Sea will manifest. However, the geographical differences between the two regions, including the influence of Atlantic Water inflows, need to be untangled from the impacts of the low the low sea ice cover.

To more accurately predict the state of the future Eurasian and full Arctic system:

1. The strong influence of the AOI on local wind stress in this region, and the increase in correlation strength over the more recent time period, highlights the need to investigate how large-scale atmospheric circulation has and will change over the Arctic to predict future changes in freshwater storage and transport from the Eurasian shelf seas.
2. Whilst the dominant role of the AOI in controlling geostrophic circulation and Eurasian runoff transport has been widely suggested, there remains debate as to the longer-term pathway of this transport. The longer-term fate of Eurasian freshwater transport, and the influence initial transport has on this longer-term fate, is key for

predicting future Arctic freshwater storage / export, and may hold vital clues to variability in the AMOC (Marsh et al., 2024). Conducting a particle tracking study to determine if the initial difference in plume transport under high/low AOI impacts longer-term freshwater storage (ideally with a model proven to be able to accurately represent freshwater transport around the Eurasian Shelf seas) would be a useful way to test this.

3. The drivers of the observed increase in variability and an acceleration of freshwater transport around the Eurasian Arctic needs to be better understood, in particularly if these constitute decadal changes or climatic changes. In particular the contribution of different mechanisms including: the shift to more positive / more variable AOI, the loss of ice cover and associated increase in atmosphere-ocean momentum transfer or the increase in coastal freshwater contribution driving increased baroclinic transport. Perturbation-based modelling studies could be targeted at addressing this.
4. A better understanding of sea ice relationships, particularly those with salinity stratification, are needed to be able to accurately predict future sea ice changes, particularly to untangle the competing feedbacks between SSS/SST/MLD and SIC. Analysis of data collected during the SASSIE campaign will likely help to illuminate some of these relationships (Drushka et al., 2024).

4. What implications do these findings have for freshwater transport in the context of climate change?

The dominance of zonal wind and the AOI as a key driver of SSS and SST interannual variability suggests that understanding variability in wind stress, and if it is likely to change, is the key to predicting future freshwater transport from the Eurasian shelf seas (section 6.8). This is all the more relevant as the loss of sea ice cover is enlarging the area in contact with the atmosphere and increasing the time of atmosphere-ocean exposure, increasing the dominance of wind stress variability.

In recent decades, there appears to be an increase in variability and an acceleration of freshwater transport around the Eurasian Arctic (section 6.7). Multiple mechanisms may contribute to this including the shift to more positive (and more variable) AOI, the loss of ice cover and increase in atmosphere-ocean momentum transfer or increases in coastal freshwater contribution driving increased baroclinic transport. This relationship is only likely to become stronger given the AOI is suggested to have increased in variability in recent decades, and as future sea ice loss will only strengthen coupling between large-scale and local wind dynamics. These changes have already and will likely continue to expand the region of potential riverine freshwater influence and have the potential to speed up transport between the shelf seas and central Arctic.

Increases in river runoff will increase the freshwater supply and riverine heat to the Eurasian shelf seas and have implications for local and Arctic-wide stratification dynamics and on the Arctic halocline as well as for sea ice and local biogeochemistry (section 6.8).

The impact the above changes have on the wider Arctic strongly depends on changes in stratification dynamics. On the one hand, having a larger open water region exposed to wind-driven mixing for longer periods could deepen stratification, increasing the tendency of a well-mixed plume. Alternatively, the increase in river runoff to the Arctic could strengthen surface stratification and increase the likelihood of a very shallow plume that extends out northwards towards the central Arctic. It is also possible that the likelihood of both of these alternating states could become more frequent, with the increased influence of wind variability with the loss of sea ice cover. Changes in stratification are crucial to understand for the future of the Arctic halocline and will be strongly coupled to changes in sea ice dynamics and persistence. This will have implications for the timing, magnitude and region of water mass formation / transformation.

Implications:

- The interconnected nature of SSS, SST and SIC, especially in the Laptev and East Siberian Sea, highlights the challenge but also the need to understand this region as a system rather than trying to understand drivers of individual components in isolation. This will prove vital to be able to predict how the conflicting changes in this region will impact both individual regions and wider Arctic sea ice dynamics and freshwater transport.

Future work:

1. We need to better understand the current Arctic system, and its natural variability in order to be able to accurately predict future Arctic changes.

Concluding Remarks

Untangling all these compounding changes remains a challenge and will only be solved by a unified approach bringing together a combination of different data products and types including in-situ data, satellite data and model output. The long satellite SSS timeseries has and will continue to be, with the launch of the Copernicus Imaging Microwave Radiometer (CIMR), an asset in understanding Arctic wide freshwater transport. Understanding these processes will be further aided by insights gained from the recently launched Surface Water and Ocean Topography (SWOT) mission, as well as from continued technological developments of higher resolution satellites for mapping sea surface geostrophic (and total) velocity, such as those proposed by SeaSTAR, Harmony and ODYSEA (Gommenginger et al., 2019; Lee et al., 2023; Morrow et al., 2019; Suess et al., 2022).

Bibliography

Aagaard, K., Carmack, E.C., 1989. The role of sea ice and other fresh water in the Arctic circulation. J. Geophys. Res. Oceans 94, 14485–14498. https://doi.org/10.1029/JC094iC10p14485

Aagaard, K., Weingartner, T.J., Danielson, S.L., Woodgate, R.A., Johnson, G.C., Whitledge, T.E., 2006. Some controls on flow and salinity in Bering Strait. Geophys. Res. Lett. 33. https://doi.org/10.1029/2006GL026612

Aksenov, Y., Ivanov, V.V., Nurser, A.J.G., Bacon, S., Polyakov, I.V., Coward, A.C., Naveira-Garabato, A.C., Beszczynska-Moeller, A., 2011. The Arctic Circumpolar Boundary Current. J. Geophys. Res. Oceans 116. https://doi.org/10.1029/2010JC006637

Aksenov, Y., Karcher, M., Proshutinsky, A., Gerdes, R., de Cuevas, B., Golubeva, E., Kauker, F., Nguyen, A.T., Platov, G.A., Wadley, M., Watanabe, E., Coward, A.C., Nurser, A.J.G., 2016. Arctic pathways of Pacific Water: Arctic Ocean Model Intercomparison experiments. J. Geophys. Res. Oceans 121, 27–59. https://doi.org/10.1002/2015JC011299

Alkire, M., Morison, J., Schweiger, A., Zhang, J., Steele, M., Peralta Ferriz, C., Dickinson, S., 2017. A Meteoric Water Budget for the Arctic Ocean. J. Geophys. Res. Oceans 122. https://doi.org/10.1002/2017jc012807

Alkire, M.B., Morison, J., Andersen, R., 2015. Variability in the meteoric water, sea-ice melt, and Pacific water contributions to the central Arctic Ocean, 2000–2014. J. Geophys. Res. Oceans 120, 1573–1598. https://doi.org/10.1002/2014JC010023

Allende, S., Treguier, A.M., Lique, C., de Boyer Montégut, C., Massonnet, F., Fichefet, T., Barthélemy, A., 2024. Impact of ocean vertical mixing parameterization on Arctic sea ice and upper ocean properties using the NEMO-SI3 model. Geosci. Model Dev. Discuss. 1–28. https://doi.org/10.5194/gmd-2024-49

Andersen, O., Nilsen, K., Sørensen, L., Skourup, H., Havelund, N., Nagler, T., Wuite, J., Kouraev, A., Zakharova, E., Fernandez, D., 2019. Arctic Freshwater Fluxes from Earth Observation Data. https://doi.org/10.1007/1345_2019_75

Anderson, L.G., Jutterström, S., Kaltin, S., Jones, E.P., Björk, G., 2004. Variability in river runoff distribution in the Eurasian Basin of the Arctic Ocean. J. Geophys. Res. Oceans 109. https://doi.org/10.1029/2003JC001773

Are, F., Reimnitz, E., 2000. An Overview of the Lena River Delta Setting: Geology, Tectonics, Geomorphology, and Hydrology on JSTOR.

Armitage, T.W.K., Bacon, S., Kwok, R., 2018. Arctic Sea Level and Surface Circulation Response to the Arctic Oscillation. Geophys. Res. Lett. 45, 6576–6584. https://doi.org/10.1029/2018GL078386

Arpaia, L., Ferrarin, C., Bajo, M., Umgiesser, G., 2023. A flexible z-coordinate approach for the accurate representation of free surface flows in a coastal ocean model (SHYFEM v. 7_5_71) (preprint). Oceanography. https://doi.org/10.5194/gmd-2023-13

Babb, D.G., Landy, J.C., Barber, D.G., Galley, R.J., 2019. Winter Sea Ice Export From the Beaufort Sea as a Preconditioning Mechanism for Enhanced Summer Melt: A Case Study of 2016. J. Geophys. Res. Oceans 124, 6575–6600. https://doi.org/10.1029/2019JC015053

Bauch, D., Gröger, M., Dmitrenko, I., Hölemann, J., Kirillov, S., Mackensen, A., Taldenkova, E., Andersen, N., 2010. Atmospheric controlled freshwater release at the Laptev Sea continental margin. Polar Res. https://doi.org/10.3402/polar.v30i0.5858

Bauch, D., Hölemann, J.A., Nikulina, A., Wegner, C., Janout, M.A., Timokhov, L.A., Kassens, H., 2013. Correlation of river water and local sea-ice melting on the Laptev Sea shelf (Siberian Arctic). J. Geophys. Res. Oceans 118, 550–561. https://doi.org/10.1002/jgrc.20076

Baumann, T.M., Polyakov, I.V., Pnyushkov, A.V., Rember, R., Ivanov, V.V., Alkire, M.B., Goszczko, I., Carmack, E.C., 2018. On the Seasonal Cycles Observed at the Continental Slope of the Eastern Eurasian Basin of the Arctic Ocean. J. Phys. Oceanogr. 48, 1451–1470. https://doi.org/10.1175/JPO-D-17-0163.1

Bertosio, C., Provost, C., Athanase, M., Sennéchael, N., Garric, G., Lellouche, J.-M., Bricaud, C., Kim, J.-H., Cho, K.-H., Park, T., 2022. Changes in Freshwater Distribution and Pathways in the Arctic Ocean Since

2007 in the Mercator Ocean Global Operational System. J. Geophys. Res. Oceans 127, e2021JC017701. https://doi.org/10.1029/2021JC017701

Biló, T.C., Straneo, F., Holte, J., Le Bras, I. a.-A., 2022. Arrival of New Great Salinity Anomaly Weakens Convection in the Irminger Sea. Geophys. Res. Lett. 49, e2022GL098857. https://doi.org/10.1029/2022GL098857

Bluhm, B.A., Kosobokova, K.N., Carmack, E.C., 2015. A tale of two basins: An integrated physical and biological perspective of the deep Arctic Ocean. Prog. Oceanogr., Overarching perspectives of contemporary and future ecosystems in the Arctic Ocean 139, 89–121. https://doi.org/10.1016/j.pocean.2015.07.011

Bourdalle-Badie, R., Treguier, A.M., 2006. A climatology of runoff for the global ocean-ice model.

Boutin, J., Vergely, J.-L., Khvorostyanov, D., 2024. SMOS Arctic SSS L3 V2 maps produced by LOCEAN Expertise Center. https://doi.org/10.17882/98769

Brown, K., Holding, J., Carmack, E., 2020. Understanding Regional and Seasonal Variability Is Key to Gaining a Pan-Arctic Perspective on Arctic Ocean Freshening. Front. Mar. Sci. 7, 606. https://doi.org/10.3389/fmars.2020.00606

Cai, D., Lohmann, G., Chen, X., Ionita, M., 2024. The linkage between autumn Barents-Kara sea ice and European cold winter extremes. Front. Clim. 6. https://doi.org/10.3389/fclim.2024.1345763

Cai, L., Alexeev, V.A., Walsh, J.E., Bhatt, U.S., 2018. Patterns, Impacts, and Future Projections of Summer Variability in the Arctic from CMIP5 Models. J. Clim. 31, 9815–9833. https://doi.org/10.1175/JCLI-D-18-0119.1

Carmack, E.C., 2007. The alpha/beta ocean distinction: A perspective on freshwater fluxes, convection, nutrients and productivity in high-latitude seas. Deep Sea Res. Part II Top. Stud. Oceanogr., Effects of Climate Variability on Sub-Arctic Marine Ecosystems 54, 2578–2598. https://doi.org/10.1016/j.dsr2.2007.08.018

Carmack, E.C., Yamamoto-Kawai, M., Haine, T.W.N., Bacon, S., Bluhm, B.A., Lique, C., Melling, H., Polyakov, I.V., Straneo, F., Timmermans, M.L., Williams, W.J., 2016. Freshwater and its role in the Arctic Marine System: Sources, disposition, storage, export, and physical and biogeochemical consequences in the Arctic and global oceans. J. Geophys. Res. G Biogeosciences 121, 675–717. https://doi.org/10.1002/2015JG003140

Charette, M.A., Kipp, L.E., Jensen, L.T., Dabrowski, J.S., Whitmore, L.M., Fitzsimmons, J.N., Williford, T., Ulfsbo, A., Jones, E., Bundy, R.M., Vivancos, S.M., Pahnke, K., John, S.G., Xiang, Y., Hatta, M., Petrova, M.V., Heimbürger-Boavida, L.-E., Bauch, D., Newton, R., Pasqualini, A., Agather, A.M., Amon, R.M.W., Anderson, R.F., Andersson, P.S., Benner, R., Bowman, K.L., Edwards, R.L., Gdaniec, S., Gerringa, L.J.A., González, A.G., Granskog, M., Haley, B., Hammerschmidt, C.R., Hansell, D.A., Henderson, P.B., Kadko, D.C., Kaiser, K., Laan, P., Lam, P.J., Lamborg, C.H., Levier, M., Li, X., Margolin, A.R., Measures, C., Middag, R., Millero, F.J., Moore, W.S., Paffrath, R., Planquette, H., Rabe, B., Reader, H., Rember, R., Rijkenberg, M.J.A., Roy-Barman, M., Rutgers van der Loeff, M., Saito, M., Schauer, U., Schlosser, P., Sherrell, R.M., Shiller, A.M., Slagter, H., Sonke, J.E., Stedmon, C., Woosley, R.J., Valk, O., van Ooijen, J., Zhang, R., 2020. The Transpolar Drift as a Source of Riverine and Shelf-Derived Trace Elements to the Central Arctic Ocean. J. Geophys. Res. Oceans 125, e2019JC015920. https://doi.org/10.1029/2019JC015920

Chen, Jinlei, Kang, S., Chen, C., You, Q., Du, W., Xu, M., Zhong, X., Zhang, W., Chen, Jizu, 2020. Changes in sea ice and future accessibility along the Arctic Northeast Passage. Glob. Planet. Change 195, 103319. https://doi.org/10.1016/j.gloplacha.2020.103319

Churakova Sidorova, O.V., Siegwolf, R.T.W., Fonti, M.V., Vaganov, E.A., Saurer, M., 2021. Spring arctic oscillation as a trigger of summer drought in Siberian subarctic over the past 1494 years. Sci. Rep. 11, 19010. https://doi.org/10.1038/s41598-021-97911-2

Cohen, J., Jones, J., Furtado, J., Tziperman, E., 2013. Warm Arctic, Cold Continents: A Common Pattern Related to Arctic Sea Ice Melt, Snow Advance, and Extreme Winter Weather. Oceanography 26. https://doi.org/10.5670/oceanog.2013.70

Cohen, J., Screen, J.A., Furtado, J.C., Barlow, M., Whittleston, D., Coumou, D., Francis, J., Dethloff, K., Entekhabi, D., Overland, J., Jones, J., 2014. Recent Arctic amplification and extreme mid-latitude weather. Nat. Geosci. 7, 627–637. https://doi.org/10.1038/ngeo2234

Cornish, S.B., Kostov, Y., Johnson, H.L., Lique, C., 2020. Response of Arctic Freshwater to the Arctic Oscillation in Coupled Climate Models. J. Clim. 33, 2533–2555. https://doi.org/10.1175/JCLI-D-19-0685.1

Dai, A., Qian, T., Trenberth, K.E., Milliman, J.D., 2009. Changes in Continental Freshwater Discharge from 1948 to 2004. J. Clim. 22, 2773–2792. https://doi.org/10.1175/2008JCLI2592.1

Dai, A., Trenberth, K.E., 2002. Estimates of Freshwater Discharge from Continents: Latitudinal and Seasonal Variations.

Davidson, N.C., 2018. Yenisei River Basin and Lake Baikal (Russia), in: Finlayson, C.M., Milton, G.R., Prentice, R.C., Davidson, N.C. (Eds.), The Wetland Book: II: Distribution, Description, and Conservation. Springer Netherlands, Dordrecht, pp. 1477–1484. https://doi.org/10.1007/978-94-007-4001-3_276

Dean, K.G., Stringer, W.J., Ahlnas, K., Searcy, C., Weingartner, T., 1994. The influence of river discharge on the thawing of sea ice, Mackenzie River Delta: albedo and temperature analyses. Polar Res. 13, 83–94. https://doi.org/10.1111/j.1751-8369.1994.tb00439.x

Delhaye, S., Massonnet, F., Fichefet, T., Msadek, R., Terray, L., Screen, J., 2024. Dominant role of early winter Barents–Kara sea ice extent anomalies in subsequent atmospheric circulation changes in CMIP6 models. Clim. Dyn. 62, 2755–2778. https://doi.org/10.1007/s00382-023-06904-6

Dianskii, N.A., Fomin, V.V., Gruzinov, V.M., Kabatchenko, I.M., Litvinenko, G.I., 2015. Estimation of influence of the ship channel of the Sabetta Harbour on change of hydrological conditions of the Gulf of Ob using numerical modelling [in Russian]. Arct. Ecol Econ 3, 18–29.

Dickson, R.R., Osborn, T.J., Hurrell, J.W., Meincke, J., Blindheim, J., Adlandsvik, B., Vinje, T., Alekseev, G., Maslowski, W., 2000. The Arctic Ocean Response to the North Atlantic Oscillation. J. Clim. 13, 2671–2696. https://doi.org/10.1175/1520-0442(2000)013<2671:TAORTT>2.0.CO;2

Ding, Q., Schweiger, A., L'Heureux, M., Battisti, D.S., Po-Chedley, S., Johnson, N.C., Blanchard-Wrigglesworth, E., Harnos, K., Zhang, Q., Eastman, R., Steig, E.J., 2017. Influence of high-latitude atmospheric circulation changes on summertime Arctic sea ice. Nat. Clim. Change 7, 289–295. https://doi.org/10.1038/nclimate3241

Ding, S., Wu, B., 2021. Linkage between autumn sea ice loss and ensuing spring Eurasian temperature. Clim. Dyn. 57, 2793–2810. https://doi.org/10.1007/s00382-021-05839-0

Ding, S., Wu, B., Chen, W., 2021. Dominant Characteristics of Early Autumn Arctic Sea Ice Variability and Its Impact on Winter Eurasian Climate. https://doi.org/10.1175/JCLI-D-19-0834.1

Dmitrenko, I., Kirillov, S., Eicken, H., Markova, N., 2005. Wind-driven summer surface hydrography of the eastern Siberian shelf. Geophys. Res. Lett. 32. https://doi.org/10.1029/2005GL023022

Dmitrenko, I.A., Kirillov, S.A., Tremblay, L.B., 2008. The long-term and interannual variability of summer fresh water storage over the eastern Siberian shelf: Implication for climatic change. J. Geophys. Res. Oceans 113. https://doi.org/10.1029/2007JC004304

Dolgopolova, E.N., 2015. Regularities in the motion of water and sediments at the mouth of a river of estuarine-deltaic type: Case study of the Yenisei R. Water Resour. 42, 198–207. https://doi.org/10.1134/S0097807815020050

Dong, J., Shi, X., Gong, X., Astakhov, A.S., Hu, L., Liu, X., Yang, G., Wang, Y., Vasilenko, Y., Qiao, S., Bosin, A., Lohmann, G., 2022. Enhanced Arctic sea ice melting controlled by larger heat discharge of mid-Holocene rivers. Nat. Commun. 13, 5368. https://doi.org/10.1038/s41467-022-33106-1

Dörr, J., Årthun, M., Docquier, D., Li, C., Eldevik, T., 2024. Causal Links Between Sea-Ice Variability in the Barents-Kara Seas and Oceanic and Atmospheric Drivers. Geophys. Res. Lett. 51, e2024GL108195. https://doi.org/10.1029/2024GL108195

Drushka, K., Westbrook, E., Bingham, F., Gaube, P., Dickinson, S., Fournier, S., Menezes, V., Misra, S., Perez, J., Rainville, E., Schanze, J., Schmidgall, C., Shcherbina, A., Steele, M., Thomson, J., Zippel, S., 2024. Salinity and Stratification at the Sea Ice Edge (SASSIE): An oceanographic field campaign in the Beaufort Sea. https://doi.org/10.5194/essd-2023-406

Dubinina, E.O., Kossova, S.A., Miroshnikov, A.Yu., Kokryatskaya, N.M., 2017. Isotope (δD, δ18O) systematics in waters of the Russian Arctic seas. Geochem. Int. 55, 1022–1032. https://doi.org/10.1134/S0016702917110052

Fofonova, V., Androsov, A., Danilov, S., Janout, M., Sofina, E., Wiltshire, K., 2014. Semidiurnal tides in the Laptev Sea Shelf zone in the summer season. Cont. Shelf Res. 73, 119–132. https://doi.org/10.1016/j.csr.2013.11.010

Fong, D.A., Geyer, W.R., 2002. The Alongshore Transport of Freshwater in a Surface-Trapped River Plume. J. Phys. Oceanogr. 32, 957–972. https://doi.org/10.1175/1520-0485(2002)032<0957:TATOFI>2.0.CO;2

Font, J., Camps, A., Borges, A., Martín-Neira, M., Boutin, J., Reul, N., Kerr, Y.H., Hahne, A., Mecklenburg, S., 2010. SMOS: The Challenging Sea Surface Salinity Measurement From Space. Proc. IEEE 98, 649–665. https://doi.org/10.1109/JPROC.2009.2033096

Fournier, S., Lee, T., Tang, W., Steele, M., Olmedo, E., 2019. Evaluation and Intercomparison of SMOS, Aquarius, and SMAP Sea Surface Salinity Products in the Arctic Ocean. Remote Sens. 11, 3043. https://doi.org/10.3390/rs11243043

Garvine, R.W., 1987. Estuary Plumes and Fronts in Shelf Waters: A Layer Model. J. Phys. Oceanogr. 17, 1877–1896. https://doi.org/10.1175/1520-0485(1987)017<1877:EPAFIS>2.0.CO;2

Giles, K.A., Laxon, S.W., Ridout, A.L., Wingham, D.J., Bacon, S., 2012. Western Arctic Ocean freshwater storage increased by wind-driven spin-up of the Beaufort Gyre. Nat. Geosci. 5, 194–197. https://doi.org/10.1038/ngeo1379

Gommenginger, C., Chapron, B., Hogg, A., Buckingham, C., Fox-Kemper, B., Eriksson, L., Soulat, F., Ubelmann, C., Ocampo-Torres, F., Nardelli, B.B., Griffin, D., Lopez-Dekker, F., Knudsen, P., Andersen, O.B., Stenseng, L., Stapleton, N., Perrie, W., Violante-Carvalho, N., Schulz-Stellenfleth, J., Woolf, D., Isern-Fontanet, J., Ardhuin, F., Klein, P.M., Mouche, A., Pascual, A., Capet, X., Hauser, D., Stoffelen, A., Morrow, R.A., Aouf, L., Breivik, Ø., Fu, L.L., Johannessen, J.A., Aksenov, Y., Bricheno, L., Hirschi, J., Martin, A.C., Martin, A.P., Nurser, G., Polton, J., Wolf, J., Johnsen, H., Soloviev, A., Jacobs, G., Collard, F., Groom, S.B., Kudryavstev, V., Wilkin, J.L., Navarro, V., Babanin, A., Martin, M.J., Siddorn, J., Saulter, A., Rippeth, T., Emery, W., Maximenko, N., Romeiser, R., Graber, H., Alvera-Azcárate, A., Hughes, C., Vandemark, D., da Silva, J., Van Leeuwen, P.J., Naveira-Gabarato, A., Gemmrich, J., Mahadevan, A., Marquez, J., Munro, Y., Doody, S., Burbidge, G., 2019. SEASTAR: A mission to study ocean submesoscale dynamics and small-scale atmosphere-ocean processes in coastal, shelf and polar seas. Front. Mar. Sci. 6. https://doi.org/10.3389/fmars.2019.00457

Gonçalves-Araujo, R., 2016. Tracing environmental variability in the changing Arctic Ocean with optical measurements of dissolved organic matter. ResearchGate. http://dx.doi.org/10.13140/RG.2.2.16968.32001

Graversen, R.G., 2006. Do Changes in the Midlatitude Circulation Have Any Impact on the Arctic Surface Air Temperature Trend? https://doi.org/10.1175/JCLI3906.1

Graversen, R.G., Burtu, M., 2016. Arctic amplification enhanced by latent energy transport of atmospheric planetary waves. Q. J. R. Meteorol. Soc. 142, 2046–2054. https://doi.org/10.1002/qj.2802

Griffin, C.G., McClelland, J.W., Frey, K.E., Fiske, G., Holmes, R.M., 2018. Quantifying CDOM and DOC in major Arctic rivers during ice-free conditions using Landsat TM and ETM+ data. Remote Sens. Environ. 209, 395–409. https://doi.org/10.1016/j.rse.2018.02.060

Haine, T.W.N., Curry, B., Gerdes, R., Hansen, E., Karcher, M., Lee, C., Rudels, B., Spreen, G., de Steur, L., Stewart, K.D., Woodgate, R., 2015. Arctic freshwater export: Status, mechanisms, and prospects. Glob. Planet. Change 125, 13–35. https://doi.org/10.1016/j.gloplacha.2014.11.013

Haine, T.W.N., Siddiqui, A.H., Jiang, W., 2023. Arctic freshwater impact on the Atlantic Meridional Overturning Circulation: status and prospects. Philos. Transact. A Math. Phys. Eng. Sci. 381, 20220185. https://doi.org/10.1098/rsta.2022.0185

Hall, S.B., Subrahmanyam, B., Nyadjro, E.S., Samuelsen, A., 2021. Surface Freshwater Fluxes in the Arctic and Subarctic Seas during Contrasting Years of High and Low Summer Sea Ice Extent. Remote Sens. 13, 1570. https://doi.org/10.3390/rs13081570

Hall, S.B., Subrahmanyam, B., Steele, M., 2023. The Role of the Russian Shelf in Seasonal and Interannual Variability of Arctic Sea Surface Salinity and Freshwater Content. J. Geophys. Res. Oceans 128, e2022JC019247. https://doi.org/10.1029/2022JC019247

Harms, I.H., Karcher, M.J., 2005. Kara Sea freshwater dispersion and export in the late 1990s. J. Geophys. Res. Oceans 110. https://doi.org/10.1029/2004JC002744

Hersbach, H., Bell, B., Berrisford, P., Hirahara, S., Horányi, A., Muñoz-Sabater, J., Nicolas, J., Peubey, C., Radu, R., Schepers, D., Simmons, A., Soci, C., Abdalla, S., Abellan, X., Balsamo, G., Bechtold, P., Biavati, G., Bidlot, J., Bonavita, M., De Chiara, G., Dahlgren, P., Dee, D., Diamantakis, M., Dragani, R., Flemming, J., Forbes, R., Fuentes, M., Geer, A., Haimberger, L., Healy, S., Hogan, R.J., Hólm, E., Janisková, M., Keeley, S., Laloyaux, P., Lopez, P., Lupu, C., Radnoti, G., de Rosnay, P., Rozum, I., Vamborg, F., Villaume, S., Thépaut, J.-N., 2020. The ERA5 global reanalysis. Q. J. R. Meteorol. Soc. 146, 1999–2049. https://doi.org/10.1002/qj.3803

Heuzé, C., Jahn, A., 2024. The first ice-free day in the Arctic Ocean could occur before 2030. Nat. Commun. 15, 10101. https://doi.org/10.1038/s41467-024-54508-3

Heuzé, C., Zanowski, H., Karam, S., Muilwijk, M., 2023. The Deep Arctic Ocean and Fram Strait in CMIP6 Models. J. Clim. 36, 2551–2584. https://doi.org/10.1175/JCLI-D-22-0194.1

Hölemann, J.A., Kirillov, S., Klagge, T., Novikhin, A., Kassens, H., Timokhov, L., 2011. Near-bottom water warming in the Laptev Sea in response to atmospheric and sea-ice conditions in 2007. Polar Res. 30, 6425. https://doi.org/10.3402/polar.v30i0.6425

Holland, M.M., Stroeve, J., 2011. Changing seasonal sea ice predictor relationships in a changing Arctic climate. Geophys. Res. Lett. 38. https://doi.org/10.1029/2011GL049303

Hordoir, R., Skagseth, Ø., Ingvaldsen, R.B., Sandø, A.B., Löptien, U., Dietze, H., Gierisch, A.M.U., Assmann, K.M., Lundesgaard, Ø., Lind, S., 2022. Changes in Arctic Stratification and Mixed Layer Depth Cycle: A Modeling Analysis. J. Geophys. Res. Oceans 127, e2021JC017270. https://doi.org/10.1029/2021JC017270

Horner-Devine, A.R., Hetland, R.D., MacDonald, D.G., 2015. Mixing and Transport in Coastal River Plumes. Annu. Rev. Fluid Mech. 47, 569–594. https://doi.org/10.1146/annurev-fluid-010313-141408

Houssais, M.-N., Herbaut, C., Schlichtholz, P., Rousset, C., 2007. Arctic salinity anomalies and their link to the North Atlantic during a positive phase of the Arctic Oscillation. Prog. Oceanogr. 73, 160–189. https://doi.org/10.1016/j.pocean.2007.02.005

Hudson, P.A., Martin, A.C.H., Josey, S.A., Marzocchi, A., Angeloudis, A., 2024. Drivers of Laptev Sea interannual variability in salinity and temperature. Ocean Sci. 20, 341–367. https://doi.org/10.5194/os-20-341-2024

IPCC (Intergovernmental Panel on Climate Change), 2019. Special Report: The Ocean and Cryosphere in a Changing Climate (final draft). IPCC Summ. Policymalers TBD, TBD. https://www.ipcc.ch/report/srocc/

Itkin, P., Krumpen, T., 2017. Winter sea ice export from the Laptev Sea preconditions the local summer sea ice cover and fast ice decay. Cryosphere 11, 2383–2391. https://doi.org/10.5194/tc-11-2383-2017

Jakob, L., Gourmelen, N., 2023. Glacier Mass Loss Between 2010 and 2020 Dominated by Atmospheric Forcing. Geophys. Res. Lett. 50, e2023GL102954. https://doi.org/10.1029/2023GL102954

Janout, M., Hölemann, J., Juhls, B., Krumpen, T., Rabe, B., Bauch, D., Wegner, C., Kassens, H., Timokhov, L., 2016. Episodic warming of near-bottom waters under the Arctic sea ice on the central Laptev Sea shelf. Geophys. Res. Lett. 43, 264–272. https://doi.org/10.1002/2015GL066565

Janout, M.A., Aksenov, Y., Hölemann, J.A., Rabe, B., Schauer, U., Polyakov, I.V., Bacon, S., Coward, A.C., Karcher, M., Lenn, Y.-D., Kassens, H., Timokhov, L., 2015. Kara Sea freshwater transport through Vilkitsky Strait: Variability, forcing, and further pathways toward the western Arctic Ocean from a model and observations: KARA SEA FRESHWATER TRANSPORT. J. Geophys. Res. Oceans 120, 4925–4944. https://doi.org/10.1002/2014JC010635

Janout, M.A., Hölemann, J., Laukert, G., Smirnov, A., Krumpen, T., Bauch, D., Timokhov, L., 2020. On the Variability of Stratification in the Freshwater-Influenced Laptev Sea Region. Front. Mar. Sci. 7.

Janout, M.A., Ivanov, V., Hölemann, J.A., Horn, M., Kassens, H., Polyakov, I., Rabe, B., Tippenhauer, S., 2019. Underway CTD measurements during Akademik Tryoshnikov cruise AT2018 to the Arctic Ocean. https://doi.org/10.1594/PANGAEA.902600

Janout, M.A., Lenn, Y.-D., 2014. Semidiurnal Tides on the Laptev Sea Shelf with Implications for Shear and Vertical Mixing. J. Phys. Oceanogr. 44, 202–219. https://doi.org/10.1175/JPO-D-12-0240.1

Johnson, M.A., Polyakov, I.V., 2001. The Laptev Sea as a source for recent Arctic Ocean salinity changes. Geophys. Res. Lett. 28, 2017–2020. https://doi.org/10.1029/2000GL012740

Jonsson, S., 1989. The structure and forcing of the large-and mesoscale circulation in the Nordic Seas, with special reference to the Fram Strait (PhD Thesis). Ph. D. dissertation, 144 pp., Univ. of Bergen, Bergen, Norway.

Juhls, B., Stedmon, C.A., Morgenstern, A., Meyer, H., Hölemann, J., Heim, B., Povazhnyi, V., Overduin, P.P., 2020. Identifying Drivers of Seasonality in Lena River Biogeochemistry and Dissolved Organic Matter Fluxes. Front. Environ. Sci. 8.

Karcher, M., Kulakov, M., Pivovarov, S., Schauer, U., Kauker, F., Schlitzer, R., 2003. Atlantic Water flow to the Kara Sea - comparing model results with observations. Sib. River Runoff Kara Sea Characterisation Quantif. Var. Environ. Significance Stein Fahl Fütterer Galimov Eds Elsevier Proc. Mar. Sci. 47–69.

Kay, J.E., L'Ecuyer, T., Gettelman, A., Stephens, G., O'Dell, C., 2008. The contribution of cloud and radiation anomalies to the 2007 Arctic sea ice extent minimum. Geophys. Res. Lett. 35. https://doi.org/10.1029/2008GL033451

Kazakova, U., Polukhin, A., Shabanov, P., 2024. Origin and evolution of the surface desalinated layer of the Kara Sea during the ice-free period. J. Mar. Syst. 243, 103950. https://doi.org/10.1016/j.jmarsys.2023.103950

Kelly, S., Popova, E., Aksenov, Y., Marsh, R., Yool, A., 2018. Lagrangian Modeling of Arctic Ocean Circulation Pathways: Impact of Advection on Spread of Pollutants. J. Geophys. Res. Oceans 123, 2882–2902. https://doi.org/10.1002/2017JC013460

Kerr, Y.H., Waldteufel, P., Wigneron, J.P., Delwart, S., Cabot, F., Boutin, J., Escorihuela, M.J., Font, J., Reul, N., Gruhier, C., Juglea, S.E., Drinkwater, M.R., Hahne, A., Martin-Neira, M., Mecklenburg, S., 2010. The SMOS L: New tool for monitoring key elements ofthe global water cycle. Proc. IEEE 98, 666–687. https://doi.org/10.1109/JPROC.2010.2043032

Koch-Larrouy, A., Madec, G., Blanke, B., Molcard, R., 2008. Water mass transformation along the Indonesian throughflow in an OGCM. Ocean Dyn. 58, 289–309. https://doi.org/10.1007/s10236-008-0155-4

Kraineva, M.V., Golubeva, E.N., 2022. Formation of Temperature Anomalies in the Laptev Sea (2000–2020 Years), in: Chaplina, T. (Ed.), Processes in GeoMedia—Volume V, Springer Geology. Springer International Publishing, Cham, pp. 169–178. https://doi.org/10.1007/978-3-030-85851-3_19

Krumpen, T., Janout, M., Hodges, K.I., Gerdes, R., Girard-Ardhuin, F., Hölemann, J.A., Willmes, S., 2013. Variability and trends in Laptev Sea ice outflow between 1992–2011. The Cryosphere 7, 349–363. https://doi.org/10.5194/tc-7-349-2013

Kryjov, V., 2002. The influence of the winter Arctic Oscillation on the northern Russia spring temperature. Int. J. Climatol. 22, 779–785. https://doi.org/10.1002/joc.746

Kubryakov, A., Stanichny, S., Zatsepin, A., 2016. River plume dynamics in the Kara Sea from altimetry-based lagrangian model, satellite salinity and chlorophyll data. Remote Sens. Environ. 176, 177–187. https://doi.org/10.1016/j.rse.2016.01.020

Lagerloef, G., Colomb, F.R., Le Vine, D., Wentz, F., Yueh, S., Ruf, C., Lilly, J., Gunn, J., Chao, Y., deCharon, A., Feldman, G., Swift, C., 2008. The Aquarius/SAC-D Mission: Designed to Meet the Salinity Remote-Sensing Challenge. Oceanography 21, 68–81. https://doi.org/10.5670/oceanog.2008.68

Lambert, E., Nummelin, A., Pemberton, P., Ilıcak, M., 2019. Tracing the Imprint of River Runoff Variability on Arctic Water Mass Transformation. J. Geophys. Res. Oceans 124, 302–319. https://doi.org/10.1029/2017JC013704

Lammers, R.B., Shiklomanov, A.I., Vörösmarty, C.J., Fekete, B.M., Peterson, B.J., 2001. Assessment of contemporary Arctic river runoff based on observational discharge records. J. Geophys. Res. Atmospheres 106, 3321–3334. https://doi.org/10.1029/2000JD900444

Lapenis, A.G., Yurganov, L.N., 2023. Increase in Arctic Oscillations explains most interannual variability in Russia's wildfires. Front. For. Glob. Change 6. https://doi.org/10.3389/ffgc.2023.1188057

LeBlond, P.H., 1980. On the Surface Circulation in Some Channels of the Canadian Arctic Archipelago. ARCTIC 33, 189–197. https://doi.org/10.14430/arctic2554

Lee, T., Gille, S., Ardhuin, F., Boland, J., Bourassa, M., Chang, P., Cravatte, S., Farrar, T., Fewings, M., Jacobs, G., Jelenak, Z., Lyard, F., May, J., Remy, E., Renault, L., Rodriguez, E., Ubelmann, C., Bôas, B.V., Wineteer, A., 2023. A satellite mission concept to unravel small-scale ocean dynamics and air-sea interactions: ODYSEA (Ocean Dynamics and Surface Exchange with the Atmosphere) (No. EGU23-4875). Presented at the EGU23, Copernicus Meetings. https://doi.org/10.5194/egusphere-egu23-4875

Lellouche, J.-M., Greiner, E., Romain, B.-B., Gilles, G., Angélique, M., Marie, D., Clément, B., Mathieu, H., Olivier, L.G., Charly, R., Tony, C., Charles-Emmanuel, T., Florent, G., Giovanni, R., Mounir, B., Yann, D., Pierre-Yves, L.T., 2021. The Copernicus Global 1/12° Oceanic and Sea Ice GLORYS12 Reanalysis. Front. Earth Sci. 9.

Lemeshko, E.M., Tsyganova, M.V., 2022. Interannual variability of surface salinity in the Kara Sea according to satellite data, in: 28th International Symposium on Atmospheric and Ocean Optics: Atmospheric Physics. Presented at the 28th International Symposium on Atmospheric and Ocean Optics: Atmospheric Physics, SPIE, pp. 861–866. https://doi.org/10.1117/12.2644223

Lentz, S.J., Fewings, M.R., 2012. The Wind- and Wave-Driven Inner-Shelf Circulation. Annu. Rev. Mar. Sci. 4, 317–343. https://doi.org/10.1146/annurev-marine-120709-142745

Lentz, S.J., Helfrich, K.R., 2002. Buoyant gravity currents along a sloping bottom in a rotating fluid. J. Fluid Mech. 464, 251–278. https://doi.org/10.1017/S0022112002008868

L'Heureux, M.L., Kumar, A., Bell, G.D., Halpert, M.S., Higgins, R.W., 2008. Role of the Pacific-North American (PNA) pattern in the 2007 Arctic sea ice decline. Geophys. Res. Lett. 35. https://doi.org/10.1029/2008GL035205

Li, F., Wang, H., 2012. Autumn Sea Ice Cover, Winter Northern Hemisphere Annular Mode, and Winter Precipitation in Eurasia. https://doi.org/10.1175/JCLI-D-12-00380.1

Lim, Y.-K., Wu, D.L., Kim, K.-M., Lee, J.N., 2022. Impact of the Arctic oscillation from March on summertime sea ice. Environ. Res. Clim. 1, 021001. https://doi.org/10.1088/2752-5295/ac91e8

Liu, Y., Key, J.R., Liu, Z., Wang, X., Vavrus, S.J., 2012. A cloudier Arctic expected with diminishing sea ice. Geophys. Res. Lett. 39. https://doi.org/10.1029/2012GL051251

Liu, Y., Wang, J., Han, G., Lin, X., Yang, G., Ji, Q., 2022. Spatio-temporal analysis of east greenland polar front. Front. Mar. Sci. 9.

Mäkinen, J., Vanhatalo, J., 2016. Hydrographic responses to regional covariates across the Kara Sea. J. Geophys. Res. Oceans 121, 8872–8887. https://doi.org/10.1002/2016JC011981

Makkaveev, P.N., Stunzhas, P.A., Khlebopashev, P.V., 2010. The distinguishing of the Ob and Yenisei waters in the desalinated lenses of the Kara Sea in 1993 and 2007. Oceanology 50, 698–705. https://doi.org/10.1134/S0001437010050073

Marsh, R., Dey, D., Lenn, Y.-D., Roberts, E.M., 2024. Shifts from surface density compensation to projected warming, freshening and stronger stratification in the subpolar North Atlantic. Clim. Dyn. 62, 8227–8253. https://doi.org/10.1007/s00382-024-07336-6

Martin, A., Guimbard, S., Reverdin, G., Kolodziejczyk, N., Hudson, P., Supply, A., Ferrari, R., 2024. [D4.1] Product Validation and Intercomparison Report (PVIR), Climate Change Initiative+ (CCI+) Phase 2 Sea Surface Salinity (No. ESA-EOP-SC-AMT-2021-26). ESA.

Martínez, J., Gabarró, C., Turiel, A., González-Gambau, V., Umbert, M., Hoareau, N., González-Haro, C., Olmedo, E., Arias, M., Catany, R., Bertino, L., Raj, R.P., Xie, J., Sabia, R., Fernández, D., 2022. Improved BEC SMOS Arctic Sea Surface Salinity product v3.1. Earth Syst. Sci. Data 14, 307–323. https://doi.org/10.5194/essd-14-307-2022

Masina, S., Storto, A., Ferry, N., Valdivieso, M., Haines, K., Balmaseda, M., Zuo, H., Drevillon, M., Parent, L., 2017. An ensemble of eddy-permitting global ocean reanalyses from the MyOcean project. Clim. Dyn. 49, 813–841. https://doi.org/10.1007/s00382-015-2728-5

Masson-Delmotte, V., Zhai, P., Pirani, A., Connors, S.L., Péan, C., Berger, S., Caud, N., Chen, Y., Goldfarb, L., Gomis, M.I., Huang, M., Leitzell, K., Lonnoy, E., Matthews, J.B.R., Maycock, T.K., Waterfield, T., Yelekçi, Ö., Yu, R., Zhou, B. (Eds.), 2021. Climate Change 2021: The Physical Science Basis. Contribution of Working Group I to the Sixth Assessment Report of the Intergovernmental Panel on Climate Change. Cambridge University Press.

McClelland, J.W., Holmes, R.M., Dunton, K.H., Macdonald, R.W., 2012. The Arctic Ocean Estuary. Estuaries Coasts 35, 353–368. https://doi.org/10.1007/s12237-010-9357-3

McClimans, T.A., Johnson, D.R., Krosshavn, M., King, S.E., Carroll, J., Grenness, Ø., 2000. Transport processes in the Kara Sea. J. Geophys. Res. Oceans 105, 14121–14139. https://doi.org/10.1029/1999JC000012

McPhee, M.G., Proshutinsky, A., Morison, J.H., Steele, M., Alkire, M.B., 2009. Rapid change in freshwater content of the Arctic Ocean. Geophys. Res. Lett. 36. https://doi.org/10.1029/2009GL037525

Meissner, T., Wentz, F.J., Scott, J., Vazquez-Cuervo, J., 2016. Sensitivity of Ocean Surface Salinity Measurements From Spaceborne L-Band Radiometers to Ancillary Sea Surface Temperature. IEEE Trans. Geosci. Remote Sens. 54, 7105–7111. https://doi.org/10.1109/TGRS.2016.2596100

Melnikov, V.P., Pikinerov, P.V., Gennadinik, V.B., Babushkin, A.G., Moskovchenko, D.V., 2019. Change in the Hydrological Regime of Siberian Rivers as an Indicator of Changes in Cryological Conditions. Dokl. Earth Sci. 487, 990–994. https://doi.org/10.1134/S1028334X19080270

Mensah, V., Fujita, K., Howell, S., Ikeda, M., Komatsu, M., Ohshima, K.I., 2023. Estimation of ice melt, freshwater budget, and their multi-decadal trends in the Baffin Bay and Labrador Sea. https://doi.org/10.5194/egusphere-2023-2492

Merchant, C.J., Embury, O., Bulgin, C.E., Block, T., Corlett, G.K., Fiedler, E., Good, S.A., Mittaz, J., Rayner, N.A., Berry, D., Eastwood, S., Taylor, M., Tsushima, Y., Waterfall, A., Wilson, R., Donlon, C., 2019. Satellite-based time-series of sea-surface temperature since 1981 for climate applications. Sci. Data 6. https://doi.org/10.1038/s41597-019-0236-x

Morison, J., Kwok, R., Dickinson, S., Andersen, R., Peralta Ferriz, C., Morison, D., Rigor, I., Dewey, S., Guthrie, J., 2021. The Cyclonic Mode of Arctic Ocean Circulation. J. Phys. Oceanogr. https://doi.org/10.1175/JPO-D-20-0190.1

Morison, J., Kwok, R., Peralta-Ferriz, C., Alkire, M., Rigor, I., Andersen, R., Steele, M., 2012. Changing Arctic Ocean freshwater pathways. Nature 481, 66–70. https://doi.org/10.1038/nature10705

Morozov, E.G., Kozlov, I.E., Shchuka, S.A., Frey, D.I., 2017. Internal tide in the Kara Gates Strait. Oceanology 57, 8–18. https://doi.org/10.1134/S0001437017010106

Morrow, R., Fu, L.-L., Ardhuin, F., Benkiran, M., Chapron, B., Cosme, E., d'Ovidio, F., Farrar, J.T., Gille, S.T., Lapeyre, G., Le Traon, P.-Y., Pascual, A., Ponte, A., Qiu, B., Rascle, N., Ubelmann, C., Wang, J., Zaron, E.D., 2019. Global Observations of Fine-Scale Ocean Surface Topography With the Surface Water and Ocean Topography (SWOT) Mission. Front. Mar. Sci. 6.

Mu, L., Nerger, L., Streffing, J., Tang, Q., Niraula, B., Zampieri, L., Loza, S.N., Goessling, H.F., 2022. Sea-Ice Forecasts With an Upgraded AWI Coupled Prediction System. J. Adv. Model. Earth Syst. 14, e2022MS003176. https://doi.org/10.1029/2022MS003176

Muilwijk, M., Ilicak, M., Cornish, S.B., Danilov, S., Gelderloos, R., Gerdes, R., Haid, V., Haine, T.W.N., Johnson, H.L., Kostov, Y., Kovács, T., Lique, C., Marson, J.M., Myers, P.G., Scott, J., Smedsrud, L.H., Talandier, C., Wang, Q., 2019. Arctic Ocean Response to Greenland Sea Wind Anomalies in a Suite of Model Simulations. J. Geophys. Res. Oceans 124, 6286–6322. https://doi.org/10.1029/2019JC015101

Münchow, A., Melling, H., Falkner, K.K., 2006. An Observational Estimate of Volume and Freshwater Flux Leaving the Arctic Ocean through Nares Strait. J. Phys. Oceanogr. 36, 2025–2041. https://doi.org/10.1175/JPO2962.1

Nghiem, S.V., Hall, D.K., Rigor, I.G., Li, P., Neumann, G., 2014. Effects of Mackenzie River discharge and bathymetry on sea ice in the Beaufort Sea. Geophys. Res. Lett. 41, 873–879. https://doi.org/10.1002/2013GL058956

Nicolì, D., Bellucci, A., Iovino, D., Ruggieri, P., Gualdi, S., 2020. The impact of the AMV on Eurasian summer hydrological cycle. Sci. Rep. 10, 14444. https://doi.org/10.1038/s41598-020-71464-2

Nielsen, D.M., Dobrynin, M., Baehr, J., Razumov, S., Grigoriev, M., 2020. Coastal Erosion Variability at the Southern Laptev Sea Linked to Winter Sea Ice and the Arctic Oscillation. Geophys. Res. Lett. 47, e2019GL086876. https://doi.org/10.1029/2019GL086876

NOAA National Centers for Environmental Information, 2024. Arctic Oscillation (AO) | National Centers for Environmental Information (NCEI).

Nost, O., Isachsen, P., 2003. The large-scale time-mean ocean circulation in the Nordic Seas and Arctic Ocean estimated from simplified dynamics. J. Mar. Res. 61. https://doi.org/10.1357/002224003322005069

Notz, D., 2009. The future of ice sheets and sea ice: Between reversible retreat and unstoppable loss. Proc. Natl. Acad. Sci. 106, 20590–20595. https://doi.org/10.1073/pnas.0902356106

Nummelin, A., Ilicak, M., Li, C., Smedsrud, L.H., 2016. Consequences of future increased Arctic runoff on Arctic Ocean stratification, circulation, and sea ice cover. J. Geophys. Res. Oceans 121, 617–637. https://doi.org/10.1002/2015JC011156

Nummelin, A., Li, C., Smedsrud, L.H., 2015. Response of Arctic Ocean stratification to changing river runoff in a column model. J. Geophys. Res. Oceans 120, 2655–2675. https://doi.org/10.1002/2014JC010571

Ogi, M., Wallace, J.M., 2007. Summer minimum Arctic sea ice extent and the associated summer atmospheric circulation. Geophys. Res. Lett. 34. https://doi.org/10.1029/2007GL029897

Olmedo, E., Gabarró, C., González-Gambau, V., Martínez, J., Ballabrera-Poy, J., Turiel, A., Portabella, M., Fournier, S., Lee, T., 2018. Seven Years of SMOS Sea Surface Salinity at High Latitudes: Variability in Arctic and Sub-Arctic Regions. Remote Sens. 10, 1772. https://doi.org/10.3390/rs10111772

Oltmanns, M., Holliday, N.P., Screen, J., Moat, B.I., Josey, S.A., Evans, D.G., Bacon, S., 2024. European summer weather linked to North Atlantic freshwater anomalies in preceding years. Weather Clim. Dyn. 5, 109–132. https://doi.org/10.5194/wcd-5-109-2024

Ono, J., Watanabe, M., Komuro, Y., Tatebe, H., Abe, M., 2022. Enhanced Arctic warming amplification revealed in a low-emission scenario. Commun. Earth Environ. 3, 1–9. https://doi.org/10.1038/s43247-022-00354-4

Osadchiev, A.A., Asadulin, E.E., Miroshnikov, A.Y., Zavialov, I.B., Dubinina, E.O., Belyakova, P.A., 2019. Bottom Sediments Reveal Inter-Annual Variability of Interaction between the Ob and Yenisei Plumes in the Kara Sea. Sci. Rep. 9, 18642. https://doi.org/10.1038/s41598-019-55242-3

Osadchiev, A.A., Frey, D., Spivak, E., Shchuka, S., Tilinina, N., Semiletov, I., 2021a. Structure and Inter-Annual Variability of the Freshened Surface Layer in the Laptev and East-Siberian Seas During Ice-Free Periods. Front. Mar. Sci. 8, 1871. https://doi.org/10.3389/fmars.2021.735011

Osadchiev, A.A., Frey, D.I., Shchuka, S.A., Tilinina, N.D., Morozov, E.G., Zavialov, P.O., 2021b. Structure of the Freshened Surface Layer in the Kara Sea During Ice-Free Periods. J. Geophys. Res. Oceans 126, e2020JC016486. https://doi.org/10.1029/2020JC016486

Osadchiev, A.A., Izhitskiy, A.S., Zavialov, P.O., Kremenetskiy, V.V., Polukhin, A.A., Pelevin, V.V., Toktamysova, Z.M., 2017. Structure of the buoyant plume formed by Ob and Yenisei river discharge in the southern part of the Kara Sea during summer and autumn. J. Geophys. Res. Oceans 122, 5916–5935. https://doi.org/10.1002/2016JC012603

Osadchiev, A.A., Kuskova, E., Ivanov, V., 2024. The roles of river discharge and sea ice melting in formation of freshened surface layers in the Kara, Laptev, and East Siberian seas. Front. Mar. Sci. 11. https://doi.org/10.3389/fmars.2024.1348450

Osadchiev, A.A., Medvedev, I., Shchuka, S., Kulikov, M., Spivak, E., Pisareva, M., Semiletov, I., 2020a. Influence of estuarine tidal mixing on structure and spatial scales of large river plumes. Ocean Sci. 16, 781–798. https://doi.org/10.5194/os-16-781-2020

Osadchiev, A.A., Pisareva, M.N., Spivak, E.A., Shchuka, S.A., Semiletov, I.P., 2020b. Freshwater transport between the Kara, Laptev, and East-Siberian seas. Sci. Rep. 10, 13041. https://doi.org/10.1038/s41598-020-70096-w

Osadchiev, A.A., Sedakov, R., Frey, D., Gordey, A., Rogozhin, V., Zabudkina, Z., Spivak, E., Kuskova, E., Sazhin, A., Semiletov, I., 2023a. Intense zonal freshwater transport in the Eurasian Arctic during ice-covered season revealed by in situ measurements. Sci. Rep. 13, 16508. https://doi.org/10.1038/s41598-023-43524-w

Osadchiev, A.A., Zabudkina, Z., Rogozhin, V., Frey, D., Gordey, A., Spivak, E., Salyuk, A., Semiletov, I., Sedakov, R., 2023b. Structure of the Ob-Yenisei plume in the Kara Sea shortly before autumn ice formation. Front. Mar. Sci. 10. https://doi.org/10.3389/fmars.2023.1129331

Overland, J.E., Wang, M., 2010. Large-scale atmospheric circulation changes are associated with the recent loss of Arctic sea ice. Tellus A 62, 1–9. https://doi.org/10.1111/j.1600-0870.2009.00421.x

Paffrath, R., Laukert, G., Bauch, D., Rutgers van der Loeff, M., Pahnke, K., 2021. Separating individual contributions of major Siberian rivers in the Transpolar Drift of the Arctic Ocean. Sci. Rep. 11, 8216. https://doi.org/10.1038/s41598-021-86948-y

Panteleev, G., Proshutinsky, A., Kulakov, M., Nechaev, D.A., Maslowski, W., 2007. Investigation of the summer Kara Sea circulation employing a variational data assimilation technique. J. Geophys. Res. Oceans 112. https://doi.org/10.1029/2006JC003728

Park, H., Watanabe, E., Kim, Y., Polyakov, I., Oshima, K., Zhang, X., Kimball, J.S., Yang, D., 2020. Increasing riverine heat influx triggers Arctic sea ice decline and oceanic and atmospheric warming. Sci. Adv. 6, eabc4699. https://doi.org/10.1126/sciadv.abc4699

Pasternak, A., Drits, A., Arashkevich, E., Flint, M., 2022. Differential Impact of the Khatanga and Lena (Laptev Sea) Runoff on the Distribution and Grazing of Zooplankton. Front. Mar. Sci. 9.

Pavlov, V.C., Timokhov, L.A., Baskakov, G.A., Kulakov, M.Y., Kurazhov, V.K., Pavlov, P.V., 1996. Hydrometeorological Regime of the Kara, Laptev, and East-Siberian Seas. Defense Technical Information Center.

Pavlov, V.K., Pfirman, S.L., 1995. Hydrographic structure and variability of the Kara Sea: Implications for pollutant distribution. Deep Sea Res. Part II Top. Stud. Oceanogr. 42, 1369–1390. https://doi.org/10.1016/0967-0645(95)00046-1

Perovich, D.K., Richter-Menge, J.A., Jones, K.F., Light, B., 2008. Sunlight, water, and ice: Extreme Arctic sea ice melt during the summer of 2007. Geophys. Res. Lett. 35. https://doi.org/10.1029/2008GL034007

Piepmeier, J.R., Focardi, P., Horgan, K.A., Knuble, J., Ehsan, N., Lucey, J., Brambora, C., Brown, P.R., Hoffman, P.J., French, R.T., Mikhaylov, R.L., Kwack, E.-Y., Slimko, E.M., Dawson, D.E., Hudson, D., Peng, J., Mohammed, P.N., De Amici, G., Freedman, A.P., Medeiros, J., Sacks, F., Estep, R., Spencer, M.W., Chen, C.W., Wheeler, K.B., Edelstein, W.N., O'Neill, P.E., Njoku, E.G., 2017. SMAP L-Band Microwave Radiometer: Instrument Design and First Year on Orbit. IEEE Trans. Geosci. Remote Sens. 55, 1954–1966. https://doi.org/10.1109/tgrs.2016.2631978

Pimenta, F.M., Kirwan Jr., A.D., 2014. The response of large outflows to wind forcing. Cont. Shelf Res., Oceanographic processes associated with the main continental shelf waters off South and Southeastern Brazil 89, 24–37. https://doi.org/10.1016/j.csr.2013.11.006

Pivovarov, S.V., 2001. Hydrochemical investigations in the Arctic Ocean, in: HYDROCHEMICAL ATLAS OF THE ARCTIC OCEAN. State Research Center of the Russian Federation – the Arctic and Antarctic Research Institute of the Russian Federal Service for Hydrometeorology and Environmental Monitoring International Arctic Research Center, University of Alaska, Fairbank, St Petersberg, Fairbanks, pp. 6–41, 48–50.

Polukhin, A.A., Makkaveev, P.N., 2017. Peculiarities of the distribution of continental runoff in the water area of the Kara Sea. Океанология 25–37.

Polyakov, I.V., Alkire, M.B., Bluhm, B.A., Brown, K.A., Carmack, E.C., Chierici, M., Danielson, S.L., Ellingsen, I., Ershova, E.A., Gårdfeldt, K., Ingvaldsen, R.B., Pnyushkov, A.V., Slagstad, D., Wassmann, P., 2020a. Borealization of the Arctic Ocean in Response to Anomalous Advection From Sub-Arctic Seas. Front. Mar. Sci. 7. https://doi.org/10.3389/fmars.2020.00491

Polyakov, I.V., Beszczynska, A., Carmack, E.C., Dmitrenko, I.A., Fahrbach, E., Frolov, I.E., Gerdes, R., Hansen, E., Holfort, J., Ivanov, V.V., Johnson, M.A., Karcher, M., Kauker, F., Morison, J., Orvik, K.A., Schauer, U., Simmons, H.L., Skagseth, Ø., Sokolov, V.T., Steele, M., Timokhov, L.A., Walsh, D., Walsh, J.E., 2005. One more step toward a warmer Arctic. Geophys. Res. Lett. 32, 1–4. https://doi.org/10.1029/2005GL023740

Polyakov, I.V., Mayer, M., Tietsche, S., Karpechko, A.Y., 2022. Climate Change Fosters Competing Effects of Dynamics and Thermodynamics in Seasonal Predictability of Arctic Sea Ice. https://doi.org/10.1175/JCLI-D-21-0463.1

Polyakov, I.V., Pnyushkov, A.V., Alkire, M.B., Ashik, I.M., Baumann, T.M., Carmack, E.C., Goszczko, I., Guthrie, J., Ivanov, V.V., Kanzow, T., Krishfield, R., Kwok, R., Sundfjord, A., Morison, J., Rember, R., Yulin, A., 2017a. Greater role for Atlantic inflows on sea-ice loss in the Eurasian Basin of the Arctic Ocean. Science 356, 285–291. https://doi.org/10.1126/science.aai8204

Polyakov, I.V., Pnyushkov, A.V., Alkire, M.B., Ashik, I.M., Baumann, T.M., Carmack, E.C., Goszczko, I., Guthrie, J., Ivanov, V.V., Kanzow, T., Krishfield, R., Kwok, R., Sundfjord, A., Morison, J., Rember, R., Yulin, A., 2017b. Greater role for Atlantic inflows on sea-ice loss in the Eurasian Basin of the Arctic Ocean. Science 356, 285–291. https://doi.org/10.1126/science.aai8204

Polyakov, I.V., Rippeth, T.P., Fer, I., Alkire, M.B., Baumann, T.M., Carmack, E.C., Ingvaldsen, R., Ivanov, V.V., Janout, M., Lind, S., Padman, L., Pnyushkov, A.V., Rember, R., 2020b. Weakening of Cold Halocline Layer Exposes Sea Ice to Oceanic Heat in the Eastern Arctic Ocean. https://doi.org/10.1175/JCLI-D-19-0976.1

Polyakova, Y., Kryukova, I., Martynov, F., Novikhin, A., Abramova, E., Kassens, H., Hoelemann, J., 2021. Community structure and spatial distribution of phytoplankton in relation to hydrography in the Laptev Sea and the East Siberian Sea (autumn 2008). Polar Biol. 44. https://doi.org/10.1007/s00300-021-02873-w

Praetorius, S., Rugenstein, M., Persad, G., Caldeira, K., 2018. Global and Arctic climate sensitivity enhanced by changes in North Pacific heat flux. Nat. Commun. 9, 1–12. https://doi.org/10.1038/s41467-018-05337-8

Preußer, A., Ohshima, K.I., Iwamoto, K., Willmes, S., Heinemann, G., 2019. Retrieval of Wintertime Sea Ice Production in Arctic Polynyas Using Thermal Infrared and Passive Microwave Remote Sensing Data. J. Geophys. Res. Oceans 124, 5503–5528. https://doi.org/10.1029/2019JC014976

Price, J.F., Weller, R.A., Schudlich, R.R., 1987. Wind-Driven Ocean Currents and Ekman Transport. Science 238, 1534–1538. https://doi.org/10.1126/science.238.4833.1534

Proshutinsky, A., Krishfield, R., Timmermans, M.-L., Toole, J., Carmack, E., McLaughlin, F., Williams, W.J., Zimmermann, S., Itoh, M., Shimada, K., 2009. Beaufort Gyre freshwater reservoir: State and variability from observations. J. Geophys. Res. Oceans 114. https://doi.org/10.1029/2008JC005104

Proshutinsky, A., Steele, M., Timmermans, M. -L., 2016. Forum for Arctic Modeling and Observational Synthesis (FAMOS): Past, current, and future activities. J. Geophys. Res. Oceans 121, 3803–3819. https://doi.org/10.1002/2016JC011898

Prowse, T., Bring, A., M\aard, J., Carmack, E., 2015. Arctic freshwater synthesis: Introduction. J. Geophys. Res. G Biogeosciences 120, 2121–2131. https://doi.org/10.1002/2015JG003127

Rabe, B., Karcher, M., Kauker, F., Schauer, U., Toole, J.M., Krishfield, R.A., Pisarev, S., Kikuchi, T., Su, J., 2014. Arctic Ocean basin liquid freshwater storage trend 1992–2012. Geophys. Res. Lett. 41, 961–968. https://doi.org/10.1002/2013GL058121

Rantanen, M., Karpechko, A.Y., Lipponen, A., Nordling, K., Hyvärinen, O., Ruosteenoja, K., Vihma, T., Laaksonen, A., 2022. The Arctic has warmed nearly four times faster than the globe since 1979. Commun. Earth Environ. 3, 1–10. https://doi.org/10.1038/s43247-022-00498-3

Reimnitz, E., Dethleff, D., Nürnberg, D., 1994. Contrasts in Arctic shelf sea-ice regimes and some implications: Beaufort Sea versus Laptev Sea. Mar. Geol., 4th International Conference on Paleoceanography (ICP IV) 119, 215–225. https://doi.org/10.1016/0025-3227(94)90182-1

Ricker, R., Hendricks, S., Kaleschke, L., Tian-Kunze, X., King, J., Haas, C., 2017. A weekly Arctic sea-ice thickness data record from merged CryoSat-2 and SMOS satellite data. The Cryosphere 11, 1607–1623. https://doi.org/10.5194/tc-11-1607-2017

Rigor, I.G., Wallace, J.M., Colony, R.L., 2002. Response of Sea Ice to the Arctic Oscillation.

Rogozhin, V., Osadchiev, A.A., Konovalova, O., 2023. Structure and variability of the Pechora plume in the southeastern part of the Barents Sea. Front. Mar. Sci. 10.

Rudels, B., Anderson, L.G., Jones, E.P., 1996. Formation and evolution of the surface mixed layer and halocline of the Arctic Ocean. J. Geophys. Res. Oceans 101, 8807–8821. https://doi.org/10.1029/96JC00143

Rudels, B., Jones, E.P., Schauer, U., Eriksson, P., 2004. Atlantic sources of the Arctic Ocean surface and halocline waters. Polar Res. 23, 181–208. https://doi.org/10.3402/polar.v23i2.6278

Rudels, B., Schauer, U., Björk, G., Korhonen, M., Pisarev, S., Rabe, B., Wisotzki, A., 2013. Observations of water masses and circulation with focus on the Eurasian Basin of the Arctic Ocean from the 1990s to the late 2000s. Ocean Sci. 9, 147–169. https://doi.org/10.5194/os-9-147-2013

Screen, J.A., 2017. Far-flung effects of Arctic warming. Nat. Geosci. 10, 253–254. https://doi.org/10.1038/ngeo2924

Semizhon, T., Röllin, S., Spasova, Y., Klemt, E., 2010. Transport and distribution of artificial gamma-emitting radionuclides in the River Yenisei and its sediment. J. Environ. Radioact. 101, 385–402. https://doi.org/10.1016/j.jenvrad.2010.02.012

Serreze, M.C., Barrett, A.P., Slater, A.G., Woodgate, R.A., Aagaard, K., Lammers, R.B., Steele, M., Moritz, R., Meredith, M., Lee, C.M., 2006. The large-scale freshwater cycle of the Arctic. J. Geophys. Res. Oceans 111. https://doi.org/10.1029/2005JC003424

Serreze, M.C., Stroeve, J., 2015. Arctic sea ice trends, variability and implications for seasonal ice forecasting. Philos. Trans. R. Soc. Math. Phys. Eng. Sci. 373, 20140159. https://doi.org/10.1098/rsta.2014.0159

Shakhova, N., Semiletov, I., Leifer, I., Sergienko, V., Salyuk, A., Kosmach, D., Chernykh, D., Stubbs, C., Nicolsky, D., Tumskoy, V., Gustafsson, Ö., 2014. Ebullition and storm-induced methane release from the East Siberian Arctic Shelf. Nat. Geosci. 7, 64–70. https://doi.org/10.1038/ngeo2007

Shiklomanov, A., Déry, S., Tretiakov, M., Yang, D., Magritsky, D., Georgiadi, A., Tang, W., 2021. River Freshwater Flux to the Arctic Ocean, in: Yang, D., Kane, D.L. (Eds.), Arctic Hydrology, Permafrost and Ecosystems. Springer International Publishing, Cham, pp. 703–738. https://doi.org/10.1007/978-3-030-50930-9_24

Shiklomanov, A.I., Lammers, R.B., 2009. Record Russian river discharge in 2007 and the limits of analysis. Environ. Res. Lett. 4, 045015. https://doi.org/10.1088/1748-9326/4/4/045015

Sime, L., Malmierca, I., Diamond, R., Schroeder, D., 2022. Better forecasts of sea ice change? Melt puddles and melt models. Past Glob. Chang. Horiz. 2, 38–40. https://doi.org/10.22498/pages.horiz.2.38

Sime, L.C., Sivankutty, R., Vallet-Malmierca, I., de Boer, A.M., Sicard, M., 2023. Summer surface air temperature proxies point to near-sea-ice-free conditions in the Arctic at 127 ka. Clim. Past 19, 883–900. https://doi.org/10.5194/cp-19-883-2023

Smedsrud, L.H., Halvorsen, M.H., Stroeve, J.C., Zhang, R., Kloster, K., 2017. Fram Strait sea ice export variability and September Arctic sea ice extent over the last 80 years. The Cryosphere 11, 65–79. https://doi.org/10.5194/tc-11-65-2017

Solomon, A., Heuzé, C., Rabe, B., Bacon, S., Bertino, L., Heimbach, P., Inoue, J., Iovino, D., Mottram, R., Zhang, X., Aksenov, Y., McAdam, R., Nguyen, A., Raj, R.P., Tang, H., 2021. Freshwater in the Arctic Ocean 2010–2019. Ocean Sci. 17, 1081–1102. https://doi.org/10.5194/os-17-1081-2021

Stadnyk, T.A., Tefs, A., Broesky, M., Déry, S.J., Myers, P.G., Ridenour, N.A., Koenig, K., Vonderbank, L., Gustafsson, D., 2021. Changing freshwater contributions to the Arctic: A 90-year trend analysis (1981–2070). Elem. Sci. Anthr. 9. https://doi.org/10.1525/elementa.2020.00098

Steele, M., Boyd, T., 1998. Retreat of the cold halocline layer in the Arctic Ocean. J. Geophys. Res. Oceans 103, 10419–10435. https://doi.org/10.1029/98JC00580

Steele, M., Ermold, W., 2004. Salinity trends on the Siberian shelves. Geophys. Res. Lett. 31. https://doi.org/10.1029/2004GL021302

Steele, M., Morison, J., Ermold, W., Rigor, I., Ortmeyer, M., Shimada, K., 2004. Circulation of summer Pacific halocline water in the Arctic Ocean. J. Geophys. Res. Oceans 109. https://doi.org/10.1029/2003JC002009

Stroeve, J., Frei, A., McCreight, J., Ghatak, D., 2008. Arctic sea-ice variability revisited. Ann. Glaciol. 48, 71–81. https://doi.org/10.3189/172756408784700699

Stroeve, J., Notz, D., 2018a. Changing state of Arctic sea ice across all seasons. Environ. Res. Lett. 13, 103001. https://doi.org/10.1088/1748-9326/aade56

Stroeve, J., Notz, D., 2018b. Changing state of Arctic sea ice across all seasons. Environ. Res. Lett. 13, 103001. https://doi.org/10.1088/1748-9326/aade56

Stroeve, J.C., Crawford, A.D., Stammerjohn, S., 2016. Using timing of ice retreat to predict timing of fall freeze-up in the Arctic. Geophys. Res. Lett. 43, 6332–6340. https://doi.org/10.1002/2016GL069314

Stroeve, J.C., Markus, T., Boisvert, L., Miller, J., Barrett, A., 2014. Changes in Arctic melt season and implications for sea ice loss. Geophys. Res. Lett. 41, 1216–1225. https://doi.org/10.1002/2013GL058951

Stroeve, J.C., Serreze, M.C., Holland, M.M., Kay, J.E., Malanik, J., Barrett, A.P., 2012. The Arctic's rapidly shrinking sea ice cover: a research synthesis. Clim. Change 110, 1005–1027. https://doi.org/10.1007/s10584-011-0101-1

Suess, M., De Witte, E., Rommen, B., 2022. Earth Explorer 10 Candidate Mission Harmony, in: EUSAR 2022; 14th European Conference on Synthetic Aperture Radar. Presented at the EUSAR 2022; 14th European Conference on Synthetic Aperture Radar, pp. 1–4.

Sumata, H., de Steur, L., Divine, D.V., Granskog, M.A., Gerland, S., 2023. Regime shift in Arctic Ocean sea ice thickness. Nature 615, 443–449. https://doi.org/10.1038/s41586-022-05686-x

Supply, A., Boutin, J., Vergely, J.-L., Kolodziejczyk, N., Reverdin, G., Reul, N., Tarasenko, A., 2020a. New insights into SMOS sea surface salinity retrievals in the Arctic Ocean. Remote Sens. Environ. 249, 112027. https://doi.org/10.1016/j.rse.2020.112027

Supply, A., Boutin, J., Vergely, J.-L., Kolodziejczyk, N., Reverdin, G., Reul, N., Tarasenko, A., 2020b. SMOS ARCTIC SSS L3 maps produced by CATDS CEC LOCEAN. https://doi.org/10.17882/71909

Swift, J.H., Jones, E.P., Aagaard, K., Carmack, E.C., Hingston, M., MacDonald, R.W., McLaughlin, F.A., Perkin, R.G., 1997. Waters of the Makarov and Canada basins. Deep Sea Res. Part II Top. Stud. Oceanogr. 44, 1503–1529. https://doi.org/10.1016/S0967-0645(97)00055-6

Tang, W., Yueh, S., Yang, D., Fore, A., Hayashi, A., Lee, T., Fournier, S., Holt, B., 2018. The Potential and Challenges of Using Soil Moisture Active Passive (SMAP) Sea Surface Salinity to Monitor Arctic Ocean Freshwater Changes. Remote Sens. 10, 869. https://doi.org/10.3390/rs10060869

Tarasenko, A., Supply, A., Kusse-Tiuz, N., Ivanov, V., Makhotin, M., Tournadre, J., Chapron, B., Boutin, J., Kolodziejczyk, N., Reverdin, G., 2021. Properties of surface water masses in the Laptev and the East Siberian seas in summer 2018 from in situ and satellite data. Ocean Sci. 17, 221–247. https://doi.org/10.5194/os-17-221-2021

Thibodeau, B., Bauch, D., Kassens, H., Timokhov, L.A., 2014. Interannual variations in river water content and distribution over the Laptev Sea between 2007 and 2011: The Arctic Dipole connection. Geophys. Res. Lett. 41, 7237–7244. https://doi.org/10.1002/2014GL061814

Tietsche, S., Notz, D., Jungclaus, J.H., Marotzke, J., 2011. Recovery mechanisms of Arctic summer sea ice. Geophys. Res. Lett. 38. https://doi.org/10.1029/2010GL045698

Timmermans, M.L., Marshall, J., 2020. Understanding Arctic Ocean Circulation: A Review of Ocean Dynamics in a Changing Climate. J. Geophys. Res. Oceans 125. https://doi.org/10.1029/2018JC014378

Timmermans, M.-L., Marshall, J., 2020. Understanding Arctic Ocean Circulation: A Review of Ocean Dynamics in a Changing Climate. J. Geophys. Res. Oceans 125, e2018JC014378. https://doi.org/10.1029/2018JC014378

Timokhov, L.A., 1994. Regional characteristics of the Laptev and the East Siberian seas: climate, topography, ice phases, thermohaline regime, circulation. Berichte Zur Polarforsch. 144, 15–31.

Umbert, M., Gabarro, C., Olmedo, E., Gonçalves-Araujo, R., Guimbard, S., Martinez, J., 2021. Using Remotely Sensed Sea Surface Salinity and Colored Detrital Matter to Characterize Freshened Surface Layers in the Kara and Laptev Seas during the Ice-Free Season. Remote Sens. https://doi.org/10.3390/rs13193828

Vihma, T., Screen, J., Tjernström, M., Newton, B., Zhang, X., Popova, V., Deser, C., Holland, M., Prowse, T., 2016. The atmospheric role in the Arctic water cycle: A review on processes, past and future changes, and their impacts, Journal of Geophysical Research G: Biogeosciences. Blackwell Publishing Ltd. https://doi.org/10.1002/2015JG003132

Walsh, J.E., 2014. Intensified warming of the Arctic: Causes and impacts on middle latitudes. Glob. Planet. Change 117, 52–63. https://doi.org/10.1016/j.gloplacha.2014.03.003

Walsh, J.E., Zhou, X., Portis, D., Serreze, M.C., 1994. Atmospheric contribution to hydrologic variations in the Arctic. Atmosphere-Ocean 32, 733–755. https://doi.org/10.1080/07055900.1994.9649520

Wang, J., Zhang, J., Watanabe, E., Ikeda, M., Mizobata, K., Walsh, J.E., Bai, X., Wu, B., 2009. Is the Dipole Anomaly a major driver to record lows in Arctic summer sea ice extent? Geophys. Res. Lett. 36. https://doi.org/10.1029/2008GL036706

Wang, P., Huang, Q., Pozdnyakov, S., Liu, S., Ma, N., Wang, T., Zhang, Y., Yu, J., Xie, J., Fu, G., Frolova, N., Liu, C., 2021. Potential role of permafrost thaw on increasing Siberian river discharge. Environ. Res. Lett. 16, 034046. https://doi.org/10.1088/1748-9326/abe326

Wang, Q., Danilov, S., Sidorenko, D., Wang, X., 2021. Circulation Pathways and Exports of Arctic River Runoff Influenced by Atmospheric Circulation Regimes. Front. Mar. Sci. 8.

Wang, Q., Shu, Q., Wang, F., 2024. Recent emergence of Arctic atlantification dominated by climate warming. Sci. Adv. 10, eadq5235. https://doi.org/10.1126/sciadv.adq5235

Wang, S., Wang, Q., Shu, Q., Song, Z., Lohmann, G., Danilov, S., Qiao, F., 2021. Nonmonotonic Change of the Arctic Ocean Freshwater Storage Capability in a Warming Climate. Geophys. Res. Lett. 48, e2020GL090951. https://doi.org/10.1029/2020GL090951

Williams, J., Tremblay, B., Newton, R., Allard, R., 2016. Dynamic Preconditioning of the Minimum September Sea-Ice Extent. J. Clim. 29, 5879–5891. https://doi.org/10.1175/JCLI-D-15-0515.1

Winkelbauer, S., Mayer, M., Seitner, V., Zsoter, E., Zuo, H., Haimberger, L., 2022. Diagnostic evaluation of river discharge into the Arctic Ocean and its impact on oceanic volume transports. Hydrol. Earth Syst. Sci. 26, 279–304. https://doi.org/10.5194/hess-26-279-2022

Wise, A., Harle, J., Bruciaferri, D., O'Dea, E., Polton, J., 2022. The effect of vertical coordinates on the accuracy of a shelf sea model. Ocean Model. 170, 101935. https://doi.org/10.1016/j.ocemod.2021.101935

Woodgate, R.A., Fahrbach, E., Rohardt, G., 1999. Structure and transports of the East Greenland Current at 75°N from moored current meters. J. Geophys. Res. Oceans 104, 18059–18072. https://doi.org/10.1029/1999JC900146

Woodgate, R.A., Weingartner, T.J., Lindsay, R., 2012. Observed increases in Bering Strait oceanic fluxes from the Pacific to the Arctic from 2001 to 2011 and their impacts on the Arctic Ocean water column. Geophys. Res. Lett. 39. https://doi.org/10.1029/2012GL054092

Wu, B., Su, J., Zhang, R., 2011. Effects of autumn-winter Arctic sea ice on winter Siberian High. Chin. Sci. Bull. 56, 3220–3228. https://doi.org/10.1007/s11434-011-4696-4

Xie, J., Raj, R.P., Bertino, L., Martínez, J., Gabarró, C., Catany, R., 2023. Assimilation of sea surface salinities from SMOS in an Arctic coupled ocean and sea ice reanalysis. Ocean Sci. 19, 269–287. https://doi.org/10.5194/os-19-269-2023

Xu, X., He, S., Zhou, B., Wang, H., 2022. Atmospheric Contributions to the Reversal of Surface Temperature Anomalies Between Early and Late Winter Over Eurasia. Earths Future 10, e2022EF002790. https://doi.org/10.1029/2022EF002790

Yang, D., Kane, D.L., Hinzman, L.D., Zhang, X., Zhang, T., Ye, H., 2002. Siberian Lena River hydrologic regime and recent change. J. Geophys. Res. Atmospheres 107, ACL 14-1-ACL 14-10. https://doi.org/10.1029/2002JD002542

Yang, D., Robinson, D., Zhao, Y., Estilow, T., Ye, B., 2003. Streamflow response to seasonal snow cover extent changes in large Siberian watersheds. J. Geophys. Res. Atmospheres 108. https://doi.org/10.1029/2002JD003149

Yang, D., Ye, B., Shiklomanov, A., 2004. Discharge Characteristics and Changes over the Ob River Watershed in Siberia. J. Hydrometeorol. 5, 595–610. https://doi.org/10.1175/1525-7541(2004)005<0595:DCACOT>2.0.CO;2

Yang, Y., Nie, H., Zhang, Y., Luo, X., Wei, H., Zhao, W., 2024. Interannual Variability in the Onset Time Distribution of the Open Water in the Kara Sea. J. Clim. 37, 1367–1381. https://doi.org/10.1175/JCLI-D-23-0073.1

Ye, K., Woollings, T., Sparrow, S.N., Watson, P.A.G., Screen, J.A., 2024. Response of winter climate and extreme weather to projected Arctic sea-ice loss in very large-ensemble climate model simulations. Npj Clim. Atmospheric Sci. 7, 1–16. https://doi.org/10.1038/s41612-023-00562-5

Yin, Z., Zhang, Y., Zhou, B., Wang, H., 2023. Subseasonal variability and the "Arctic warming-Eurasia cooling" trend. Sci. Bull. 68, 528–535. https://doi.org/10.1016/j.scib.2023.02.009

Zatsepin, A.G., Kremenetskiy, V.V., Kubryakov, A.A., Stanichny, S.V., Soloviev, D.M., 2015. Propagation and transformation of waters of the surface desalinated layer in the Kara Sea. Oceanology 55, 450–460. https://doi.org/10.1134/S0001437015040153

Zatsepin, A.G., Zavialov, P.O., Kremenetskiy, V.V., Poyarkov, S.G., Soloviev, D.M., 2010. The upper desalinated layer in the Kara Sea. Oceanology 50, 657–667. https://doi.org/10.1134/S0001437010050036

Zeng, J., Yang, Q., Li, X., Yuan, X., Bushuk, M., Chen, D., 2023. Reducing the Spring Barrier in Predicting Summer Arctic Sea Ice Concentration. Geophys. Res. Lett. 50, e2022GL102115. https://doi.org/10.1029/2022GL102115

Zhang, J., Rothrock, D.A., Steele, M., 1998. Warming of the Arctic Ocean by a strengthened Atlantic Inflow: Model results. Geophys. Res. Lett. 25, 1745–1748. https://doi.org/10.1029/98GL01299

Zhang, R., 2008. Coherent surface-subsurface fingerprint of the Atlantic meridional overturning circulation. Geophys. Res. Lett. 35. https://doi.org/10.1029/2008GL035463

Zhang, X., Fu, Y., Han, Z., Overland, J.E., Rinke, A., Tang, H., Vihma, T., Wang, M., 2022. Extreme Cold Events from East Asia to North America in Winter 2020/21: Comparisons, Causes, and Future Implications. Adv. Atmospheric Sci. 39, 553–565. https://doi.org/10.1007/s00376-021-1229-1

Zhang, Y., Cheng, X., Liu, J., Hui, F., 2018. The potential of sea ice leads as a predictor for seasonal Arctic sea ice extent prediction. https://doi.org/10.5194/tc-2018-108

Zhang, Y., Yin, Z., Wang, H., 2023. Subseasonal transition of Barents–Kara sea-ice anomalies in winter related to the reversed warm Arctic–cold Eurasia pattern. Atmospheric Ocean. Sci. Lett. 16, 100392. https://doi.org/10.1016/j.aosl.2023.100392

Zhao, J., Cao, Y., Shi, J., 2006. Core region of Arctic Oscillation and the main atmospheric events impact on the Arctic. Geophys. Res. Lett. - GEOPHYS RES LETT 332. https://doi.org/10.1029/2006GL027590

Zhuk, V.R., Kubryakov, A.A., 2021. Interannual Variability of the Lena River Plume Propagation in 1993–2020 during the Ice-Free Period on the Base of Satellite Salinity, Temperature, and Altimetry Measurements. Remote Sens. 13, 4252. https://doi.org/10.3390/rs13214252

Appendices

Appendix A Laptev Sea validation

Only observations in the upper 10 m are used for comparison with satellite data (Appendix Figure A.1, Appendix Table A.1). The same analysis was conducted using only data in the upper 5 m with no significant improvement. The analysis shown here is for the upper 10 m to retain as much data as possible.

Appendix Table A.1: Cruises, vessels and time-periods of salinity and temperature in-situ data used for analysis of vertical profiles and comparison with satellite data

Cruise Name	Vessel	Time Period	Reference
UDASH dataset (incl NABOS cruises 2013, 2015)	Numerous	2010-2015	(Behrendt et al., 2017)
NABOS cruise 2018 UCTD	Akademik Tryoshnikov	3rd -17th October 2018	(Janout et al., 2019)
	Akademik Lavrentyev Akademik Mstislav Keldysh	20th September – 20th October 2016 23rd September – 13th October 2019	Supplementary materials (Osadchiev et al., 2021a)

All satellite and reanalysis products described above are compared with in-situ data over 2015-2020. The regridded SMOS data and GLORYS12V1 reanalysis (on a 0.25 ° grid) are used for comparison with in-situ data. Both Pearson correlation coefficients and root-mean square difference (RMSD) values are calculated for each individual product at all collocations (across the entire area and time period) between in-situ data and that product. Correlation coefficients and RMSD values are also calculated only where all products have a collocation with in-situ data. However, over 2015-2020, few in-situ observations are collected sufficiently near the surface (< 10 m) over regions where all satellite products obtain an SSS measurement (only 37 collocations). Therefore, RMSDs and correlation coefficients are also calculated for SMOS products and reanalyses over the longer SMOS time period (2011-2020) to obtain more collocations (228). JPL SMAP and LOCEAN SMOS have particularly high correlation coefficients and low RMSD values and agree well so are used for further analysis.

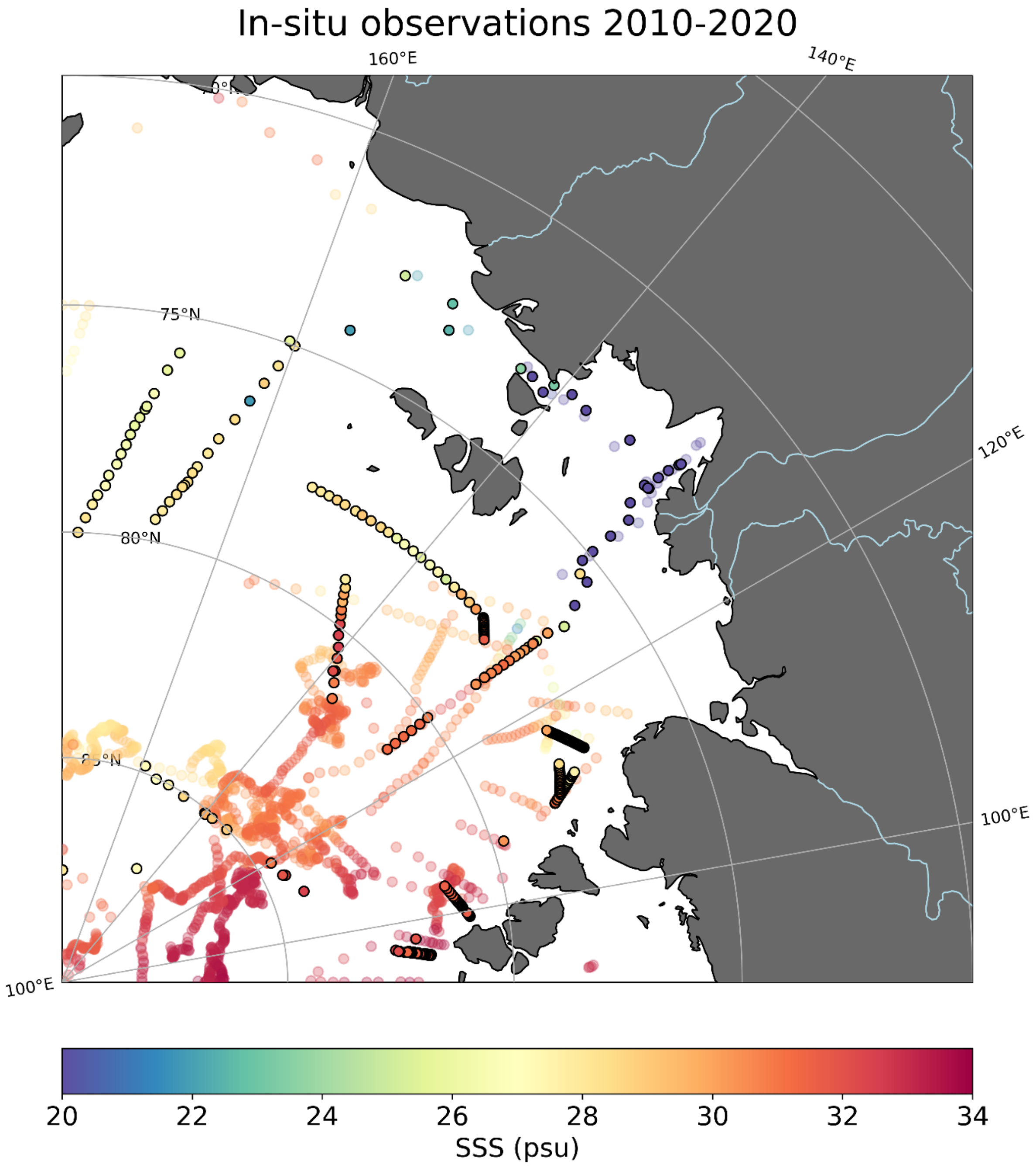

Appendix Figure A.1: In-situ data (<10 m) used for validation of satellite and reanalysis products, coloured by their salinity value. Data with black circles were collected over the SMAP period (2015-present), and those without black circles were collected over the SMOS period (2010-present).

Appendix Table A.2: Correlation coefficients from in-situ SSS data < 10 m over 2015-2020 (left) and 2010-2020 (right) with GLORYS12V1, BEC SMOS and LOCEAN SMOS products regridded at a 0.25 degree spatial resolution, JPL SMAP in regions where the provided SSS uncertainty is less than 1, RSS SMAP and the three CMEMS global ensemble reanalysis products: GLORYS2V4, ORAS5, and C-GLORS05. Correlation coefficients are calculated both at all points where an individual product is collocated with in-situ data (All obsv <10 m) and for only where all products had a collocation point near in-situ data (Common obsv <10 m). There are 57 collocations between all products over 2015-2020 and 377 collocations over 2010-2020. The p values associated with correlation coefficients are not included but are all << 0.01.

	2015-2020				**2010-2020**			
	All obsv <10 m		**Common obsv <10 m**		**All obsv <10 m**		**Common obsv <10 m**	
	Num obsv	**Corr coeff**	**Num obsv**	**Corr coeff**	**Num obsv**	**Corr coeff**	**Num obsv**	**Corr coeff**
GLORYS12V1 regridded onto 0.25° grid	222	**0.80**	57	**0.75**	1667	**0.78**	377	**0.65**
BEC SMOS regridded onto 0.25° grid	133	**0.79**		**0.79**	396	**0.76**		**0.75**
LOCEAN SMOS regridded onto 0.25° grid	132	**0.86**		**0.92**	406	**0.84**		**0.84**
JPL SMAP (where uncertainty < 1)	100	**0.92**		**0.95**				
RSS SMAP	67	**0.93**		**0.93**				
C-GLORS05	219	**0.75**		**0.73**	1672	**0.72**	377	**0.61**
GLORYS2V4	219	**0.81**		**0.75**	1672	**0.72**		**0.48**
ORAS5	219	**0.85**		**0.83**	1672	**0.89**		**0.80**

Appendix Table A.3: Root mean square differences (RMSD) from in-situ SSS data < 10 m over 2015-2020 (left) and 2010-2020 (right) with GLORYS12V1, BEC SMOS and LOCEAN SMOS products regridded at a 0.25 degree spatial resolution, JPL SMAP in regions where the provided SSS uncertainty is less than 1, RSS SMAP and the three CMEMS global ensemble reanalysis products: GLORYS2V4, ORAS5, and C-GLORS05. RMSDs are calculated both at all points where an individual product is collocated with in-situ data (All obsv <10 m) and for only where all products had a collocation point near in-situ data (Common obsv <10 m). There are 57 collocations between all products over 2015-2020 and 377 collocations over 2010-2020.

	2015-2020				**2010-2020**			
	All obsv <10 m		**Common obsv <10 m**		**All obsv <10 m**		**Common obsv <10 m**	
	Num obsv	**RMSD**	**Num obsv**	**RMSD**	**Num obsv**	**RMSD**	**Num obsv**	**RMSD**
GLORYS12V1 regridded onto 0.25° grid	222	**3.16**	57	**4.28**	1667	**1.88**	377	**2.69**
BEC SMOS regridded onto 0.25° grid	133	**2.90**		**3.74**	396	**2.21**		**2.25**
LOCEAN SMOS regridded onto 0.25° grid	132	**2.53**		**2.74**	406	**2.07**		**1.97**
JPL SMAP (where uncertainty < 1)	100	**1.85**		**2.19**				
RSS SMAP	67	**2.77**		**2.16**				
C-GLORS05	219	**3.75**		**4.18**	1672	**2.30**	377	**2.67**
GLORYS2V4	219	**3.04**		**3.93**	1672	**2.14**		**3.25**
ORAS5	219	**2.75**		**3.74**	1672	**1.41**		**2.42**

The satellites products show a good agreement with in-situ measurements within the top 10 m, with a correlation coefficient typically higher than 0.62 and up to 0.83. The RMSD with in-situ is typically between 1.1 and 1.65. Despite this relatively high error in RMSD, due to the large range of SSS observed over this small area (5 to 35), both datasets are well correlated. JPL SMAP, LOCEAN SMOS, and the median sat product stand out as having particularly high correlation (r ~ 0.8) coefficients compared to all other products. Over the full SMOS period, the LOCEAN product correlates strongly with in-situ data (r = 0.83) but the BEC product is less strongly correlated (r = 0.67).

The collocated in-situ data (common obsv <10 m) are all located in low sea ice regions (< 30% SIC), where satellite SSS retrievals are possible. Over the Laptev Sea, the strong horizontal gradient in SSS maintains lower salinities nearshore on the continental shelf and relatively higher salinities > 30 offshore. Therefore, the salinity range captured by in-situ observations only collocated with one satellite product/GLORYS12V1 typically includes a larger range of salinities (with more SSS values <30) than that captured by in-situ observations collocated with all products. Hence, the correlation coefficients of almost all products are larger when considering all in-situ observations collocated with that product due to the larger range in SSS than when considering only in-situ observations collocated with all products.

Whilst GLORYS12V1 appears to correlate well with in-situ data when considering all its collocations ($r > 0.79$ over 2015-2020 and $r > 0.78$ over 2011-2020), the correlation deteriorates when only considering observations where all satellite products have a collocation ($r < 0.35$ over 2015-2020 and $r < 0.63$ over 2011-2020). This same pattern is visible in all other reanalysis products considered. This decrease in correlation indicates that the reanalyses manage to replicate the large-scale horizontal gradient in SSS (between the fresh plume on the shelf and the more saline water that sits off the shelf, under sea ice) but are not capable of representing the spatial variability at lower SSS values and hence of finer scale river plume dynamics. Reanalysis RMSDs from in-situ data are also all larger than those of any satellite product. The lower RMSDs and stronger correlation coefficients of all satellite products compared to reanalyses highlight the value satellite SSS products bring to Arctic-based process studies.

Appendix B Laptev Sea additional figures

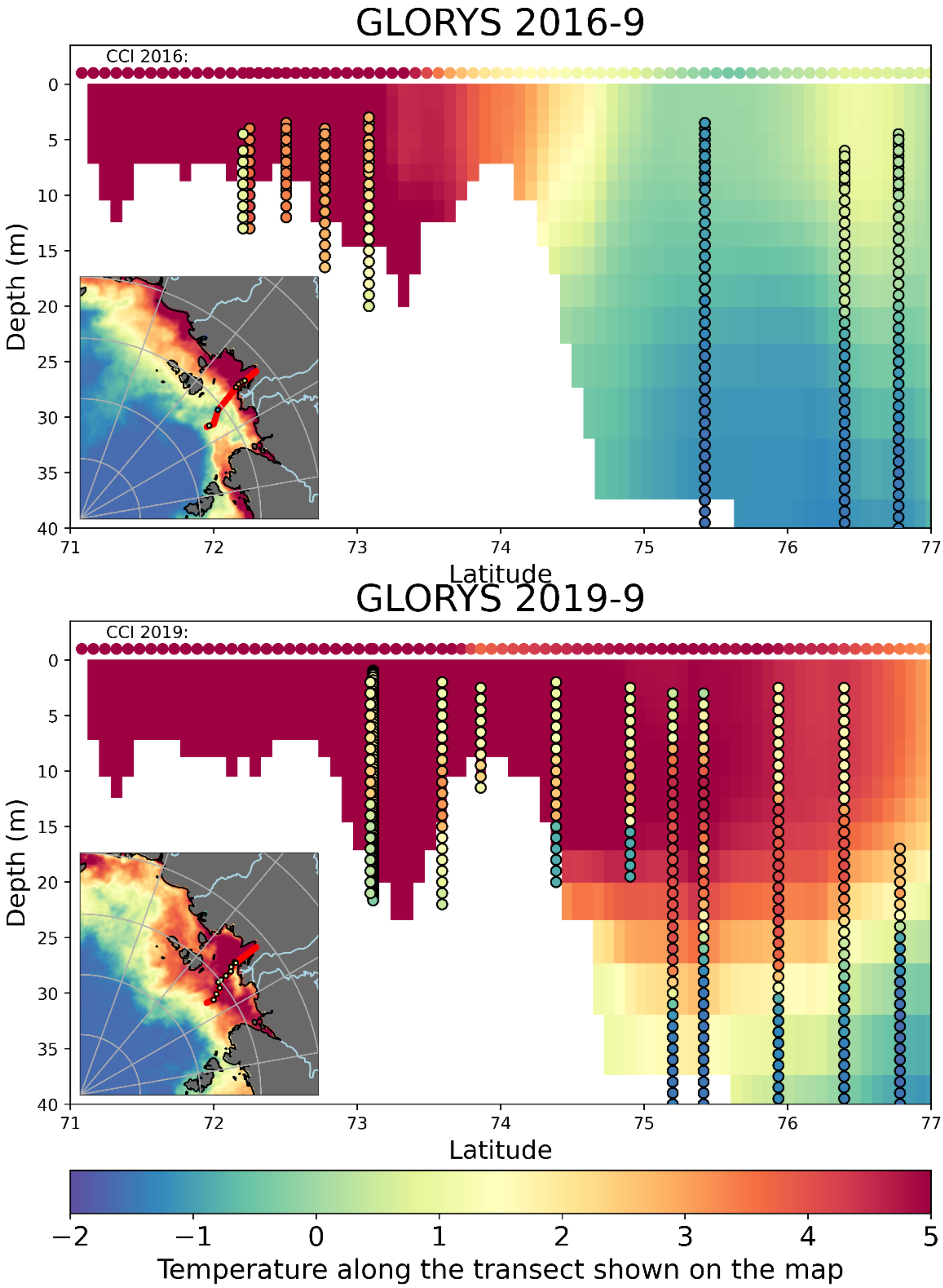

Appendix Figure B.1: GLORYS12V1 SST vertical transect in 2016 (top) and 2019 (bottom) along red transect interpolated through in-situ data (shown in map of CCI SST in bottom left for each year) with in-situ data overlaid with black rings and satellite data for that transect in CCI SST shown as a line of points.

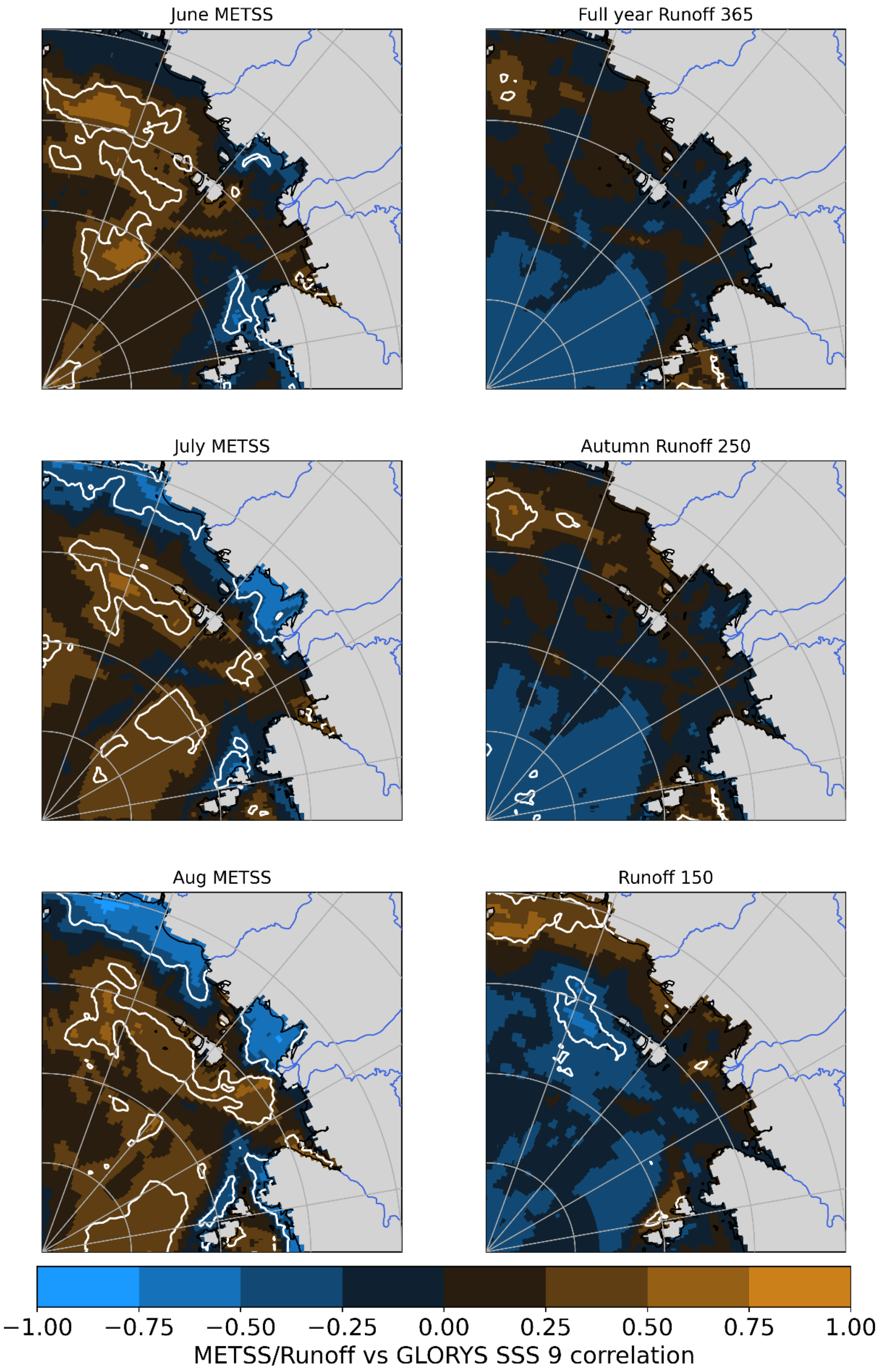

Appendix Figure B.2: Correlation between GLORYS12V1 September SSS and mean eastward turbulent surface stress (METSS) over 70-80 North and 120-160 East in June (6), July (7), August (8) (left column) over 1993-2022. Correlation between GLORYS12V1 September SSS and cumulative Lena River runoff over the full year (Julian day 365), in autumn (Julian day 250) and in spring (Julian day 150) (right column) over 1993-2022. Regions where correlations are statistically significant ($p \leq 0.05$) are denoted by the white contour and brighter colours.

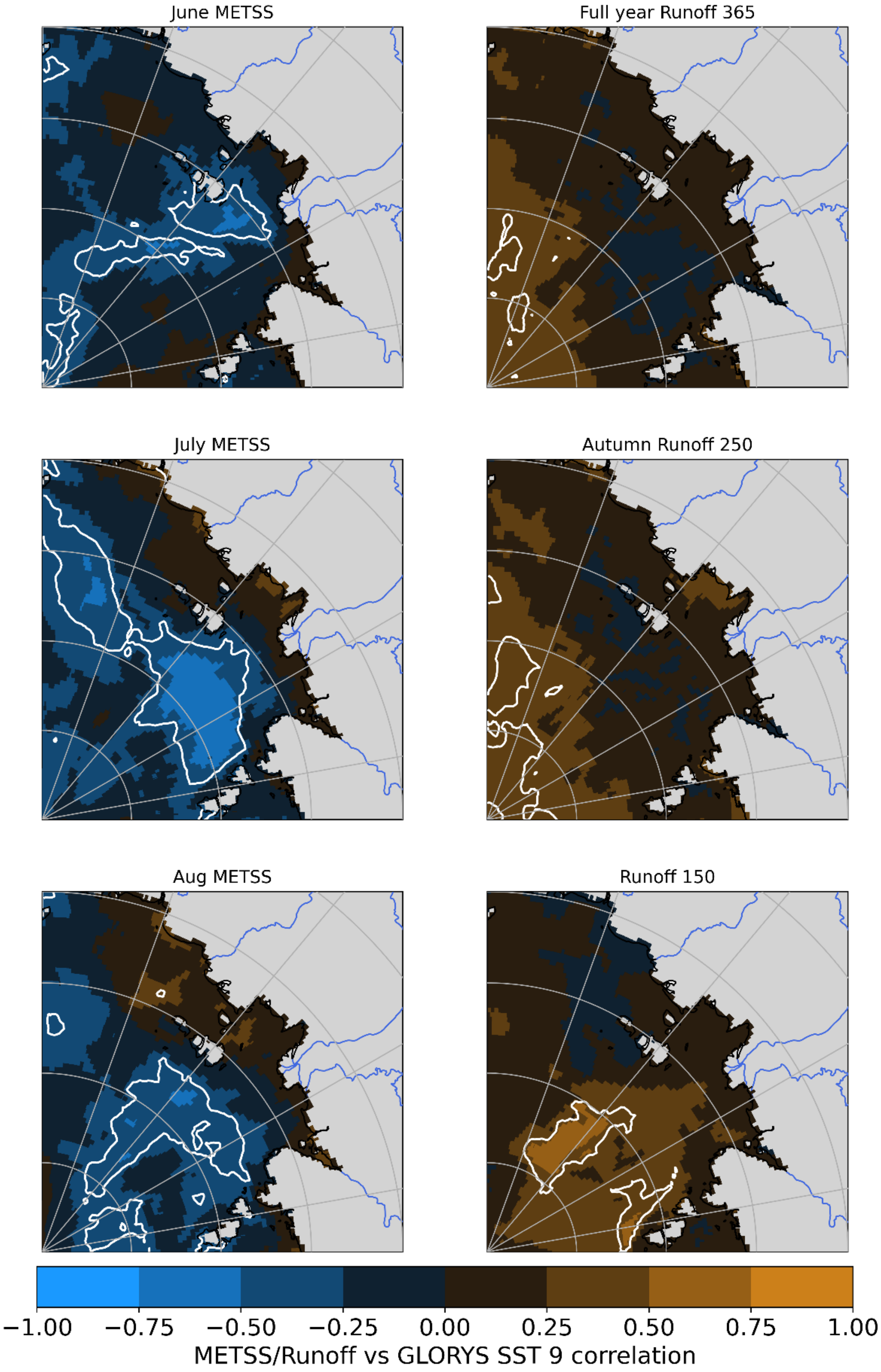

Appendix Figure B.3: Correlation between GLORYS12V1 September SST and mean eastward turbulent surface stress (METSS) over 70-80 North and 120-160 East in June (6), July (7), August (8) (left column) over 1993-2022. Correlation between GLORYS12V1 September SST and cumulative Lena River runoff over the full year (Julian day 365), in autumn (Julian day 250) and in spring (Julian day 150) (right column) over 1993-2022. Regions where correlations are statistically significant ($p \leq 0.05$) are denoted by the white contour and brighter colours.

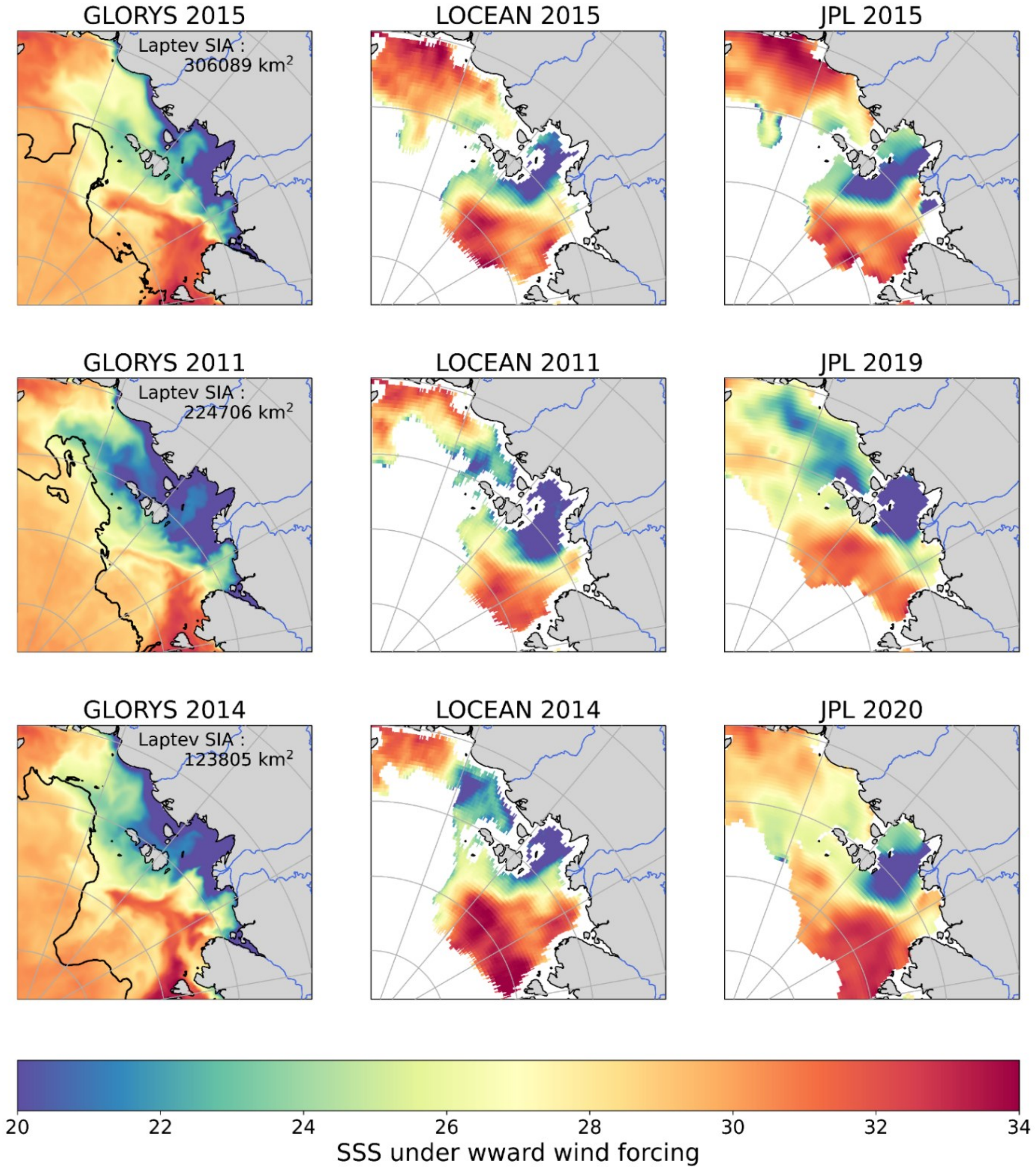

Appendix Figure B.4: Years of westward wind forcing for all years used to calculate westward composites for (left to right) GLORYS12V1 SSS and LOCEAN SMOS (2019, 2011, 2013) and for JPL SMAP (2019, 2015, 2020). The GLORYS12V1 mean 30% sea ice concentration contour and mean GLORYS12V1 sea ice area (SIA) in the Laptev Sea (120-140, 68-85N) for each year shown is overlaid on that year's plot.

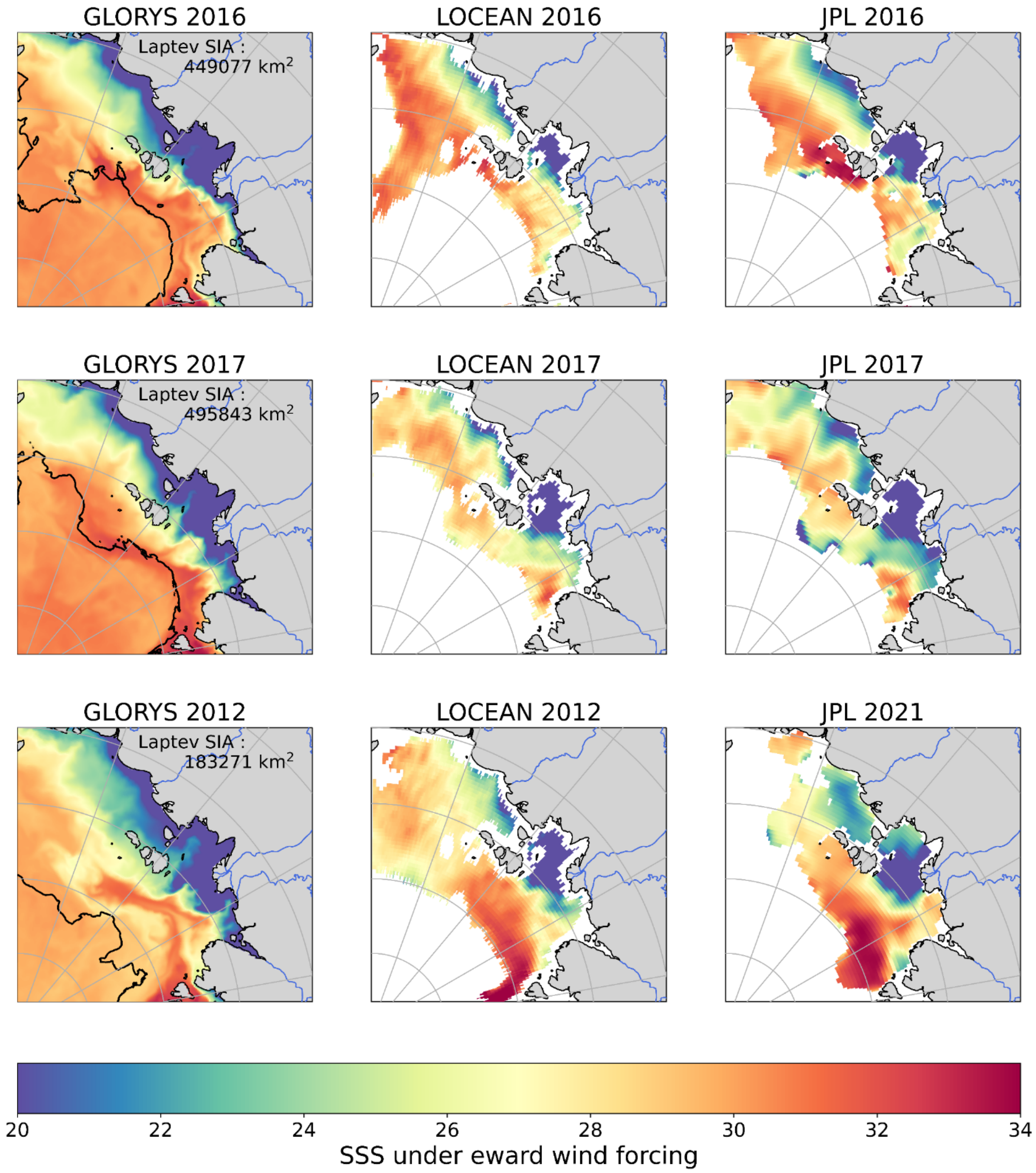

Appendix Figure B.5: Years of eastward wind forcing for all years used to calculate eastward composites for (left to right) GLORYS12V1 SSS and LOCEAN SMOS (2016, 2017, 2012) and for JPL SMAP (2016, 2017, 2021). The GLORYS12V1 mean 30% sea ice concentration contour and mean GLORYS12V1 sea ice area (SIA) in the Laptev Sea (120-140, 68-85N) for each year shown is overlaid on that year's plot.

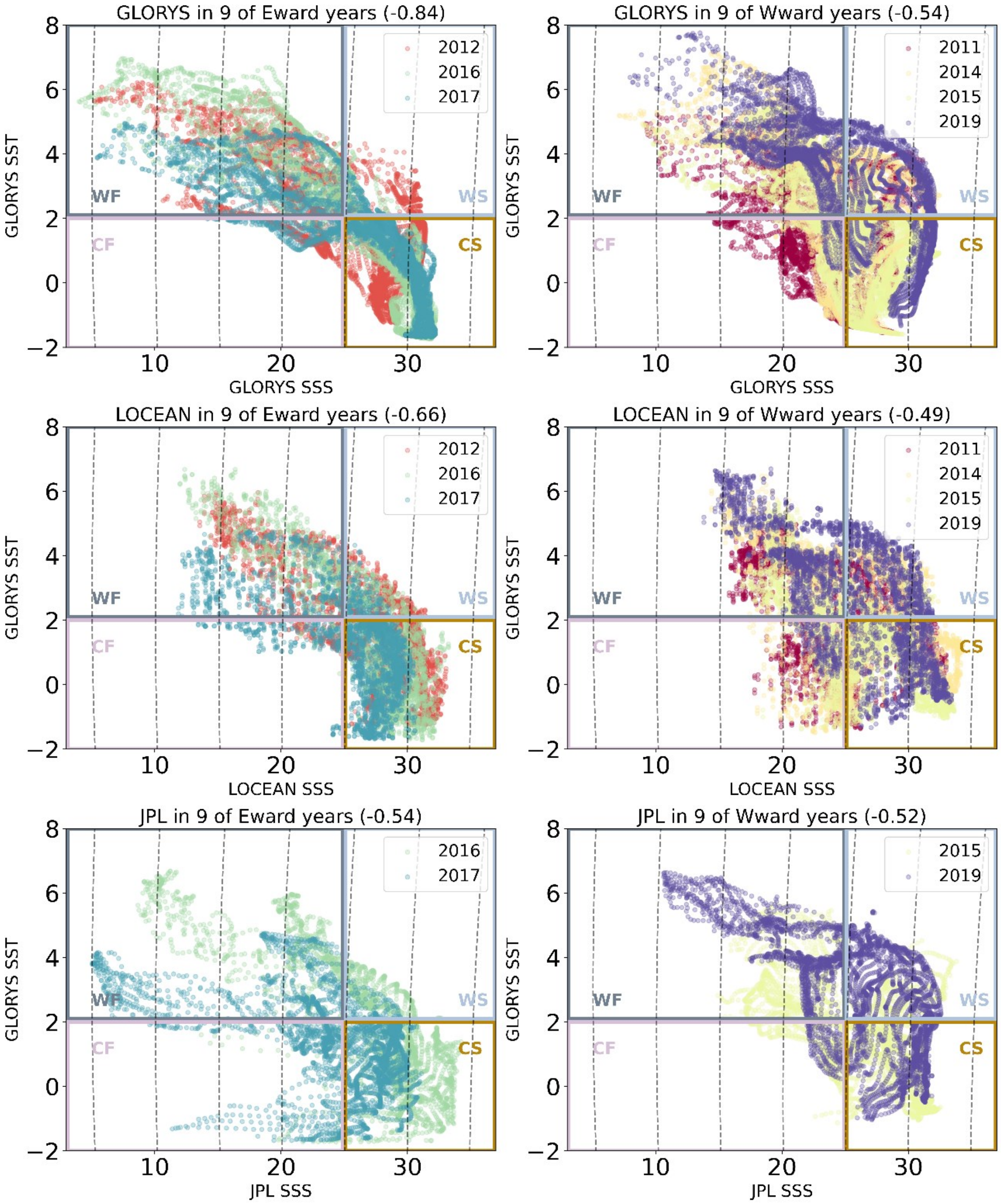

Appendix Figure B.6: T-S diagrams over the Laptev Sea (65-80 °N, 120-160 °E)-for September under eastward (2012, 2016, 2017) (left column) and westward (2011, 2014, 2015, 2019) (right column) wind forcing for GLORYS12V1 SST and GLORYS12V1 SSS (top), LOCEAN SMOS SSS (middle) and JPL SMAP SSS (bottom) colour coded by year over 2010-2020. Density contours are overlaid as dashed black lines. Spearman correlation coefficients between the SSS product and GLORYS12V1 SST across all eastward/westward years shown is displayed in the title of each subplot. Boxes are overlaid for 4 water masses depicting warm, fresh water (WF, SST>2 °C, SSS<25 pss), cold, fresh water (CF, SST<2 °C, SSS<25 pss), warm salty water (WS, SST>2 °C, SSS>25 pss) and cold, salty water (CS, SST<2 °C, SSS>25 pss)

Appendix C Kara Sea additional figures

Wind stress SSS

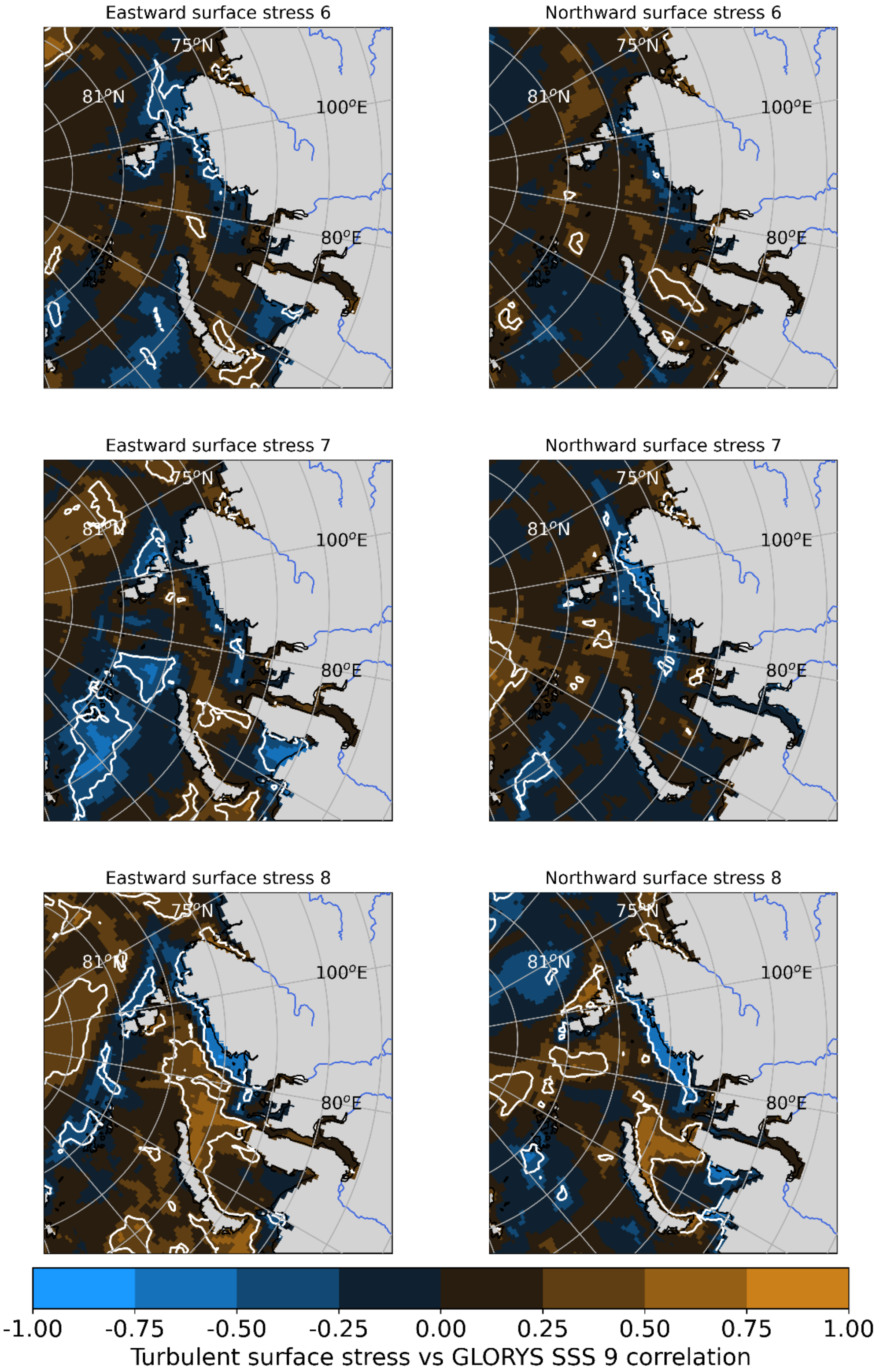

Eastward surface stress 6

Northward surface stress 6

Eastward surface stress 7

Northward surface stress 7

Eastward surface stress 8

Northward surface stress 8

Appendix Figure C.1: Correlation between GLORYS12V1 September SSS and ERA5 eastward and northward turbulent surface stress in June, July and August (6-8) over 1993-2023. Regions where correlations are statistically significant ($p \leq 0.05$) are denoted by the white contour and brighter colours.

The August eastward turbulent surface stress correlation pattern is by far the largest and most significant. This pattern consists of a large region of strong positive correlation (> 0.75) in the central Kara Sea, which extends from the Novaya Zemlya Archipelago almost all the way to the Severnaya Zemlya Archipelago. A notable region of strong negative correlation (< -0.75) is present from the outflow of the Ob-Yenisei plume all the way along the coast through the Vilkitsky Strait and into the Laptev Sea. A large region of strong positive correlation is also present in the central Arctic, from around 80 °N.

Small regions of significant positive (> 0.75) and negative correlations (< -0.75) are also present in June and July eastward turbulent surface stress correlation plots. The most notable region of negative correlation with July eastward turbulent surface stress is in the southwestern Kara Sea and in a band offshore between 77 and 80 °N. Some small regions of significant negative correlation along the coast are also present in June and July, particularly in the southwestern and southeastern Kara Sea in July, and particularly in the eastern Kara, Vilkitsky Strait and western Laptev in June. A notable region of significant positive correlation is also present in June offshore in the eastern Kara Sea.

In the Kara Sea, the spatial correlation patterns between GLORYS12V1 SSS and mean northward turbulent surface stress over 1993-2023 (Figure 4.2, right), resemble those with mean eastward turbulent surface stress but are generally weaker and smaller. The band of negative correlation near the coast, to the east of the Ob and Yenisei deltas, visible in correlation plots with eastward turbulent surface stress is also visible in July-August northward turbulent surface stress plots. This band of negative correlation is only significant in the central Kara Sea in August but is significant in the Vilkitsky Strait in July (Appendix Figure C.1). A band of positive correlation is also visible somewhere offshore in northward turbulent surface stress in all months. Whilst there are small regions where this positive correlation is significant in almost all months, there are only notable regions of significant positive correlation in August.

The August northward turbulent surface stress pattern is the largest, and closely resembles that of eastward turbulent surface stress in August, but with less extensive regions of significant positive/negative correlations. Most notably, these significant correlations are more extensive in the western Kara Sea than in the eastern Kara Sea. Unlike with eastward wind stress, the correlation pattern with September northward turbulent surface stress resembles that with August northward turbulent surface stress and has a notable (but smaller) region of positive correlation in the western Kara Sea, as well as the strip of significant negative correlation nearshore.

Wind stress SST

As for GLORYS12V1 SSS, spatial correlations between April-September eastward wind stress and GLORYS12V1 September SST are examined to understand the influence of zonal wind stress in controlling Kara Sea SST. Only correlations with June, July and August are shown here to be consistent with SSS (Appendix Figure C.2, left). The same is then done for northward wind stress (Appendix Figure C.2, right).

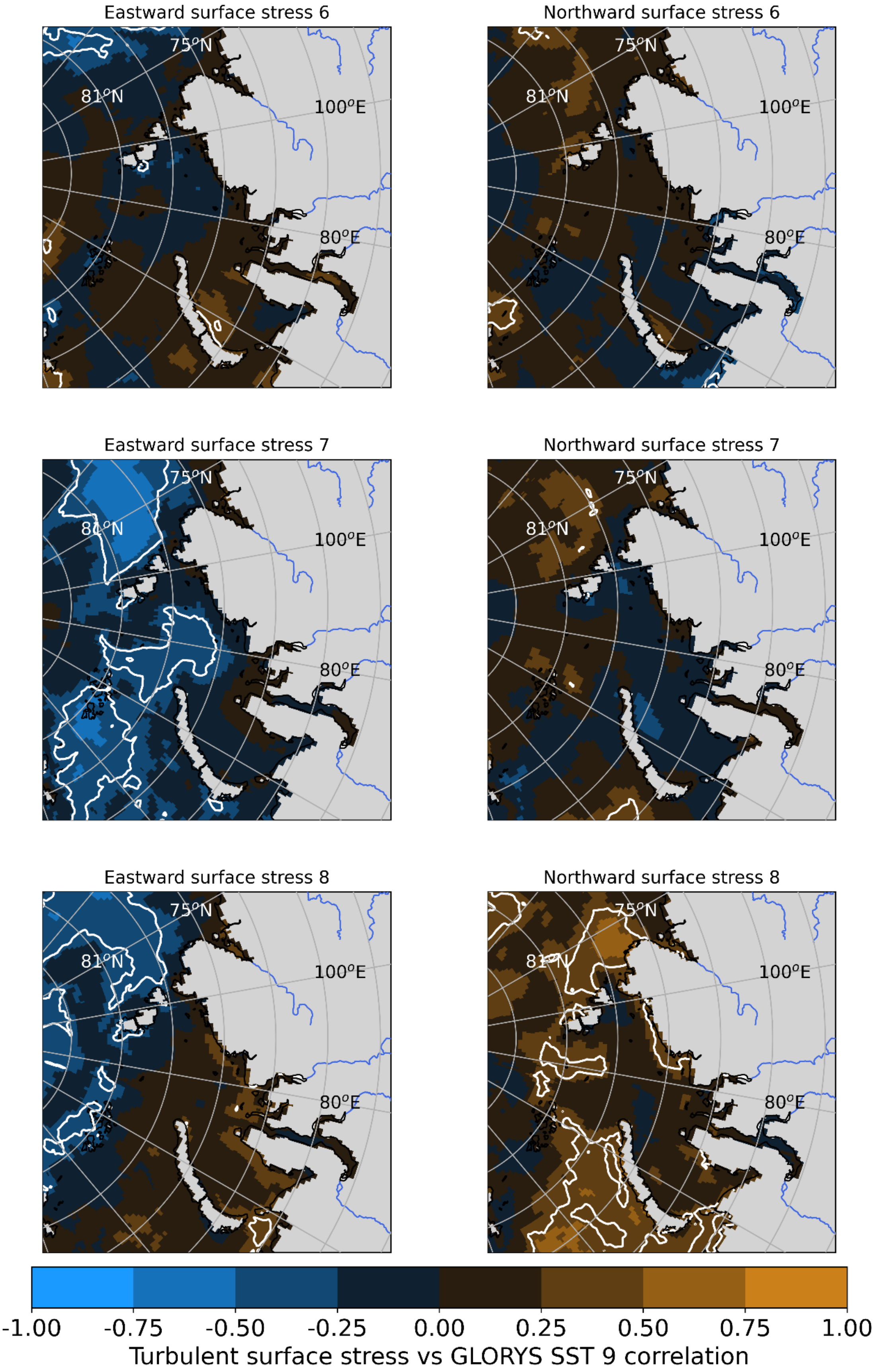

Appendix Figure C.2: Correlation between GLORYS12V1 September SST and ERA5 eastward turbulent surface stress (METSS) over June-August (6-8) over 1993-2022. Regions where correlations are statistically significant ($p \leq 0.05$) are denoted by the white contour and brighter colours.

The correlation patterns between eastward turbulent surface stress with GLORYS12V1 September SST are also notably different to those with GLORYS12V1 SSS and there is also no consistent correlation pattern in the three months shown (Appendix Figure C.2). There is a similar pattern in negative correlation pattern offshore in July and August. The regions where this correlation is significant differ by month. July eastward turbulent surface stress has relatively extensive regions of significant negative correlation (< -0.75) but these are only situated between 75 and 80 °N. August eastward turbulent surface stress has notable regions of significant negative correlation in the central Arctic, above 80 °N. August eastward turbulent surface stress also has small regions of significant positive correlation (> 0.75) nearshore, particularly in the eastern Barents Sea and western Kara Sea. No similar positive correlation pattern is visible in July. There are almost no regions of significant correlation between eastward turbulent surface stress in June and GLORYS12V1 September SST. Hence, whilst it is clear that July and August eastward turbulent surface stress is consistent with low SSTs offshore, there is no notable relationship with SSTs nearer shore in the central Kara Sea.

The correlation pattern of northward turbulent surface stress and GLORYS12V1 September SST over the 1993-2023 time period (Appendix Figure C.2) is notably different to that with eastward turbulent surface stress. There is also no consistent correlation pattern between GLORYS12V1 September SST and northward turbulent surface stress over the months shown. However, in all months there is a large region of positive correlation, which differs in areal extent and region. This positive correlation has no notable regions of significance in June or July. In August, there are multiple small regions of significant positive correlation in the eastern coastal Kara Sea, in the offshore Kara Sea, and in the eastern Barents and western Laptev Sea. There are no notable regions of significant negative correlation. Hence, whilst there is no notable correlation between June or July northward turbulent surface stress and SST in the Kara Sea, August northward turbulent surface stress is consistent with warm SSTs in the eastern Kara Sea.

Unlike with SSS, where both zonal and meridional wind stress appear to play a dominant role in controlling SSS, there are few regions in the Kara Sea where eastward / northward wind stress appear coincident with variability in SST. The only exception to this is in the coastal eastern Kara Sea, where August northward wind stress appears coincident with increased SSTs.

Wind stress SIC

As for GLORYS12V1 SSS and SST, spatial correlations between April-September eastward wind stress and GLORYS12V1 September SST are examined to understand the influence of zonal wind stress in controlling Kara Sea SST. Only correlations with June, July and August are shown here, consistent with SSS and SST (Appendix Figure C.3, left). The same is then done for northward wind stress (Appendix Figure C.3, right).

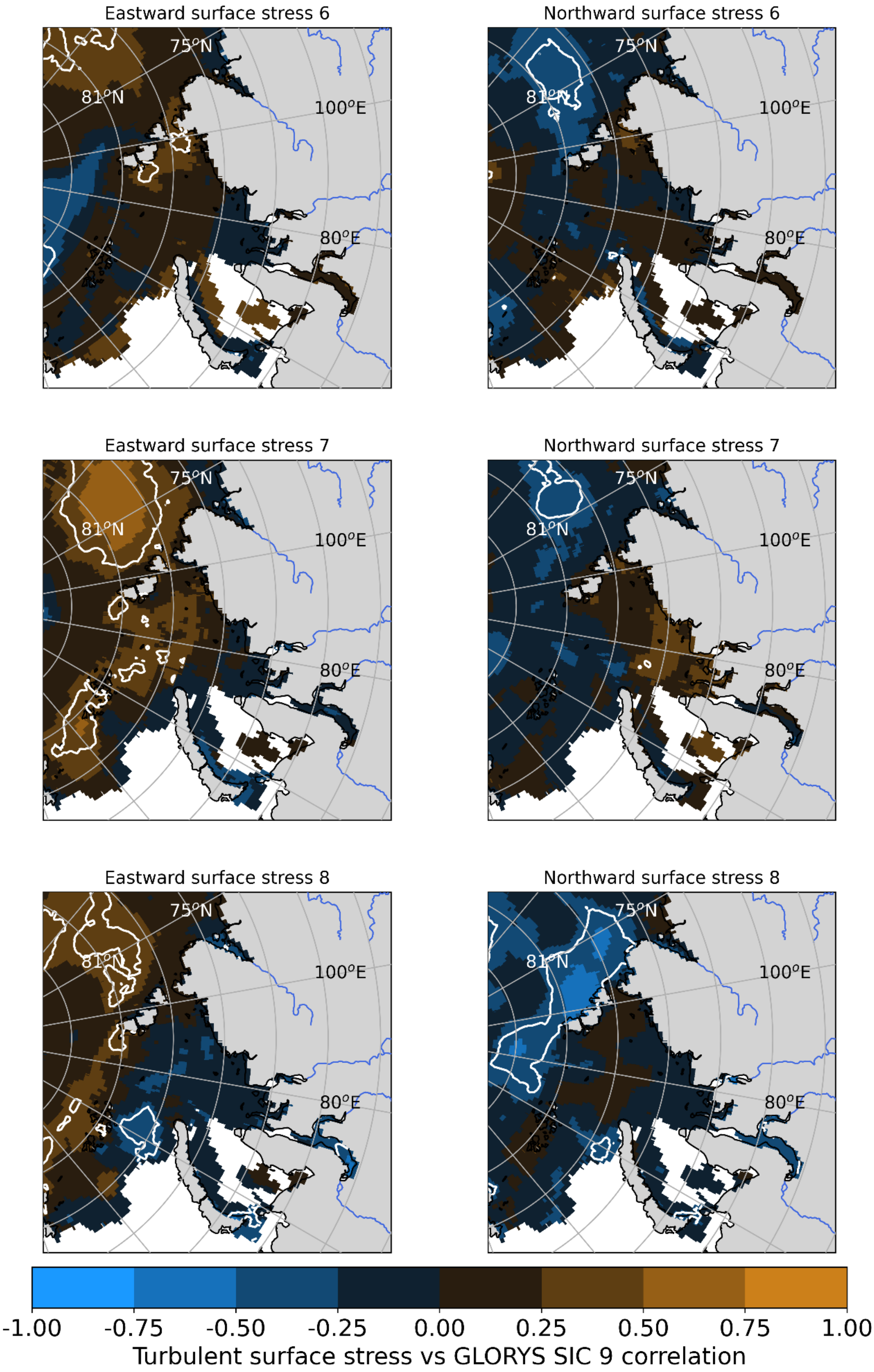

Appendix Figure C.3: Correlation between GLORYS12V1 September SIC and ERA5 eastward turbulent surface stress (METSS) over June-August (6-8) over 1993-2022. Regions where correlations are statistically significant ($p \leq 0.05$) are denoted by the white contour and brighter colours.

The correlation patterns between GLORYS12V1 September SIC and eastward turbulent surface stress for the 1993-2023 time period (Appendix Figure C.3) are almost the exact opposite of those with GLORYS12V1 September SST. Whilst there is no consistent correlation pattern over April to September, there is a relatively consistent pattern in the months shown. This pattern suggests a negative correlation nearshore, which shifts east from the Barents Sea into the Kara Sea over June to August, and a positive correlation offshore. The regions where this correlation is significant varies between months, and differs from the regions where eastward turbulent surface was significantly correlated with SST. The positive correlation pattern with SIC tends to only be significant in the central Arctic, above 77 °N. In August, the negative correlation pattern is only significant in parts of the eastern Barents Sea and western Kara Sea in July. The correlation pattern in June is notably weaker than the July and August pattern, with few very small regions of negative correlation in the Barents/Kara Sea. June eastward turbulent surface stress is very weakly positively correlated with GLORYS12V1 SIC over most of the Kara Sea, and over parts of the Laptev Sea. June turbulent surface stress has small regions where this positive correlation is significant, in the eastern Kara Sea, just west of the Vilkitsky Strait. This correlation pattern suggests June eastward wind stress is coincident with increased SIC in the eastern Kara Sea. Conversely, July and August eastward wind stress are consistent with low SIC in the western Barents and eastern Kara Sea, and increased SIC in the central Arctic.

As was true of eastward turbulent surface stress, the correlation patterns between GLORYS12V1 SIC and northward turbulent surface stress over the 1993-2023 time period (Appendix Figure C.3) are almost the exact opposite of those with GLORYS12V1 SST. As with correlations with GLORYS12V1 SST, there is no clear resemblance between correlation patterns of GLORYS12V1 SIC with northward turbulent surface stress and eastward turbulent surface stress. There are large regions of negative correlation between GLORYS12V1 SIC and northward turbulent surface stress in all months shown, but as with SST, these vary with month in areal extent and region. In August, this negative correlation extends throughout much of the western Laptev Sea. In June and July, there are small regions of significant negative correlation in the offshore western Laptev Sea. Hence, there are no notable regions where June, July or August northward wind stress appears to vary with SIC in the Kara Sea.

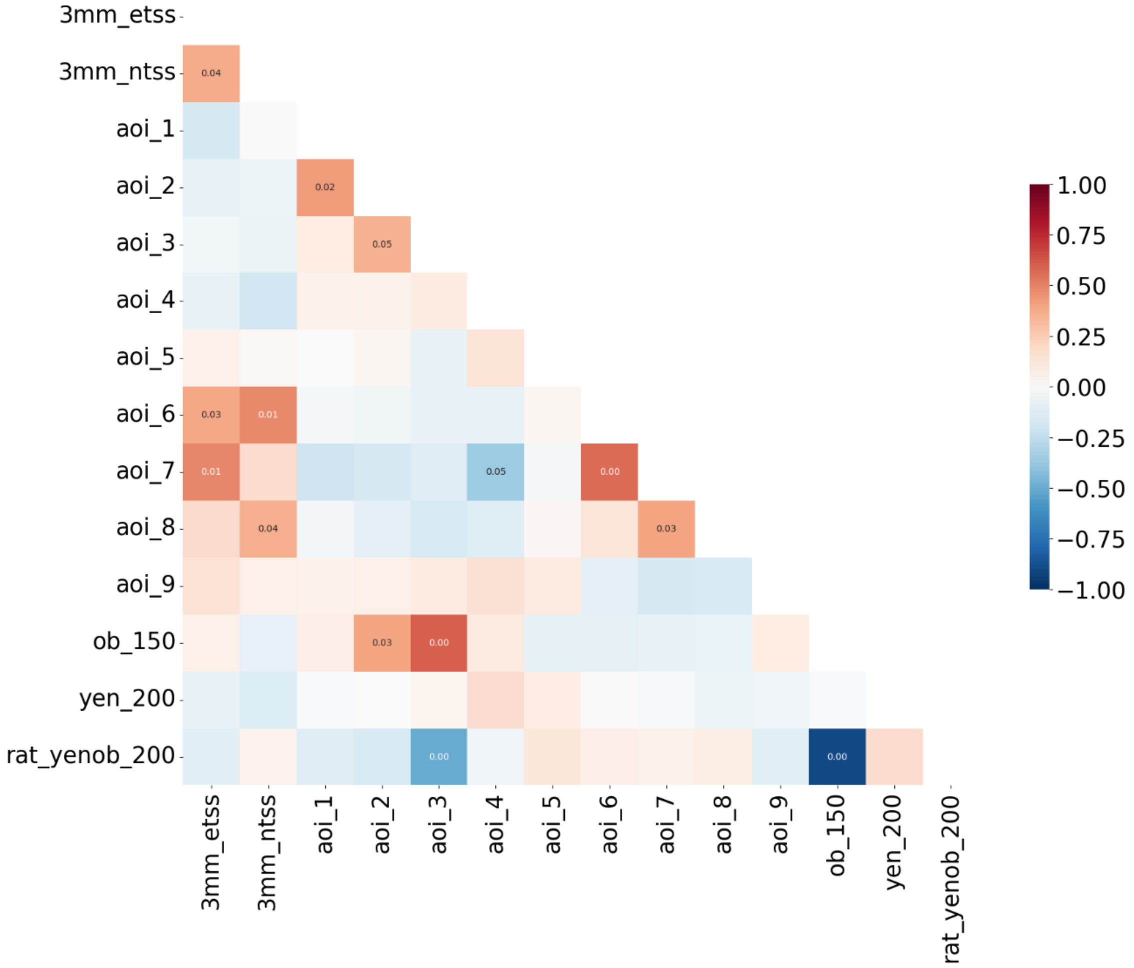

Appendix Figure C.4: Correlation matrix between June to August ERA5 eastward (3mm_etss) and northward turbulent surface stress (3mm_ntss), the AOI in different months and Ob and Yenisei runoff and their ratio (rat_yenob_200). The p-values of correlation coefficients are overlaid where correlations are significant ($p < 0.05$).

Appendix D Vilkitsky Strait additional figures

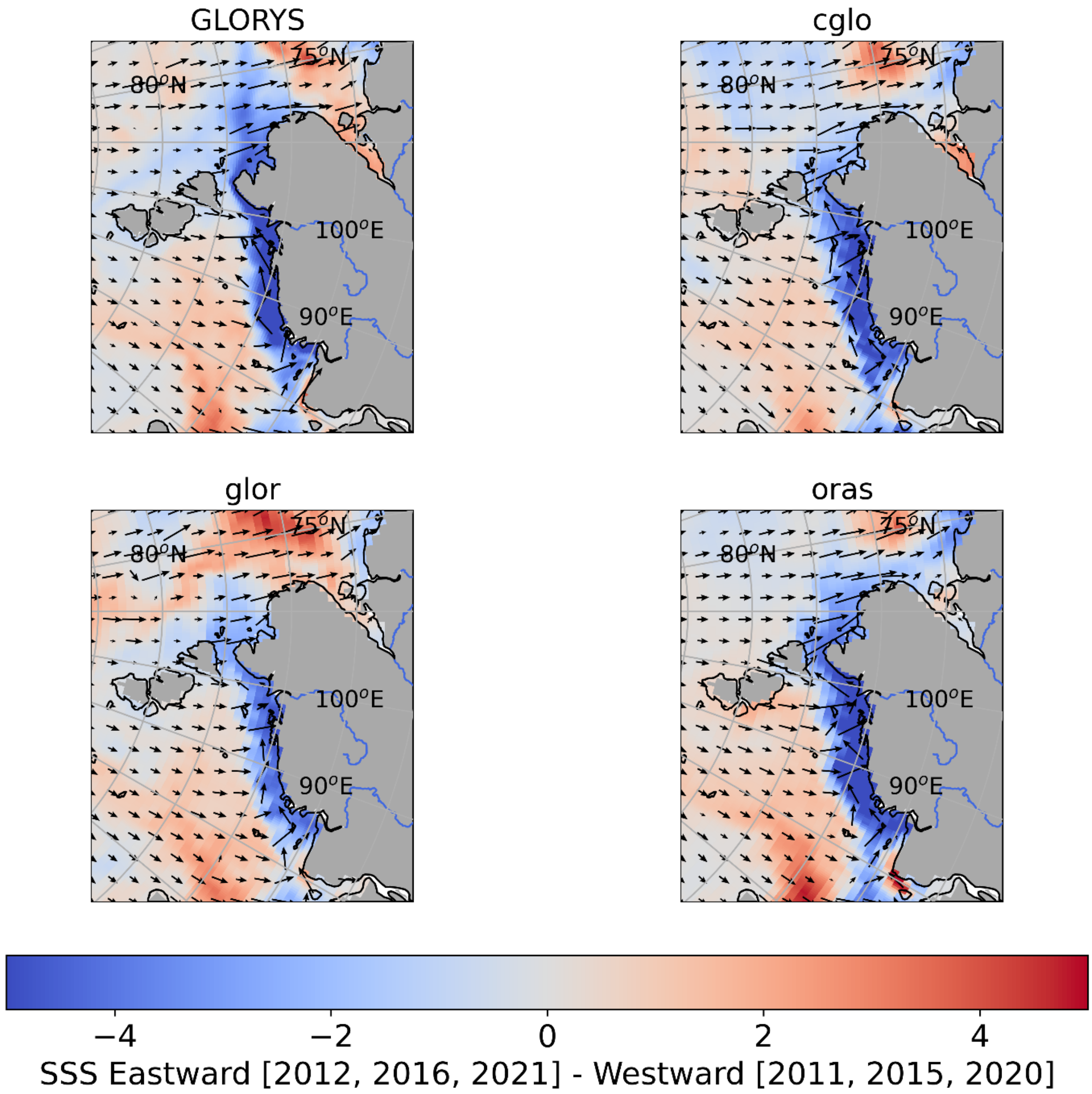

Appendix Figure D.1: The difference between eastward and westward September SSS composites calculated for GLORYS12V1 SSS, CGLO SSS, GLOR SSS, and ORAS SSS, from the identified three years of most eastward and westward wind forcing (over 2011-2023). Regions in blue represent regions with lower salinities under eastward wind forcing and regions in red represent lower salinities under westward wind forcing.

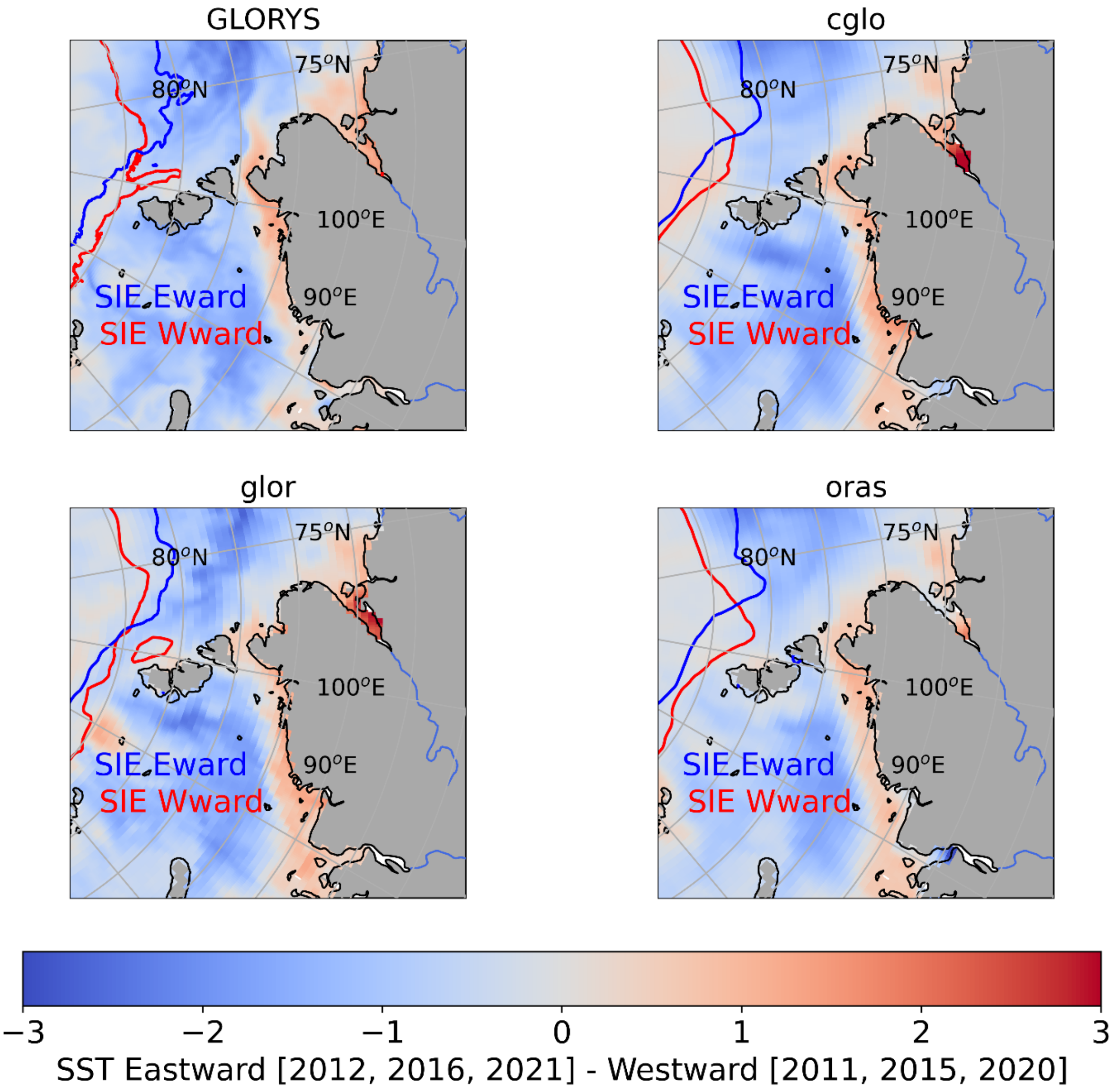

Appendix Figure D.2: The difference between eastward and westward September SST composites calculated for GLORYS12V1 SSS, CGLO SSS, GLOR SSS, and ORAS SSS, from the identified three years of most eastward and westward wind forcing (over 2011-2023). Regions in blue represent regions with cooler water under eastward wind forcing and regions in red represent warmer waters under westward wind forcing. The mean 30% sea ice concentration (SIE) is plotted under eastward (blue) and westward (red) wind forcing.

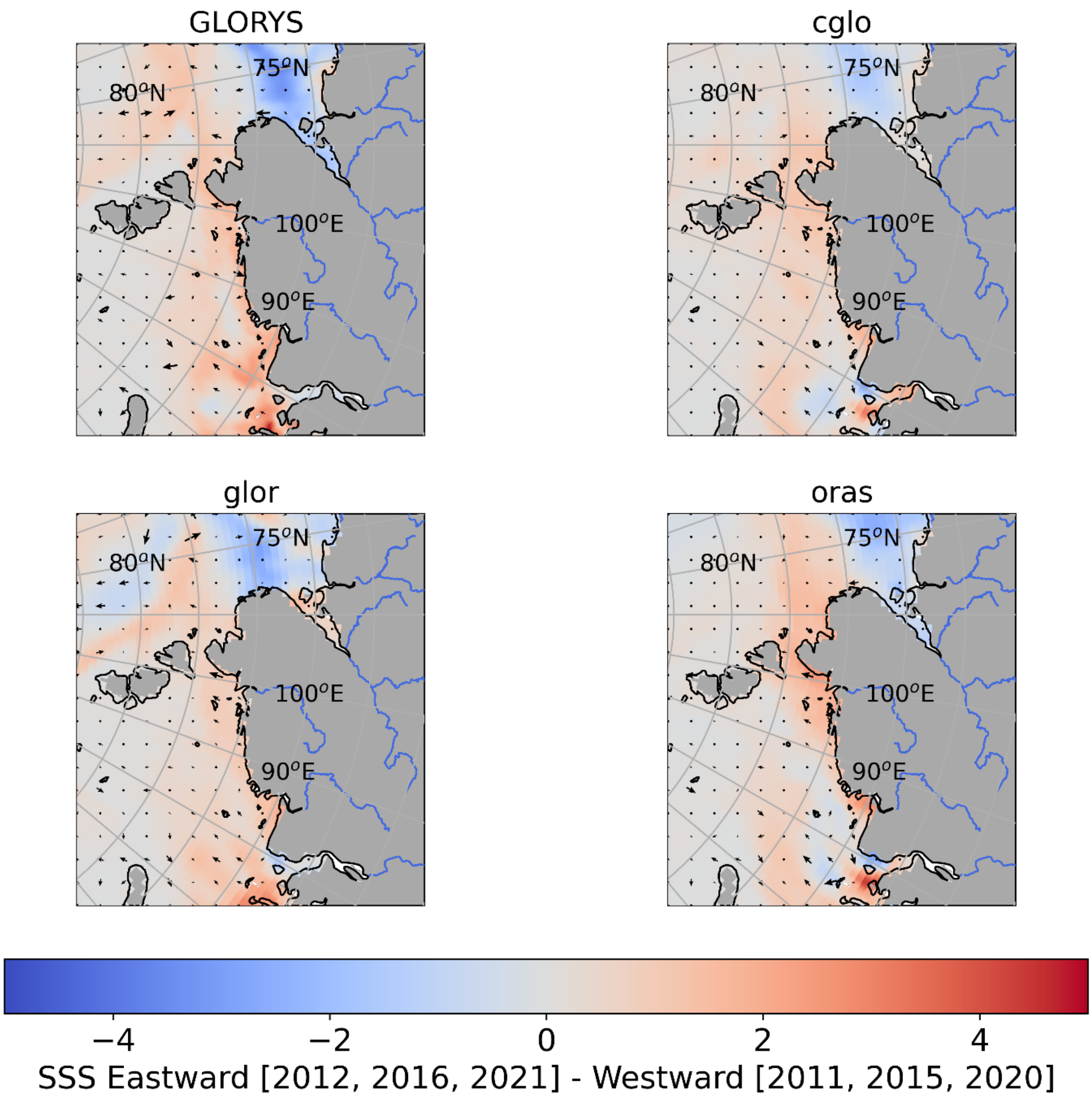

Appendix Figure D.3: The difference between eastward and westward March SSS composites calculated for GLORYS12V1 SSS, CGLO SSS, GLOR SSS, and ORAS SSS, from the year following the identified three years of most eastward and westward wind forcing (over 2011-2023). Regions in blue represent regions with lower salinities under eastward wind forcing and regions in red represent lower salinities under westward wind forcing.

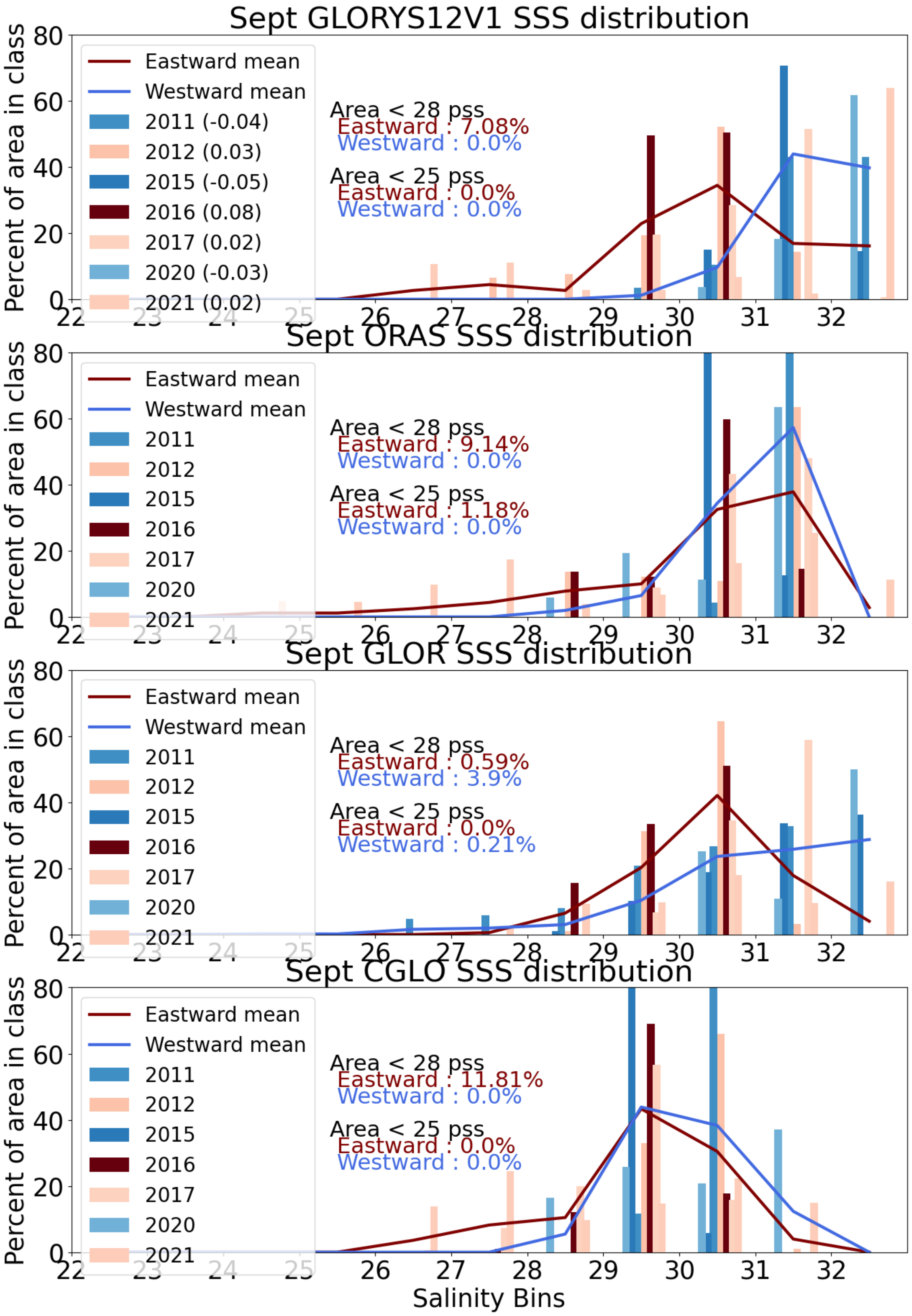

Appendix Figure D.4: Reanalysis SSS distribution in the Vilkitsky Strait for GLORYS12V1, ORAS, GLOR and CGLO for years of strong (> 0.02 N m^{-2}) eastward (red) and westward (blue) wind stress. The distribution is shown as the percentage of total area in each 1 pss salinity bin over the 22 to 33 pss range. The total area used is the common area where all satellite products have retrievals in all years. Darker red and blue colours indicate stronger eastward/westward wind stress. The mean values for all eastward (red) and westward (blue) years are overlaid as lines across all bins. The total percentage of cells below 28 pss and 26 pss in the eastward and westward means are overlaid as text.

Under westward wind forcing (2011, 2015, 2020), all reanalysis products have the highest percentage of the region in high SSS bins. For GLORYS12V1, on average under westward wind forcing, most (84%) of the total area was above 31 pss, with 44% between 31 and 32 pss, and 40% above 32 pss. For ORAS, on average, most of the area (57%) was between 31 and 32 pss, with 34% between 30 and 31 pss. For GLOR, on average, most of the area (29%) was above 32 pss, with significant proportions between 31 and 32 pss (26%) and between 30 and 31 pss (24%). For CGLO, on average, most of the area (44%) was between 29 and 30 pss, with significant proportions between 30 and 31 pss (38%) and between 31 and 32 pss (12%). Both ORAS and CGLO seemed to be the only reanalysis products without the saline bias (compared to satellite products and in-situ observations) as they both have 0% of the total area above 32 pss.

Under eastward wind forcing (2012, 2016, 2017, 2021), both GLORYS products (GLORYS12V1 and GLOR) have distributions shifted to lower SSS values (IE the largest proportions of the total area in lower SSS bins) but this is not true for ORAS or CGLO. For GLORYS12V1, on average under eastward wind, the majority (34%) of the area has SSS values between 30 and 31 pss, with a significant portion (23%) between 29 and 30 pss, 17% between 31 and 32 pss and 16% over 32 pss. For ORAS, on average, the majority (38%) of the area has SSS values between 31 and 32 pss, with a considerable proportion (32%) also between 30 and 31 pss, similar to under westward wind forcing. For GLOR, on average under eastward wind forcing, the majority (42%) of the area has SSS values between 30 and 31, with significant proportions between 29 and 30 pss (20%) and between 31 and 32 pss (18%). For CGLO, on average, most of the area (43%) was between 29 and 30 pss, with significant proportions between 30 and 31 pss (30%), similar to under westward wind forcing.

Whilst the distinction between SSS distribution under eastward and westward wind forcing is less clear in reanalysis products, most products do still show a difference. Under westward wind forcing, most reanalyses only have SSS values above 28 pss (0% of the total area is below 28 pss for GLORYS12V1, ORAS and CGLO), consistent with satellite products and in-situ data (except GLOR, which has 4% of the total area with SSS < 28 pss). Conversely, under eastward wind forcing, all products except GLOR have a higher percentage of area below 28 pss (7% for GLORYS12V1, 9% for ORAS, 12% for CGLO, 1% for GLOR) than under westward wind forcing. This pattern is consistent with that observed in satellite products. However, whilst satellite products suggest notable regions with SSS < 26 pss under eastward wind, only ORAS has SSS values < 26 pss under eastward wind forcing and has notably less area in this bin (2%) than most of the satellite products, and the in-situ data. GLOR is the only other product that ever has SSS values < 26 pss, but only suggests a very small region that falls within this bin (< 1%), and only under westward wind forcing (rather than eastward wind forcing as is suggested by satellite and in-situ data.

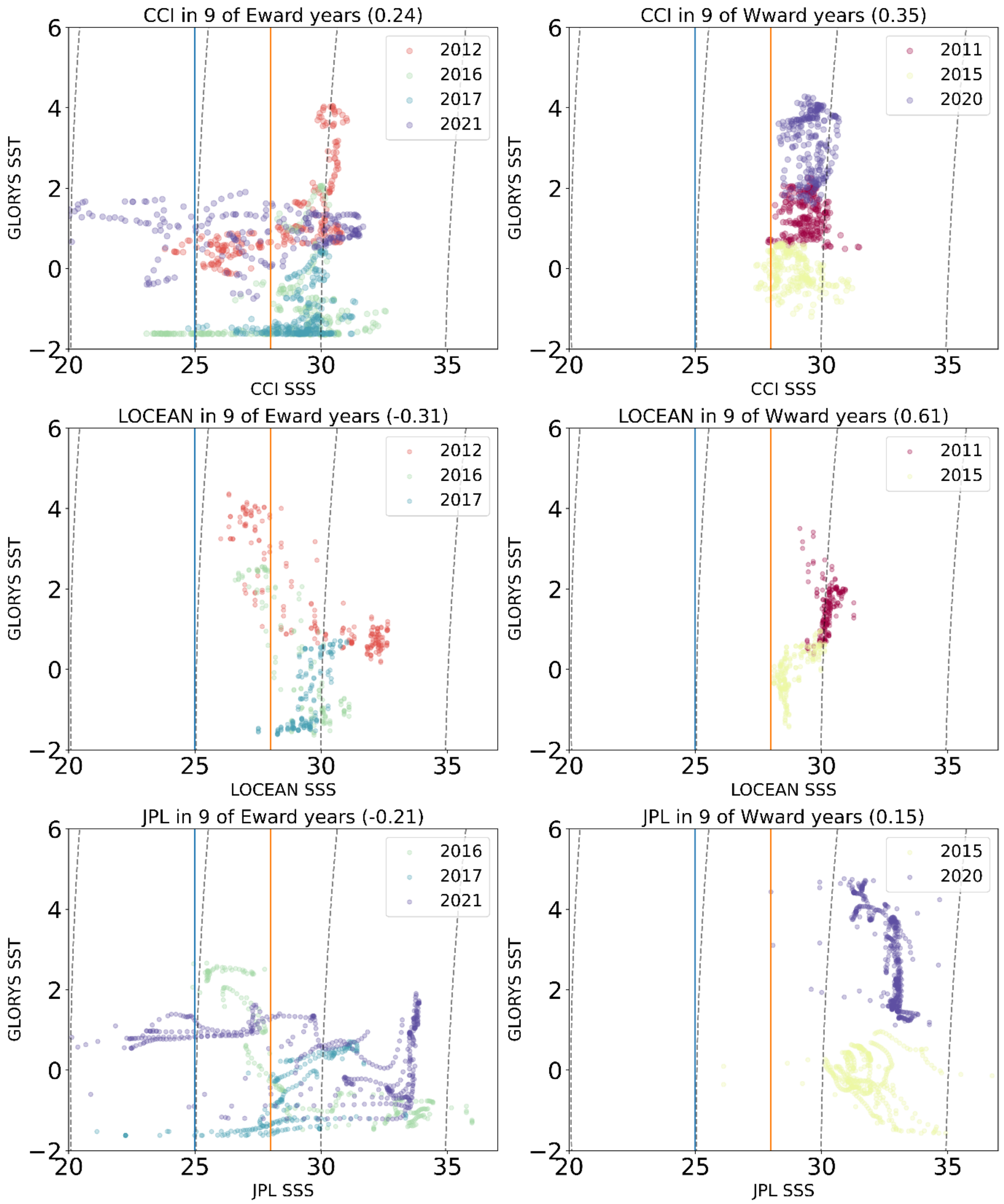

Appendix Figure D.5: Satellite TS plots in the Vilkitsky Strait for CCI, LOCEAN and JPL (vs GLORYS12V1 SST) for years of strong (> 0.02 N m^{-2}) eastward (2016, 2017, 2021) and westward (2011, 2015, 2020) wind stress. The data shown is over 77-80 °N and 100-115 °E. The 25 and 28 pss isohalines are overlaid in blue and orange. Correlations between SSS and SST are included in titles.

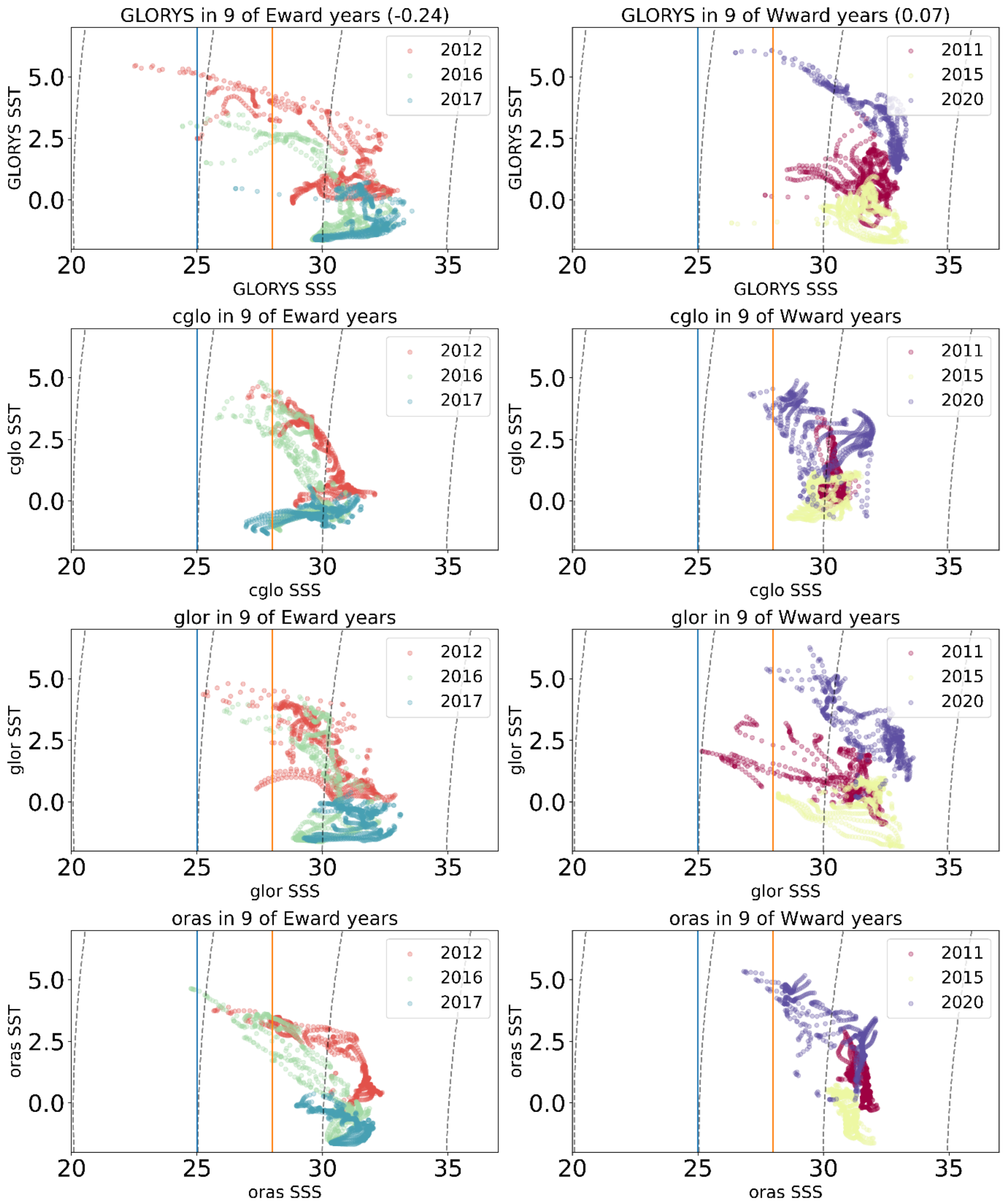

Appendix Figure D.6: Reanalysis TS plots in the Vilkitsky Strait for GLORYS12V1, ORAS, GLOR and CGLO for years of strong (> 0.02 N m^{-2}) eastward (2016, 2017, 2021) and westward (2011, 2015, 2020) wind stress. The data shown is over 77-80 °N and 100-115 °E. The 25 and 28 pss isohalines are overlaid in blue and orange. Correlations between SSS and SST are included in titles.